Tribological Investigation for Next-generation Polymeric Micro-systems

by
Zhongnan Wang

A thesis submitted in partial fulfilment of the requirements
for the degree of Doctor of Philosophy in Engineering

School of Engineering,
University of Warwick
United Kingdom

October 2016

Table of Contents

List of Figures

Chapter 1

Chapter 2

Chapter 3

Chapter 4

Chapter 5

List of Tables

Chapter 2

Chapter 3

Chapter 4

Chapter 5

Chapter 6

Acknowledgement

I would like to express my special thanks to my supervisors, Professor Derek Gordon Chetwynd and Dr. Ken Mao, for their academic guidance, constant encouragement, constructive advice and extremely valuable support throughout the whole my study.

I would like to thank my parents for their financial and moral support which made possible of my PhD study. I would not complete this work without their support and encouragement.

I was fortunate to work in a very pleasant group (Precision Engineering and Surfaces); I would also like to take the opportunity to appreciate Dr. Xianping Liu, Dr. Haroon Ur-Rashid, Dr. Khalid Thamer Althagafy, Dr. Huaiju Liu, Dr. Lei Wang, Dr. Xinyao Zhu, Mrs. Hui Niu and Ms. Zedong Hu from the University of Warwick for their fruitful discussions and valuable advices.

Many thanks to Mr. David Robinson and Mr. Martin Davis for their meticulous supports in the laboratory.

Declaration

This thesis is submitted in accordance with the regulations for the degree of Doctor of Philosophy by the High Degree Committee at the University of Warwick. The work described in this thesis was conducted by Zhongnan Wang, under the supervision of Prof. Derek Gordon Chetwynd and Dr. Ken Mao in the School of Engineering, University of Warwick between the dates of Nov. 2012 and Oct. 2016. Information derived from the published or unpublished work of others has been acknowledged in the text and a list of references is given. This thesis has not been submitted in any previous application for a higher degree.

Signature:

Date:

Abstract

The development of micro-fabrication processes for 3D microstructures has led to the production of low-cost, low-energy devices at millimeter scales known as MEMS for a wide range of electronic, mechanical, mechatronic and biomedical applications. As surface-to-volume ratio increases drastically with decreasing dimension, surface properties of the materials are the prominent factor at the interface between two solids and consequent tribological issues such as adhesion, friction and wear will arise in MEMS devices when surfaces are in, or have the potential for, sliding contact. Measurement techniques and principles used in micro-tribology are quite different from those in macro-tribology. Various specialized micro-tribometers have attracted recent attention in attempts to obtain consistent, accurate tribological measurements that could provide information for the design of MEMS components. However, even these have operational parameters quite different to those in the regime typical of MEMS devices. For example, the thermal properties of polymers might mean that they are especially sensitivity to the speeds and reciprocating scan frequencies of measurements. This is a serious concern because the selection of appropriate materials for such applications is very important in order to reduce not only friction and wear, but also the stiction of the parts. The immediate challenge is that there is very little reliable information about the properties of this new generation of engineering materials because of insufficient understanding and characterization of their behaviour at the microscale under a wide range of experimental conditions.

With these points in mind, this thesis aims to prompt wide study of the micro-tribological properties of polymers for MEMS applications, providing preliminary new data on them while exploring in some detail possible uncertainty effects that could arise from the testing regimes of most micro-tribometers. It starts by re-commissioning and characterizing a unique, wide-bandwidth prototype micro-tribometer developed at Warwick, establishing good operating procedures by comparing measurements on materials widely discussed in the literature. New data has been collected on an acrylate resin typically used for micro-stereo-lithography, PTFE and oxide-coated silicon. It suggests that deviations from Amonton's law in the ten millinewton range might be less severe than previously reported. Observing that the skill and time required for such testing makes it unattractive for a production control environment, the thesis then explores, via contact modelling, whether there is a useful correlation between Berkovich tip nano-hardness and the micro-friction of the polymeric samples: several plausible modelling assumptions are shown to lead to inconsistencies. Final discussions and recommendations consider how to move on from these experimental scoping studies to acquire detailed evaluations of the properties of the best candidates under typical usage conditions prior to designers of potential products taking these materials and processes at all seriously.

List of Abbreviations and Acronyms

ADC	Analog-digital converter
AFM	Atomic Force Microscope
CoF	Coefficient of Friction
DAC	Digital-to-Analog Converter
DAQ	Data Acquisition
D.C.	Direct Current
DDM	Direct Digital Manufacture
DLC	Diamond-like Carbon
FFM	Friction Force Microscope
FOS	Fiber Optical Sensor
HFCVD	Hot-filament Chemical Vapor Deposition
LIGA	Lithographie, Galvanoformung and Abformung
LPS	Linear Positioning System
MEMS	Micro-Electro-Mechanical System
MSL	Micro-Stereolithography
NCD	Nanocrystalline Diamond Films
NEMS	Nano-Electro-Mechanical System
NIST	National Institute of Standards and Technology
PDMS	Poly-dimethyl-siloxane
PMMA	Poly-methyl-methacrylate

PTFE	Poly-tetra-fluoro-ethylene
PSI	Phase-shifting Interferometry
RMS	Root Mean Square
SEM	Scanning Electron Microscope
SFM	Scanning force microscope
Si	Silicon
SiO_2	Silicon Dioxide
SL	Stereolithography
TiC	Titanium Carbide
UMT	Universal Mechanical Tester
UV	Ultra-violet
VSI	Vertical-scanning Interferometry
2D/3D	Two/Three Dimensional

List of Symbols

a contact radius

$a(t)$ acceleration

A contact area

A_p the projected contact area of the indent at the peak load

b the unloading curve

c the short dashed line

E elastic modulus

E^* plane strain modulus

E_{ball} the elastic modulus for the ball

E_e the effective elastic modulus

E_{flat} the elastic modulus for the flat

E_i the given elastic modulus of the diamond indenter

E_{IT} the Young's modulus of the specimen

E_r the reduced modulus

f the reciprocating frequency

F the applied dead weight

F_a the adhesion force

F_c the actuator demand force

F_f friction force

F_k the tangential forces to maintain the relative movement between two surfaces

F_N the externally applied normal force

F_0 the amplitude

F_{plough} the force required to push material aside so as to maintain a constant depth of indentation of one part into the other (the ploughing effect)

F_s the tangential forces to prevent the relative movement between two surfaces

F_{shear} the lateral force required to overcome the shear strength of the interface layer assumed to be "welding" the surface together wherever there is real contact

F_{total} total normal force

G gain

h the indentation depth

H hardness

h_c contact depth of the indenter with the sample

h_p the permanent indentation depth

h_r the tangent indentation depth and calculated

h_s the elastic surface displacement at the perimeter of contact

$\hat{k}$ the measurement estimates for stiffness

k_x the beam stiffness constants for vertical axes

k_z the beam stiffness constants for lateral axes

L displacement

m the total mass of the reciprocating mechanism

m a constant factor dependent on the geometry of the indenter shape.

N the force applied to the interface between the sliding bodies

P contact pressure

P_0 the maximum contact pressure

R an elastic sphere with the radius

R_a 2D average surface roughness

R_q root mean square

S the sensitivity of the sensor.

S the contact stiffness

S_a 3D average roughness

S_{ku} kurtosis

S_{sk} skewness,

S_z the sensitivity of the vertical actuator

V the output voltage of the sensor produced by deflection of the sensing beam

V_A the voltage amplitude

v the velocity

$v(t)$ the scan speed of the notch-hinge mechanisms

W the applied load

Δx the voltages of the deflection of the sensing-beam measured by the lateral sensor without applied loads in the vertical position

Δx_n the voltages of the deflection of the sensing-beam measured by the lateral sensor with applied loads in the vertical position,

Δz the voltages of the deflection of the sensing-beam measured by the

vertical sensor without applied normal forces in the vertical position.

$\Delta\hat{z}$ the measurement estimates for deflection

Δz_n the voltages of the deflection of the sensing-beam measured by the vertical sensor with applied normal forces in the vertical position.

φ initial phase-angle of the electromagnetic driving force.

δ the deflection of the sensing beam

δ depth of indentation

ε a geometric constant dependent on the indenter shape

σ tensile strength

τ shear strength of the material at the interface surface.

λ_s the related contact stiffness

β the geometric factor which is dependent of the shape of the indenter tip

ω the circular frequency of the electromagnetic driving force

μ coefficient of friction

μ_k kinetic friction coefficient

μ_s static friction coefficient

υ Poisson's ratio

υ_{ball} Poisson's ratios for the ball

υ_{flat} Poisson's ratios for the flat

υ_i Poisson's ratio of the diamond indenter

1 Introduction

Overview

This chapter gives a brief description relevant to MEMS tribology. The research motivation of the project is introduced here together with the layout of the thesis.

1.1 Overview and Current Challenges of MEMS Tribology

In recent years, the development of various fabrication techniques and design strategies, including bulk micro-machining and surface micro-machining for two dimensional (2D) microstructures, and other micro-fabrication processes for 3D microstructures, such as the LIGA (Lithographie, Galvanoformung, and Abformung) process and the micro-stereo-lithography (MSL) process, has led to the production of low-cost, low-energy devices at millimeter scales, or smaller, known as micro-electromechanical systems (MEMS) for a wide range of electronic, mechanical, mechatronic and biomedical applications (Xu, 2011). Xu (2011) has provided a convenient summary of these developments. These MEMS devices can be largely classified into actuator-based and sensor-based systems; the former undergoes relative mechanical motion such as micro-motor, mini-robots, micro-shutters and micro-gears while there are only sensing elements in the latter case (Singh, 2013).

As surface-to-volume ratio increases drastically with decreasing dimension, surface properties of the materials are the prominent factor at the interface between two solids and the consequent tribological issues such as adhesion, friction and wear will arise in the actuator-based devices when surfaces are in, or have the potential

for, sliding contact. Adhesion is the main reason that leads to early failure of micro-devices, while friction and wear will have great influence on smooth operation and lifespan of productions. Obviously, tribological investigation is critical to control these barriers and promote development for the next generation of micro-devices (Liu, 2003). The increasing use of polymeric materials with poorly characterized surface-dominated phenomena with little reliable information in the public domain adds further to the needs.

However, measurement techniques and principles used in micro-tribology are quite different from those in macro-tribology or nano-tribology. On the one hand, conventional macro-tribotesters are not suitable for evaluating tribological properties of materials used in MEMS applications where sliding occurs over small displacements in the range of micrometers and the contact loads are a few micro/milli-newton in these devices (Bhushan, 1995). On the other hand, compared with nano-tribology measurement techniques, larger contact area and higher sensor sensitivity are involved in micro-tribometers. Currently, many tribological test methods and apparatus have been adopted for the analysis of the friction mechanisms at the micro-scale, as will be explored in more detail later. Many investigations in micro-scale measurements have been conducted using commercial atomic force microscopes (AFM). However, interaction studies between an AFM tip and a sample are not of the sliding interface of interest as an AFM tip generally simulates a single asperity contact. The fabrication of custom-built micro-devices is another approach to measure adhesion, friction and wear (Tanner, 1999). However, it

has many disadvantages such as the high manufacturing costs, low reproducibility from device to device and non-direct acquisition of the tribological data, which lead to a lack of widespread applications. Therefore, in many recent studies, various specialized micro-tribometers have attracted increasing attention as they are not only used for contact simulation and consistently accurate tribological measurements in the regime typical of MEMS devices, but also provide information for the design of MEMS components.

The paper (Miller, 2010), in 2010, reported an example of using an AFM, a micro-tribometer, and a macroscopic tribometer to investigate the lubrication performance of a bound self-assembled monolayer (perfluorodecyltrichlorosilane, PFTS) with and without a lubricant (tricresyl phosphate, TCP), over a broad range of contact stresses and length scales in sliding contact. From Figure 1.1, a lateral force AFM was used for a nanometer-scale model single-asperity contact at relatively high mean contact stresses (about 1.8 GPa), whereas a reciprocating micro-tribometer applied higher mean contact stresses (around 2 GPa) for micrometer-scale measurements. However, a macroscopic reciprocating tribometer was used for millimeter-scale tests at relatively low mean contact stresses (about 0.6 GPa). These experiments span contact pressures and length scales both above and below MEMS operational specifications.

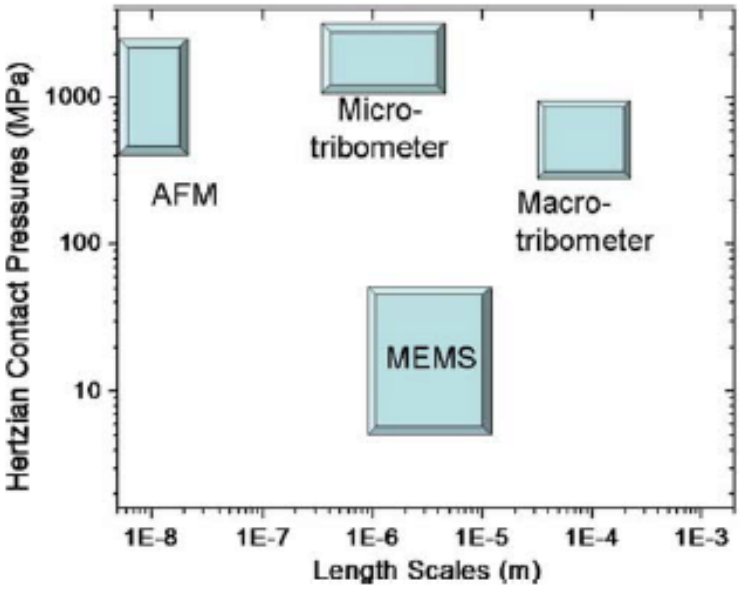

Figure 1.1 Schematic showing contact pressures and length scales of tribometer families compared to a MEMS device (Miller, 2010)

Many engineering materials such as silicon, ceramics, metals, polymers and composites are applied to MEMS fabrication for applications within various industrial fields. Currently, as the basic material for the majority of actuator-based micro-devices, many studies have concentrated on various special films, coatings and protective layers, ranging from a few monolayers (i.e., about a nanometre) to micrometre thicknesses, to improve the tribological properties of silicon, which has high surface energy and inherent brittleness (Kim, 2007; Maboudian, 1997). Although many research approaches in micro-tribology, such as molecular dynamics analysis and experimental testing methods, have been extensively used for tribological investigations of many kinds of micro-devices and considerable amounts of engineering data have been obtained, adding a whole range of fundamentally interesting and valuable measurements in MEMS devices from μm to

mm scale mechanisms is yet to be done. Recently, more and more designers are eager to learn more about the properties of a new generation of engineering materials because they lack sufficient understanding and characterization data of materials behavior at the microscale under a wide range of experimental conditions.

1.2 Project Motivation

The motivation and rationale for this work arise from the potential for several manufacturing routes, including direct digital manufacture (DDM), for making various kinds of devices at millimeter scales and some at slightly smaller scales that are included by some, but not all, authorities within the class of MEMS. They offer potential in biomedical applications (implanted prosthetics; implanted or consulting room micro-analysis), transportation (low-mass sensing and actuation) and other industrial applications (micro-motors, micro-gears and micro-shutters) (Bhushan, 1999; 2005; 2007). The basic material for these process routes is always a polymer resin; there is great scope for adding micro- or nano-powders to produce composites with specifically customized functions: e.g., to give electrical or magnetic properties, to add, e.g., alumina for strength and stiffness, to add carbon for mechanical and sensor properties, *etc*. Friction and wear have not been important in previous uses but will be so in production devices that involve sliding motion. For small mechanisms, the contact force and wear will be small and it is widely known that many material combinations do not have friction coefficients independent of load once it reduces to the sub-N regime (Corwin, 2004). However, under these

conditions, instrument designers face some challenges from contact, friction and wear of research materials in micro-tribological measurement, which result inevitably in compromises in the actual testing. Current research in the aspect of important micro-tribological techniques and measurement principles for investigation of friction mechanisms has aroused wide concern. Micro-tribometers have largely been used for study of surface properties or special applications (coatings) (Kaneko, 1996). The immediate challenge is that very little reliable information about the mechanical properties of DDM materials (polymers of certain type) currently exists, and virtually nothing relating to functionalized composite materials. In the case of tribological properties, we note also that typical applications may well involve sub-newton contact forces, a regime where it is well known that the standard empirical laws of friction (Amontons' laws) (Tichy, 2000) tend to become imprecise. Prior to designers of potential products taking these materials and processes at all seriously, it is therefore necessary first to provide experimental scoping studies and then acquire detailed evaluations of the properties of the best candidates under typical usage conditions. The current project concentrates on the potential for use of polymers and closely associate micro-tribological properties in these types of situation, as the selection of appropriate materials for such applications is very important in order to reduce not only friction and wear, but also the stiction of the parts.

With these points in mind, the present PhD project aims to explore and quantify some uncertainty effects likely to be present in most micro-tribometers. Also,

bearing in mind the potential for compensation of such uncertainties, to study and report on the micro-tribology of a range of materials suited to additive manufacture, hoping thereby to establish some design rules for their application. Finally, in pursuit of these aims, specific objectives include:

1. Re-commissioning a unique prototype micro-tribometer developed at Warwick.

2. Use its force control features and high bandwidth, to quantify sensitivity to normal force variations carried by non-ideal specimens.

3. Run and analyse the data from the updated test systems with the DDM materials. We expect that this dependency is higher with polymers than with other classes of materials, because of their thermal characteristics and surface chemistry, so bulk property data of them is likely to be especially unreliable in our context.

4. Use the tribometer as a non-destructive diagnosis tool for MSL polymeric materials on the ball-on-flat configuration and polymer coatings on the crossed-cylinder configuration.

1.3 Layout of the Thesis

This thesis deals with a broad content of instrumentation re-installation, re-calibration, development and tribological investigation of diverse engineering materials with various tribological test configurations and conditions. The background of micro-tribology and the motivation of the project research are briefly introduced in Chapter 1 together with the layout of the thesis. Following this, Chapter 2 gives literature reviews presented in the respect of micro-fabrication

technology and friction mechanisms at the micro-scale, micro-tribology issues of MEMS and research progress of the micro-tribology instruments including commercial systems and self-developed micro-tribometers.

Chapter 3 involves description and critical review of the main micro-tribometer instrument for the majority of the work in parallel with re-commissioning and re-calibrating experimental systems. The instrument is the design by Alsoufi (2011), which offers suitable force ranges, a better operational bandwidth than conventional systems and, crucially, a 'constant force' mode which corrects for the effects of non-flat specimen surfaces. Then, the machine has been reset for the present work, with potential advantages in developing modified control software (in LABview®) for efficient data recording and the re-calibration results for the micro-tribometer measuring-head and the reciprocating motion mechanism are discussed with the original ones.

Following the re-calibration, Chapter 4 further demonstrates the potential of the micro-tribometer by amounts of illustrative experimental results on harder surfaces of some typical materials including steel, glass and silicon wafer with silicon dioxide film with a range of test conditions relevant to sliding speeds, sliding distances and applied forces under dry sliding conditions where there are no applied lubricants. They provide some new information from materials already documented in the literature. Surface topographic characterization for test materials is first measured to test for any correlation between the sample surfaces and their friction properties. Then, approaches to tribometer signal processing and calculation of

friction measurements, at the micro-scale are analysed. This highlights and explores the computational accuracy of friction measurement at the micro-scale. Finally, test results are obtained, analysed and compared to theoretical calculation and other experimental tests to sufficiently demonstrate the validity and consistency of the developed test system with ball-on-flat configurations and crossed-cylinders configurations.

Having now established that the updated micro-tribometer is a reliable tool, Chapter 5 concentrates on nominally flat polymeric specimens of R11 resins, which derive from micro-stereo-lithography, and PTFE that might be found in micro-mechanical system. The overall procedure is broadly similar to, with test conditions informed by the results of, those for the test materials in Chapter 4. For each material a steel counterface is used; all data on them are novel. This addresses one of the major motivations for this work by observing some behaviour patterns of the polymer materials, noting their variability and paving the way for future work.

In Chapter 6, nanoindentation tests are executed to explore the correlations between nano-indentation measurement and micro-friction. First, MEMS materials and MSL polymeric materials, including silicon wafer with silicon dioxide coating, PTFE, and acrylic-based R11 resin, are chosen to measure their mechanical properties including the elastic modulus, hardness, indentation depth and contact area using nanoindentation tester with a Berkovich indenter tip. Then, mathematical modelling is carried out to examine the friction force, coefficient of friction (CoF) and Berkovich nano-indentation against applied normal loads to obtain comparisons

between the contact model theories and experimental investigations. Theoretical predictions of friction measurements for a ball-on-flat configuration at the micro-scale are compared to the trends of experimental friction force and CoF with the similar normal loads.

Finally, Chapter 7 draws conclusions about the work presented in this thesis with a summary of its highlights and indicates the directions of future research.

2 Literature Review

Overview

This chapter gives an overview of the main concerns and contributions that are related to the interests of this thesis. A brief description starts with fabrication techniques and related friction mechanisms for microstructures. A more detailed review is given for current research in mN tribology with an extensive list of references about friction coefficient vary with normal force and MEMS materials tribology. Research progress in micro-tribology instruments, including commercial systems and their limitations, is introduced together with custom-built micro-tribometers.

2.1 Microfabrication Technology and Micro-tribology of MEMS Devices

2.1.1 Overview of Micro-Fabrication Technology

Compared with macro-scale counterparts, many small-size, low-energy devices can be fabricated with various microsystem technologies, common ones being bulk micromachining, surface micromachining, the LIGA process and the MSL process. The first two approaches use the planar fabrication processes developed for 2D structural semiconductor devices, while the latter two processes can produce 3D MEMS devices (Kovaks, 1998; Gardner, 2005).

Bulk and surface micromachining are both commonly used and between them cover the majority of current MEMS device fabrication. However, the process of bulk micromachining is entirely different from that of surface micromachining. Bulk micromachining is a process that first creates structures on the substrates with various techniques, generally involving creating masks for subsequent etching processes, and then obtains the desired structures for the MEMS device by

selectively removing materials from the substrates. In contrast, during the surface micromachining process layers of materials, which will become a part of the structure of the MEMS device, are added to build mechanical structures on top of the substrate and then some of the added materials are selectively taken away. Single-crystal silicon is the basic material used in bulk micromachining whereas polycrystalline silicon (polysilicon) is the most common material in surface micromachining (Maboudian, 2002). Figure 2.1 and Figure 2.2 show the basic steps in typical bulk and surface micromachining processes, respectively (Adams, 2010; Niels Tas, 2000).

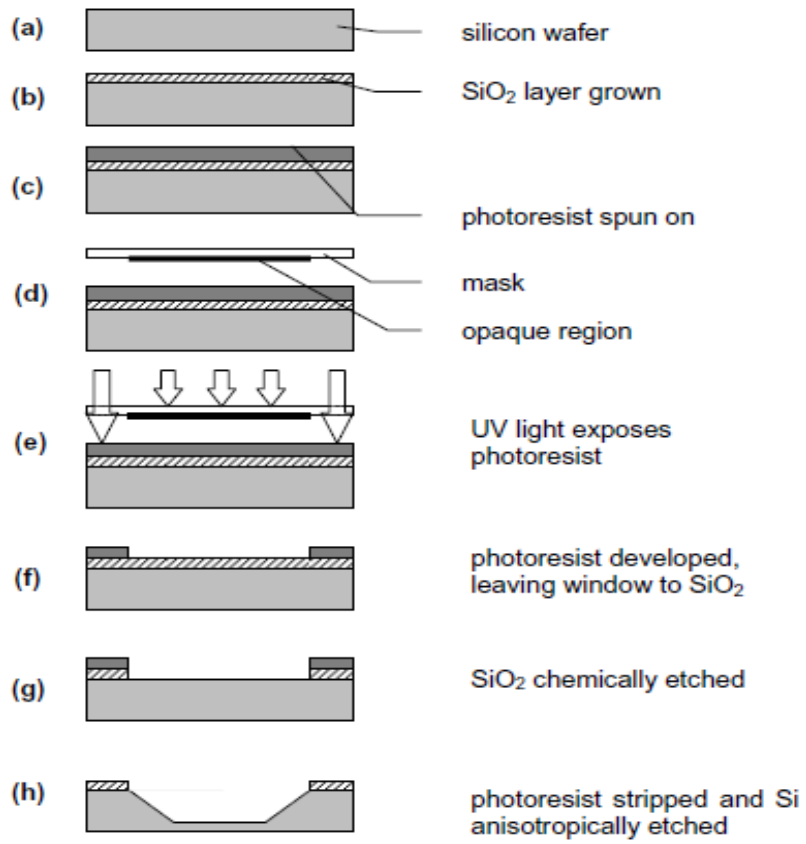

Figure 2.1 Steps in a typical bulk micromachining process (Adams, 2010)

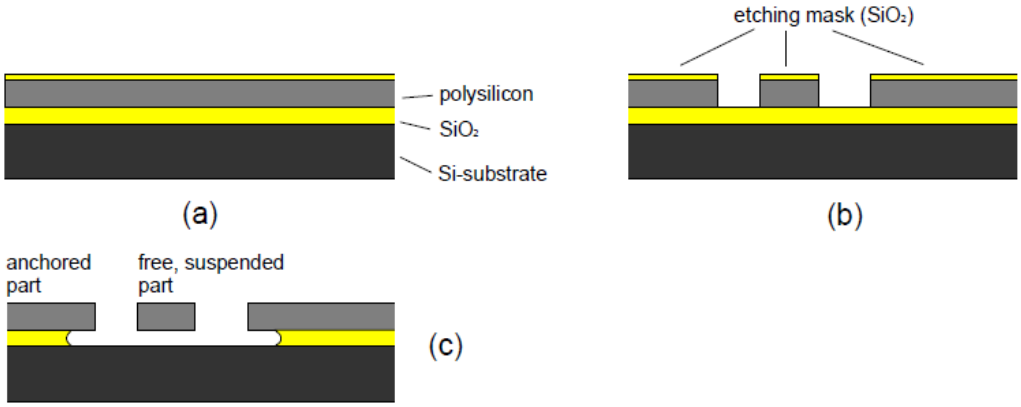

Figure 2.2 Basic steps in surface micromachining (Niels Tas, 2000)

Growing recent interest in fabricating 3D microstructures using various materials has led to the development of many novel 3D microfabrication techniques, with the LIGA process and MSL technique the most frequently-used. LIGA is a German acronym for Lithographie, Galvanoformung, Abformung (Lithography, Electroplating, and Molding) that describes a fabrication technology used to create high-aspect-ratio microstructures. The two most important LIGA-fabrication technologies are X-Ray LIGA and UV-LIGA, each of which is composed of three main processing steps: Lithography, Electroplating, and Moulding (Takada, 1997; Mohr, 1988; Munchmeyer, 1992; Ehrfeld, 1991). X-rays produced by synchrotron are used in X-Ray LIGA to create high-aspect-ratio structures, while UV-LIGA adopts a more accessible method that uses ultraviolet light to create structures with relatively low aspect ratios. The basic process is one of exposing polymers to radiation patterns to modify their properties, and UV penetrates less well into the resins. Figure 2.3 describes the schematic view of each

phase of LIGA process (Hirata, 2003). Although the LIGA process is valuable and important in offering a broad range of materials from polymers to metals, alloys, silicon and ceramics compared with other technologies, it is currently too expensive, slow and unreliable for many industry applications and also there is a lack of resources to establish professional manufacture. In any case, LIGA still retains the potential for large-volume mass manufacturing.

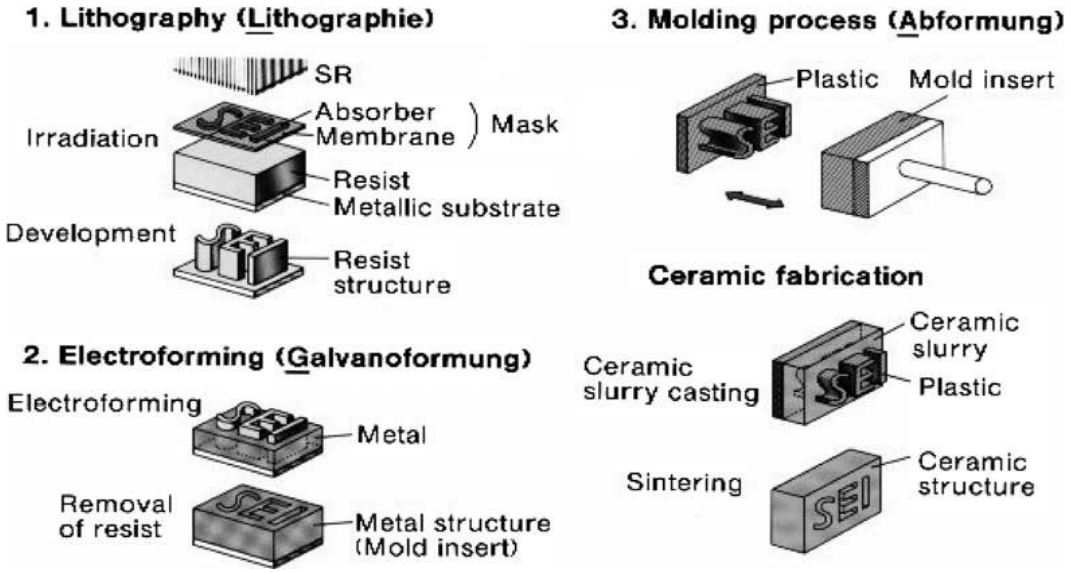

Figure 2.3 Schematic view of the LIGA process (Yoshihiro Hirata, 2003)

The Micro-stereo-lithography (MSL) technique, as microfabrication processes of growing applicability and importance, almost always uses the additive layer-by-layer method which shares the same principles with earlier conventional stereolithography techniques to build various 3D microstructures with the engineering materials such as polymers, metals and ceramics (Bertsch, 2003). Compared with the subtractive methods used in bulk micromachining and to some

extent even in surface micromachining, MSL employs an additive approach to fabricate complex microstructures (Ikuta, 1993; Katagi, 1993). Figure 2.4 shows a working principle diagram of a typical MSL system.

The scanning process adopts a point-by-point and line-by-line method to build solid micro-parts by superimposing the layers and during the process a precisely focused UV-beam is used to scan the surface of a photopolymerizable resin by moving the translation stage in the x-y direction. In contrast, the projection process is an integral process that builds a complete layer of the 3D microstructure with one exposure. During the process, the shape of each layer that is fabricated by the light beam and a pattern generator is projected onto the surface of the photopolymerizable resin (Provin, 2003). It has a great advantage of fabrication time-saver as projection time is only decided by the number of layers. Currently, the MSL is becoming a popular tool that enables to fabrication high-resolution 3D micro-parts.

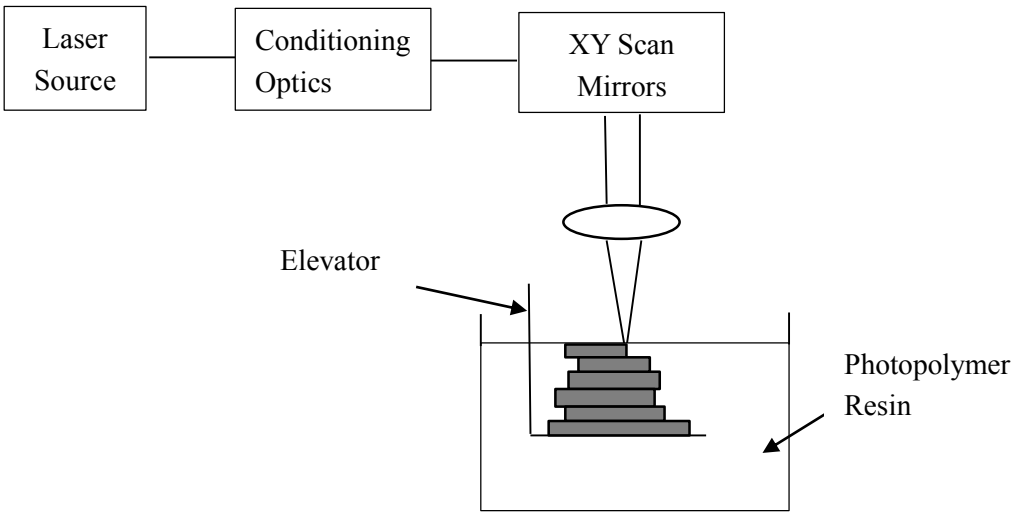

Figure 2.4 Schematic diagram of a typical micro-stereo-lithography system (adapted from Ikuta, 1996)

2.1.2 Friction Mechanisms at the Micro-scale

With the dimensions reduced, the increase of the surface-to-volume ratio means surface effects will play a greater influence than inertia effects in micro-scale systems. Adhesion, friction and wear induced by surface effects at the micro-scale have become challenging issues that limit the development of many types of MEMS devices during the fabrication and operation processes (Maboudian, 1998; 2000).

During the MEMS fabrication phase, the unintentional adhesion of compliant structural elements can be caused by the attractive effects of interfacial forces such as capillarity, van der Waals effects or other kinds of 'chemical' attraction (Zhao, 2003). Many findings support the idea that under low contact pressures, an adhesion force occurs between two mechanically contacting surfaces due to van der Waals attraction and acts as an additional force parallel to the applied normal force during friction measurements (Van Spengen, 2003). The total normal force, F_{total}, in contact, can then be expressed as

$$F_{total} = F_N + F_a \tag{2-1}$$

where F_N is the externally applied normal force, and F_a the adhesion force. Figure 2.5 shows the contribution of the adhesion force as additional normal load to the total normal loads ranging from 0.8 μN to 350 μN confirmed from the tribological measurement experiments for steel against steel by Ando (1995).

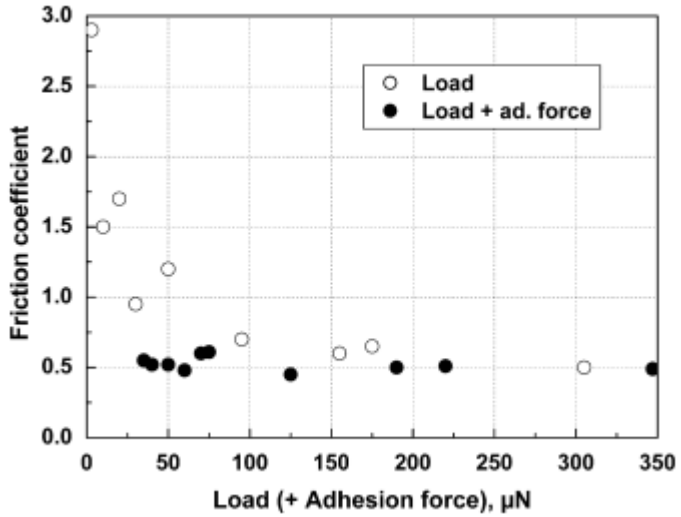

Figure 2.5 Variation of friction coefficient with load or with load and adhesion force for steel against steel during reciprocating test at 1.66 mm/s sliding speed and sliding distance of 0.031 mm (Ando, 1995)

Although some experimental and analytical research has been reported, clear understanding and explanations for friction and wear mechanisms on the micro-scale are yet to be realized. One reason may be the extreme sensitivity to the experimental conditions when investigating tribological interactions at the microscale, which implies that researchers always face many queries and challenges about the repeatability and validity of their tribological measurement results.

In micro-tribological studies, there is a widely accepted relationship reported by numerous studies that the contact size dominates friction force and also the surface roughness under elastic loading conditions (Zhang, 2003). For example, in a demonstration experiment of a silicon nitride ball sliding on structured silicon wafer at the sliding speed of 0.7 mm/s under the normal force of 180 mN; as shown in

Figure 2.6, there is a correlation between friction force and surface roughness, which can be attributed mainly to the elastic contact deformation at the leading edge of the advancing tip of the ball (Achanta, 2009).

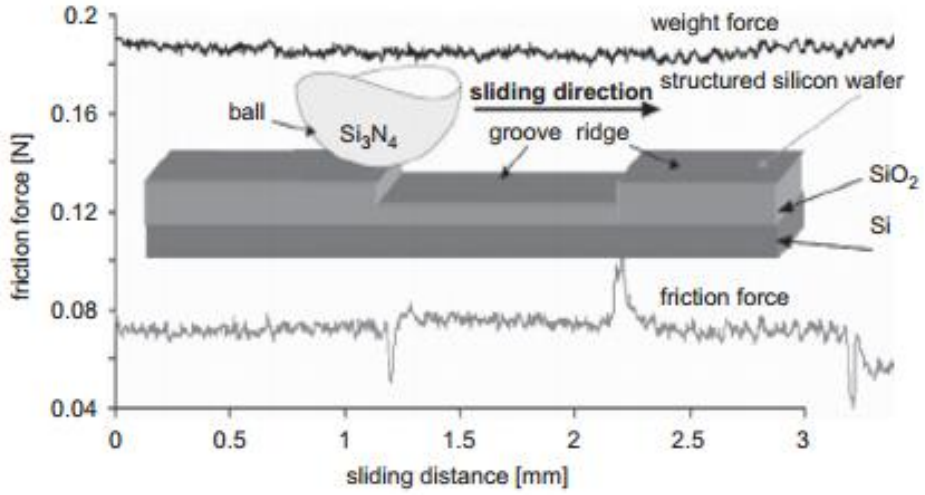

Figure 2.6 Friction force dependence on surface features at normal forces in mN range (Achanta, 2009)

2.2 Current Research in Millinewton Tribology

2.2.1 Coefficient of Friction

The concept and basic ideas about friction coefficient are evolved from many scientists over several centuries, notably such as da Vinci, Amonton and Coulomb, who had attempted to understand and explain the phenomenon of the sliding resistance between solid bodies (Blau, 2001). For example, Amonton gave the definition of the friction coefficient and Kotel'nikov used the symbol 'μ' to represent it in the later 1700s (Dowson, 1998). For solid-on-solid friction with or

without lubricants, coefficients of friction can be distinguished as static friction coefficient μ_s and kinetic friction coefficient μ_k: the former is defined as the ratio of the friction opposing the onset of relative motion to the normal force between the surfaces, whereas the latter represents the ratio of the friction force to the normal force when two surfaces are moving relative to each other (Blau, 2001). The measured formulas are

$$\mu_s = F_s/N \tag{2-2}$$

$$\mu_k = F_k/N \tag{2-3}$$

where F_s and F_k are the tangential forces to prevent and maintain the relative movement between two surfaces, and N is the force applied to the interface between the sliding bodies. F_s is the maximum force that can be generated to prevent the relative movement between two surfaces. The point is that if the externally applied force is tending to cause sliding is lower than F_s, there will be friction-generated reaction just sufficient to maintain static conditions.

The values for μ_s and μ_k of various engineering materials have been recorded into engineering handbooks for at least 300 years and continue to be published for more new materials today (Blau, 2001). Many studies have focused on the dynamic friction coefficient when two surfaces move with different test parameters, which mainly include normal load, velocity, distance, temperature, material properties and surface films.

In 1699, based on the famous friction calculations inspired from da Vinci, and by numbers of friction tests, G. Amontons had concluded that friction force is

always equal to a third of the normal load, but independent of the contact area between the materials. Then, the physicist C. A. Coulumb had attempted many experimental investigations in more detail, in 1785, to further confirm Amontons' friction laws and established the Coulomb law (Blau, 2001). In the old frictional laws, the dynamic friction coefficient is constant for some materials regardless of sliding velocity or applied load during the measurement. However, after years of friction studies, many experimental results had shown that friction coefficient is related to both material- and environment-dependencies rather than an intrinsic property of the two contacting materials due to the limitation and ambiguity of many friction laws. Furthermore, many famous academics all over the world have studied the influence of different test conditions on the friction coefficient and reached widely inconsistent test results. In 1882, the German researcher J. Franke presented an expression for the relationship of friction coefficient and velocity (Jones, 2003),

$$\mu = \mu_0 e^{-cv} \tag{2-4}$$

where μ_0 is the static friction coefficient and c is constant.

The former Soviet Union expert И. В. Крагельский (I. V. Kragelsky), in 1982, had been engaged in friction coefficient measurement of metal materials including cast-iron and steel, over ranges of velocity (0.004 – 25 m/s) and pressure (0.0008 – 0.17 MPa), to obtain the relationship of friction coefficient with sliding velocity under different normal loads, as shown in Figure 2.7 (Kragelsky, 1982),

$$\mu = (a + bv)e^{-cv} + d \tag{2-5}$$

where a、b、c、d are constants relevant to friction materials and normal loads. Table

2.1 gives the values of materials and parameters with different pressures.

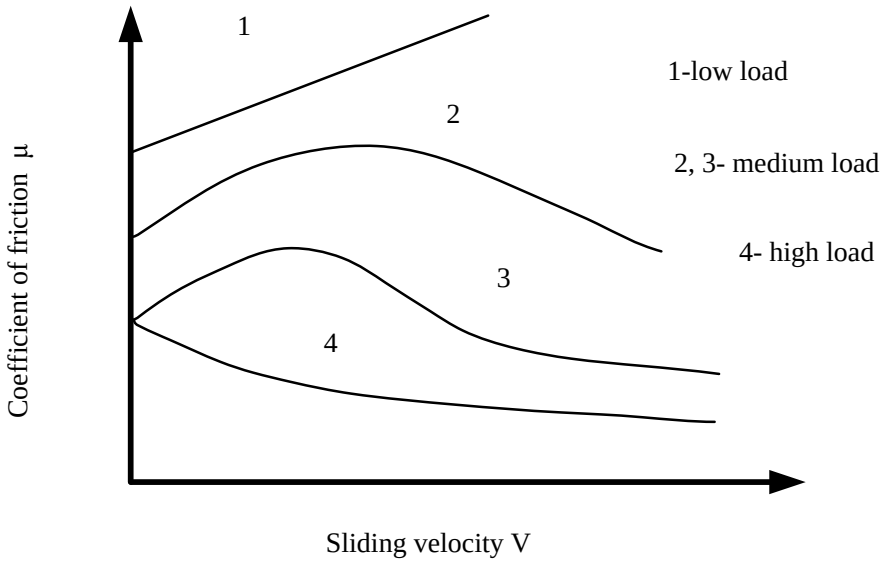

Figure 2.7 Curve of sliding speed upon CoF under different loads; 1 - low load; 2, 3 - medium load; 4 - high load (adapted from Kragelsky, 1982)

Table 2.1 The values of materials parameters with pressure (adapted from Kragelsky, 1982)

Materials	Pressure	Parameters			
		a	b	c	d
Cast-iron against steel	0.019	0.006	0.114	0.94	0.226
	0.216	0.004	0.110	0.97	0.216
Cast-iron against Cast-iron	0.081	0.022	0.054	0.55	0.125
	0.297	0.022	0.074	0.59	0.110

Overall, the literature indicates that Amontons' empirically-derived law of friction which states that the coefficient of friction is independent of apparent contact area and normal load, does not hold for micro-scale measurements, and thus friction coefficient is possibly significantly dependent on normal load, speed and

nominal dimensions. It cannot therefore be considered as a constant within the range of applications to which this thesis is addressed.

2.2.2 Current Status of MEMS Materials Tribology

This section provides a brief overview of friction mechanisms on micro-scales, especially on the variation of the friction coefficient of silicon and silicon-related materials, polymers and lubricated samples under different test conditions, so as to bring forth an overall understanding of the materials and their tribological behaviour for application in MEMS devices. To date, there is little data on a whole range of near-surface materials properties specifically at scales relevant to, MEMS devices from μm to mm scale mechanisms. Recently, more and more designers are eager to learn more about the properties of a new generation of engineering materials because the adoption of potentially effective novel designs is held back by a lack of sufficient understanding of materials behaviour on the micro-scale.

The basic material used for MEMS devices is virtually always silicon due to the process knowledge from semiconductor industries (Angell, 1983). However, silicon does not have good tribological properties owing to inherent brittleness (Liu, 2001), and thus various selective and designed films or coatings with different thicknesses (less than a few micrometers and typically applied by deposition methods such as solution casting, dip coating or spin coating) have been investigated to improve the tribological properties of the silicon substrate materials; examples are diamond-like carbon (DLC) coatings, and polymer films (Singh, 2009; Yoon, 2006).

Various test conditions (normal load, sliding speed, ambient conditions and materials) were studied by Ando in 2003 using a self-designed reciprocating apparatus to obtain the lower friction coefficient between a metal pin (copper or gold) and a plate (steel or single crystal silicon). In vacuum, the CoF has an increasing tendency with sliding speed for a copper pin against a steel plate at two different loads of 130 μN and 340 μN with a range of the sliding speed of 0.01 - 10 μm/s, whereas there is a higher increasing rate at lower effective load (Figure 2.8a). However, it is not affected by the sliding speed and thus remains at a relatively higher level between a gold pin and a silicon plate with the same test conditions (Figure 2.8b), possible reasons being differences in the material properties between copper and gold. (Ando, 2003).

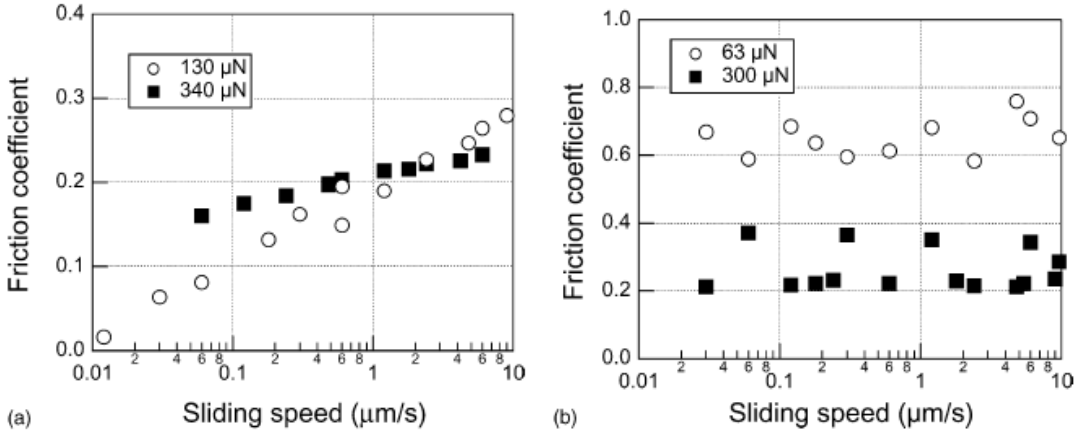

Figure 2.8 CoF as a function of sliding speed, measured between (a) a copper pin and a steel plate and (b) a gold pin and a silicon plate (Ando, 2003)

Liu H and Bhushan reported in Achanta (2009) investigated the variation of friction coefficient with different relative humidity for Si (100) (R_a: 1 nm) and DLC film (R_a: 28 nm) against Al_2O_3 and Si_3N_4 balls at the micro-scale using a micro-tribometer with fiber optic detection system as shown in Figure 2.9. They confirmed that hydrophilic surface like Si (100) shows a strong dependence of friction on relative humidity and adhesion force with loads. This study also suggests that DLC films can be used as anti-adhesion coatings for MEMS/NEMS at different environments due to no apparent influence on its tribological performance.

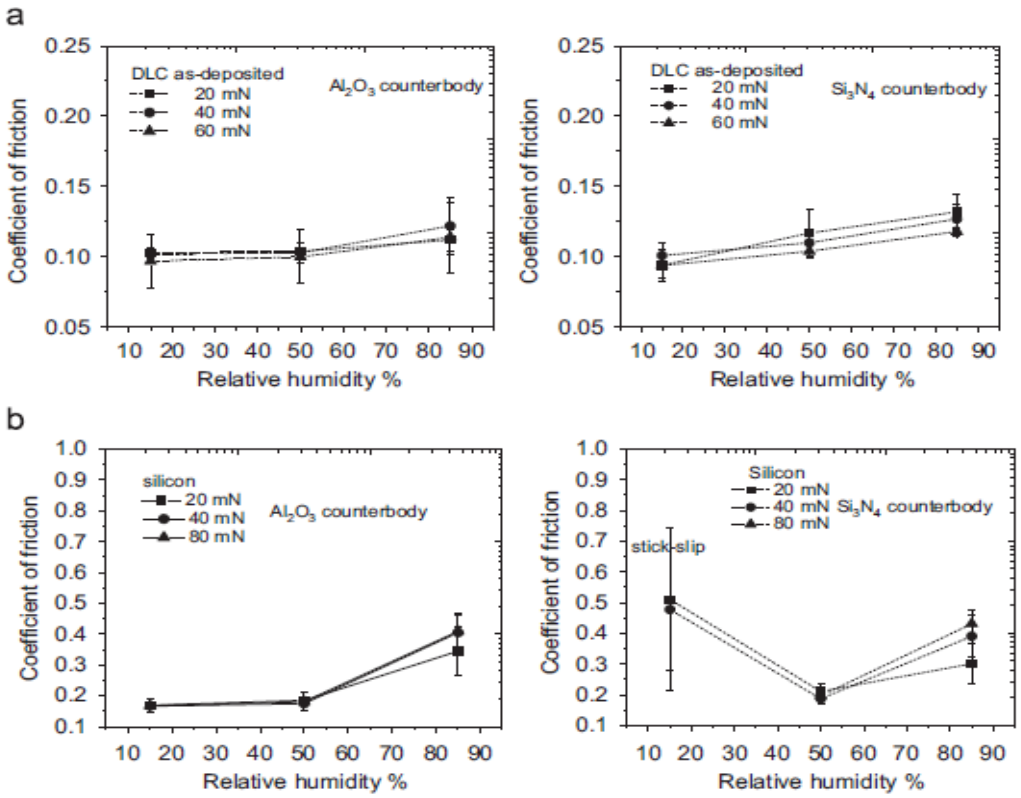

Figure 2.9 Average CoF versus relative humidity on: (a) DLC and (b) silicon at mN normal forces during reciprocating sliding tests against 5 mm counterbody (Achanta, 2009)

Amongst polymer materials, SU-8, a negative, epoxy-based near-UV photoresist used for micro-fabrication, and poly-methyl-methacrylate (PMMA), also commonly used as a photoresist, are the most widely used materials for micro/nano-scale devices, such as micro-fluidic and micro-optical systems (Zhuang and Menon, 2005).

Based on the capillarity-directed soft lithographic technique, poly (methyl methacrylate) (PMMA) film was spin-coated on silicon wafers by poly (dimethylsiloxane) (PDMS) molds that were adapted by Singh from the Korea Institute of Science and Technology in 2007 (Singh, 2007). Figure 2.10(a) show a typical example of the processing sequence of replication of the surface of a fresh Lotus leaf. The same sequence was repeated to replicate the surfaces of Colocasia leaves (fresh and dry). A ball-on-flat type micro-tribotester used soda lime glass balls of radius 0.5 mm as counterface sliders for friction experiments at controlled temperature (24 ± 1 °C) and relative humidity (45 ± 5%) with the setting test condition (normal load 3 mN, sliding speed 1 mm/s, scan length 3 mm) in reciprocating motion. Compared with PMMA thin film and uncoated silicon wafer at the micro-scale, the replicated surfaces showed several times lower friction coefficients during the micro-friction tests and their superior micro-tribological properties might be attributed to potential applications in micro-components, as shown in Figure 2.10(b).

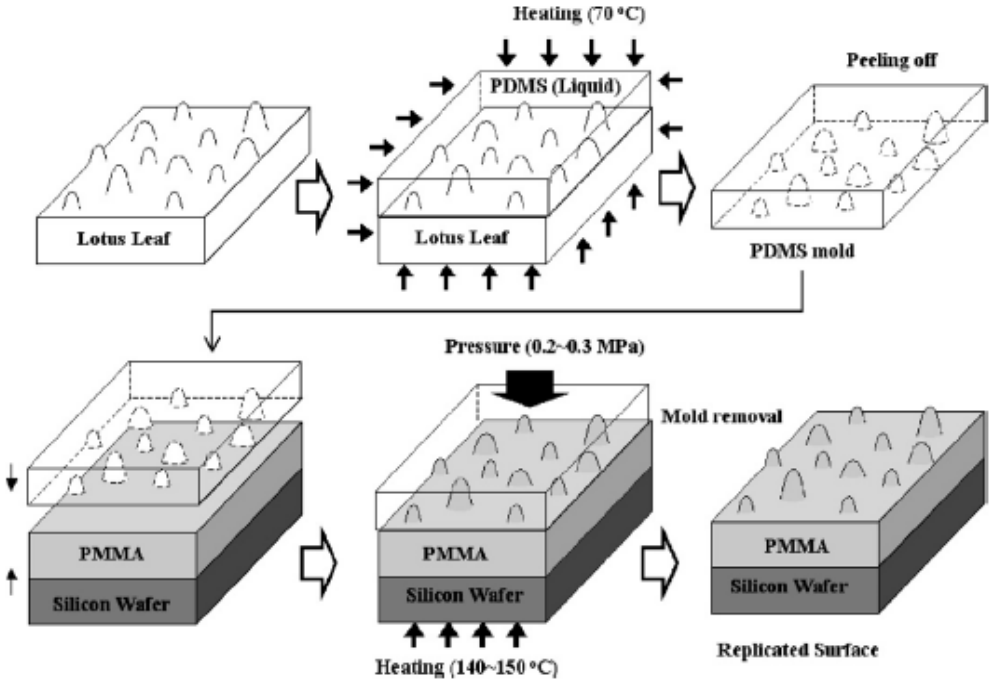

(a) Processing sequence of replication of the surface of a fresh Lotus leaf

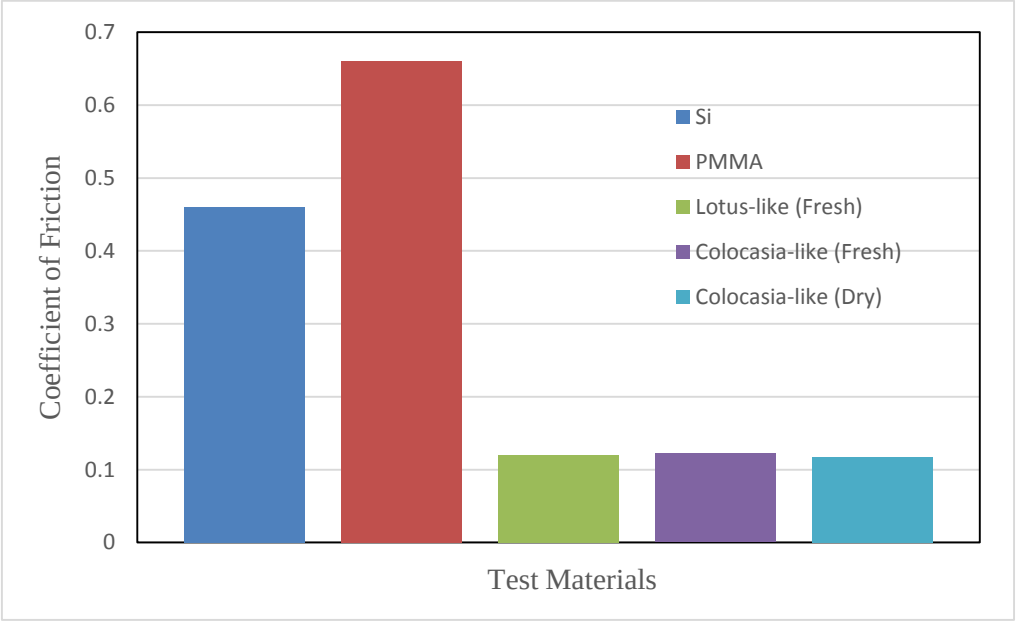

(b) Friction coefficients of test materials including Si, PMMA and replicated surfaces

Figure 2.10 Processing sequence of replicated surfaces and friction coefficients of test materials (adapted from Singh, 2007)

Tribological behaviors of pure PTFE and PTFE-based composites were investigated (Wang, 2006) at room temperature by Yunxia Wang from Chinese Academy of Sciences using a DFPM (Japan) reciprocating tribometer in 2006. Figure 2.11 shows the variations of friction coefficient of the transfer films sliding against a steel ball with the given normal loads of 0.5 N, 1.0 N, 2.0 N and 3.0 N and the speed of 2.5 mm/s. Also, the number of sliding cycles at the inflexion of the CoF curve means the wear life of the transfer film. Generally, tribological properties of these transfer films are sensitive to load change and their wear life will be shortened if load is increased. However, compared with the transfer film of pure PTFE, fillers including MoS_2, graphite, aluminum and bronze powders all offered various load capabilities to prolong the wear life of the composites. This is mainly attributed to strongly adhering transfer film and smaller wear debris particles caused by addition of fillers that stably stay in the roughness valleys during the friction process. Thus, these fillers may be useful to improve load bearing capability and prolong the wear life of the transfer films.

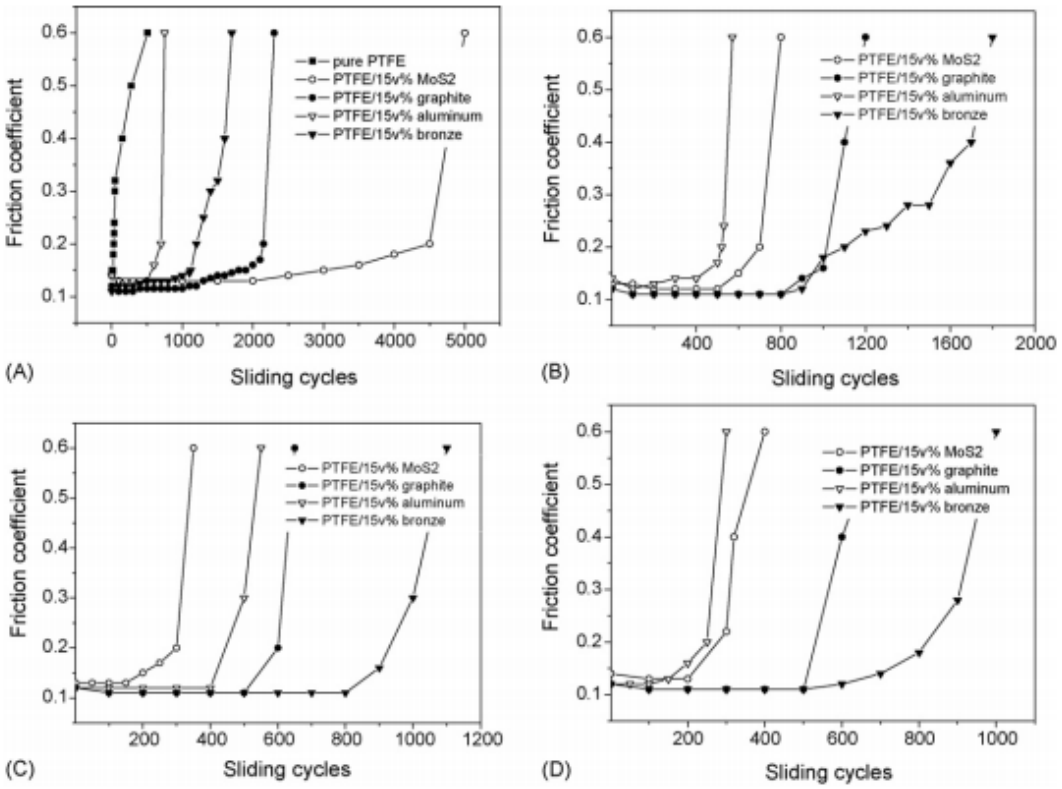

Figure 2.11 Changes in friction coefficient of transfer films under given load (A) 0.5 N, (B) 1.0 N, (C) 2.0 N, (D) 3.0 N. (Wang, 2006)

Many tests show that surface films have significant impacts on tribological behavior and generally make the friction coefficient decrease. This is not only because there is small shear resistance at the sliding interface due to the lower shear strength of surface film comparative to the substrate material, but also because the film can help to prevent the appearance of adhesion. It is worth noting that the thickness of the surface film is an important parameter for friction force.

In 2011, micro-tribology experiments on the surface of engineering coatings were investigated by Gee from Linkoping University using a self-designed tribometer for micro- and nano-tribology experiments. The friction that was obtained

in the experiments shows similar test results on a range of commercial engineering coatings including Linkoping CPx, Balinit Alchrona, Balinit A, Balinit C, Balinit DLC, Teer MOST, Teer Graphitic, Tecvac TiAlN with 1 µm diamond indenters at 50 mN applied load, as shown in Figure 2.12 (Gee, 2011). In most cases, the CoF of these coatings droped quickly to a relative stable low value between around 0.05 and 0.08 from an initial value that was slightly higher, despite the reported values in macroscopic tests are higher from 0.05 to 0.5. This study gives two possible reasons affected from the probe material and a lubricating layer formed from water in the moist atmosphere between the indenter and the coating for this observation

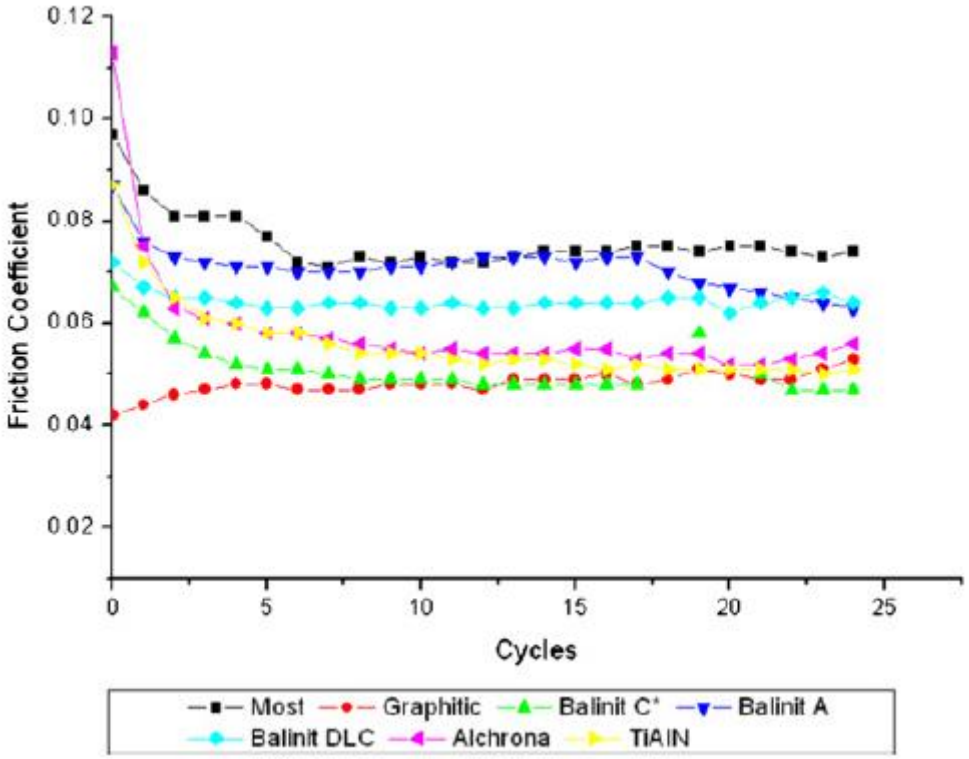

Figure 2.12 Comparative friction results for tests on different coatings using 1 µm indenter with a 50 mN applied load (Gee, 2011)

Currently, the nano-crystalline diamond thin film is rapidly becoming a popular research material in the fields of MEMS and the biosensor. Some researchers from India and Austria in 2011 (Roy) adapted hot-filament chemical vapor deposition (HFCVD) to develop hydrogen- and oxygen-terminated nano-crystalline diamond films (NCD) and used a MUST commercial micro-tribometer to investigate their tribological behavior with a Ø 6 mm steel ball in the load range of 25 to 200 mN and at a sliding frequency of 0.2 Hz. Figure 2.13

The paper reports on the variation of the friction coefficient as a function of the sliding distance for both types of films at loads in the range 25 mN to 200 mN. The experimental results showed that the CoFs at low load (25 and 50 mN) and higher load (200 mN) for both types of films have the significant influence on different friction mechanisms. Also, compared with O-terminated films at low load, H-terminated films have the lower friction coefficient, partly attributed to the hydrophobic nature of the film resulting in a lower pull-off force. The purpose of the investigation is not only to evaluate the tribological behaviour of nano-crystalline diamond films sliding against a steel ball, but also assess the influence of H-termination resulting in a hydrophobic surface and O-termination leading to a hydrophilic surface on the tribological behavior of NCD films at the micro-scale.

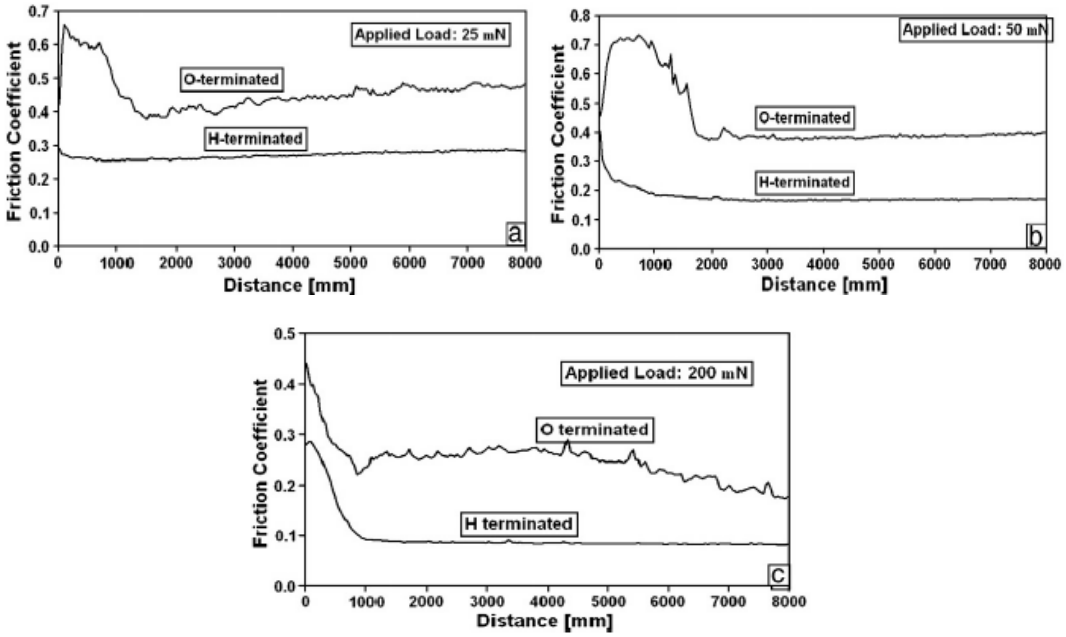

Figure 2.13 Variation of the friction coefficient as a function of distances for both types of films at different applied load, a) 25 mN, b) 50 mN, c) 200 mN (Roy, 2011)

In most published studies, the micro-tribometer test-rig used to measure the friction force is at the micro- to millinewton scale. However, there has been only limited progress in gaining a sound understanding of materials behaviour on micro-scale for testing MEMS friction at the lower millinewton scale. To the author's knowledge, there are no studies published containing useful data on polymeric material combinations at the scales being considered here. It is time to produce instruments that better simulate conditions in real MEMS devices. It is too difficult and expensive (Van Spengen, 2007) to build special, internally instrumented MEMS devices for the general study of new materials.

2.3 State of the Art in Micro-Tribology Instruments

Traditional studies in tribology have typically been performed at load and length scales compatible with the macroscopic devices being designed and studied. These largely empirical studies are often unsatisfactory in the present context because they operate in mechanical regimes very different to the dynamics of MEMS and other small mechanisms, and they lack quantitative analysis based on fundamental atomic-scale phenomena. Commercial atomic force microscopy (AFM), scanning force microscope (SFM) and various custom-built or commercially available micro-tribometers have been expanded and improved since 1996 to examine tribological behavior at the atomic-scale that involved in friction, wear, lubrication and the interaction of contacting surface (Singer, 1992). However, conventional tribological testers, such as pin/ball-on-disk equipment, are not suitable for evaluating tribological properties of materials used in MEMS applications as the contact areas involved in these devices are only a few hundreds of nm^2 and the contact loads are in the μN or mN range. There is a significant gap between the parameter ranges accessible to these different scales of instruments and more traditional tribology test tools (see figure 2.14) (Dvorak, 1998).

Many attempts over many years have been made by researchers to expand the possibilities of unknown laws of micro-tribology and tribological processes with the determination of quantitative characteristics by establishing more appropriate methodology and applying better experimental equipment.

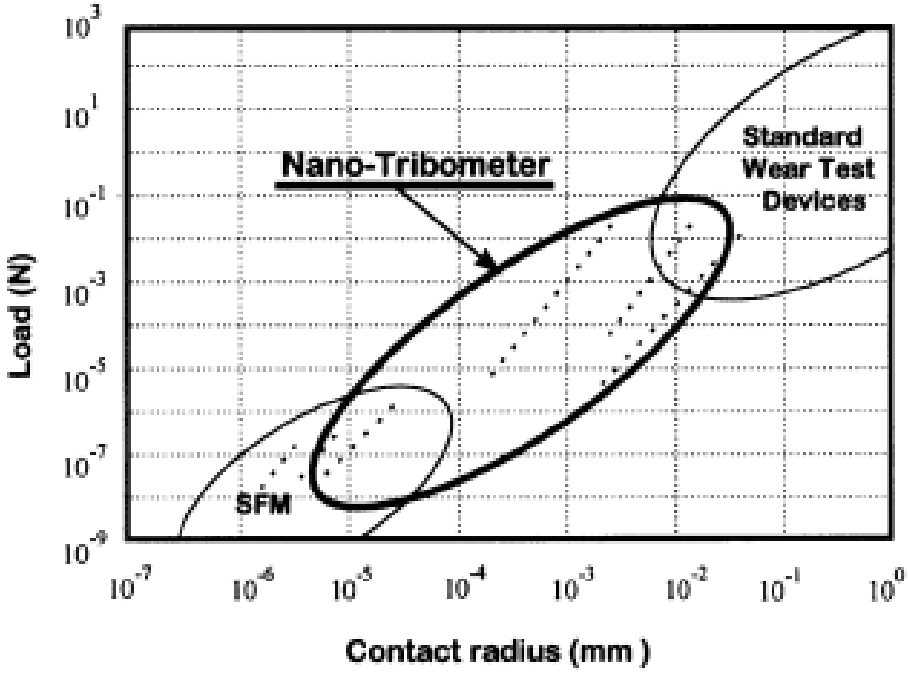

Figure 2.14 Operation range for which the nano-tribometer was designed compared to SFM and standard wear test devices such as the pin-on-disk. The rows of dots indicate the regions where experiments have been carried out with the nano-tribometer. (Dvorak, 1998)

2.3.1 Commercial Systems and their Limitations

Currently, there are a few companies that manufacture commercial tribometers for micro-tribological measurement such as Nanovea, CETR, TETRA and CSM Instruments. These testing devices are certainly used to measure at micro-scales to contribute to the investigation of microscopic friction mechanisms, but high prices and the restriction of (especially their dynamic) measurement magnitudes means that they are unable to meet the requirement for overall feedback to device designers about micro-tribology in the μN and mN ranges

AFM is a popular surface profiler that applies a tip mounted on a cantilever

beam of known stiffness to analysis topographic measurement for all conducting or insulating engineering surfaces on the micro- and nanoscale, while FFM is a modified version of AFM to measure both normal and friction forces. They can be both used to investigate for surface roughness, adhesion, friction, wear, indentation and lubrication at the interface between two solids with and without liquid films from micro- to atomic scales and nanofabrication/nanomachining. Figure 2.15 shows an outline schematic of a typical commercial AFM; it uses a laser beam deflection technique to measure normal and frictional forces applied at the tip sample, which is by far the most common approach (Burns, 2004).

However, an AFM tip generally can be only provided to simulate a single asperity contact, resulting in a relatively low sliding speed, and thus it is difficult to meet the requirement of the real micro-friction movement (Qing, 2007).

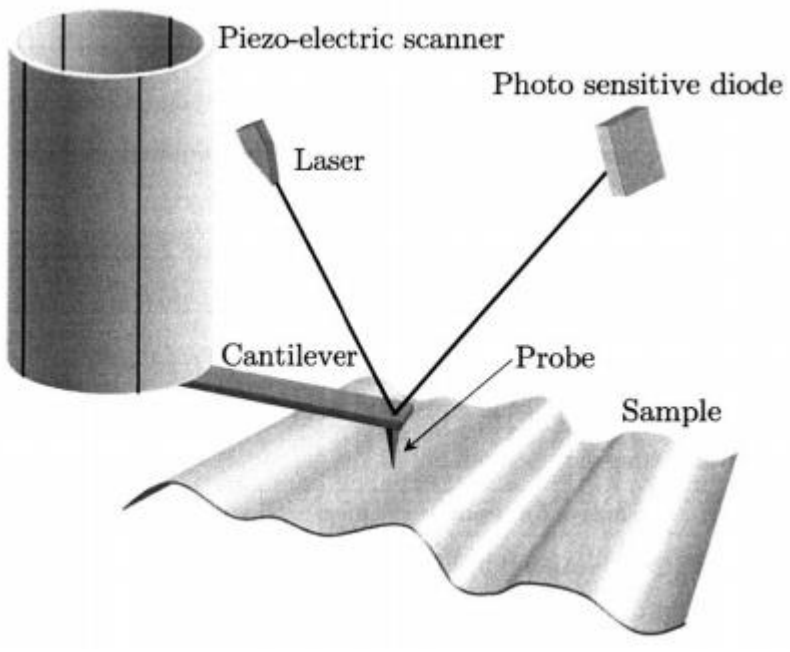

Figure 2.15 Schematic of the principal components of a AFM (Burns, 2004)

The BASALT –MUST Precision Tester is made by a Germany company called TETRA GmbH (see Figure 2.16) (2008). This device can be used for determination of friction force on polymer surfaces, analysis of lubricating systems, real-time study of lubricating film formation on surfaces and identification of the wear resistance of thin layers with controlled air humidity or in all liquid media under various biologically relevant conditions for long-term studies. Its modular structure is claimed to offer flexible, high precision operation through two basic experimental modes for specimen motion (pin-on-disc and reciprocating motion) to measure surface interactions over a wide range of forces. A fiber optical sensor (FOS) is aimed to measure the deflection of a special cantilever and the force range of the linear positioning system (LPS) is available from 1 μN to 1 N. In addition, the closed loop position control enables long stroke experiments up to 20 mm with a repeatability of 50 nm. A measuring module with strain gauge extends the force range up to 10 N. It has good capabilities for many MEMS-related measurements but is still clearly aimed at larger scales as well, suggesting practical some promises in some of its characteristics.

Figure 2.16 BASALT–MUST Precision Tester (TETRA GmbH, 2008)

In 2009, the Nanovea Company (Hopton, 2009) provided highly accurate and repeatable friction measurement in rotating and linear reciprocating modes on a single system with a wide range of environmental conditions including varying temperature and atmosphere and in liquids. The micro-tribometer is designed to use a flat, pin or ball tip loaded onto a test sample with the loads from 100 mN to 40 N at a specific position from the center of rotation. Friction coefficient is measured during the test by the deflection of a load cell which is precisely calibrated and friction forces are recorded for both forward and backward movements of the stroke. Figure 2.17 shows a picture of T50 micro-tribometer made by Nanovea.

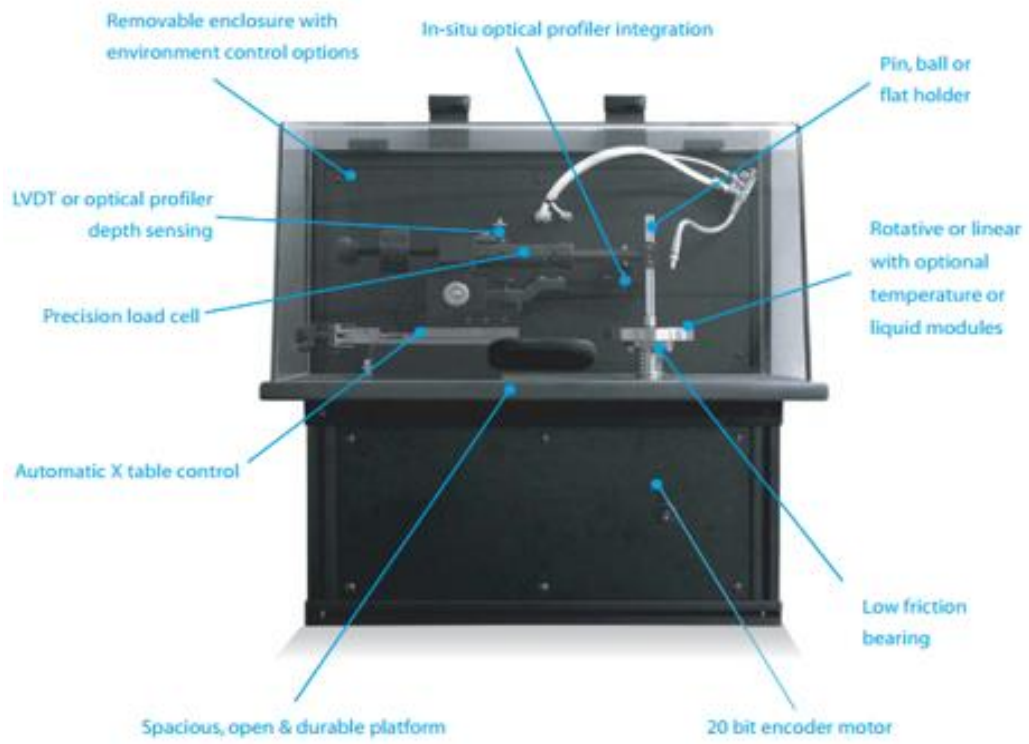

Figure 2.17 Nanovea tribometer pin-on-disk and linear reciprocating setup (Hopton, 2009)

CETR-Bruker Universal Mechanical Tester (UMT) has been the most versatile and widely used tribometer on the market since the first model debuted in 2000, as shown in Figure 2.18 (CETR-Bruker, 2013). The UMT tribometer is designed for ball/pin-on-disk tests with the rotating speed in the range of 0.1 to 5000 rpm and the torque of 5 N/m and ball/pin-on-plate tests with the sliding speed of 0-60 Hz and track length of 0.1-25 mm under a full range of environmental testing from room temperature up to 1000°C. The force measurement is applied from 1 mN up to 2 kN and all data collected by the sensors are presented in tables and graphs to provide a complete picture of the entire test procedure for full understanding of the dynamics around friction, wear, or coating failure.

Figure 2.18 A picture of Universal Mechanical Tester (UMT) made by CETR-Bruker (2013)

CSM Instruments has been a leader in the development of instruments for surface mechanical properties characterization for over 30 years in both research and industrial fields. They offer a reciprocating micro-tribometer adapted to investigate the tribological properties of cell surfaces with the normal load of 0.1 mN - 1 N, track length of 0 - 600 μm and velocity ranging from 0.01 to 18 mm/s. Normal and tangential forces are continually measured from the stiffness and measured displacement of flexures. Data of average normal force F_N and friction force F_f can be recorded at 1.2 kHz for each test and kinetic coefficients of friction (CoFs) can be calculated as the ratio of F_f to F_N. Figure 2.19 shows the schematic of the operation of micro-tribometer.

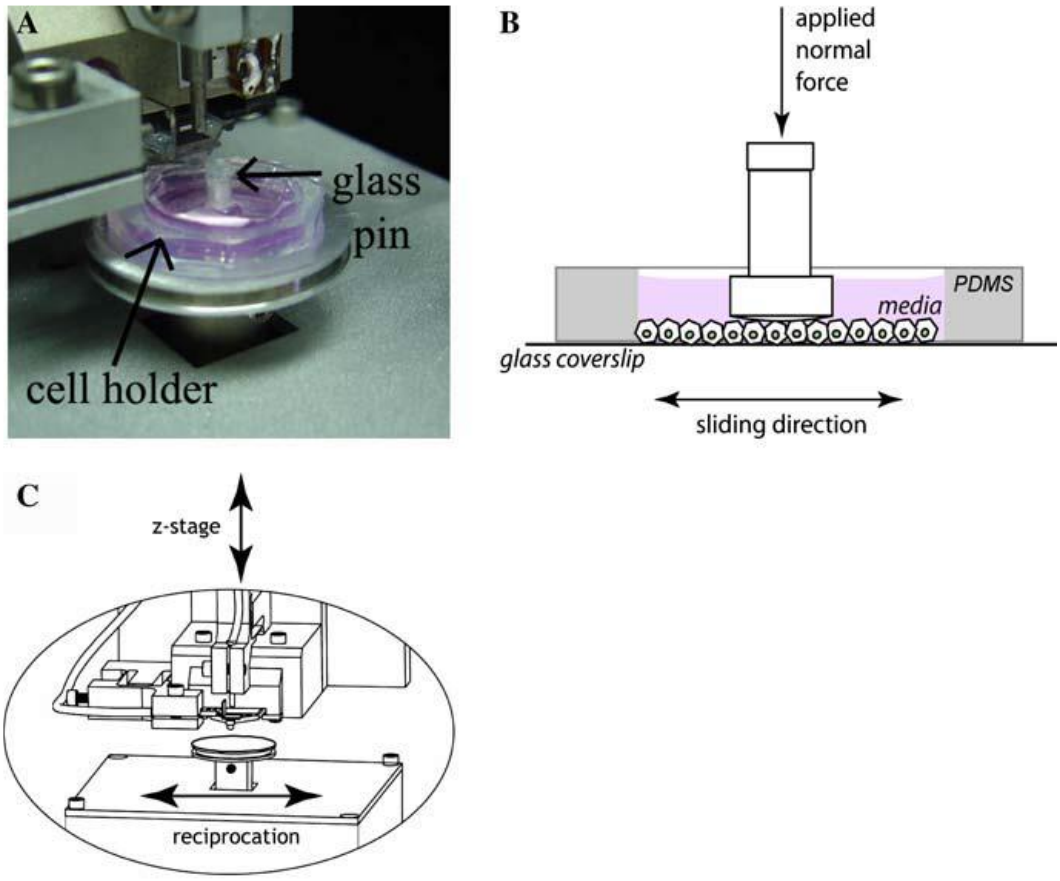

Figure 2.19 (a) Cell holder in place on the micro-tribometer with the pin lowered onto the cell surface; (b) Schematic of pin running across cell surface within the cell holder; (c) Schematic of micro-tribometer showing the axis of applied load, z, and the direction of reciprocation (Cobb, 2008)

2.3.2 Self-developed Micro-tribometers and their Applications

A new instrument for nano-scale to micro-scale friction and wear measurements was developed by Dvorak in 1998 (Dvorak, 1998). The nano-tribometer is based on a scanning force microscope design developed at NIST (National Institute of Standards and Technology, USA). Interferometers and capacitance gages are used in a closed-loop digital control system to accurately determine and control the position

and motion of the sample. The instrument incorporates several design features, including three-axis feedback of the sample position, a position-sensitive PIN photodiode for large dynamic range force measurements, and available various cantilever probes. The force head can measure continuous changes in both normal and lateral forces over three orders of magnitude within the range of nN to mN. The nano-tribometer can be used at a constant normal load of 40 nN and a constant speed of 14.4 μm/s for each test, but little experimental data is currently available.

A ball-on-flat reciprocating micro-tribometer was designed by Le in 2005 at Cambridge to measure the friction coefficient for an aluminium alloy strip sliding against a Ø 3 mm steel ball (AISI 52100) as shown in Figure 2.20. The normal load is applied in the range of 0.1-10 N by a flexible wall soft spring made from a single block of aluminium alloy and the spring only allows vertical displacement with a stiffness of 7 N/mm. The sample holder is fixed to a thin-walled octagonal ring aluminium alloy load cell fitted with strain gauges in full-bridge configurations. The sample stage can be driven by a D.C. mini-motor at reciprocating speeds of 0.02 mm/s, 0.1 mm/s and 0.5 mm/s, with a sliding distance of up to 10 mm. This micro-tribometer was used to assess the effectiveness of various boundary additives and the development of a transfer film in engineering applications of aluminium alloys and their metal forming processes.

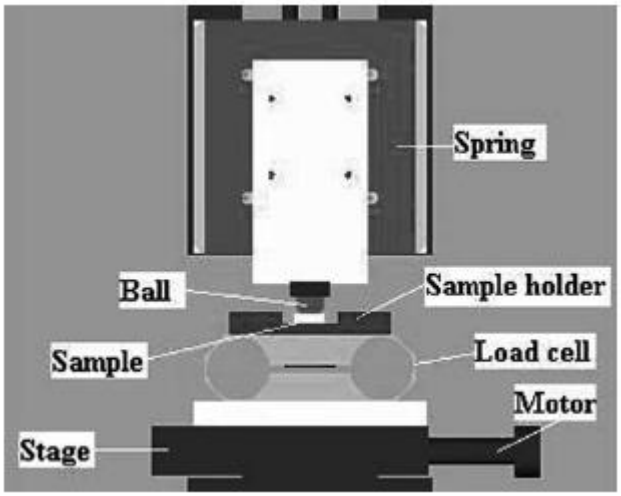

Figure 2.20 Schematic of the micro-tribometer (Le, 2005)

Recent research efforts by O. Mollenhauer in 2006 at the Ilmenau University of technology (Germany) had focused on using a new generation of micro-tribometer, which consists of three main components including precision motion mechanisms, force transducers and fiber-optic length detection system (Mollenhauer, 2006). Figure 2.21 shows the main components marked: (1) x-y micro-positioning stage powered by stepper motors (2) reciprocating unit, (3) sample, (4) counter body, (5) force transducer, (6) fiber-optic sensors to detect normal and lateral deflections of the force transducer. The inset shows a glass spring force transducer mounted on a steel support.

The precision motion mechanisms are used to drive sample position, reciprocating motion and to adjust normal force. A double leaf spring made from photo-structured glass is applied for the force transducer to measure lateral and normal forces. In this work, friction force was studied as a function of the relative

humidity with the test conditions including 0.2 mN normal load, 50 μm/s sliding speed and 100 μm stroke. The counterbodies were 2 mm diameter steel AISI 440C balls coated with titanium carbide (TiC) with an S_q roughness of 2.8 ± 1 nm and were polished after deposition.

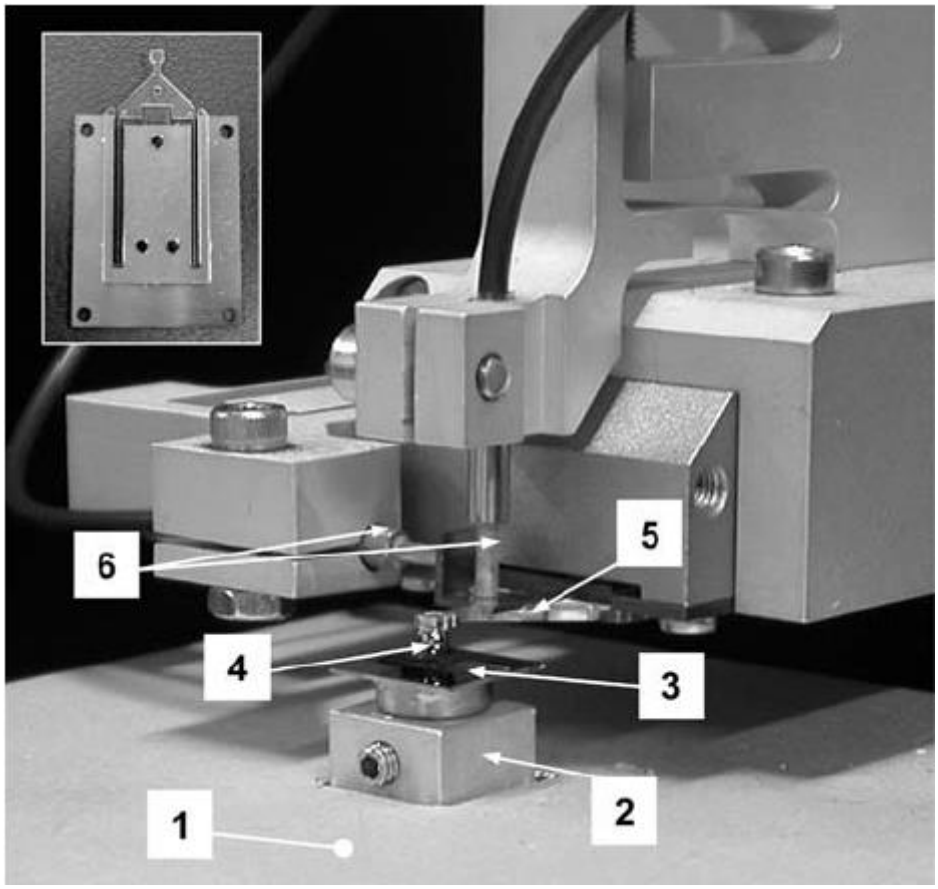

Figure 2.21 A picture of Mollenhauer's micro-tribometer (Mollenhauer, 2006)

A micro-friction test apparatus was specifically developed by Qing Tao in 2007 at Tsinghua University to measure the maximum static friction, the sliding friction and the adhesion. Figure 2.22 shows the schematic diagram of the micro-friction test apparatus. The apparatus includes two cantilevers with mounted strain gauges for

the force measurement in the lateral and vertical directions, a precise vertical movement for load generation, a horizontally moving table and the data acquisition system. The force measurement range was 10 μN to 2000 μN with a force resolution of 10 μN. The movement of the vertical table created a controllable deformation of the vertical cantilever to generate the required normal loads. The horizontal table was driven by a stepped motor with the horizontal speeds of 10 μm/s - 400 μm/s. The data acquisition system uses a voltage amplifier, a wave filter and a computer with an analog-digital converter (ADC) for the measurement of the normal load and the friction force. The measurement experiments were carried out using a 0.7-mm diameter steel ball as the counter-body to study the micro-friction behavior of a single crystal Si (100) wafer and a TiB_2 thin solid film as a function of the load, sliding speed, and rest time in terms of the micro-friction and adhesion.

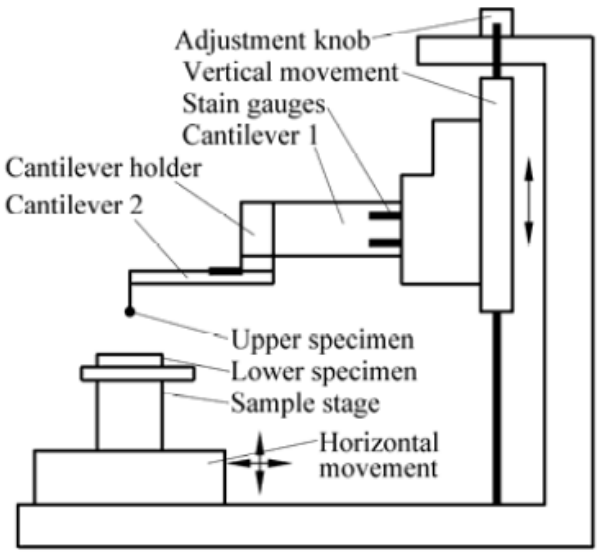

Figure 2.22 Schematic diagram of Qing's micro friction test apparatus (Qing, 2007)

A reciprocating ball-on-flat tribometer (Kosinskiy, 2012) was developed by Mikhail Kosinskiy in 2012 at Technische Universität Ilmenau to evaluate the tribological behavior such as adhesion, friction and wear of materials and coatings in vacuum and controllable atmospheres on a microscale with applied normal loads of 0-50 mN and sliding speeds of 10-180 μm/s. For this tribometer, a flat sample with 5-15 mm in linear dimensions and heights ranging from to 0.5-3 mm, is mounted on the 2D actuator that provides the horizontal and vertical motion. A ball with a diameter in the range of 1-3 mm is attached to the force sensor. The sensor itself is fixed onto the base unit of the tribometer. During the measurement, a cantilever with an attached tip is fixed and a sample performing relative motion by a piezo-actuator. The force sensor consists of a couple of springs, which deforms in the horizontal and the vertical direction. These deflections are monitored by an optical detection system consisting of small square aluminum coated silicon mirrors, which are diced from the Si (100) wafers, along with a couple of commercial miniature laser interferometers (SIOS GmbH, Germany) mounted outside the vacuum chamber.

Friction experiments involving a Ø 2 mm Si ball sliding against a flat Si (100) wafer (thickness: 300–350 μm) and SiO_2 layer with a thickness of 2 nm, at a sliding speed of 180 mm/s and a normal load of 50 mN, demonstrated the validity of the new vacuum micro-tribometer compared with a commercially available instruments in the literature and other types of tribometers under similar conditions. Also, the CoF as a function of sliding cycles showed a stable behaviour for vacuum measurements, while there is a higher value but similar variation in CoF between the

microtribometer and the commerical avaliable instrument under ambient conditions.

2.4 Conclusions & Implication for this Project

Micro-tribology instruments and polymeric materials continue to be really worthwhile topics for deeper and extended investigation. The literature reviews show considerable gaps between the needs of designers and the current research data on MEMS thin film tribology and state of the art in micro-tribology instruments.

Tribological properties of a wide range of different materials clearly need to be investigated first on the micro scale, perhaps then on the nano-scale. An extended range of parameters, including force and speed regimes, is also necessary. There appears to be a particular need to address the dynamical conditions of measurements because current instruments cannot simulate at all well those found in many MEMS applications. This thesis contributes some first steps towards the satisfaction of these urgent needs. It will examine a range of relevant and exciting materials in bulk form and, especially, thin film polymers for different parameters such as sliding speed and cycle rate in tests using reciprocating motion. The new data will directly provide design-relevant information about different material surface properties. However, a major part of the contribution here concerns better scoping and refinement of the test ranges and methods recommended for study to build up design-oriented databases. With these aims, the work must step beyond measurement conditions readily set up on existing commercial systems. Alsoufi's instrument (reviewed briefly above and in more detail in later chapters) was intended as a test-bed for ideas about how to

develop high dynamic range micro-tribometers and so offers a useful starting point. So, re-assessing and modifying Alsoufi's instrument is a vital part of this study, in particular, concerning thin film polymers for high sliding speed and also because of its potential to explore the effect of humidity, temperature, high speeds and lower load on micro-friction by using the universal micro-tribometer measuring head in different overall test configurations. This program will lead to the detailed evaluations of the properties of the polymer materials under typical usage conditions.

3 Recommissioning and Characterization of the Custom Micro-tribometer

Overview

This chapter describes the custom-designed reciprocating tribotester and gives a critical review of the developed system with its characteristics including the novel micro-tribometer sensing head and notch-hinge mechanisms for the reciprocating scan mode. The next-generation tester, orginally designed by Alsoufi at Warwick, can be applied flexibly in ball-on-flat and crossed-cylinders configurations for micro-friction measurement with control of critical friction-related test conditions such as sliding velocity, scan length and applied forces in the vertical and lateral directions. The test-rig was re-calibrated to determine the input-output relationships, minimize the system error and improve the overall accuracy of the instrument. Calibration results were compared with the original ones for consistency checking. Finally, the system integration including updated operating software and repaired hardware is given as the guidance for tribologists and designers.

3.1 Tribometer for Micromechanical Systems

It would self-evidently be very expensive to design, build and operate a micro-tribometer that was itself a micromechanical device using the modern measurement and control technology to investigate the friction properties of MEMS materials. Hence, tribological data has to be obtained or inferred from more general-purpose instruments that do not readily simulate typical MEMS operating conditions. Currently, most commercial and self-developed micro-tribometers are self-contained to offer many sample motion mechanisms but for different functions and mechanical configurations in details. In particular, for very sensible commercial reasons they tend to operate only at slow sliding speeds and have poor dynamic response, such as AFM presented in Chapter 2.3.1 (Bhushan, 1998). This restriction might not matter all that much for hard, high

melting temperature materials that have tended to be used in MEMS. However, prospects for using softer polymeric materials, such as PTFE and MSL acrylic-based R11 resin, also raise questions about new needs to study their tribology under conditions that at least approach rather more closely the dynamic ones of such applications. In most cases, small amplitude reciprocating tests will come closer to such conditions than will the continuous sliding pin-on-disc configuration common in larger-scale tribology. For example, in Chapter 2.3.2, the literature (Kosinskiy, 2012) illustrated that a reciprocating motion most closely simulates the operation of the nano-positioning stage of a vacuum-based nano-positioning and nano-measuring machine. But the instrument resonances impose major constraints on the frequency of reciprocating scans.

For such reasons Alsoufi (2011) developed and demonstrated practically a prototype custom-design of micro-tribometer head in which a considerably stiffer than usual spring system within the friction force detection led to higher resonant frequencies and improved dynamic response. However, this introduces new challenges, for example, in the micro regime, the coefficient of friction is often sensitive to load and thus the variation in the set force is highly undesirable during the friction and wear measurements (Czichos, 1992). The new design therefore includes various extra electromechanical systems to provide some compensation.

Sliding motion in micromechanical devices will involve very small real area of contact. Small real components, such as low-mass sensing and actuation, in continuous contact may use this application, while some situations will happen in

the stationary pin and the reciprocating pin (Torbacke, 2014). This could be simulated (for low normal loads) by a ball-on-flat or sliding crossed-cylinder sample configuration, as shown in Figure 3.1. As a variant of the pin-on-disc test, the ball-on-flat configuration is widely used in industry for almost all materials in both lubricated and non-lubricated conditions to measure tribology parameters such as CoF and wear. In some cases, this configuration is applied for reciprocating motion in order to achieve one more function in a micro-tribometer in addition to the rotating disc technique. The latter is rarely used today to acquire distinct small contact regions due to the same linear direction from the sample movement and surface roughness, as well as the sliding velocity that is independent of the contact area. However, it might have advantages in some specific cases at this level. For example, it was used for tribological testing by Cruzadoa (2010) to simulate the fretting wear behaviour of the wires in ropes used in many industrial applications, such as structural elements (reinforcement for tires, bridges brace) or as elements for transporting purposes (cranes, lifts, funicular railway, ski lifts) due to their high axial strength and bending flexibility, and allow for an exact determination of wear under the required conditions (Wasche, 2008).

The experimental work in this thesis will use a re-built version of Alsoufi's micro-tribometer. The scan length, sliding frequency and applied normal load can offer various combinations for the friction force measurement. The forward and backward movements of the stroke directly determine the coefficient of friction. Moreover, small oscillation amplitudes can usually simulate fretting wear

experiments to evaluate the size of the wear scar of the moving specimen by using a profilometer at high frequency (Buyanovskii, 1994; Hasegawa, 2008).

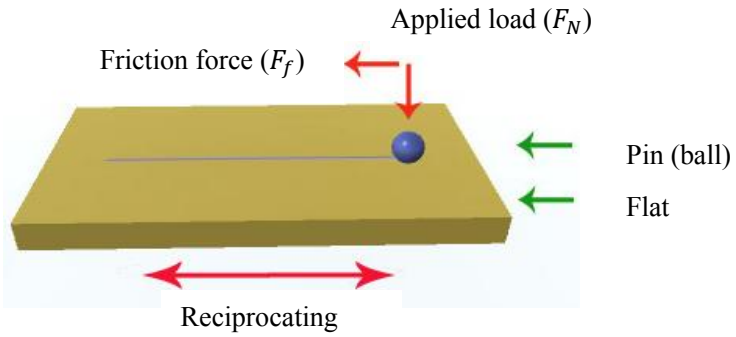

(a) Ball-on-flat configuration

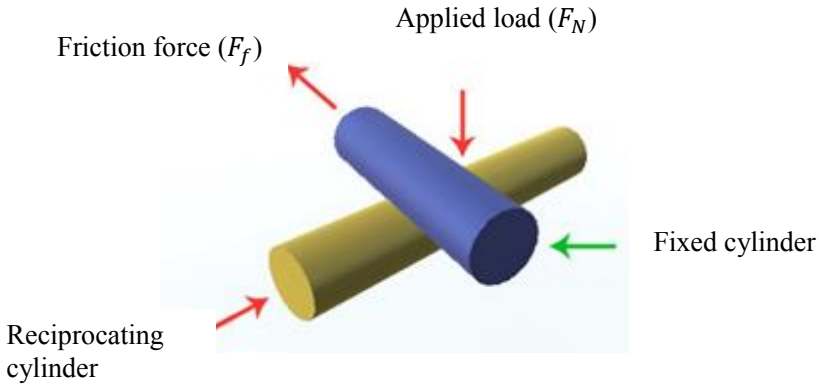

(b) Crossed-cylinders configuration

Figure 3.1 Two contact models adapted from (Buyanovskii, 1994)

3.2 Major Features of the Custom Micro-tribometer

The experimental studies in this thesis will use a rebuilt version of Alsoufi's custom-design tribotester. Full details of the original design and justification for the design decision are given in Alsoufi's thesis (2011). Therefore, only the critical features are discussed here.

The key features of sliding friction between the surfaces of the micro-components rely on modes of motion and types of friction pairs. Based on the above-mentioned tribological measurement techniques used for pin-on-flat or cross-cylinders tests, a micro-tribometer with reciprocating scan mode was designed by Alsoufi at Warwick in 2011. Figure 3.2 shows the 3D model and the picture of the main components of the test-rig, which comprises:

① A lightweight stainless steel rod (Ø 2 mm × 50 mm) used as a cantilevered force sensing element to increase in resonant frequencies and robustness of the instrument, but with the penalty that any sample misalignment that deflects the spring will have significant influence on the nominal normal force applied.

② Two high-compliance magnet-coils used as force actuators for both normal force and counter-body lateral force (or position control) during the friction measurement and also for dynamic imbalance loads. Another relatively larger one applied for reciprocating motion of the specimens and notch-hinge mechanisms.

③ Bases for fixed micro-positioning flexure stages in x-y-z directions for adjusting the position of the whole head relative to the sample on a scanning stage and holding up the notch-hinge mechanisms in the horizontal direction.

④ Notch-hinge flexure used for carrying and fixing the specimen.

⑤ The rigid block at the free end of the sensing beam carries magnets for lateral and transverse force actuators, provides flat target surfaces for the two eddy-current sensors, and accepts interchangeable small sample counter-faces. There will typically be (mm-scale) balls but could also be short lengths of (mm-diameter)

cylinders. The notch-flexture also carries interchangeable small flat or cylindrical samples and provide typically ball-on-flat or crossed-cylinders configurations with sample counterfaces for friction measurement.

⑥ Two unshielded non-contact eddy-current sensors (Model: Micro-Epsilon DT3010-U50, <25 nm resolution) are placed about 0.3 mm from the target flats on the sample holder to be used for the measurement of the vertical and lateral deflections of the sensing bending beam and a non-contact laser placement sensor (Model: AR200-6M, <1.9 μm resolution) to monitor the track length and scanning direction of the notch hinge mechanism with the specimens.

According to Alsoufi's calibration in his thesis, the beam stiffness constants k_z and k_x for both vertical and lateral axes are 2778 N/m and 2703 N/m, respectively. It can provide for a resonance at around 160 Hz and the sub-50 nm working resolution for displacement, showing the resolution as a force sensor would be better than 0.1 mN in both axes under typical operating conditions, consistent with normal loads down to about 10 mN for regular use. Based on Alsoufi's design (Alsoufi, 2010), steel material was used as the sensing beam because the stiffness judged more important than density in this component to give higher resonance. The end deflection of the sensing beam is given by

$$\delta_{max} = \frac{FL^3}{3EI} \tag{3-1}$$

where L is the rod length, F is the force, E is the elastic modulus and I is the second moment of area of cross-section. For the circular section,

$$I = \frac{\pi d^4}{64} \tag{3-2}$$

where d is the diameter of the rod, and the stiffness k is given by

$$k = \frac{3EI}{L^3} \tag{3-3}$$

If k_{beam} is relatively lower, the forces acting on the beam will bring more deflections so that it cannot be used for short oscillating tracks. End mass (from sample holder) dominates over beam mass so dynamically, an adequate representation is

$$\omega = (\frac{k}{m_{eff}})^{\frac{1}{2}} \tag{3-4}$$

where ω is the natural frequency and m_{eff} is the mass of the sample holder plus $1/3$ of the mass of the beam.

The magnet-coil force transducers that comprise force actuators and a pair of identical moving permanent magnets centred along the axis of two solenoid coils in the vertical and lateral directions, are designed by Alsoufi to use as a drive system for micro-tribometer sensing head and notch-hinge mechanisms. In the new micro-tribometer head, coil current directly controls a magnetic field which interacts with that from the hard, saturated magnet to produce a force and, potentially, beam deflection, but there is no mechanical contact between coil and magnet. The magnets (sintered rare earth cobalt – SmCo 2:17 grade, Ø 3 mm × 2 mm) are glued to the sample holder and surrounded by fixed coils which is nominally 5 mm long with external and internal diameters of 10 mm and 5 mm, wound onto a brass former. The force between the magnet and solenoid is linear with current and almost independent of small axial deflections. The actuator sensitivity calibrated by Alsoufi shows close to 0.11 mN/mA. Current-drive amplifiers deliver up to ±500 mA to the

coils, providing up to ±20 μm free beam deflection in the vertical and lateral directions, limited to keep magnets nearly central in their coils. Also, the relatively larger version of magnet-coil actuator is utilized to drive the notch hinge mechanisms for reciprocating motion and provide precisely scan speeds for test specimens. Thus, these actuators have high-compliance, decouple frame vibration from the specimen and readily self-align to the primary translation axis, all but eliminating cross-axis force.

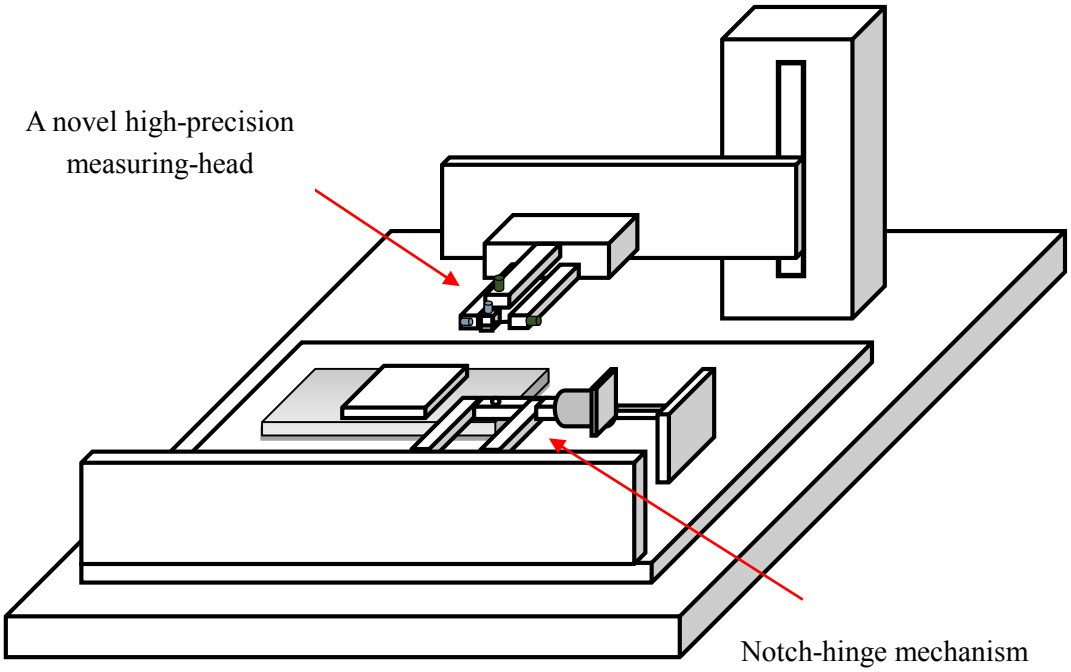

(a) (part) 3D model of the test-rig

Figure 3.2 Micro-friction measurement test-rig (continues)

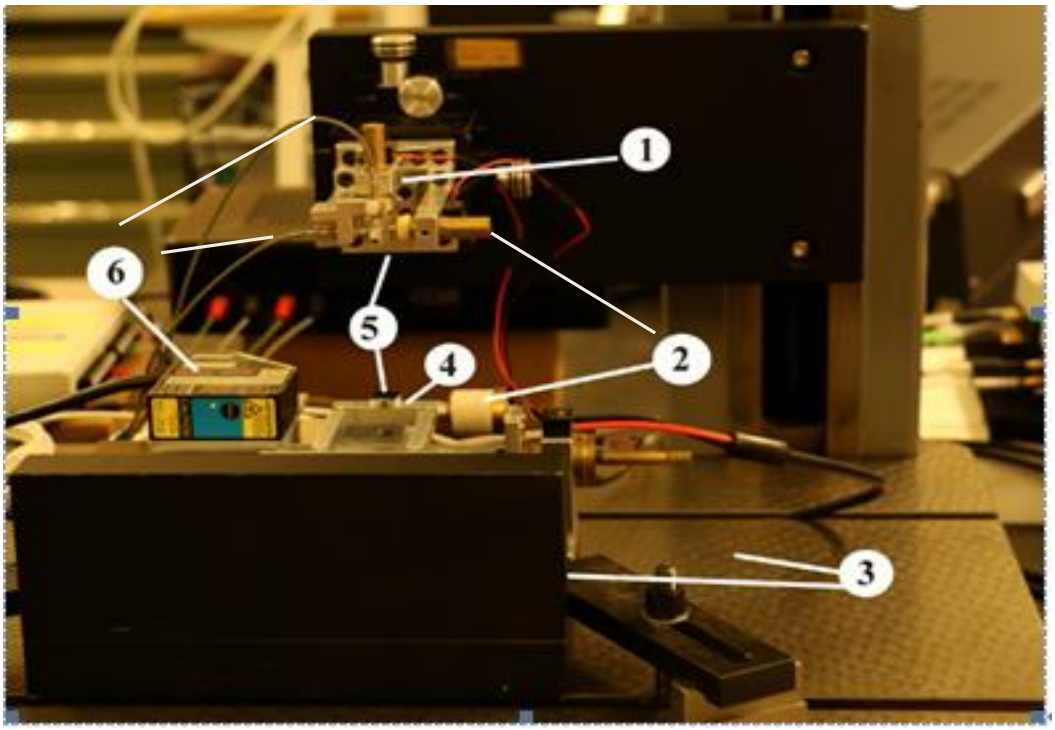

(b) (part) Image of the test-rig

Figure 3.2 Micro-friction measurement test-rig (continues)

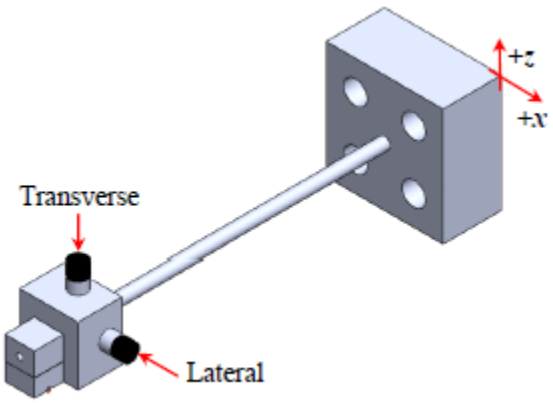

(c) (continued) Sensing beam with Al sample holder and two permanent magnets, and changeable Al carrier tip with counterbody (ball/cylinder) (Alsoufi, 2011)

Figure 3.2 Micro-friction measurement test-rig

The notch-hinge translation device that is made of a notch-hinge flexure, a single magnet-coil drive, an AR200-6M displacement sensor, a power oscillator (LOS TPO25 – power oscillator) and an oscilloscope is used for the high-precision, small displacement with the reciprocating scan mode to obtain high repetition rates of the oscillating scan contact points at up to some tens of hertz during the experiments. It is made of a notch-hinge flexure, a single magnet-coil drive with a well-controlled stroke profile and sufficient power supply to drive the notch hinge forwards and backwards under frictional loading, a AR200-6M displacement sensor used for monitoring the movement of the flexure platform, a power oscillator with a range of frequency from 0 to 25 Hz scaled by (×1, ×10, ×100, and × 1000) and a voltage range of 0 - 25 volts manually set by a “gain” control, and an oscilloscope connected to monitor the output frequency.

Working at higher scanning speeds than commercial systems means considerably higher (lowest) natural frequecies in the sensing system. This implies a stiffer spring for the force sensing, leading to more challenging measurements of smaller deflections and possibility of inducing ‘error’ force components that might not be negligible compared to the desired normal force. Extra complexity of the beam sensors and actuators is a consequence.

Models for both the linear flexure mechanism (scanner) and the sense beam can be realistically reduced to a simple spring-mass-damper systems. Figure 3.3 shows the schematic of the reciprocating tribotester. The scanner will be driven by a periodic, sinusoidal input in the planned experiments. The sense beam will be driven

laterally by friction induced from the scan at the same frequency as the scan but unlikely to be simply sinusoidal. It may be driven vertically by parasitic motion from imperfect alignment of the scanner/sample: these will be sinusoids at the scan frquency for first-order mis-alignments. The reciprocating scan is driven by a force F_g as (3-5):

$$F_g = F_0 \sin(2\pi f t + \varphi) \tag{3-5}$$

where F_0 is the amplitude, f is the reciprocating frequency, φ is initial phase-angle of the electromagnetic driving force.

However, the friction force present here means that the total force acting on the scanner is not simply the input drive. By using a relatively stiff flexure and a relatively large drive actuator, the anticipated friction force (no more than a few tens of mN) will have no significant effect on the scan consistency. The stiff sense beam ensues sufficiently high natural frequencies and also its deflection under friction will be small compared to the (still quite small) scan distance.

The generic 2nd order response is described by (3-6) with general solution (3-7).

$$m\ddot{x} + c\dot{x} + kx = F_0 cos(\omega t + \varphi) \tag{3-6}$$

$$x(t) = x_1(t) + A_0 e^{-\delta t} cos(\omega_1 t + \varphi) \tag{3-7}$$

where m is the total mass of the reciprocating mechanism, ω is the circular frequency of the electromagnetic driving force, respectively. $x_1(t)$ is the particular solution of formula (3-6), A_0 and φ are the constant determined by initial conditions. c is the resistance coefficient, depending on the shape and size of flexure and medium property. k is the stiffness coefficient. ω_1 is defined by

$$\omega_1 = \omega_0\sqrt{1-\delta^2} \tag{3-8}$$

where ω_0 is the circular frequency of the electromagnetic driving force without damping and δ is the critical damping factor.

As a tribometer, there is frictional dissipation and so fairly high damping. The transient in (3-7) will then decay very quickly on the scanner, so the drive can be assumed to be steady state (as in (3-9)) throughout.

$$x(t) = Acos(\omega t) \tag{3-9}$$

where,

$$A = \frac{F_0}{m\sqrt{({\omega_0}^2-\omega^2)^2+4\omega^2\delta^2}}; \quad {\omega_0}^2 = \frac{k}{m}; \quad \delta = \frac{c}{2m} \tag{3-10}$$

$$v(t) = \dot{x}(t) = -\omega Asin(\omega t) \tag{3-11}$$

where A is the constant determined by steady state and $v(t)$ is the scan speed of the notch-hinge mechanisms.

The effective end-mass of the sense beam and holder will introduce an error into the set normal force if any vertical motion is induced from variations in the sample surface height (either misalignment or shape-related). The acceleration $a(t)$ is given at (3-12), which leads to an estimate for how much vertical motion can be tolerated (and provides a model for a control algorithm).

$$a(t) = \ddot{x}(t) = -\omega^2 Acos(\omega t) \tag{3-12}$$

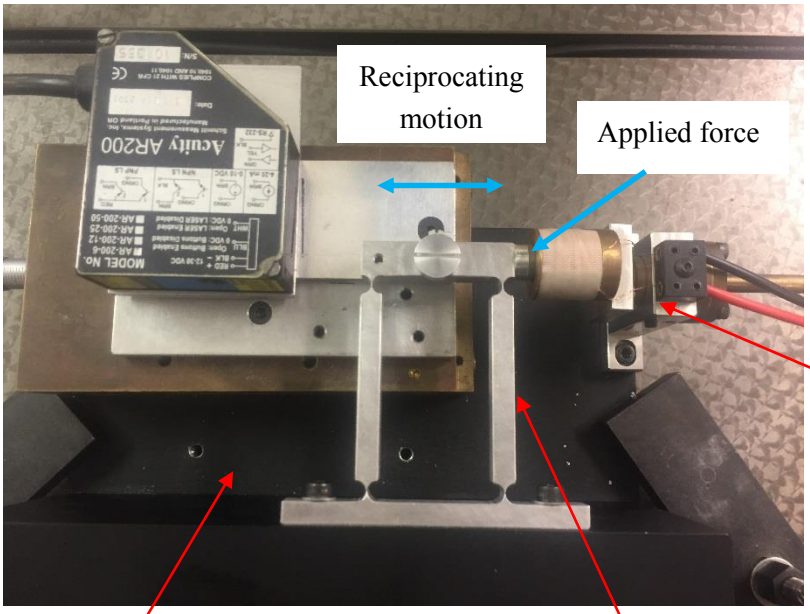

(a) The picture of the notch-hinge mechanisms

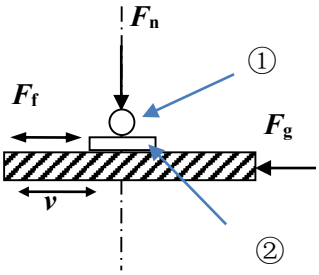

① Sample counter-face (ball or cylinder) ② Sample (flat or cylindrical)

(b) Schematic of the friction measurement

Figure 3.3 Flexure-based reciprocating scanner

3.3 Re-calibrations of the Test-rig

The primary calibration results of the first prototype reciprocating micro-tribometer had been obtained and reported by Alsoufi in his thesis. The sensitivity, the stability and the repeatability of the system were demonstrated to be sufficient for use in the

micro-friction measurements for that work. However, for the re-establishment of the test-rig, re-calibrations of the test-rig are essential to obtain the same, or higher degree of precision as Alsoufi's results for further tribological investigations of the polymers applied in ball-on-flat and crossed-cylinders configurations.

3.3.1 Multipoint Calibration for Vertical and Lateral Position Sensors

A RENISHAW, XL-80 laser interferometer (0 - 40 m standard linear measurement, 1nm resolution), that had been adopted in Alsoufi's thesis, was again used to re-measure the sensitivity of the non-contact eddy current sensors in the vertical and lateral directions. It offers ease of use with more than adequate system accuracy, high reliability and good dynamic measurement performance.

Figure 3.4 illustrates the basic set-up of the laser interferometer including an XL-80 laser head mounted on a tripod, an interferometry retro-reflector and a remote interferometry optic fixed on a cast iron instrument base. A manually-driven short-range linear ball-bearing translation stage was used to carry and adjust the interferometry retro-reflector and an aluminium target plate for the gauges, see Figure 3.5. There was approximately 0.5 m dead-path for laser beam between the laser head and the remote interferometry optic. Figure 3.5 shows that both gauges had been clamped to the cast iron base and were placed at approximately 0.3 mm from the aluminium plate and about 10 mm apart. The calibration experiments were repeated three times at nominally 22 ± 1˚C and 40 ± 5% relative humidity in the same metrology laboratory being used for the tribology experiments.

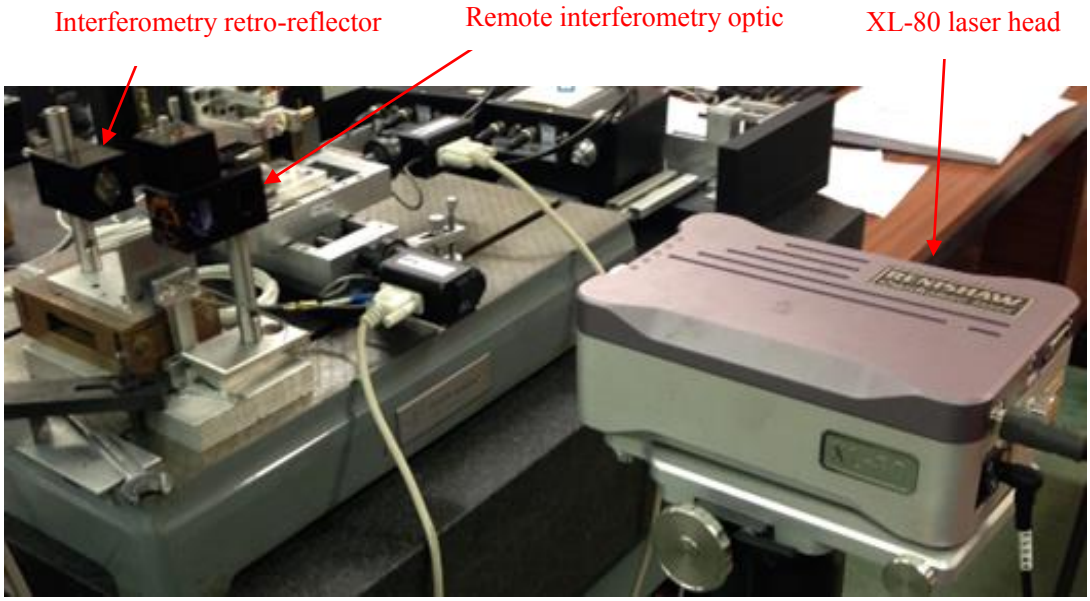

Figure 3.4 The set-up of the laser interferometer

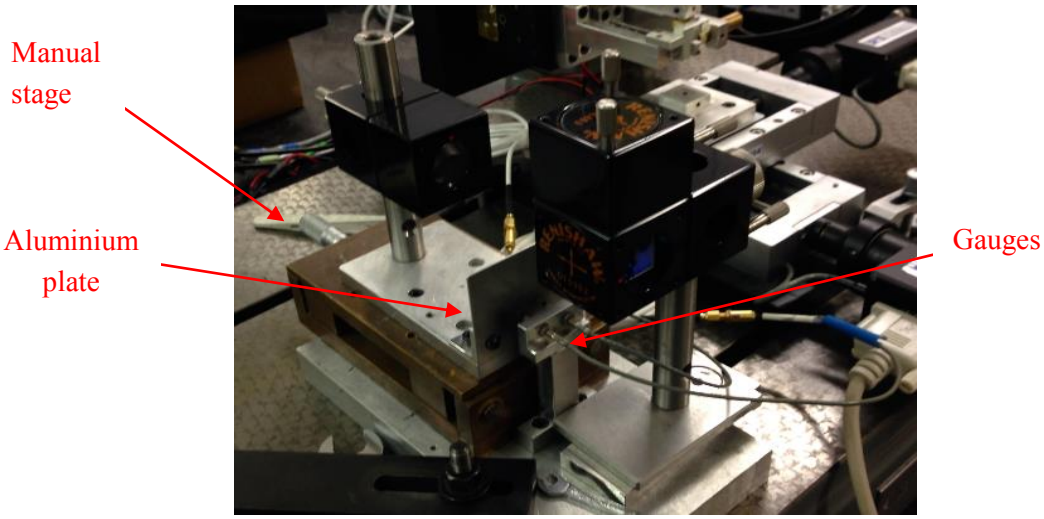

Figure 3.5 Positions of gauges and aluminum plate

A multi-point calibration measurement that took eleven points from a starting point (0.0 mm) to an end measuring point (0.5 mm) with an interval size of 0.05 mm was used to re-investigate the sensitivity and the linearity of the sensors for both the transverse and lateral positions. Figure 3.6 shows the multi-point re-calibration

results for the sensitivity of the lateral position sensor. Specifically, Figure 3.6 (a) displays the three measurement curves and their respective sensitivity evaluated from a linear least-squares fit using the standard algorithms of the Excel software, while Figure 3.6 (b) plots the point by point the average of the three measurements. Based on these graphs, linearity is excellent over the working range ($R^2 > 0.999$) for the lateral axis sensor. Its sensitivity is 48.6 µm/V; in fact, the mean of the three sensitivities given in Figure 3.6 (a) is 48.616 µm/V, the same as that obtained from Figure 3.6 (b). By using the interferometer, the uncertainty in this value will be dominated by that of recording the sensor output voltage and is estimated to be comfortably below 1%.

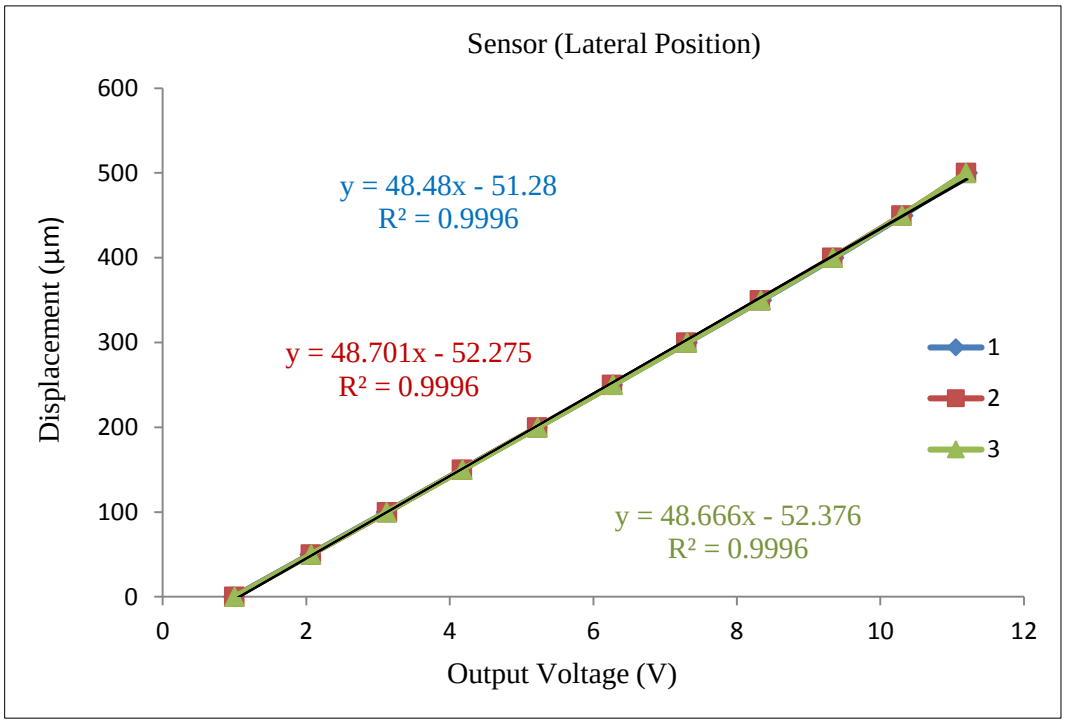

(a) Three measurements calibrations

Figure 3.6 Multipoint calibrations for the position of lateral sensor (continues)

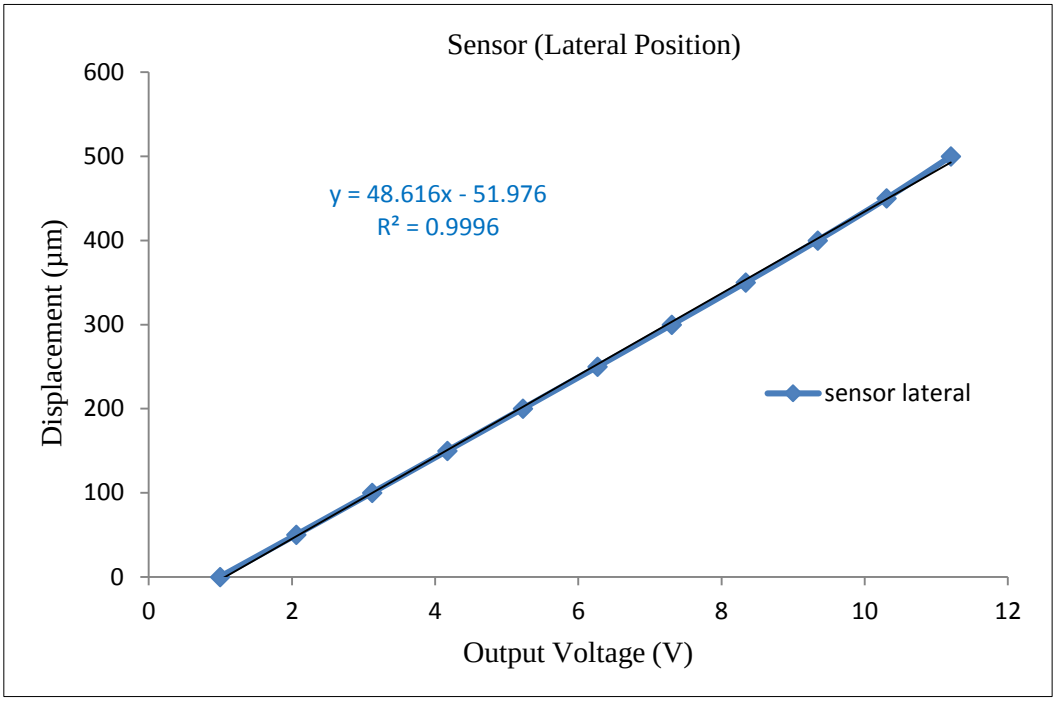

(b) Mean value of every measuring point in three measurements

Figure 3.6 (continued) Multipoint calibrations for the position of lateral sensor

Figure 3.7 shows the multi-point re-calibration results for the sensitivity of the vertical position sensor, which is a replacement for the one originally installed. It has rather poorer linearity that might lead to a restriction of the working range. Avoiding the measuring points in the larger displacements could clearly lead to a more precisely linear fitting curve. However, selecting less measuring points will lead to a shorter measuring range. There is need to select a good practical compromise between the requirements for good linearity, high sensitivity and sufficient working range of the sensor.

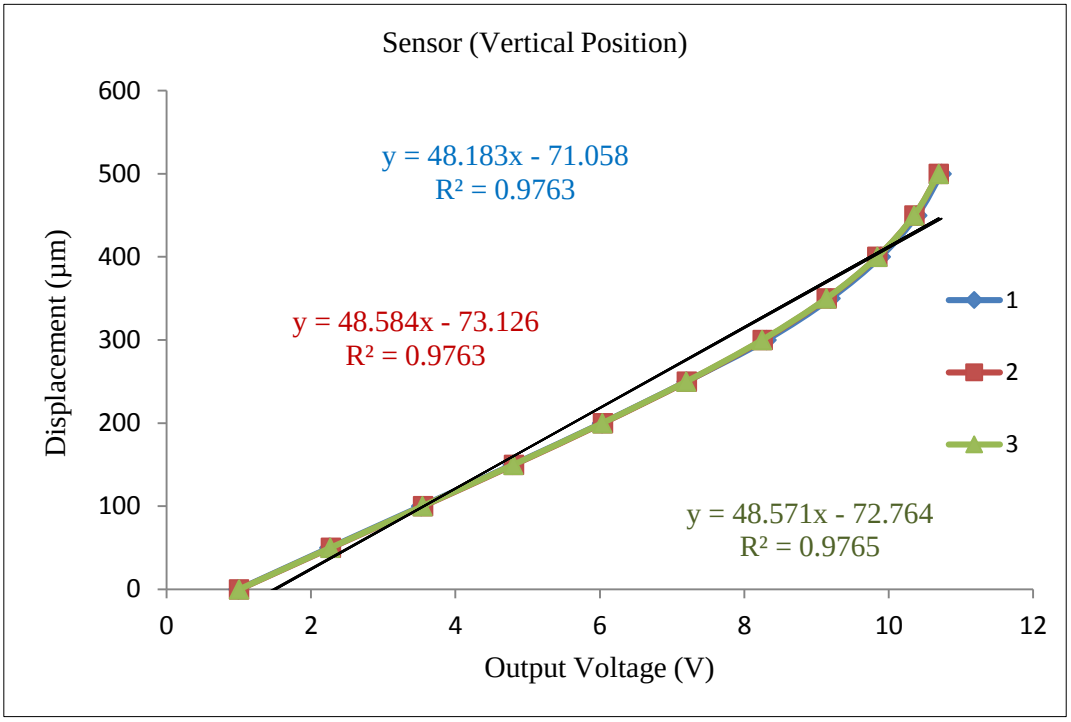

Figure 3.7 Multi-point re-calibration for the position of vertical sensor

Figure 3.8 shows two more different multi-point calibration results for the sensitivity of the vertical position sensor. Figure 3.8 (a) chose a larger displacement to provide a wider working range for sensor measurement but obtained a relatively low linearity measurement ($R^2 < 0.999$). Instead, linearity is excellent ($R^2 > 0.999$) over the relatively lower measurement range shown in Figure 3.8 (b). According to the calculations of the mean value of three different calibration results, the sensitivities of the sensor in these two situations are 42.2 µm/V and 40.9 µm/V respectively. In this thesis, we use 42.2 µm/V for the sensitivity of the vertical sensor based on the practical observation that convenient setting up of the whole instrument tends to be using the upper part of the sensor range.

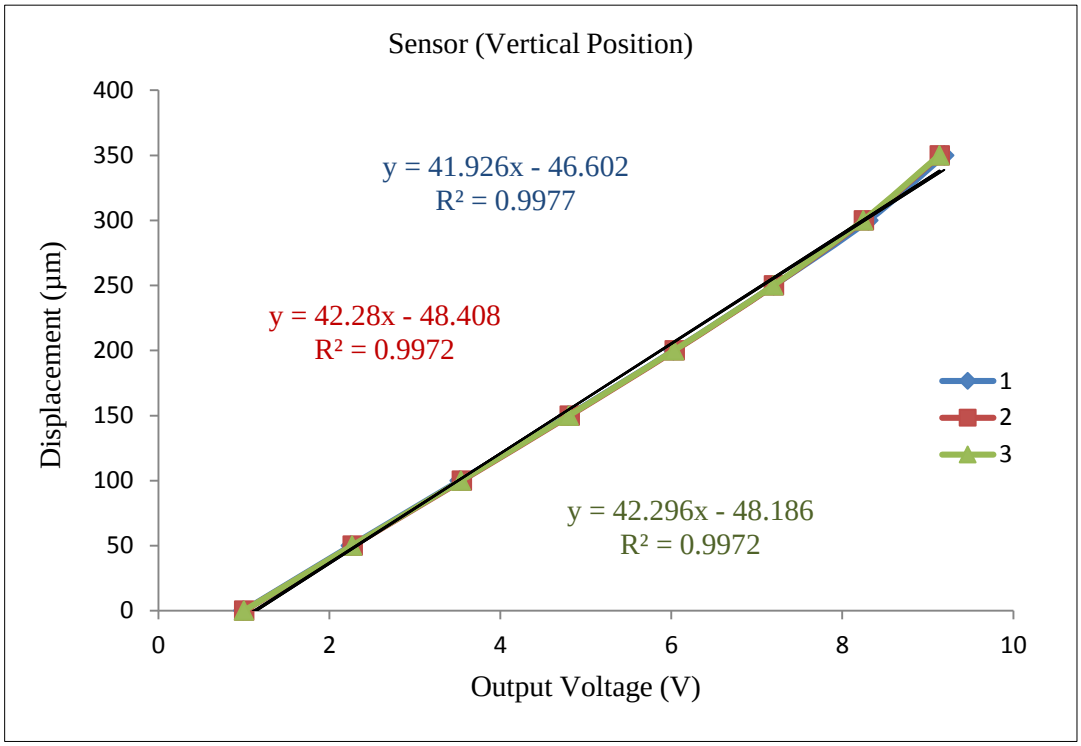

(a) Eight-point calibration for the position of the vertical sensor

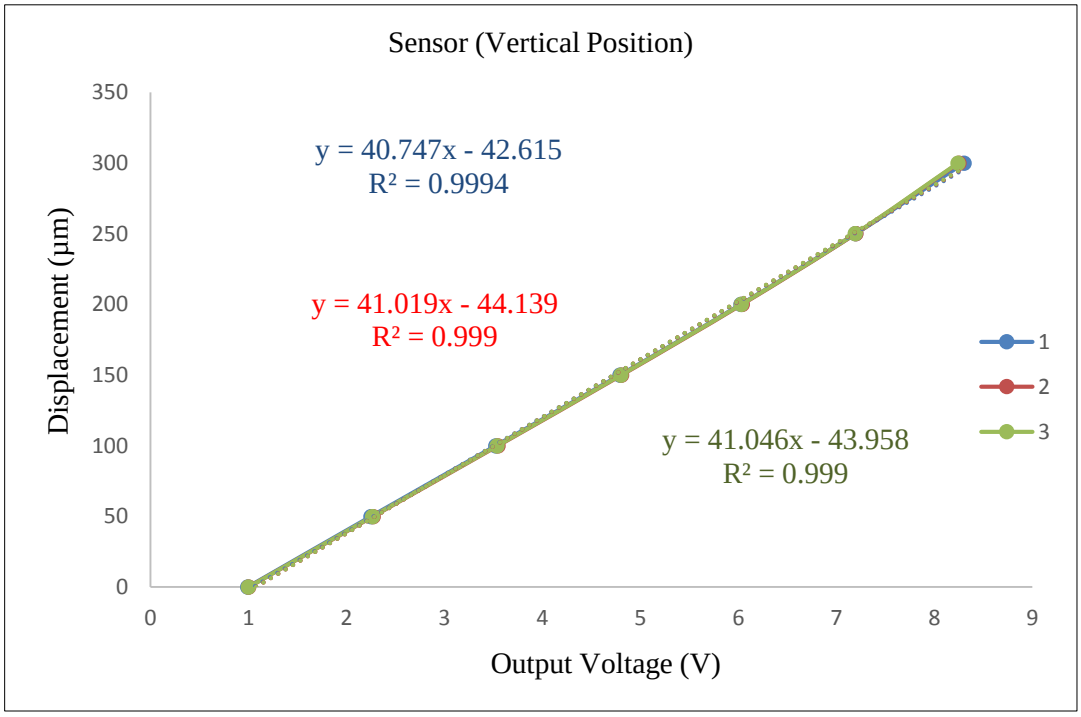

(b) Seven-point calibration for the position of the vertical sensor

Figure 3.8 Two different multi-point calibration results for the position of vertical sensor

3.3.2 Dead-weight re-calibration of the sensing beam stiffness

The dead-weight calibration method is used to acquire the stiffness constant of the sensing beam element in the vertical and lateral axes calculated from testing data that is directly converted into the corresponding force-deflection curve (F-δ). Dead weights in the range of 10 mN to 200 mN were placed in turn to hang from cotton thread, just resting on the end-block of the sensing beam, in order to avoid a potentially significant uncertainty in the position. The free beam deflection was measured by reading output voltage of the vertical sensor on a digital multimeter (34401, Agilent) and applying the sensitivities calibrated in the previous section, and its range were taken at up to ±80 μm by turning the rig upside-down to give gravity acting in the upward vertical direction of the rig. This method is convenient, but possible useful, to calibrate for lateral stiffness and avoid potentially significant uncertainty in the position between the sensing-beam and rigid block.

According to the material mechanics, the calculation formula of the sensing beam stiffness k is

$$k = \frac{F}{\delta} \tag{3-13}$$

where F is the applied dead weight and δ is the deflection of the sensing beam.

The deflection of the sensing beam δ is calculated from

$$\delta = VS \tag{3-14}$$

where V is the output voltage of the sensor produced by deflection of the sensing beam and S is the sensitivity of the sensor. Therefore, the sensing beam stiffness k can be calculated by

$$k = \frac{F}{VS} \tag{3-15}$$

Four experimental tests were carried out independently for each of k_x and k_z, respectively. As shown in Figure 3.9, the linearity of the lateral force-deflection relationship for all four measurements was excellent over the working range ($R^2 >$ 0.999). The mean value of the compliance of the *F*-δ fitting curves was 0.363 μm/mN for the lateral axes, with the sensing beam stiffness constants of k_x = 2760 N/m. The *F*-δ fitting curve for lateral stiffness calibration, in Figure 3.10, was plotted by the mean value of every measuring point in four measurements. It still revealed excellent linearity and the compliance for the lateral axes was then 0.360 μm/mN with the sensing beam stiffness constants of k_x = 2780 N/m. These graphs include any non-linearity of the sensor characteristic (pretty small over the amount of the range being used here) and the uncertainty in the sensor sensitivity itself. The actual magnitudes of the weights were determined by measuring the force applied by gravity on each kilogram of mass *g* (taking 9.8 N/kg).

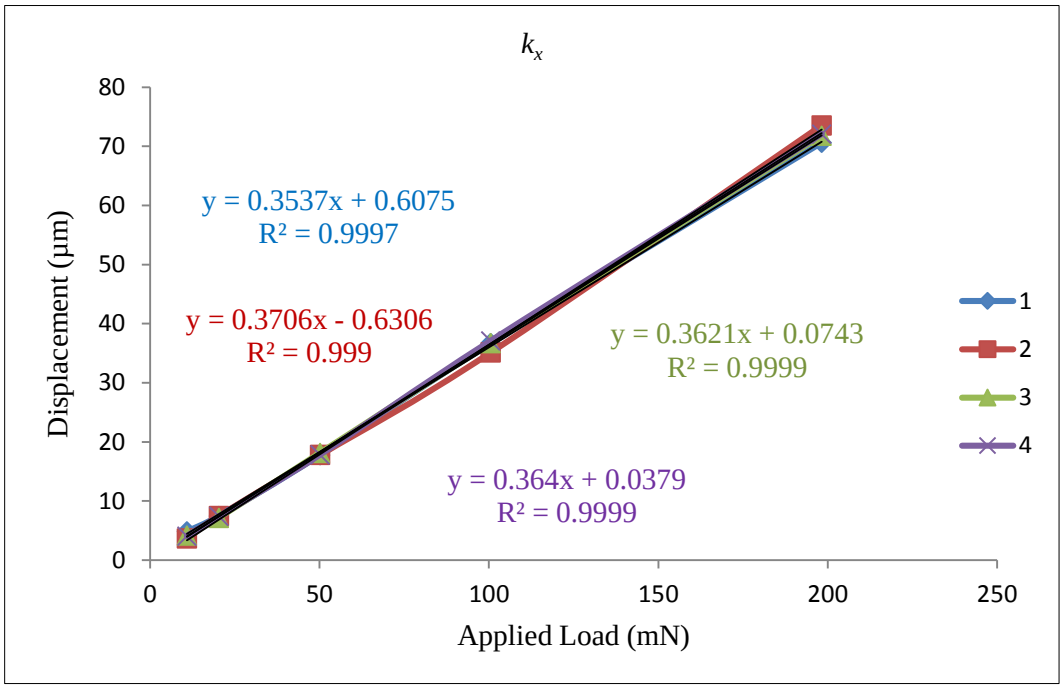

Figure 3.9 *F-δ* fitting curve of lateral stiffness calibration for four different tests

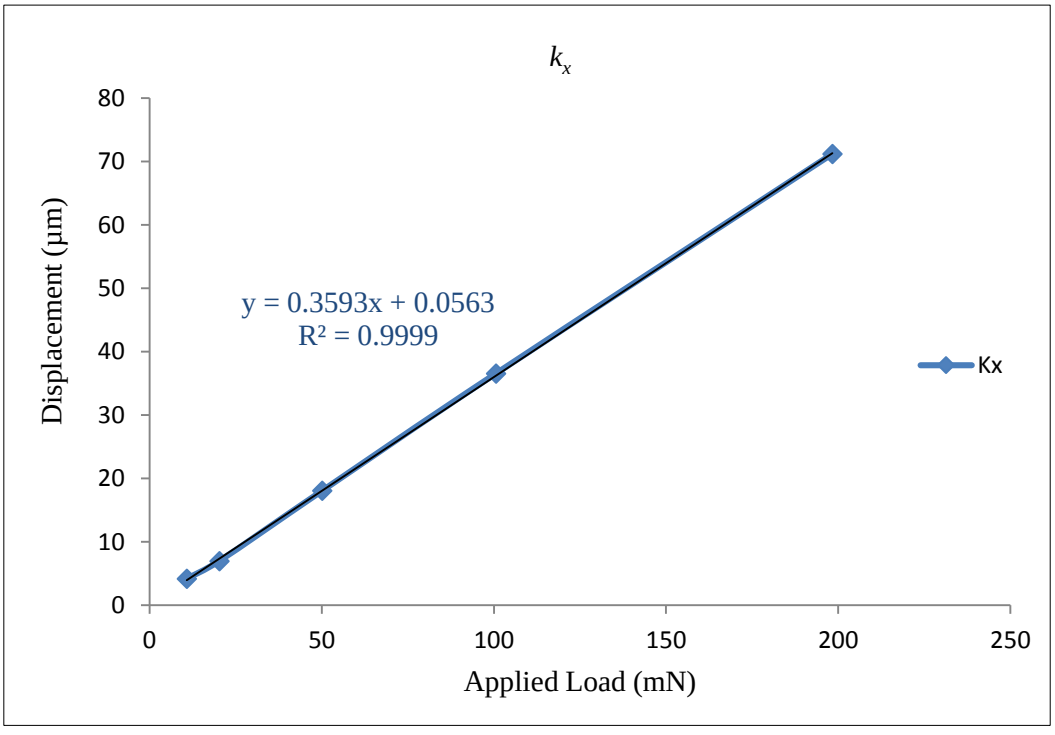

Figure 3.10 *F-δ* fitting curve of lateral stiffness calibration

Figure 3.11 shows the excellent linearity of the force-deflection relationship over the working range ($R^2 > 0.999$) for the vertical axes. The mean value of the compliance of the *F-δ* fitting curves are 0.372 μm/mN, with a sensing beam stiffness constant of k_z = 2690 N/m. Similarly, the mean value of every measuring point in four measurements was calculated for vertical stiffness calibration to draw the *F-δ* fitting curve shown in Figure 3.12, and obtained almost uniform results compared with those in Figure 3.11. Small deviations of the value from the re-calibrated k_x and k_z might be due to the slight asymmetry arises from geometric and materials imperfections. However, the first set of calculation results for both lateral and vertical axes have smaller deviations between k_x and k_z and thus we use k_x = 2760 N/m as the lateral stiffness constant of the sensing beam during the friction tests.

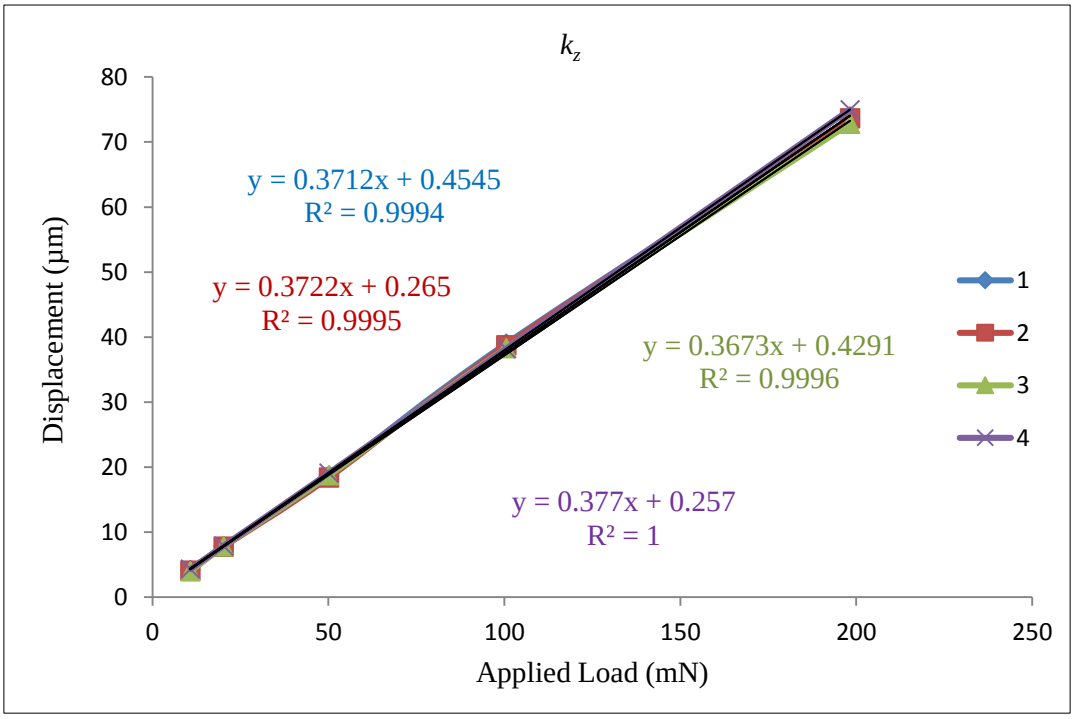

Figure 3.11 *F-δ* fitting curve of vertical stiffness calibration for four different tests

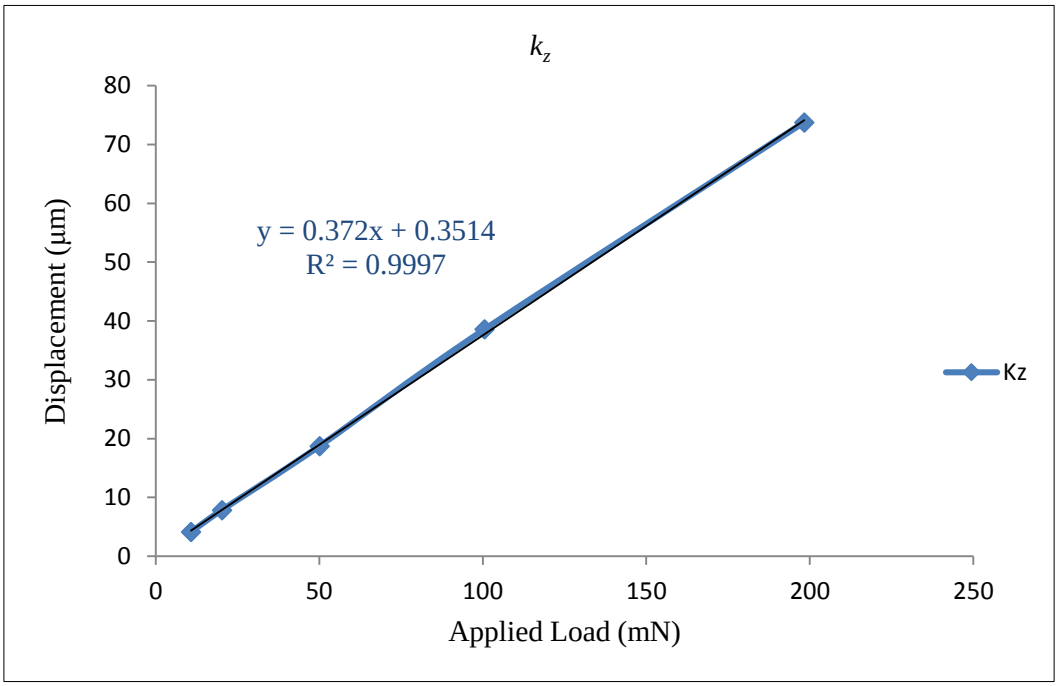

Figure 3.12 *F-δ* fitting curve of vertical stiffness calibration

3.3.3 Re-calibration of the force actuator

Having re-calibrated the sensing beam stiffness k_z and k_x, the re-calibration of the force actuator can use the vertical sensor in a set-up similar to that for the dead-weight calibration. The voltage to the actuator was simply incremented in steps to measure the deflection by the eddy-current sensor. This is easy but the final calibration incorporates the effects of sensor non-linearity and its calibration uncertainty, as well as that for the beam stiffness. This time, step changes in normal load applied by the coil current of the force actuator are related to the vertical deflection of the sensing beam. *F-V* fitting curves are mainly used as an important parameter for the calculation of friction force. Strictly, the linear control input to the actuator coil should be current and Alsoufi's thesis reports a sensitivity close to 0.11

mN/mA. However, the test-rig incorporates a feedback-controlled current source and it is operationally convenient to use the input voltage to the current source to set the force. Calibration here is for this approach. The measured beam deflections are converted to force using the measured beam stiffness contacts, to provide the actuator constants. Thus,

$$F_N = V \times S_z \times k_z \tag{3-16}$$

where F_N is applied force, S_z is the sensitivity of the vertical actuator, V is the output voltage from the vertical deflection of the sensing-beam measured by the vertical sensor and k_z is the stiffness of the sensing-beam in the vertical position.

Figure 3.13 shows the voltage-force graph on the vertical axis and the applied force saturation at a level of around 50 mN when the input voltage was beyond 2.5 V. This reflects the peak capability of the current source to drive into the resistance of the coil and illustrates the slight disadvantage of using voltage as the input parameter. However, linearity was excellent over the range of the output voltage of 0 - 2.5 V ($R^2 > 0.999$) for the vertical axes confirming deflection from the force actuator and eddy-current sensor, as shown in Figure 3.14. Therefore, the effective range of the output voltage is considered as that of 0 V to 2.5 V and the corresponding maximum applied force is below 60 mN over the actual operating range. The mean value of every measuring point in five measurements was calculated to draw the *F*-*V* fitting curve, as shown in Figure 3.15, to obtain accuracy and consistent relationship ($R^2 = 0.9996$).

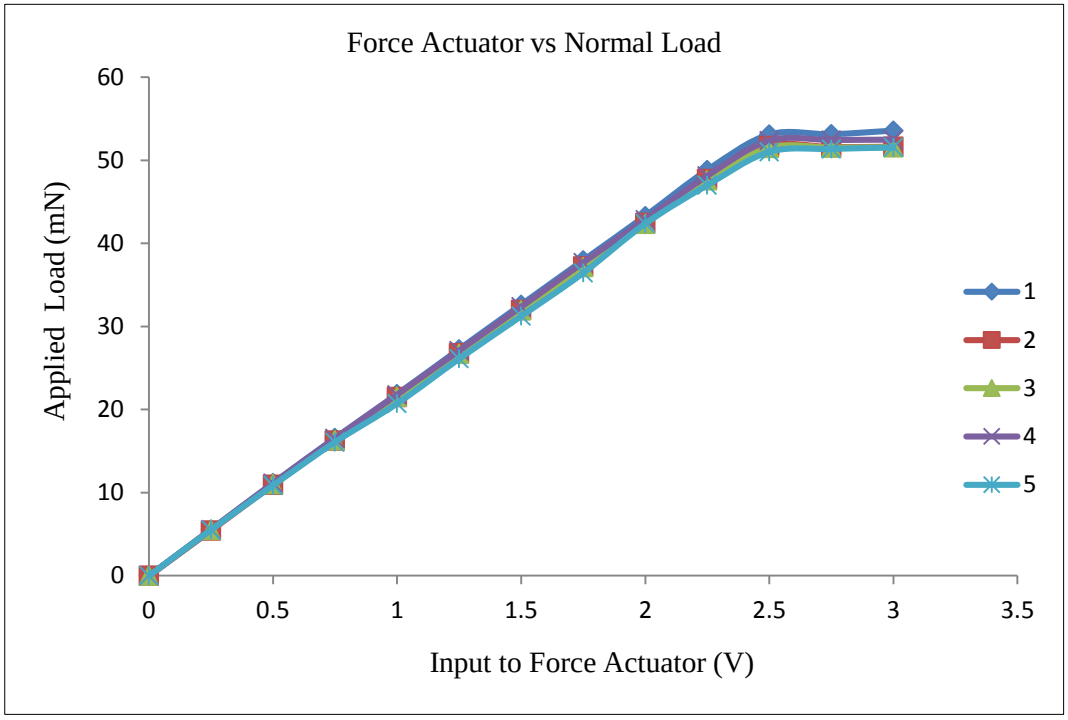

Figure 3.13 Correlation between input voltage and output load from force actuator

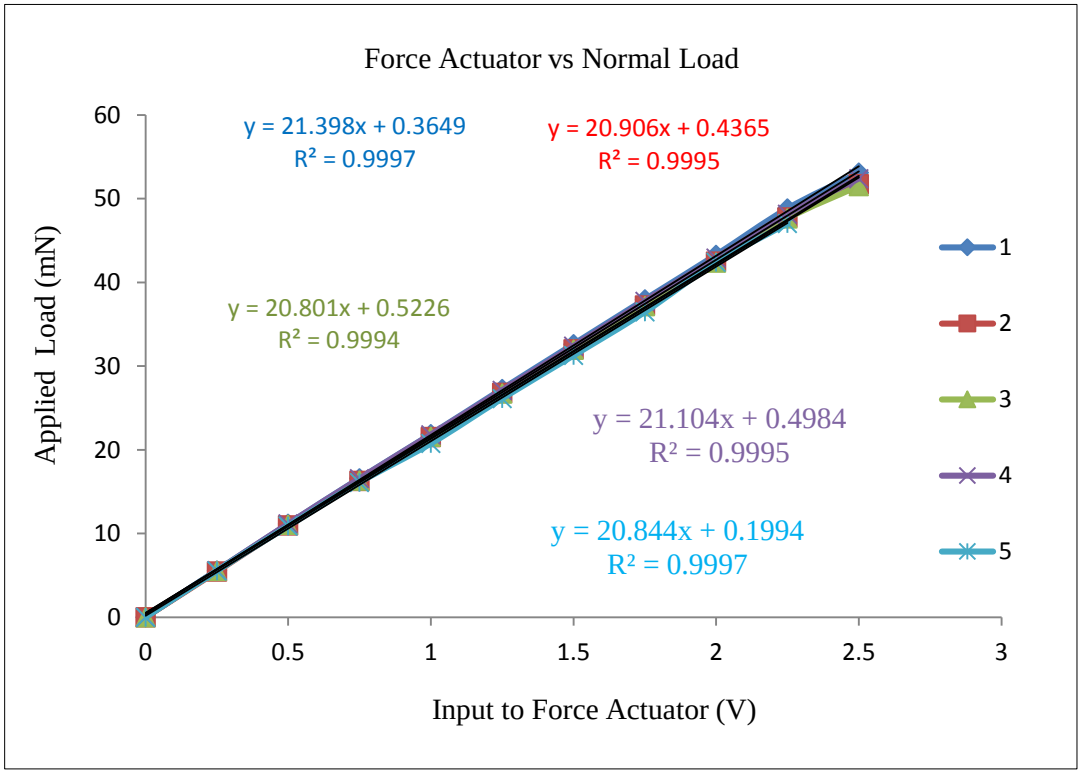

Figure 3.14 *F-V* fitting curves of force actuator calibrated with sensor

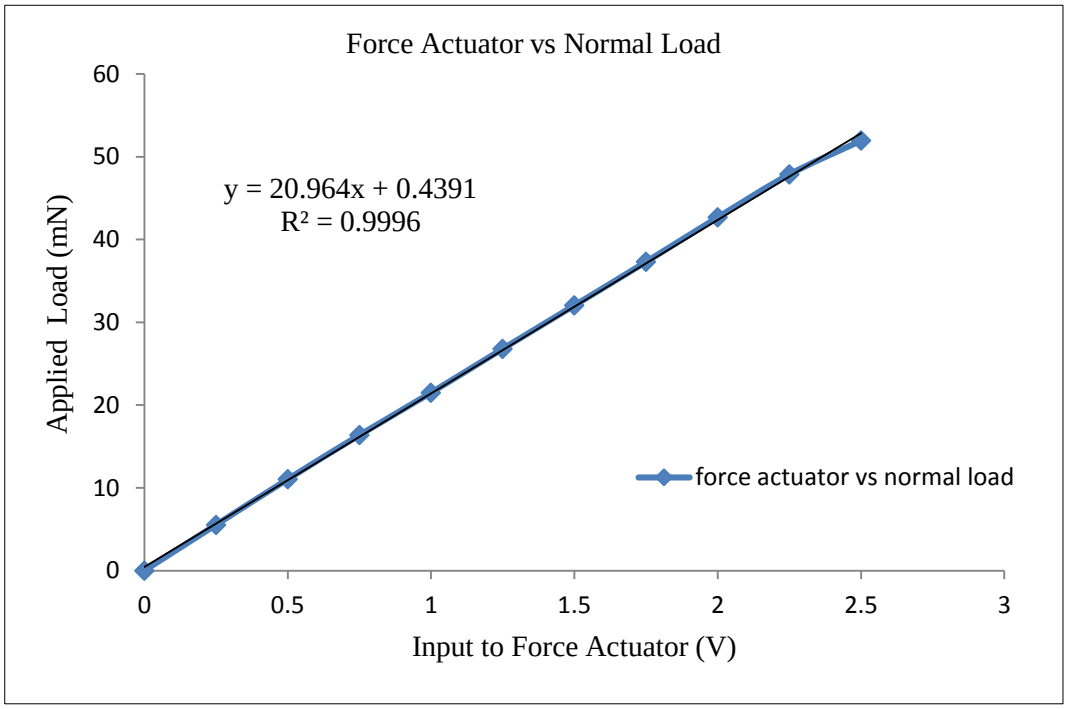

Figure 3.15 Mean value of every measuring point in five measurements for *F-V* fitting curve of force actuator calibrated with sensor

3.3.4 Calibrations of the Notch-hinge Flexure Mechanisms

The reciprocating mode of the notch hinge flexure and its magnet-coil force actuator can be regarded as a simple harmonic vibration driven by an input sine wave. The frequency and amplitude (actually labelled as 'gain' on the controls) of a model LOS TPO 25 power oscillator are used to control the track length and scan speed of the specimens. The notch hinge flexure mechanism is calibrated to the *G-L* fitting curves between the gain of the power oscillator and the reciprocating displacement of the notch hinge flexure measured by a AR200-6M non-contact optical displacement sensor and the variations of the f v $G - V_A$ relationship between the reciprocating frequency, the gain and the output voltage of the power oscillator. This

is needed because this output voltage is the only convenient way to monitor oscillator stability during routine operation of the system. These parameters are used to provide the critical test conditions for the scan modes of the micro-tribological measurement. Figure 3.16 shows the variations of the gain G and the voltage amplitude V_A over the frequency range of 0-15 Hz. Changes in frequency have an impact on V_A over the whole range. However, the G-L fitting curves calibrated with two setting frequencies of 4.5 Hz and 7 Hz reveal that changes in the frequency have hardly any influence on the relationship between the gain and the physical displacement, as shown in Figure 3.17. Thus, the track length of the notch hinge flexure is here regarded as only dependent of the gain controlled by the power oscillator and shows a greater variation tendency when G is beyond 10. Figure 3.18 shows the relationship between the displacement and the gain according to the calculated mean value of every measuring point in three measurements under different frequencies, and will be used to provide accuracy and consistent test conditions for friction measurement.

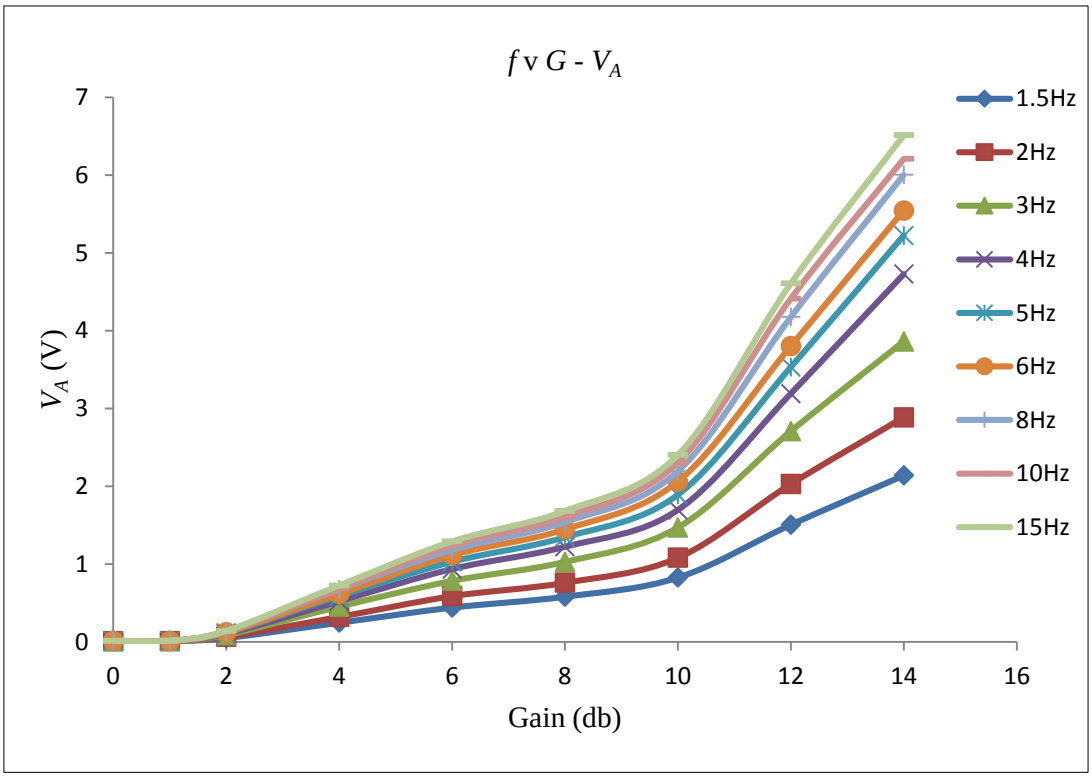

Figure 3.16 Variations of the amplitude and the gain under nine different frequencies from 1.5 Hz to 15 Hz

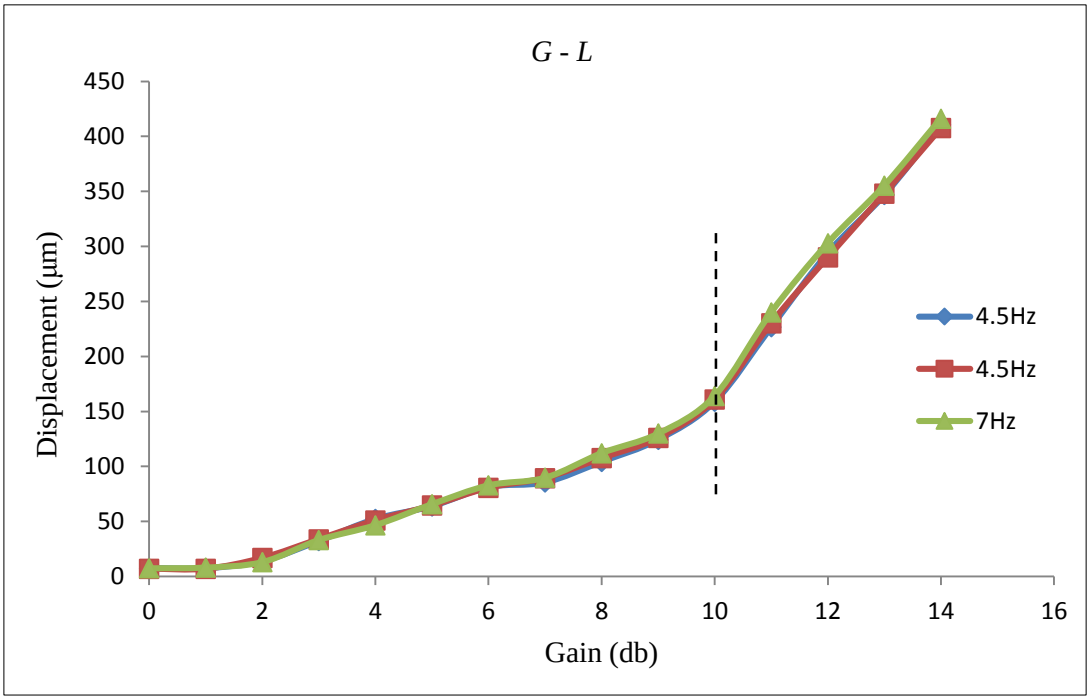

Figure 3.17 Variations of the gain and the displacement under two different frequencies

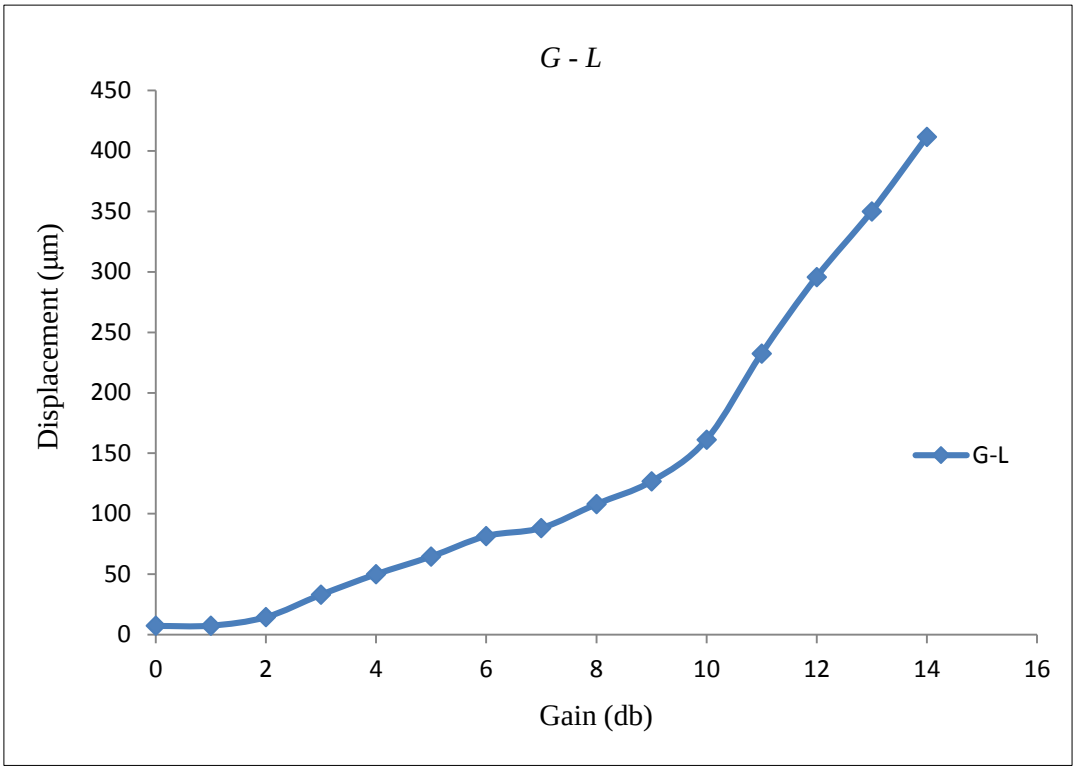

Figure 3.18 Relationship between the displacement of the notch-hinge mechanisms and Gain from the power oscillator

3.3.5 Summary of Results and Comparisons

The relationship between the force actuator and the vertical sensor, and between the gain and the displacement are summarised in Table 3.1 and Table 3.2, respectively.

The re-calibration results of the test-rig are summarised in Table 3.3 including the sensitivity of the sensors, the stiffness of the sensing beam, the actual application ranges between the output voltage of the force actuator and applied normal load, and the parameter configurations of the notch hinge mechanisms, to make a comparison with original ones from Alsoufis Thesis (2011). They provide the parameters for the data processing for further tribological investigations at the micro-scale.

Table 3.1 The relationship between the output force (load applied to the beam and the input voltage to the force actuator system

Force Actuator (V)	Applied Load (mN)
0	0
0.25	5.53
0.5	11.03
0.75	16.37
1	21.49
1.25	26.80
1.5	32.04
1.75	37.31
2	42.68
2.25	47.87
2.5	51.95
2.75	52.02
3	52.17

Table 3.2 The relationship between the gain and the displacement

Gain(db)	Displacement(μm)
0	7.35
1	7.57
2	14.59
3	33.12
4	50.01
5	64.70
6	81.59
7	88.28
8	108.02
9	126.77
10	161.32
11	232.38
12	295.77
13	350.05
14	411.47

Table 3.3 Comparison of the re-calibration results and original ones from Alsoufi thesis

Items	Calibration Results from Alsoufi	Re-Calibration Results
Sensitivity of the Sensors		
Lateral	47.711 μm/V	48.6 μm/V
Vertical	46.152 μm/V	42.2 μm/V
Stiffness of the Sensing-beam		
k_x	2703 N/m	2760 N/m
k_z	2778 N/m	2690 N/m
The Relationship between Force Actuator and Applied Load		
Driving Voltage V	0 - 2.15 V	0 - 2.5 V
Applied normal load F_N	10 - 50 mN	0 - 60 mN
Notch-hinge Mechanisms		
Gain G		0 - 14 db
Oscillator output V_A		0 - 7 V
Frequency f		1.5 - 15 Hz
Displacement L	0 - 100 μm	7 - 420 μm
Testing Environment		
Temperature	20 ± 1˚C	22 ± 1˚C
Relative humidity	40 ± 5%	40 ± 5%

3.4 System Reintegration

Based on the updated LabVIEW software package and Microsoft Windows 7 platforms, three PCs with embedded data acquisition cards (NI USB-6215, 16-Bit, ±10 Volts, analog-to-digital converter) are used to provide real-time measurements of the output data from the magnet-coil force actuator, the micro-epsilon eddy-current sensors in the sensing head and the AR200-6M displacement sensor in the notch hinge mechanisms. Using several computers make it possible to obtain higher operating speed for friction measurement and prevents mutual interference

between signals.

In normal operation, two magnet-coil force actuators in the vertical and lateral directions are driven by a PC connected with a data acquisition card (digital-to-analog converter) as output signals to provide both vertical force and counter body lateral force (or position control) while measuring friction. Then, two unshielded non-contact eddy current sensors (<25 nm resolution, ideally) are also used to monitor the vertical, and lateral deflections of the sensing beam generated by the magnet coil force actuators and friction forces and output data recorded and stored into another PC with a data acquisition card (analog-to-digital converter). Finally, the AR200-6M displacement sensor is used with the third data acquisition card (analog-to-digital converter) to measure the specimen scanning length and the data saved in a format of (*.lvm) for further analysis when the reciprocating mechanism is started. The whole system is intended to permit the performance of a wide variety of tests on the micro-scales with wide ranges for loading and oscillating scan speed. Figure 3.19 shows the operating schematic diagram of the reciprocating scan system.

The system integration provides the operation instruction of the computer controlled parts, including the application of the transverse force and the measurement of the lateral force, and the monitoring of specimen scanning length while measuring friction, as the guidance for tribologists and designers.

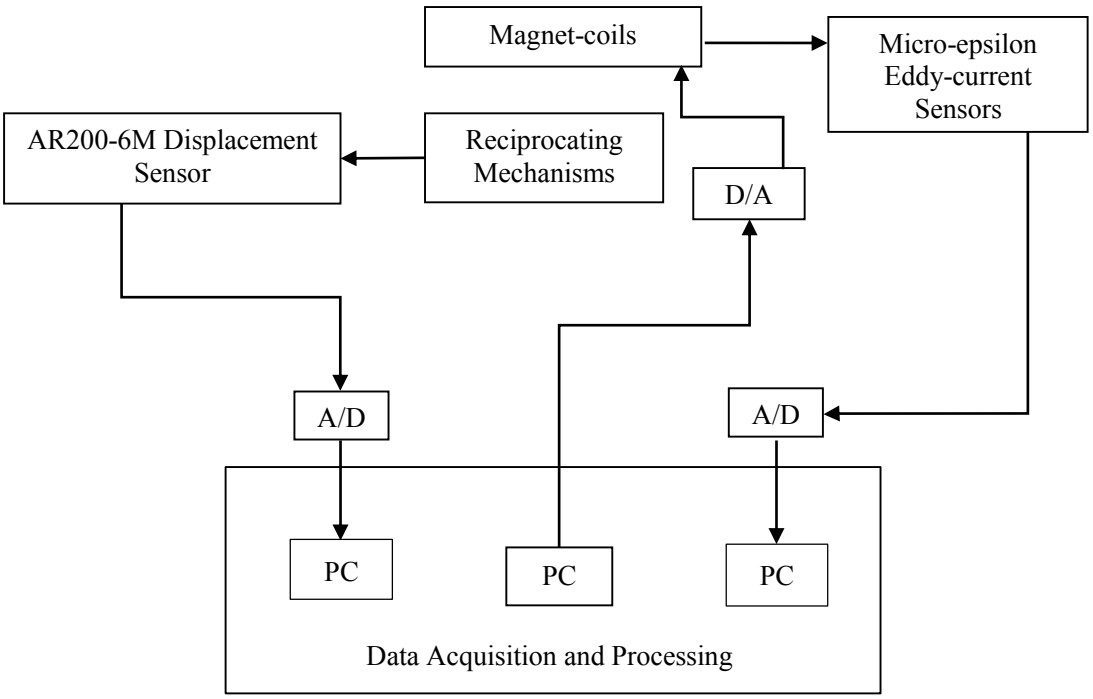

Figure 3.19 Operating schematic diagram for monitoring of the reciprocating scan system

4 Demonstrating the Custom Micro-tribometer in Reciprocating Mode

Overview

Demonstration of the test-rig was carried out to examine the friction force and coefficient of friction against applied normal loads (in the range of 10 – 60 mN), sliding frequency (between 3 Hz and 9Hz), track length (in the range of 66 – 130 μm) of the test specimens using ball-on-flat and crossed-cylinders configurations under dry sliding conditions where there are no applied lubricants. First, a micro-tribological test method for the reciprocating micro-tribometer is summarized, and surface topography of test specimens measured to test for any correlation between the sample surfaces and their friction properties. Then, tribometer signal processing, including signal variations in the vertical and lateral deflections, and static and transient uncertainties, at the micro-scale were analysed. The experimental calculation methods for normal load, friction force, and coefficient of friction are established for friction measurement according to our experiment calibrations and compared to the related literature. After that, approaches to tribometer signal processing and calculation of friction measurements, at the micro-scale were analyzed. This highlights and explores the computational accuracy of friction measurement at the micro-scale. Finally, test results are obtained, analysed and compared to theoretical calculation and other experimental tests to sufficiently demonstrate the validity of the developed test system with a ball-on-flat configuration. Also, two modes were tested to make a comparison in order to analyse the availability and consistency of the crossed-cylinders test with ball-on-flat test. It is shown capable of giving very useful information, over the range of materials examined, on the influence of parameters such as applied load, sliding velocity, track length for the tribological behaviour and underlying mechanisms under the specified micro-scale conditions.

4.1 Experimental Set-up and Procedure

4.1.1 Sample Selection and Surface Topography Studies

Figure 4.1 shows examples of the several types of specimens used in this set of experimental demonstrations. Ball-on-flat configurations used always a stainless steel AISI 440C (grade 10) ball as the tip, while the flat specimens were either of the same steel or pieces of silicon wafer with a silicon dioxide film. Specimens for

crossed-cylinder configurations were of stainless steel and glass.

(a) Tip - ball (b) Specimen - steel (c) Speicmen - Si/SiO_2

(i) Ball-on-flat configuration

(a) Specimen - steel (b) Specimen - glass (c) Pin - glass (d) Pin - steel

(ii) Crossed-cylinders configuration

Figure 4.1 Pictures of the counterbodies and samples

Prior to friction testing, the surface topography of the samples was investigated, to allow consideration of whether any standard roughness parameters might be correlated with micro-tribological behaviours. Measurements were made using a Bruker ContourGT-K1 3D non-contact optical surface profiler, using its software for all the analysis. The surface profiler is versatile bench-top optical surface profiling systems with automated stages and automated optics selection. It can be used to

measure surface topography of a wide variety of sample surfaces from optical-quality glass to automotive parts with high accuracy in a range from several nm up to approximately 10 mm and provide the analysis for solar cell, thick films, semiconductor, medical device, MEMS and tribology applications.

Before the measurement of all the samples, a scratched silicon surface was selected deliberately to adjust the lateral position of the sample stage. The VSI mode was chosen with a 50X camera lens for this particular test. Then, the selected specimen was placed on the sample stage and adjusted for the scanning area. After that, the instrument settings including measurement parameters, measurement type, and measurement area were set for different scans of sample surfaces. Finally, a measurement was performed simply by clicking the measurement button, and the measured data was saved in configuration files for analysis. To some extent, this technique is used for topography measurement to expect an extensive correspondence and represent a range of values in the parameters reported. An example of a steel specimen is shown in Figure 4.2, to show that the relative heights are built up by scanning the objective vertically and recording the position of which each pixel has maximum contrast.

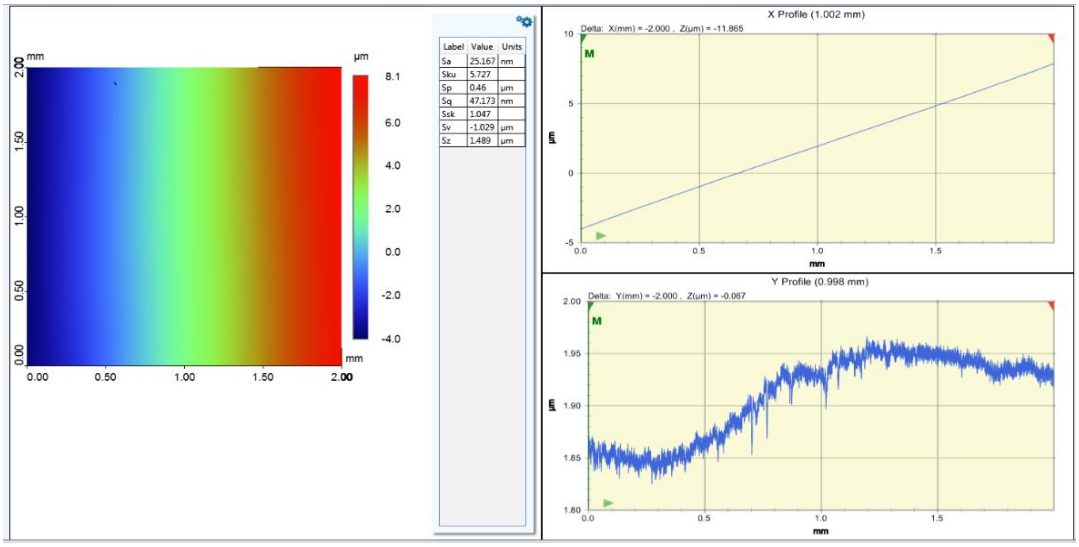

Figure 4.2 Relative heights and recording the position of steel specimen

The topographic parameters 2D average roughness (R_a), root mean square (RMS, R_q), skewness (S_{sk}), kurtosis (S_{ku}) and 3D average roughness (S_a), were assessed and summarized in Table 4.1. As might be expected from the images in Figure 4.1, the silicon wafer is notably smoother than the steel flat sample and steel rod. However, the glass rod was not measured by the Bruker white-light interferometer due to its limited reflectivity. Figure 4.3 illustrates typical 3D surface topography obtained. They show a scan area of 3 mm × 3 mm for flat samples and the whole scan area for a steel rod.

Table 4.1 Topographic surface parameters

	Si/SiO_2 (Flat)	Steel (Flat)	Steel (Rod)
R_a	7.697 nm	85.04 nm	4.738 µm
R_q	9.761 nm	0.111 µm	5.674 µm
S_{sk}	1.047	-1.002	-1.135
S_{ku}	5.727	1.006	1.39
S_a	25.167 nm	5.507 µm	19.245 µm

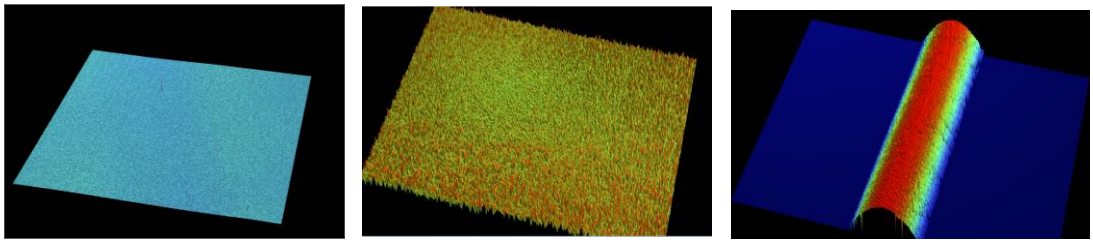

(a) Si/SiO_2 flat (b) Steel flat (c) Steel rod

Figure 4.3 3D topography of test samples

4.1.2 Micro-tribological Test Methods

For all the testing procedures, the counterbody was first taken to gently touch the surface of the specimen at zero set force by observing the onset of the vertical sensing-beam deflection. This was taken as adequately a ‘zero-force’ contact and a normal load was then applied through the transverse force actuator. Then, the specimen reciprocating traverse was started by applying a specified voltage to the flexure stage driver, reading its steady-state condition for oscillation stroke length and time after a very brief period of acceleration. A specified number of cycles of the sensor signals was recorded using the USB data acquisition card and LabVIEW program. Finally, the mechanism stage was stopped, and the counterbody lifted when the test was on completion. The applied load, the sliding velocity, and track length could be varied between tests and the whole sequence of every test condition was repeated three times at different “new” locations which were approximately ±200 μm from the previous one on the sample surface in order to ensure reproducibility of the results and avoid any alteration of the counter body surface, e.g., due to wear, which might occur during the test and affect the measurements in

the following tests.

Prior to each measurement, all samples and tips were cleaned with isopropanol on a cotton-bud and then blow-dried with clean air, so that there would be no significant influence on the results from natural contaminant films. After the cleaning procedures, all the tests were carried out using the reciprocating micro-tribometer in a controlled environment at nominally 22 ± 1˚C and 40 ± 5% relative humidity.

4.2 Tribometer Signals Analysis

4.2.1 Signals Variation in the Vertical Deflection

Figure 4.4 shows the signal variation of the sensing-beam deflections in the vertical direction when the beam is hanging freely. The vertical deflection shows a consistent variation with time and provides the possibility of using its arithmetic mean value as a datum for the calculation of the normal loads, before the tip is in touch with the specimen surface. The signal is almost periodic, dominated by a sinusoidal variation of period close to 20 ms with some added noise and perhaps some small harmonic components. The fundamental resonance of the sensing beam is considerably higher than 50 Hz, so this signal is attributed directly to interference deriving from the main electrical supply. It nevertheless represents an upper limit on real measurements that can be detected in the present environment.

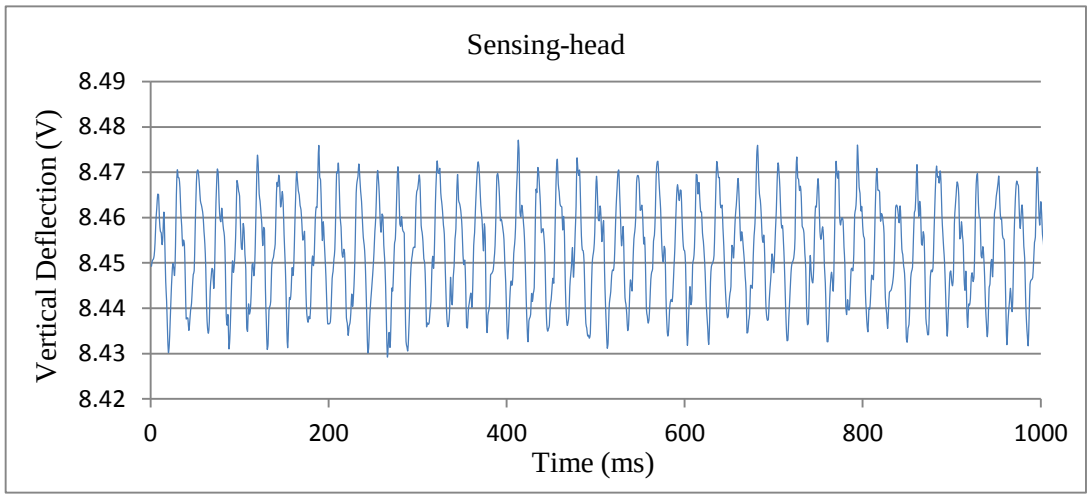

Figure 4.4 Signal variations of the deflection of the sensing beam in the vertical position without applied normal load

Figure 4.5 shows the signal of the sensing-beam deflections in the vertical position for the silicon wafer specimen at a sliding frequency of about 6 Hz with a load of 26.80 mN and track lengths of 66 μm. Figure 4.6 shows a broadly similar pattern with the vertical deflection for a glass rod specimen at a sliding speed of 1.17 mm/s with a load of 42.68 mN. The vertical deflections both show a stable, closely sinusoidal, variation with time (two periods are indicated by the red line) of about 160 ms in Figure 4.5 and much clearer 110 ms in Figure 4.6, consistent with the given sliding frequencies (6 Hz and 9 Hz) of the notch-flexure scanning mechanism. However, these sinusoids both carry an obvious, mainly periodic signal of approximately 20 ms period, indicating the superimposition of a noise signed very similar to that shown in Figure 4.4. The basic signal arises because the sample surface is not sliding exactly orthogonal to the vertical axis of the sense beam. As will be seen in later results, this baseline noise level was often suppressed in specific

measurements, in a consistent way on flat and cylindrical specimens. However, for the present work the only safe assumption is that the uncertainly in all measurements is surround by this full noise signal by Figures 4.5 and 4.6.

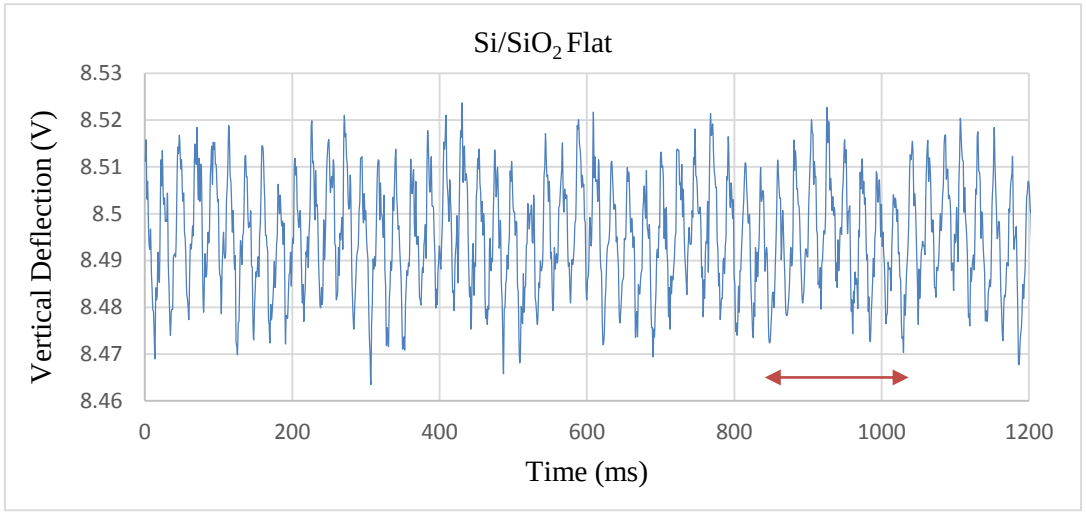

Figure 4.5 Signal variations of the deflection of the sensing beam in the vertical position for a silicon wafer specimen at a sliding speed of 396 μm/s with the load of 26.80 mN

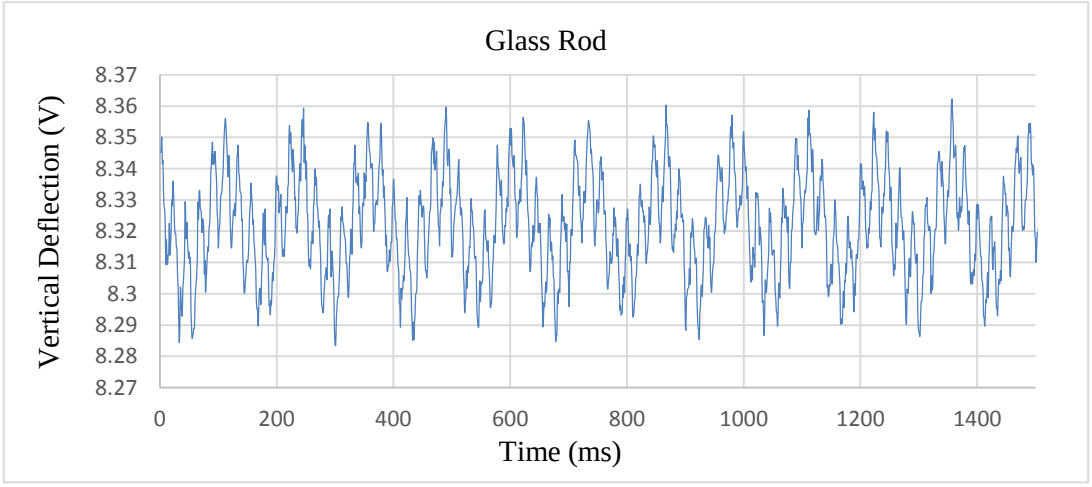

Figure 4.6 Signal variations of the deflection of the sensing beam in the vertical position for a glass rod specimen at a sliding speed of 1.17 mm/s with the load of 42.68 mN

4.2.2 Signals Variation in the Lateral Deflection

The sensor signal for lateral deflection with the beam hanging freely is given in Figure 4.7. It shows similar variations as in Figure 4.4, with a mid-range value of about 5.935 volt, which might provide a possible reference (before contact) for the calculation of friction force. The signal is again dominated by a consistent and stable near-sinusoid having the same 50 Hz frequency and a similar amplitude as that of the unloaded vertical deflection signal of the sensing-head.

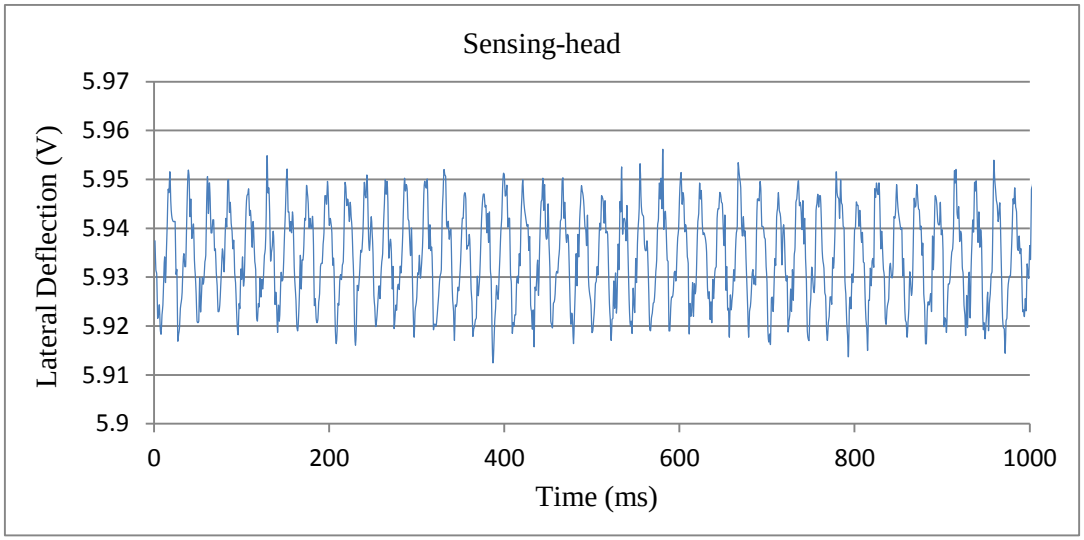

Figure 4.7 Signal variations of the deflection of the sensing beam in the lateral position without applied normal force

Figure 4.8 shows some cycles of the signal from the lateral sensing-beam deflections for contact with a steel flat specimen at a sliding frequency of 3 Hz with an applied load of 11.03 mN. Figure 4.9 shows another example of the lateral signals of the sensing-beam for a steel rod sample at a higher sliding speed (1.17 mm/s)

with a load of 37.31 mN.

The friction force signals are consistent and stable with time for the two different test configurations, some having suppressed noise levels. They show different variations in the shapes of the curves, possibly because of different sliding frequency and material surface topography. However, the friction force signal is almost a rectangular wave with good symmetry at the top and bottom of the curves of each cycle, indicating behaviour similar to the ideal friction force signals in a reciprocating scan mode described in Chapter 3.

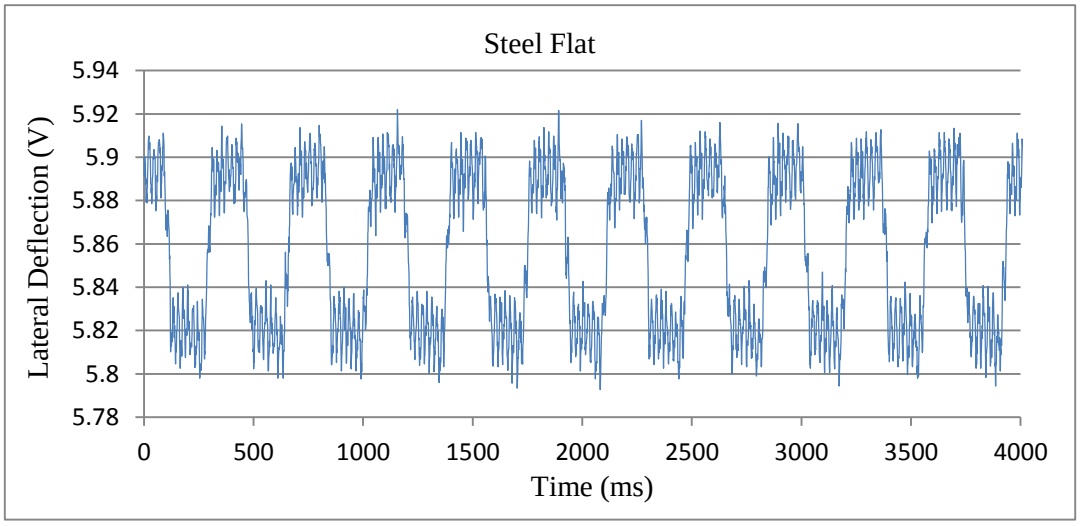

Figure 4.8 Signal variations of the deflection of the sensing beam in the lateral position for steel flat specimen at a sliding speed of 198 μm/s with the load of 11.03 mN

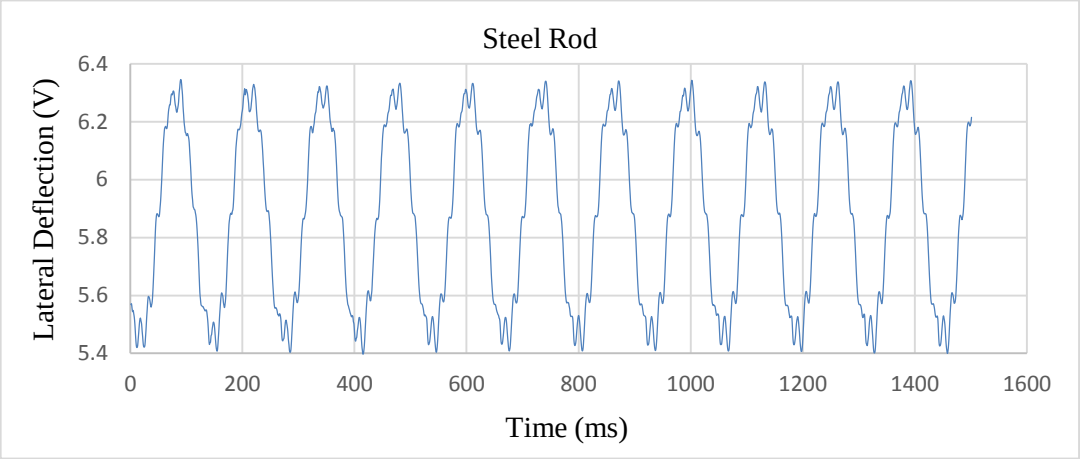

Figure 4.9 Signal variations of the deflection of the sensing beam in the lateral position for steel rod sample at a sliding speed of 1.17 mm/s with a load of 37.31 mN

4.2.3 Static and Transient Uncertainties

The micro-tribometer uses elastic elements in its sensing systems, as do virtually all tribometer designs. There is, therefore, always a residual risk of transient, resonance-based error signals being excited if the operational conditions change suddenly. Also, it is inevitable that the main measurement loops will have a notable compliance that should be accounted for to avoid the risk of misinterpreting certain types of results. So, a short static loading and start-up test was run to assess the characteristics of the new rig.

Figure 4.10 illustrates the effect of the vertical load when the specimen is mounted on the flexure scanning stage but is stationary. The specimen used was a flat silicon wafer covered with a 300 nm thick layer of silicon dioxide. The pin was lowered to make very gentle contact with the sample surface and allowed to settle. The noise floor of the system is seen to be a few mV, corresponding to an RMS

displacement of around 100 nm. Then at around 1 s and 2 s, the contact force was step increased from nominally zero to 21.49 mN and then 47.87 mN. The vertical channel shows a highly typical under-damped transient in response to the step change. It decays in less than 100 ms, suggesting a time constant of 20-30 ms that is consistent with the original instrument design specifications. The steady response to each step is 150 mV, corresponding to about 6.33 μm of vertical displacement. The effective vertical stiffness of the system in this test regime is of the order of 4 kN/m, which is lower than expected. For comparison, the Hertz contact stiffness is of the order of 1 MN/m under the conditions used and a load of 30 mN. The horizontal trace shows a similar but much smaller response, indicating a cross-talk (or parasitic error) of around 0.36 μm (5%), attributable to sample misalignment and manufacturing errors such as imperfect orthogonality of the channels.

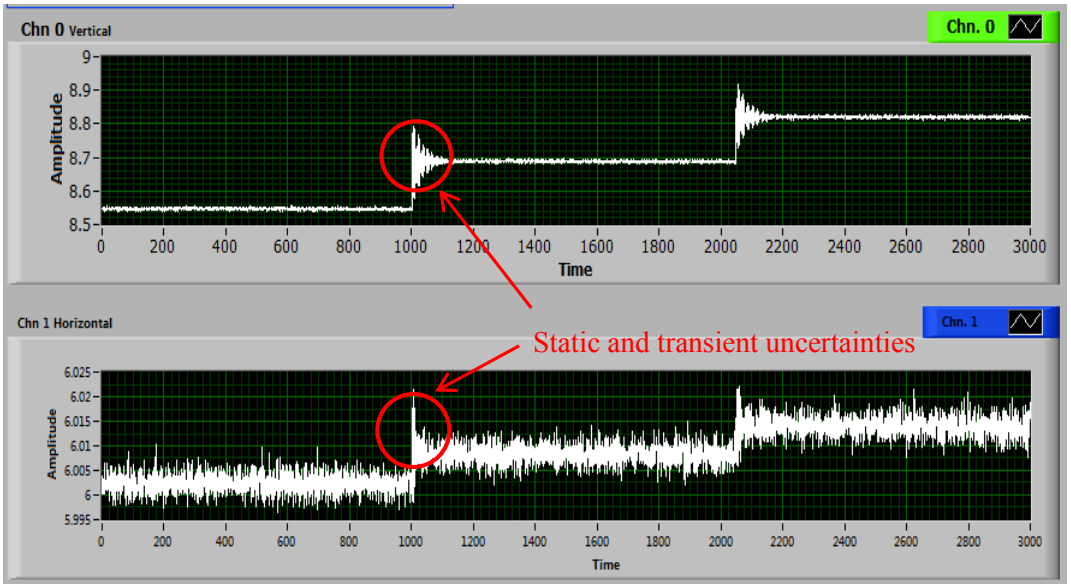

Figure 4.10 Vertical and lateral deflection signals of the sensing beam with applied normal load when the test-rig is static

The pin and the specimen were placed in contact again without any deliberately applied normal load and then the notch-hinge mechanisms were driven in reciprocating movement. Figure 4.11 shows the variations of vertical and lateral deflections of the sensing beam measured by the eddy-current sensors at a sliding speed of 195 μm/s.

It is rather unclear what is happening throughout Figure 4.11, but a few points having potential relevance can be extracted from the information in the graphs.

- The vertical and lateral deflections start with a fairly stable and low noise floor while the flexure scanning stage is static.
- When the stage starts there is a significant transient, perhaps including effects of the probe being also out of ideal alignment because of the system compliance. From the upper trace, the tip moves in both directions, seeming first to jump out of contact.
- The horizontal trace at first behaves quite wildly and is seemingly unpredictable, but this is not surprising if the probe is bouncing. It takes around 300 ms for bouncing-like behavior to fade out and then for the next 600 ms, there is a currently unexplained modulation in both channels at 5 Hz.
- After 1500 ms, there appears to be a small lowering of the probe in the vertical channel; one cause might be that the contact force has increased.
- There might be some stiction-like, adhesive effects at startup, helping to create the large transients, but it is not possible to separate them out from other possible sources of excitation using the data available here.

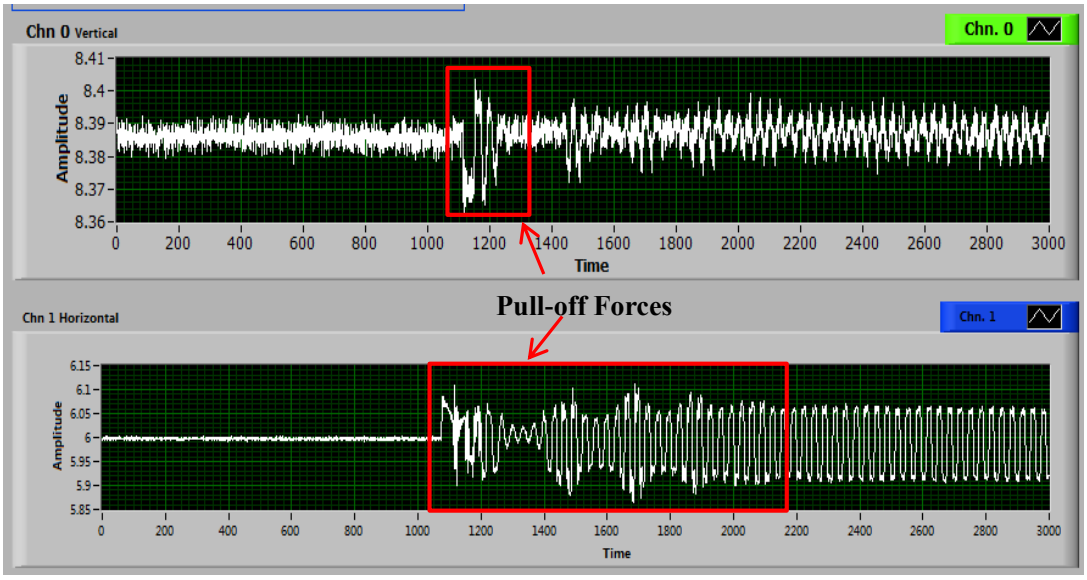

Figure 4.11 Variations of vertical and lateral deflections of the sensing beam measured by the eddy-current sensors without applied normal load when the test-rig is reciprocating at a sliding speed of 195 μm/s

4.3 Reciprocating Friction Calculation

4.3.1 Calculation Method of Reciprocating Friction Signals

During the current work, the ranges of the reciprocating sliding motion and the applied normal load were 1.5-15 Hz and 0.5-60 mN, respectively. Figure 4.12 shows some periods of the sliding cycle for typical measured curves of friction force and applied normal load, when a steel ball slides against a silicon wafer flat with two different forces. The stability of the traces confirms that the measurement process itself is stable and suggests that little wear occurs since it would probably change the material and properties of surface layers relevant at this scale.

Curve 1 and Curve 2 in Figure 4.12 show an example of the raw signals measured by the reciprocating micro-tribometer at a sliding speed of 195 μm/s with

a track length of 65 μm. There is an about 0.015 V step in vertical mean levels, for the second half part of Curve 1 corresponding to about 47.87 mN in the nominal applied force, suggesting a force change of about 1.7 mN. This means the sample moves down a little bit and about 1.7 mN of the nominal applied force gets shunted into deflecting the beam at the contact. Thus, the actual normal load shows a step up from an average 11.03 mN to 46.17 mN, and the equal friction forces are 4.72 mN and 18.05 mN. The output signal shows some evidence of dynamic linking between channels: residual specimen misalignment introduces this as the sensing beam deflects, in which case the use of the mean value is acceptable

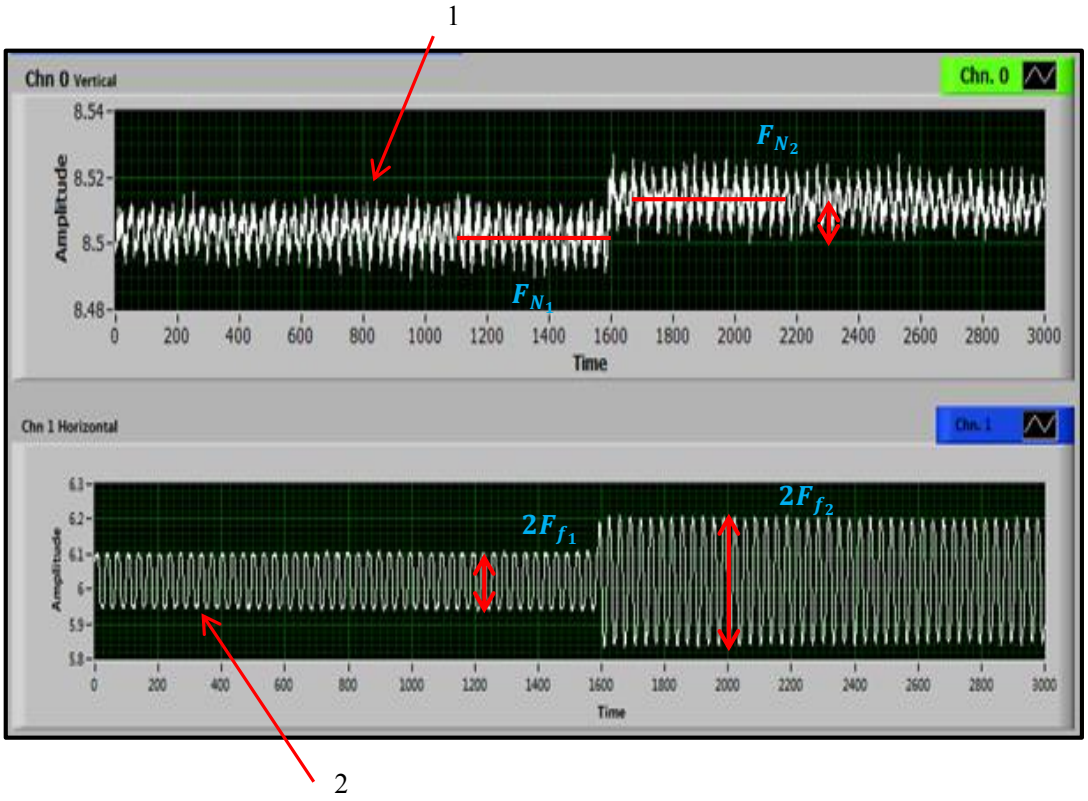

Figure 4.12 Silicon wafer sample of signal measured by the reciprocating micro-tribometer for the friction vs. load experiments: 1. normal load signal and 2. friction signal

The dynamic friction force was calculated by the distance between the peak values and valley values that are determined by an average of the friction signals and the conversion equation is given as (Kosinskiy, 2012; Gardos, 1999),

$$\Delta x = \frac{mean(\Delta x_{(peak)}) - mean(\Delta x_{(valley)})}{2} \tag{4-1}$$

$$F_{f_n} = (\frac{\Delta x_n - \Delta x}{2}) \times k_x \times S_x \tag{4-2}$$

where Δx_n and Δx are the voltages of the deflection of the sensing-beam measured by the lateral sensor with and without applied loads in the vertical position, while k_x and S_x are the stiffness of the sensing-beam and the sensitivity of the sensor in the horizontal position, respectively.

The new tribometer can function in a passive mode, similar to most commercial instruments in which any z-direction motion at the sample acts against the flexure suspension to create some variations in the set (and nominally constant) normal force. Our instrument has relatively high z-stiffness to gain dynamic range, but this increases the sensitivity to z-motion. Hence, it can also operate in an active compensation mode (Alsoufi, 2010), which attempts to hold normal force always close to the set value. Therefore, based on the normal force F_N, constant and equal to the actuator demand force, F_c, in the presence of an unwanted transverse motion Δz, the rules for doing this are given by the equations,

$$F_c = F_N + F_{comp} \tag{4-3}$$

$$\begin{cases} F_{comp} = \begin{matrix} 0 & compensation\ \ off \\ k_z S_z \Delta z = k_z S_z (z - z_0) & compensation\ \ on \end{matrix} \end{cases} \tag{4-4}$$

where z and z_0 are the voltages of the deflection of the sensing-beam measured by the vertical sensor with and without applied normal forces in the vertical position.

k_z and S_z are the beam stiffness and sensor sensitivity in the vertical position respectively.

4.3.2 Calculation Analysis of Applied Normal Load

The vertical deflection of the sensing beam Δz is calculated using Matlab software by taking the mean value of the sinusoidal signal curves collected from Labview software. Generally, the first 2-5 cycles at the start are ignored because they may be influenced by surface contamination or some transients such as overshoot and decay. Then, in order to check for any instrument inconsistencies or data trends from friction heating, unexpectedly rapid wear and so on, sub-sections of the signal were evaluated independently. Four different conditions were considered for measurements taken at loads and speeds high in the working range: the whole signal (sequence) ensuring that evaluation was over a whole number of traces; 30 successive cycles taken from the middle of the traces (mid-30); the 10 successive cycles taken from the front of the traces (first-10); the 10 successive cycles taken from the rear of the traces (last-10). Figure 4.13 shows a typical example for the whole-signal, mid-30, first-10 and last-10 cycles from a steel rod specimen at a sliding frequency of 9 Hz, load of 51.95 mN and length of 130 μm. All the cases analysed are very consistent and stable with time.

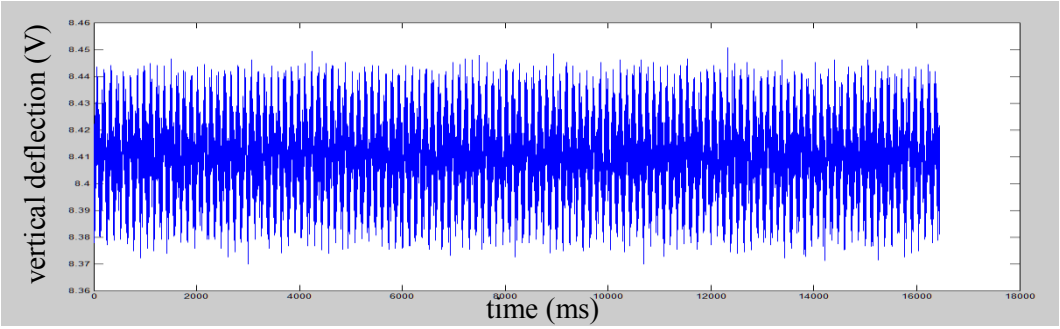

Whole trace

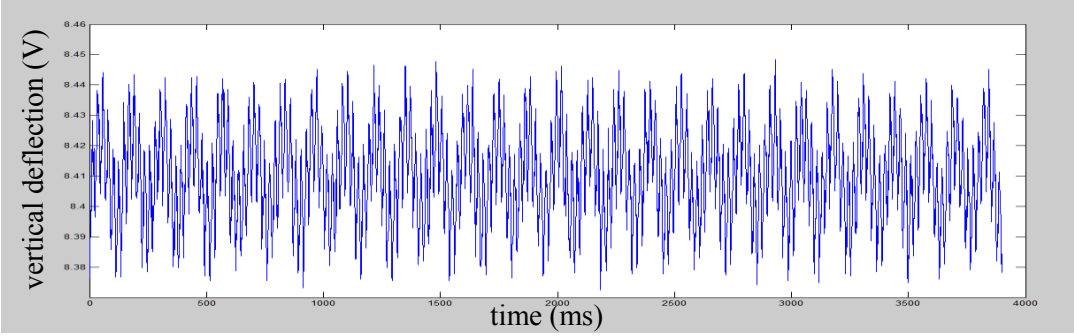

Mid-30 cycles

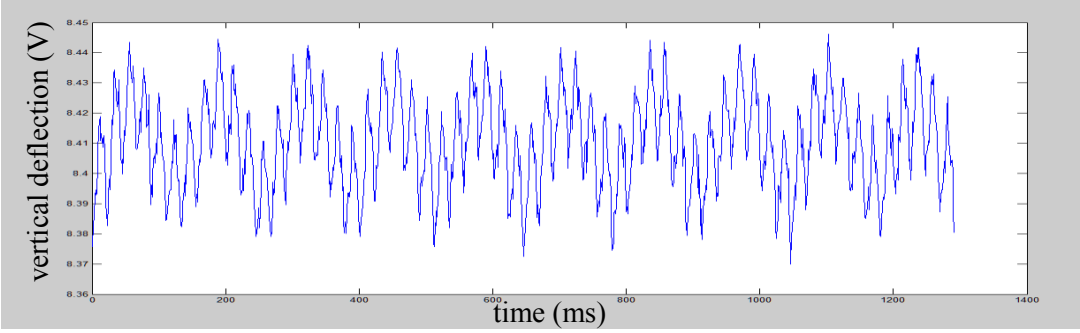

First 10 cycles

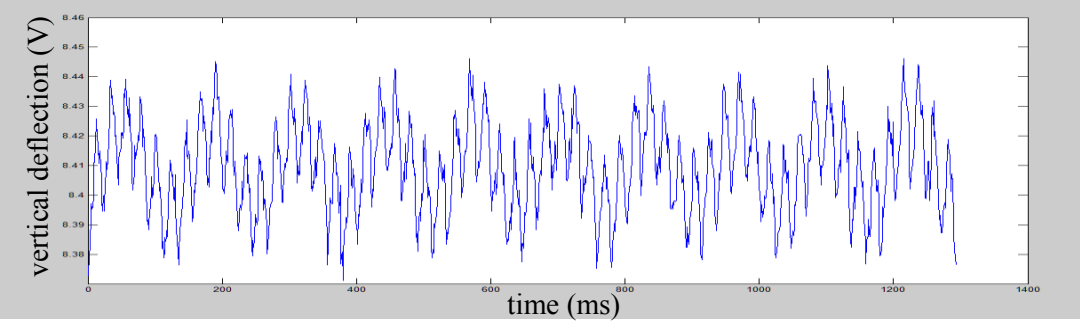

Last 10 cycles

Figure 4.13 The whole trace, mid-30, first-10 and last-10 cycles from a steel rod specimen at a sliding frequency of 9 Hz with the load of 51.95 mN and the length of 130 µm

Table 4.2 Comparison of the calculated average of the vertical deflection for four types of test specimens with the largest loads, longest length and highest sliding frequency for the whole trace, mid-30, first-10 and last-10 cycles

Specimens	Test Conditions	Cycles Selected	Mean Value of Δz (V)
Steel (Flat)	Track length -130 µm Sliding frequency – 9 Hz Normal load – 50 mN	Full	8.5537
		Mid-30	8.5535
		First-10	8.5536
		Last-10	8.5538
Si/SiO_2 (Flat)		Full	8.4602
		Mid-30	8.4604
		First-10	8.4603
		Last-10	8.4599
Steel (Rod)		Full	8.4103
		Mid-30	8.4102
		First-10	8.4106
		Last-10	8.4100
Glass (Rod)		Full	8.3309
		Mid-30	8.3309
		First-10	8.3306
		Last-10	8.3309

Table 4.2 shows a comparison of the calculated average voltage of the vertical deflection signal for different materials with different configurations at the largest loads, longest length and highest sliding frequency for the four different analyses taken over the whole signal, middle 30 cycles, first 10 cycles, and last 10 cycles. For the test samples, these four mean values show remarkable consistency, while the slightly greater variation for the steel rod sample is still of no practical significance. With no more than 0.0003 V (equivalent to 0.0345 mN) variation across all these assessment methods, the measurements are clearly highly insensitive to the choice between them. Thus, the whole signal, as saved in text file for each test condition, is

used for the analyses here. This is convenient, requiring minimal data manipulation, and provides the greatest degree of averaging as protection against any occurrence of larger noise spikes.

4.3.3 Calculation Analysis of Friction Force

4.3.3.1 Theory for Signals Analysis for Friction Force

For oscillatory flexure scan motion, a periodic, sinusoidal input by the power oscillator is applied to drive the specimen with reciprocating movement in the lateral direction. Ideally, if the normal load *N* and friction force F_f are constant, the basic motion of sliding friction is always opposing sliding direction, or the velocity, *v*. There will be always positive value for the instantaneous friction coefficient μ_i and ideally the same amount of the friction force F_f is positive and negative in different parts of the oscillatory scan. However, real, non-ideal measurements will deviate from this in several ways. There might be a constant offset between the +ve and –ve region values (because of zero-error in the instrument, possible because of asymmetry in the scanning). The changes of direction cannot be instantaneous but still involve significant accelerations so the ideal verticals of the rectangular wave take on a high but finite slope and a dynamic overshoot is likely. Also, the signal of the normal force may vary along the motion direction with the speed on sinusoidal oscillations as the specimen surface is always not parallel to the motion axis. There might be a speed effect and on sinusoidal oscillations, speed variation cannot be avoided. These transient regions are difficult to predict closely and so represent poor

quality data.

In 1999, Gardos had taken the maximum range of this trace as a measure of peak CoF, or the static CoF (Gardos, 1999). However, instrument transients are virtually certain to contribute to the peaks and may dominate them; the measure might be the only available estimate of static CoF from such measurements, but it is likely to be a poor one, and probably an overestimate. Similarly, there is a tendency to use the range between minima, or some degree of averaging as an estimate of the dynamic CoF. In this work, an algorithmic approach is used to analyse the signals of the friction force and determine an average (dynamic) CoF that avoids transient regions safely while gaining reliability through averaging a significant fraction of the total signal. The approach is,

1) Identify zero crossings as nominal points of direction reversal and fit best straight line through equal numbers of upper and lower regions to get overall offset and trend.

2) Look for an appropriate central segment of each half cycle of the friction signals that can be used consistently. The real size for this region might be judged by regarding observations of the time taken for transients to settle. Specifically, the scheme adopted here as a good compromise was to find the numbers of data points between two successive reversals, n. Then, an average was calculated for all points in the region between, such as $n/4$ and $3n/4$, in order to avoid any transients that might occur. Finally, take this average as the best estimate for the force in this half cycle.

3) Use the means of cycles to establish the instrument offset and so desire find estimates for lateral force in each direction, to obtain the least effects from the speed variation and least chance of transients during the micro-tribological tests.

For force offset, the following equation is given as,

$$F_0 = mean(|F_i|) \tag{4-5}$$

But only if equal amounts of upper and lower regions are included, the transient areas probably ought to be ignored. After that, instantaneous friction coefficient μ_i of each segment is calculated according to the following equation,

$$\mu_i = \frac{mean(|F_i - F_0|)}{N_i} \tag{4-6}$$

where N_i are the normal load of the corresponding segment in accordance with μ_i and the changes of each N_i should be estimated. Finally, we can have

$$mean(\mu) = mean(\mu_i) \tag{4-7}$$

This might be preserved 50% of the data, but other values might be used, judged regarding observations of the time taken for transients to settle.

4.3.3.2 Signals Analysis for Friction Force

Friction force is calculated using Matlab software from the height difference between the top and bottom regions of the curves of the lateral deflections of the sensing beam Δx collected from Labview software. The first 2-5 cycles at the start of the trace are ignored to avoid uncertainty from effects such as contaminated specimen surface or signal transients. Then, in order to check for any instrument inconsistencies or data trends from friction heating, unexpectedly rapid wear and so

on, sub-section, of the signal were evaluated independently. Two conditions were considered for measurements taken at loads and speeds high in the working range: whole trace (sequence) ensuring that evaluation was over full points, parts of full points at the top and bottom of each cycle for the 10 successive cycles selected from the front and the rear of the whole signal.

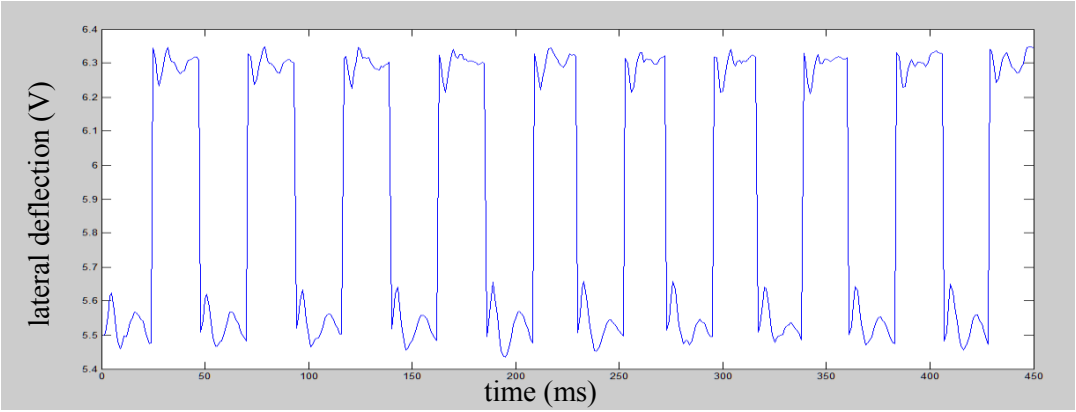

(a) Full points at the top and bottom of each cycle for the 10 successive cycles

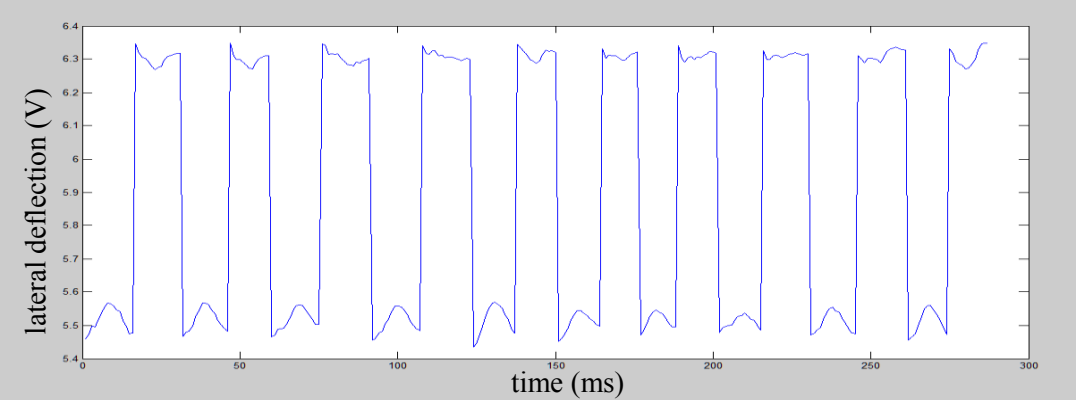

(b) Parts of full points collected in (a)

Figure 4.14 A typical example for a silicon wafer sample at a sliding frequency of 9 Hz with the load of 50 mN and length of 130 µm with the conditions including the full points and parts of the full points at the top and bottom of each cycle for the 10 successive cycles selected from the front of the whole signal

Figure 4.14 shows a typical example for a silicon wafer flat sample at a sliding frequency of 9 Hz with the load of 50 mN and length of 130 μm with the conditions including the full points and parts of the full points at the top and bottom of each cycle for the 10 successive cycles selected from the front of the whole signal. All the cases analysed are very consistent and stable with time. There is an obvious variation at the start of each top and bottom of the cycle in Figure 4.14 (a), whereas Figure 4.14 (b) shows the vertical deflection signal with fewer points at the top and bottom of each cycle, in order to compare the calculation precision and explore more possibilities of avoiding transients.

Figure 4.15 shows a typical example of the vertical deflection signal for a steel rod sample at a sliding frequency of about 9 Hz with the load of 51.95 mN. There is no obvious signal transient in the whole trace and thus full points at the top and bottom of the cycle in any 10 successive cycles of the whole signal could be considered as a selection for the calculation of the friction force.

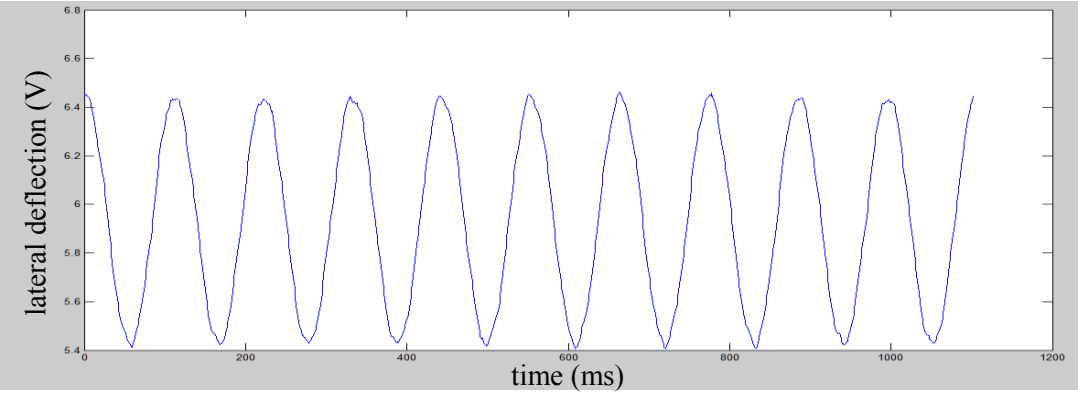

Figure 4.15 Vertical deflection signal for a glass rod specimen at a sliding frequency of about 9 Hz with the load of 51.95 mN

Table 4.3 Comparison of the calculated average of the lateral deflection for test specimens with the largest loads, longest length and highest sliding frequency for the full points and parts of the full points at the top and bottom of each cycle in the 10 successive cycles selected from the front and rear of the whole signal

Material	Test Conditions: Track length - 130 μm Frequency – 9 Hz Normal load – 50 mN	Data Selected at the Top and Bottom of Each Cycle	Mean (bottom) (volt)	Mean (top) (volt)	Δx (volt)
Steel (Flat)	First-10 cycles	Full points	5.7266	5.8827	0.1561
		Parts of full points	5.7258	5.8766	0.1508
	Last-10 cycles	Full points	5.7260	5.8828	0.1568
		Parts of full points	5.7257	5.8743	0.1485
Si/SiO_2 (Flat)	First-10 cycles	Full points	5.5274	6.3002	0.7728
		Parts of full points	5.5128	6.3086	0.7958
	Last-10 cycles	Full points	5.5254	6.3014	0.7760
		Parts of full points	5.5116	6.3086	0.7970
	Middle-10 cycles	Full points	5.5246	6.3001	0.7755
		Parts of full points	5.5104	6.3094	0.7991
Steel (Rod)	First-10 cycles	Full points	5.4406	6.4320	0.9914
		Parts of full points	5.4245	6.4188	0.9943
	Last-10 cycles	Full points	5.4339	6.4306	0.9967
		Parts of full points	5.4260	6.4369	1.0109
Glass (Rod)	First-10 cycles	Full points	5.8781	5.9772	0.0990
		Parts of full points	5.8767	5.9712	0.0945
	Last-10 cycles	Full points	5.8777	5.9787	0.1010
		Parts of full points	5.8769	5.9740	0.0971

Table 4.3 shows a comparison of the calculated average voltage of the lateral deflection for polymers at the largest loads, longest length and highest sliding frequency for the different analyses taken over the full points and parts of the full points at the top and bottom of each cycle for the 10 successive cycles selected from the front and rear of the whole signal. For four different specimens, there are all very

significant changes in the calculation results of the lateral deflection Δx for two different types of point selections, but it remains rather little change with full points when the 10 successive cycles are selected from the front and rear of the whole signal. Thus, full points at the top and bottom of each cycle in any 10 successive cycles of the whole signal should be selected to obtain the accurate algorithm of the lateral deflection due to no signal transient.

4.4 Results and Discussion

4.4.1 Tribological investigations of Silicon-Based materials on the Ball-on-Flat Configuration

Figure 4.16 and Figure 4.17 show the variations of friction force and friction coefficient with normal load for a silicon wafer with a SiO_2 coating at the same scan length of 66 μm and three different scan frequencies of 3 Hz, 6 Hz and 9 Hz. Based on these graphs, linearity is as good over the working range ($R^2 > 0.99$) for friction forces against load as that of the Si/SiO_2 specimen (see Figure 4.16). The friction force values remain in the 2 mN - 10 mN range but has a consistent tendency with the sliding frequency and normal load at the same scan length. Similarly, the CoF remains around 0.18 as the scan speed is increased to 9 Hz. However, there is little fluctuation in CoF with normal load at each single test condition (see Figure 4.17).

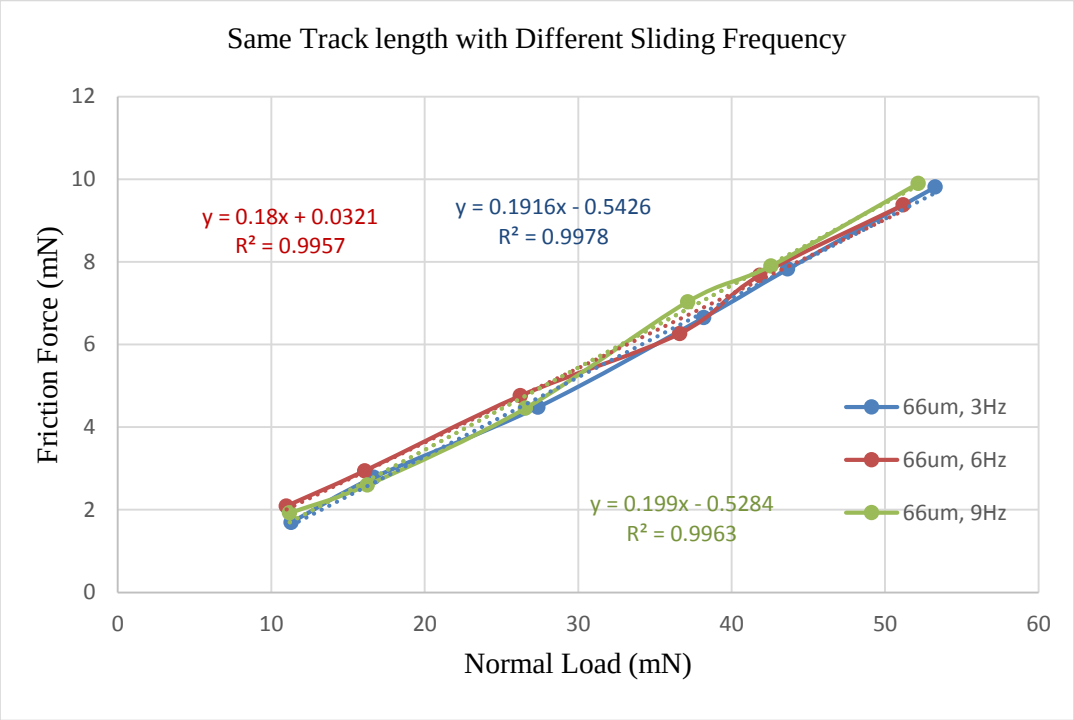

Figure 4.16 Variations of friction force with normal load for Si/SiO_2 specimen at the same scan length of 66 µm and three different scan speeds of 3 Hz, 6 Hz and 9 Hz

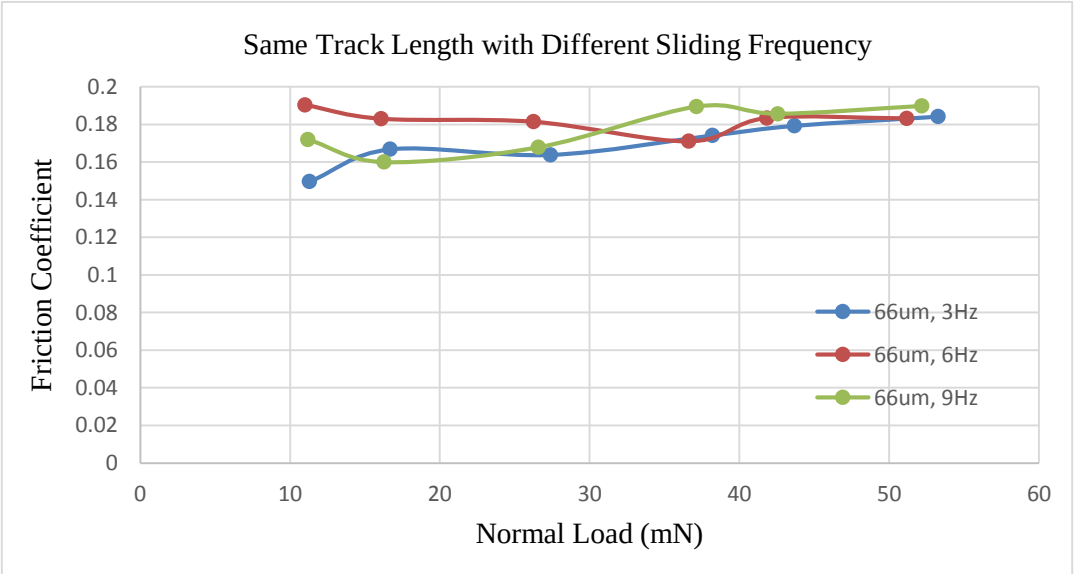

Figure 4.17 Variations of CoF with normal load for Si/SiO_2 specimen at the same scan length of 66 µm and three different scan speeds of 3 Hz, 6 Hz and 9 Hz

Figure 4.18 and Figure 4.19 show the variations of friction force and friction coefficient with normal load for a Si/SiO_2 sample at the same scan speed of 3 Hz and three different track lengths of 66 µm, 90 µm and 130 µm. Based on these graphs, linearity is still good over the working range ($R^2 > 0.99$) for friction forces compared to those shown in Figure 4.16. However, there is almost no change in the value for different scan lengths, in the range between 2 mN and 10 mN, which means the friction force is independent of track length (sliding speed) but has just the linear relationship with normal load predicted by Amonton's law in this test regime (Dowson, 1998). Note that other published work, including by Alsoufi using the original version of the current test-rig (Alsoufi, 2011), has suggested that the CoF for Si/SiO_2 would rise perceptibly as the normal load reduces across this test range. Similarly, in Figure 4.19, the CoF has some obvious fluctuations but has no clear trend with track length, remaining in a stable range at around 0.18 when the normal load is applied from 10 mN to 60 mN. The CoF appear to be independent of the track length and sliding speed under these test conditions, close to Amonton's law prediction. Also, the CoF of Si/SiO_2 sample, close to 0.2, matches well with its known properties as an ideal silicon-based material.

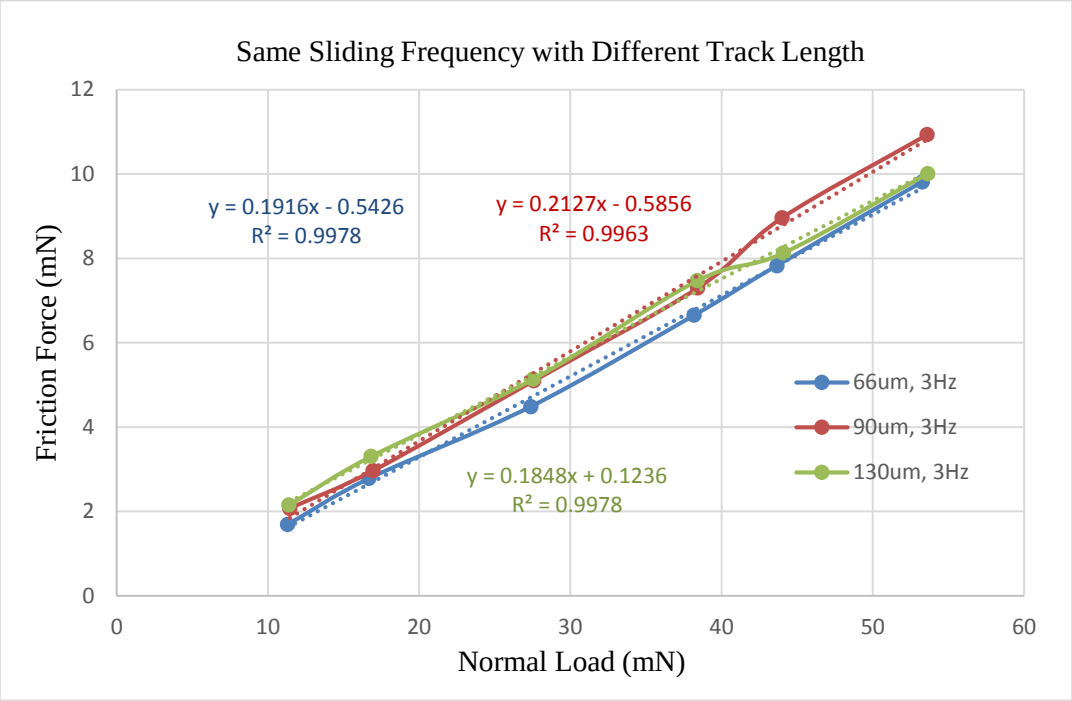

Figure 4.18 Variations of friction force with normal load for Si/SiO_2 specimen at the same scan speed of 3 Hz and three different track lengths of 66 µm, 90 µm and 130 µm

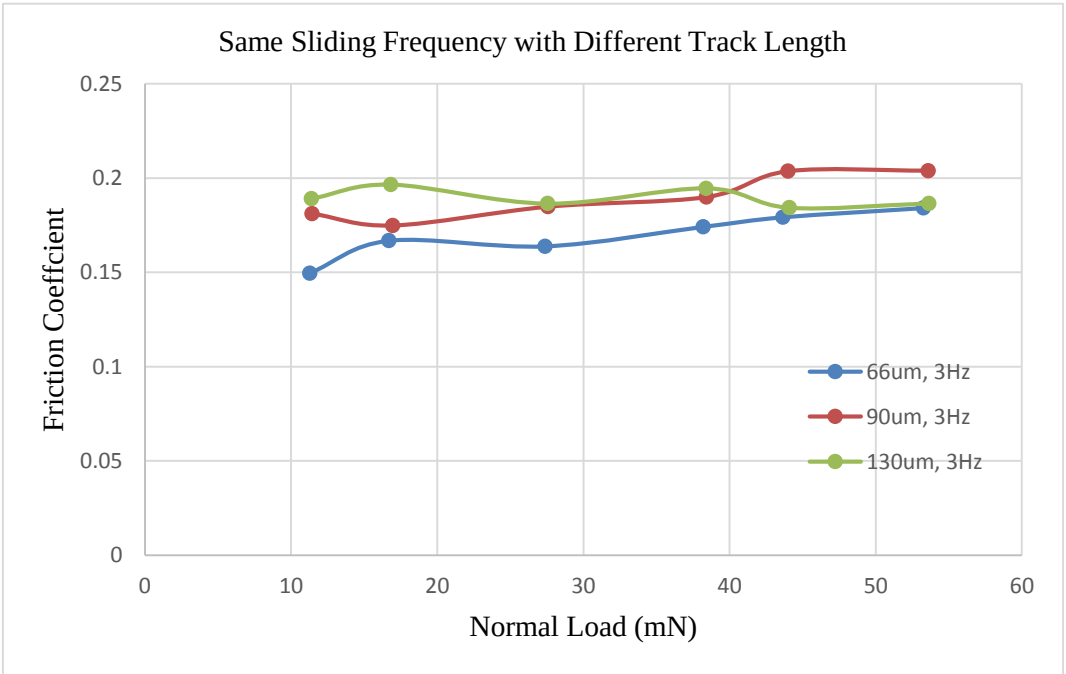

Figure 4.19 Variations of CoF with normal load for Si/SiO_2 specimen at the same scan speed of 3 Hz and three different track lengths of 66 µm, 90 µm and 130 µm

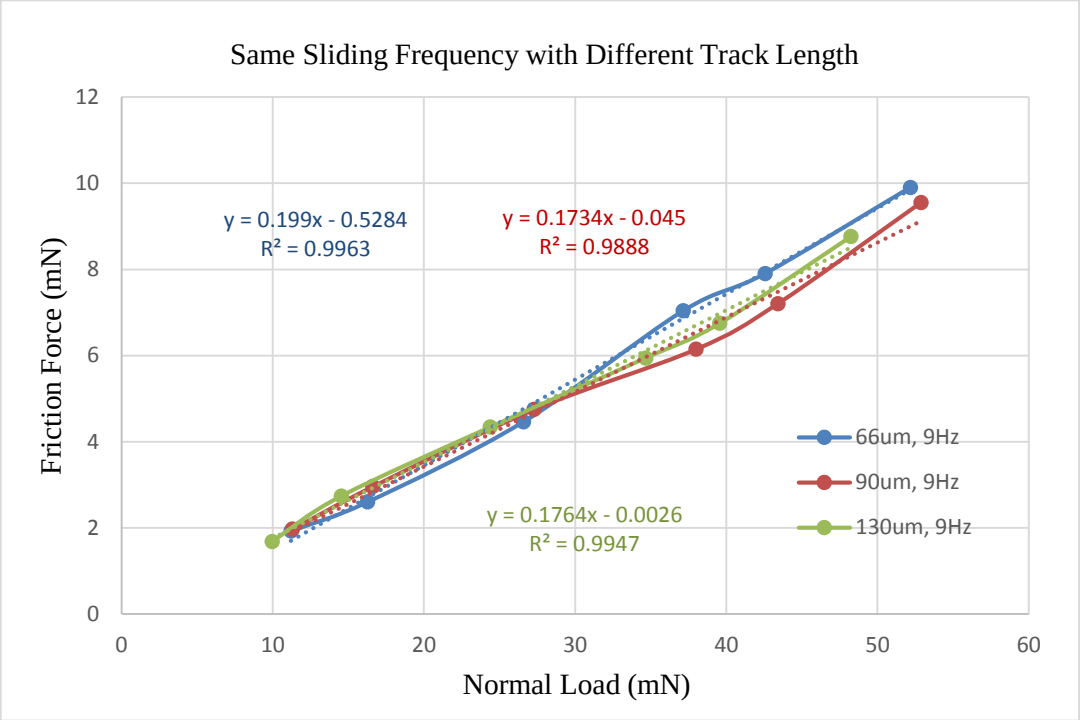

Figure 4.20 Variations of friction force with normal load for PTFE sample at the same scan speed of 9 Hz and three different track lengths of 66 µm, 90 µm and 130 µm

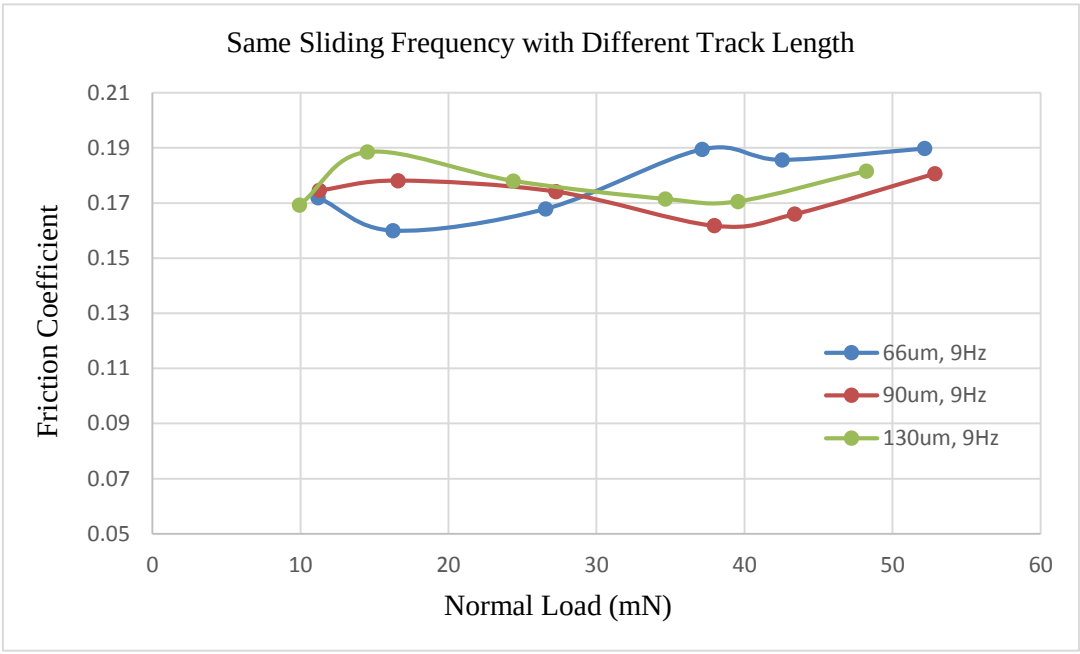

Figure 4.21 Variations of CoF with normal load for Si/SiO_2 specimen at the same scan speed of 9 Hz and three different track lengths of 66 µm, 90 µm and 130 µm

Figure 4.20 and Figure 4.21 show the variations of friction force and friction coefficient with normal load for a Si/SiO_2 sample at the same scan speed of 9 Hz and three different track lengths of 66 µm, 90 µm and 130 µm. Based on these graphs, linearity is still good over the working range ($R^2 > 0.99$) for friction forces compared to those shown in Figure 4.18. Friction force and CoF still appear to be independent of track length and sliding speed, whereas friction force has just the linear relationship with normal load, matching well with Amonton's law in this test regime.

4.4.2 Consistency Analysis of Friction Properties of Steel materials between Ball-on-Flat and Crossed-Cylinders Configurations

Table 4.4 shows the variations of friction coefficient with normal load for a steel flat and a steel rod sample at three different scan lengths of 66 µm, 90 µm and 130 µm and three different scan frequencies of 3 Hz, 6 Hz and 9 Hz. Based on these values, there are large variation ranges between around 0.2 and above 0.9 at different track length and sliding frequencies. For different tests at the same mode, there is not a nearly consistent behaviour under the same test condition, but the considerable variation shows some common tendencies. For example, the first run of each sub-test generally reports a lower value. Some reasons might be presented to explain the phenomenon: 1) steel materials with different compositions might have the influence on the test results, which leading to different CoF in the two measurements for ball-on-flat and crossed-cylinder configurations. 2) Stainless steel samples might

be expected to have a hard oxide layer that is stable before the first run, but the sample surface might be modified (without time to recover) after measurement to have an influence on CoF.

However, there are still enough similarities in variations under the same test conditions between the two modes to show the availability and validity of the crossed-cylinders configuration as shown in Table 4.4 (red font). These relatively consistent tendencies illustrate a reasonable level of variations of the CoF with normal load for steel material, compared with other literature (Bowden, 1964), but the values are a little higher than expected ones. Figure 4.22 shows a typical example of variation of CoF with normal load for steel flat and steel rod specimens at the same scan length of 66 µm and the same scan speeds of 6 Hz.

Table 4.4 Comparison of variation of the CoF with applied normal load between a steel ball against a steel flat and a steel rod against a steel rod under different test conditions

Test conditions			Steel ball against steel flat		Steel rod against steel rod	
Length (µm)	Frequency (Hz)	Load (mN)	1st test CoF	2nd test CoF	1st test CoF	2nd test CoF
66	3	10 – 50	0.2 - 0.26	0.98 – 0.50	0.2 – 0.27	0.65 –0.54
66	6	10 – 50	0.81 – 0.55	0.34 – 0.61	0.70 - 0.17	0.88 – 0.58
66	9	10 – 50	0.62 – 0.56	0.94 – 0.53	0.44 – 0.43	0.96 – 0.67
90	3	10 – 50	0.21 – 0.52	0.16 – 0.60	0.85 – 0.34	0.61 – 0.74
90	6	10 – 50	0.92 – 0.77	0.72 – 0.83	0.73 – 0.38	0.85 – 0.81
90	9	10 – 50	0.83 – 0.76	0.87 – 0.79	0.86 – 0.64	0.94 – 0.70
130	3	10 – 50	0.52 – 0.78	0.86 – 0.95	0.71 – 0.84	0.82 – 0.98
130	6	10 – 50	0.62 – 0.62	0.67 – 0.89	0.66 – 0.88	0.92 – 0.85
130	9	10 – 50	0.90 – 0.74	0.91 – 0.74	0.96 – 0.95	0.84 – 0.78

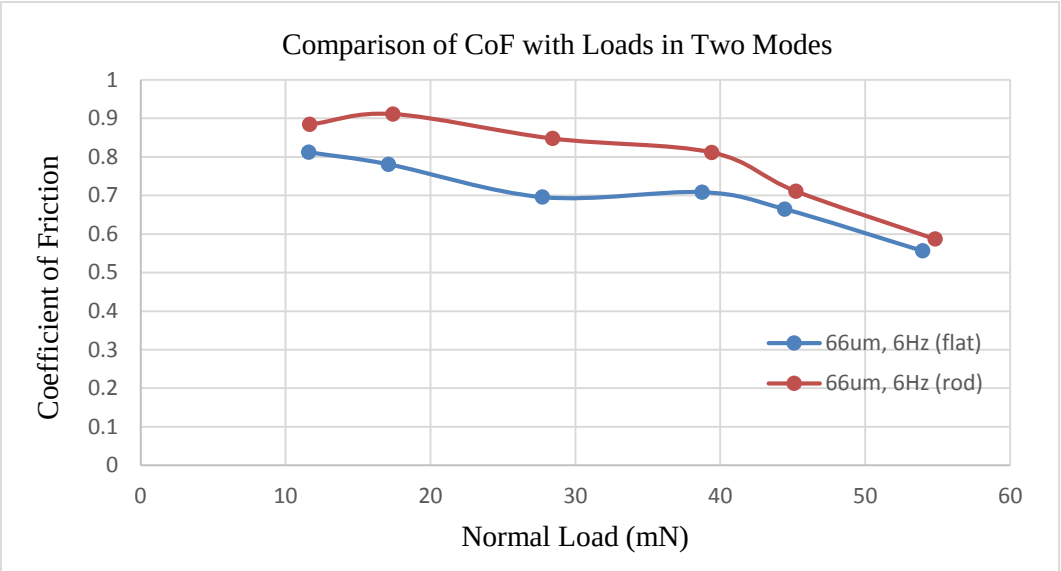

Figure 4.22 Variations of CoF with normal load for steel flat and steel rod specimens at the same scan length of 130 µm and three different scan speeds of 3 Hz, 6 Hz and 9 Hz

4.4.3 Tribological investigations of Glass materials on the Crossed-Cylinders Configuration

Figure 4.23 and Figure 4.24 show the variations of friction force and friction coefficient with normal load for a glass rod sample at the same scan length of 130 µm and three different scan frequencies of 3 Hz, 6 Hz and 9 Hz. Based on these graphs, linearity is excellent over the working range ($R^2 > 0.99$) for friction forces, in the ranges between 0.5 mN and 4.5 mN, when the load applied is from 10 mN to 60 mN. There is a declining tendency in the friction force with the increase of the sliding frequency at the same scan length, shown in Figure 4.23. Similarly, the CoF reduces from around 0.08 to about 0.06 when the scan frequency is increased to 9 Hz. This drop could possibly be related to a higher contact repetition rate in crossed-cylinder configuration leading to greater surface thermal variation but there

is also increasing sliding speed and this might itself be the major cause. There is only slight fluctuation in CoF with normal load in each single frequency test condition, as shown in Figure 4.24. Therefore, it is reasonable to conclude that the friction force and CoF for crossed glass rods are not independent of the sliding frequency at the same track length. The CoF of the glass rod specimen falls with the increase of the track length and sliding frequency at normal loads applied in the range 10 mN to 60 mN. This strongly suggests that the common cause is an inverse relationship between CoF and sliding speed across the present test regime. However, the CoF of glass materials is generally rather lower than expected from the literature (Bowden, 1958), leading to possible concerns about the use of this method with the current tribometer design.

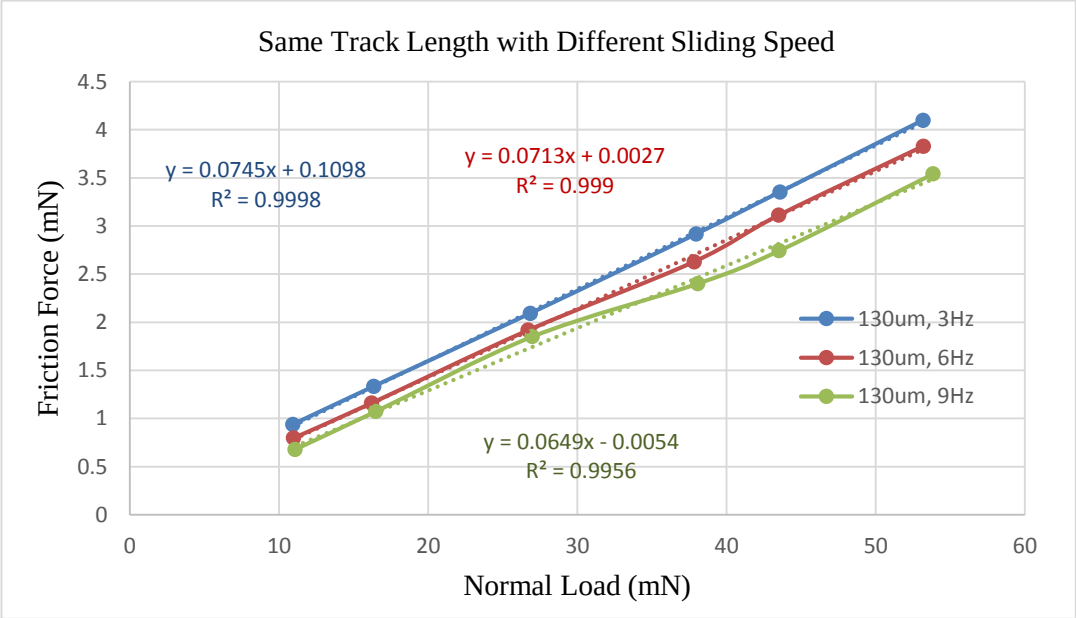

Figure 4.23 Variations of friction force with normal load for glass rod specimen at the same scan length of 130 µm and three different scan speeds of 3 Hz, 6 Hz and 9 Hz

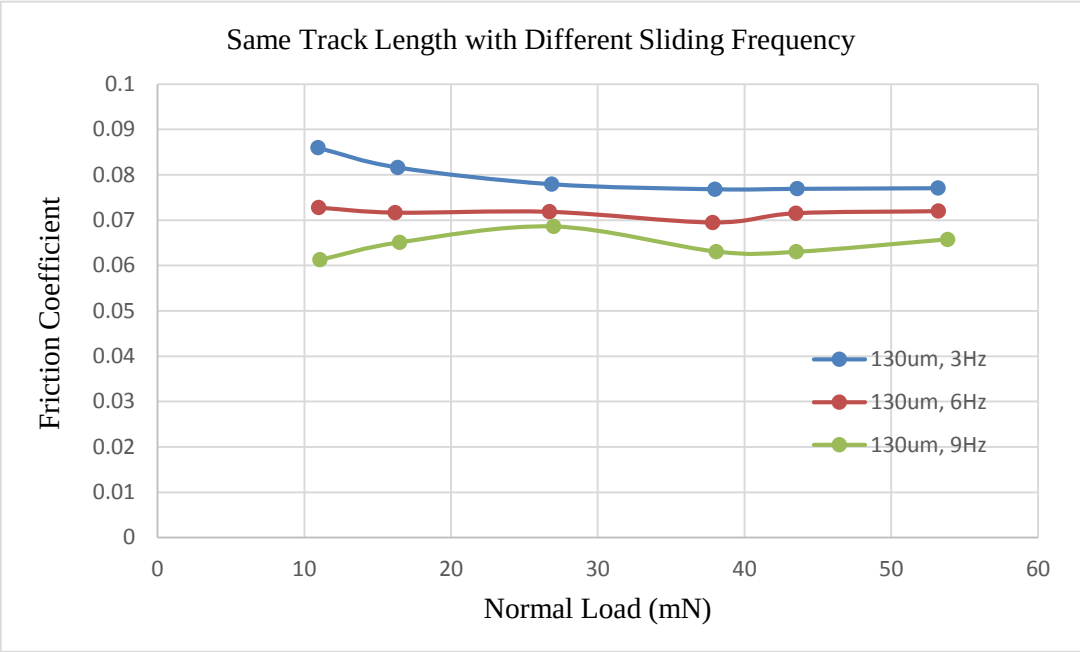

Figure 4.24 Variations of CoF with normal load for glass rod specimen at the same scan length of 130 µm and three different scan speeds of 3 Hz, 6 Hz and 9 Hz

Figure 4.25 and Figure 4.26 show the variations of friction force and friction coefficient with normal load for a glass rod specimen at the same scan frequency of 9 Hz and over three different track lengths of 66 µm, 90 µm and 130 µm. Assuming the scan remains sinusoidal, the maximum and average sliding speeds for these conditions are about 650 µm/s, 900 µm/s and 1.3 mm/s and 450 µm/s, 630 µm/s and 1 mm/s respectively. Based on these graphs, linearity is excellent over the working range ($R^2 > 0.99$) for friction forces, which mostly remain in the range between 0.5 mN and 4.5 mN, at each different track length. However, there is a slight decline in the friction force with the increase of the track length at the same normal load, shown in Figure 4.25. Although the differences between the individual points at any one set load might have limited significance relative to the measurement

uncertainties, the consistent separation of the graphs suggests that there is a real physical effect here. Similarly, the CoF also has a downward tendency from around 0.08 to about 0.06 when the track length is increasing from 66 µm to 130 µm. The most likely cause appears to be a slight (inverse) relationship between CoF and sliding speed within this test regime. However, there is almost no variation of CoF with normal load at a single test condition shown in Figure 4.26, and the small fluctuation in CoF might be caused by instrument effects or calculation accuracy.

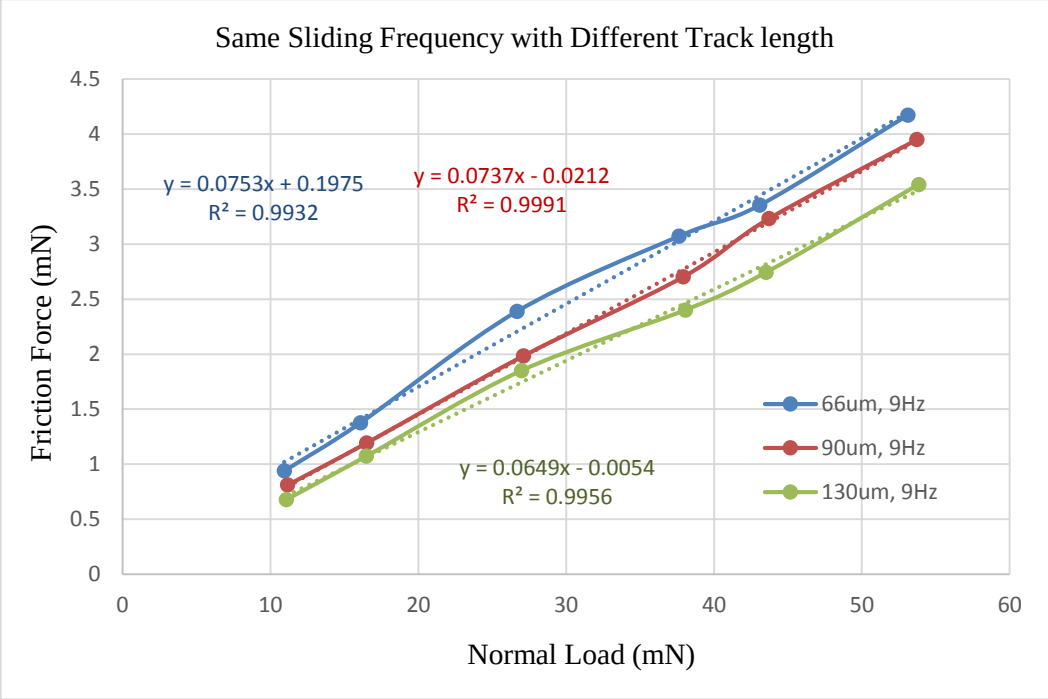

Figure 4.25 Variations of friction force with normal load for glass rod specimen at the same scan speed of 9 Hz and three different track lengths of 66 µm, 90 µm and 130 µm

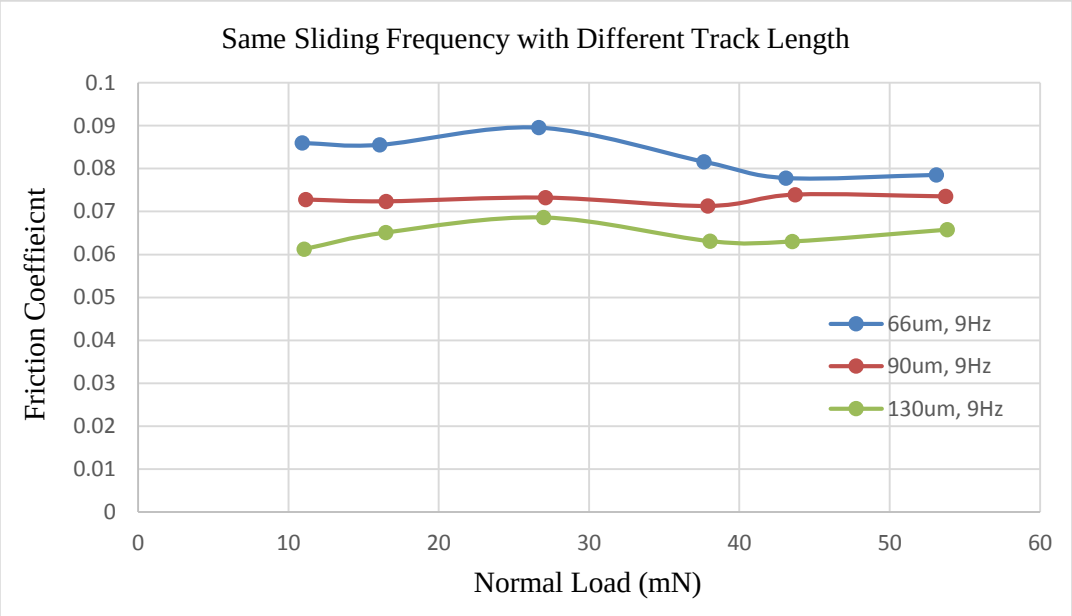

Figure 4.26 Variations of CoF with normal load for glass rod specimen at the same scan speed of 9 Hz and three different track lengths of 66 µm, 90 µm and 130 µm

However, there is a different pattern of variation in friction force and CoF for a glass rod specimen shown in Figure 4.27 and Figure 4.28 at the same scan length of 130 µm and three different scan frequencies of 3 Hz, 6 Hz and 9 Hz. Based on these graphs, linearity is a little poorer, but still not at all bad, over the working range ($R^2 > 0.98$) for friction forces, in the greater ranges between 5 mN and 35 mN, compared with the previous test results, when the normal load applied is from 10 mN to 60 mN. There is no obvious declining tendency in the friction force with the increase of the sliding frequency at the same scan length, shown in Figure 4.27. Similarly, the CoF has some obvious fluctuations but has no clear trend with track length, remaining in a stable range between around 0.5 to about 0.7, as shown in Figure 4.28. Therefore, it is reasonable to conclude that the friction force and CoF

for crossed glass rod are independent of the sliding frequency at the same track length. However, this conclusion is not according with that in Figure 4.23 and Figure 4.24, which leads to a strong suspicion that this test is an outlier. Nevertheless, according to the variation of friction force with normal load in Figure 4.27, it seems that higher consistency in the pattern of behaviour as parameter vary as the friction forces in both two scan lengths show a good linear increase with normal loads. Thus, some reasons might be presented to explain the phenomenon, some characterisable as ‘operator error’:

1) Sample cleaning could be point of vulnerability to affect the test results.

2) A fault in the set-up parameters or a wrong operational procedure during measurement might lead to different values of friction force and CoF.

3) This measurement method in the crossed-cylinder configuration might be vulnerable to the exact positioning of samples caused by instrument limitations.

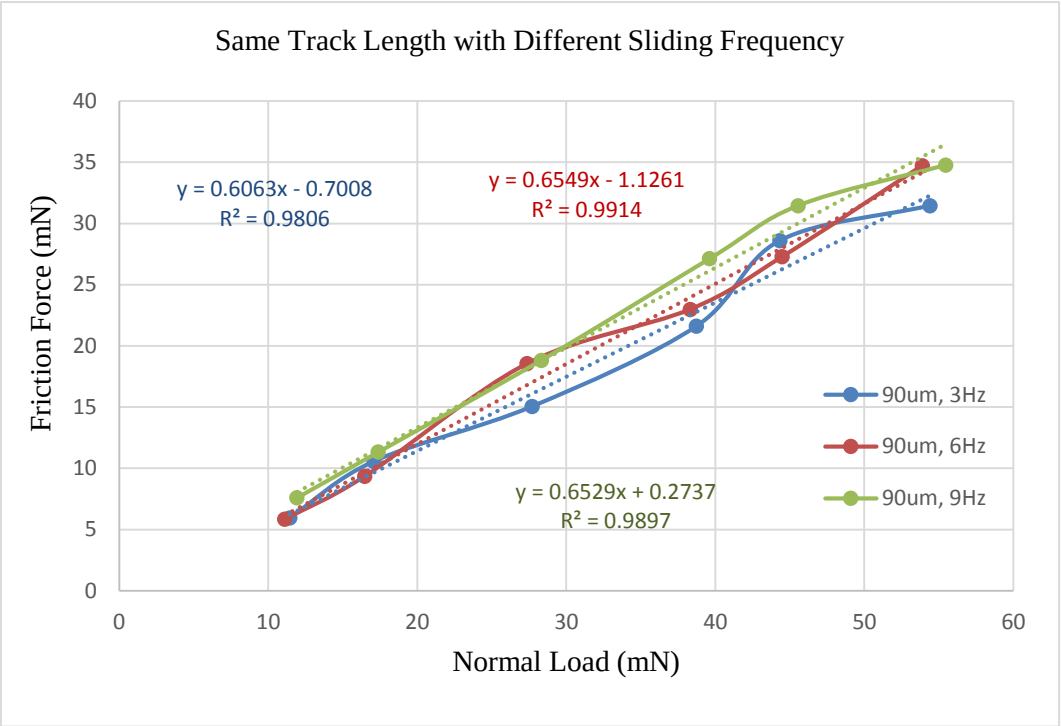

Figure 4.27 Variations of friction force with normal load for glass rod specimen at the same scan length of 90 µm and three different scan speeds of 3 Hz, 6 Hz and 9 Hz

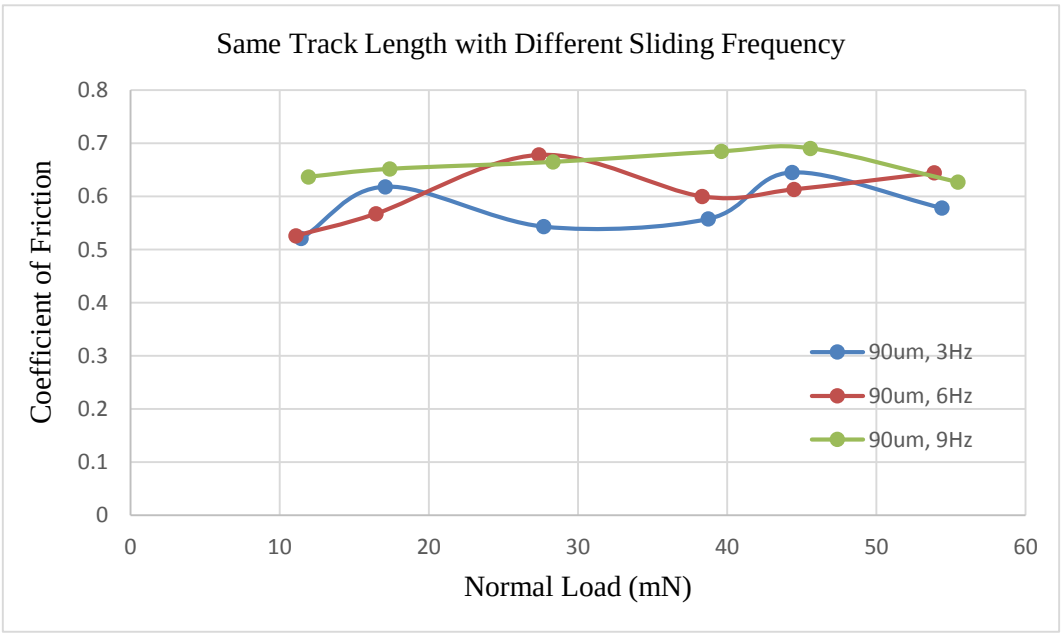

Figure 4.28 Variations of CoF with normal load for glass rod specimen at the same scan length of 90 µm and three different scan speeds of 3 Hz, 6 Hz and 9 Hz

5 Initial Study of Micro-friction of Polymers

Overview

Having now established that the updated micro-tribometer is a reliable tool, it is used for an initial set of experimental studies on polymeric materials typical of those that might be found in micro-mechanical system. This addresses one of the major motivations for this work by observing some behaviour patterns of the polymer materials, noting their variability and paving the way for future work. The specific experimental investigations focus mainly on examining the friction force and coefficient of friction against applied normal forces in the range of 10-52 mN, sliding frequency in the range of 2.5-10 Hz and track length in the range of 60-130 μm using ball-on-flat configurations under dry sliding conditions where there are no applied lubricants. First, surface topographies of the nominally flat specimens of PTFE and acrylic-based R11 resins fabricated by micro-stereo-lithography were measured. Then, approaches to tribometer signal processing and calculation of friction measurements, including friction force and coefficient of friction, at the micro-scale are analysed. This highlights and explores the computational accuracy of friction measurement at the micro-scale. Finally, the experimental results are analysed to produce new data for the PTFE and MSL polymeric materials.

5.1 Introduction

The re-commissioned test-rig, demonstrated to be a reliable micro-tribometer in previous chapter, was used for the investigation of typical polymeric materials including PTFE and the acrylic-based R11 resin made by micro-stereo-lithgraphy (MSL) technique that might be found in micro-mechanical system. The ball-on-flat configurations were used to investigate the variations of friction force and coefficient of friction for polymeric materials against specified measuring conditions, such as normal force, track length and sliding frequency. The motivation for this work, in this chapter, was to observe some behaviour patterns for the polymer materials, analysis their variability and obtain new data to provide useful imformation for future potential MEMS productions.

5.2 Experimental Procedures and Specimens

Chapters 3 and 4 have covered the updating, characterization and re-commissioning trials for the prototype micro-tribometer. They have thus refined a set of good working practices that can now be applied to the investigation of poorly documented cases, notably polymeric materials being considered for MEMS applications. In particular, the reciprocating scan mode can be used with various geometries of the counterbodies and specimens to obtain friction measurement with smaller contact areas with higher speeds. It provides the possibility of revealing new information about micro-friction in relatively new materials such as thin film polymer contact in MEMS.

In this set of micro-friction experiments, the counterbody was a 1 mm diameter ball made from stainless steel AISI 440C (grade 10) and the flat specimens were of PTFE and acrylic-based R11 resin fabricated by micro-stereo-lithography, as shown in Figure 5.1. All the friction experiments included in this chapter use the same measurement methods, cleaning procedures, and test environment as those established in the previous chapter.

Prior to friction testing, the surface topography of the samples was investigated, to allow consideration of whether any standard roughness parameters might be correlated with micro-tribological behaviours. Measurements were made using a Bruker ContourGT white-light interferometer, using its software for all the analysis. Figure 5.2 illustrates typical 3D maps obtained. They show the surface topography of polymeric materials including PTFE and acrylic-based R11 resin with a scan area

of 3 mm x 3 mm. Colour variations in the sample surfaces, including red, green and blue, show the decrease of the surface heights with the measuring position.

The topographic parameters 2D average roughness (R_a), root mean square (RMS, R_q), skewness (S_{sk}), kurtosis (S_{ku}) and 3D average roughness (S_a), were assessed under the following instrument settings including the measurement type, objective, backscan, length and bounding box. Table 5.1 summarizes these values. As might be expected from the images in Table 5.1, the acrylic-based R11 resin specimen is rather smooth, especially in the central position, whereas the PTFE is notably rougher due to a little scratch in the surface.

(a) Steel ball (b) PTFE (c) R11 MSL specimen

Figure 5.1 Images of the tip and flat specimens. Images are approximately 12 mm square.

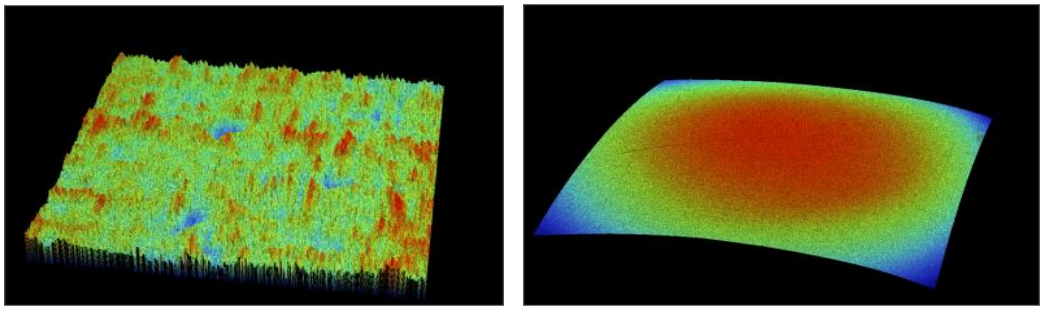

Figure 5.2 Typical 3D maps of PTFE and acrylic-based R11 resin specimen

Table 5.1 Topographic surface parameters

Parameters	PTFE	MSL Specimen
R_a	110.922 nm	1.045 μm
R_q	135.643 nm	1.271 μm
S_{sk}	0.283	-3.338
S_{ku}	6.528	11.944
S_a	1.523 μm	0.272 μm

5.3 Tribometer Signals Analysis

The following subsections examine signal quality and methods of analysis in the present context, closely following the approach used in Chapter 4. While large changes from the patterns seen earlies seem unlikely, especially the basic instrument noise levels, repeating a full process using the polymeric samples provides additional levels of confidence in the results. Additionally, this investigation will help to confirm the extent to which the new micro-tribometer can be used with a common procedure over a wide range of materials.

5.3.1 Signals Variation Analysis in the Vertical Deflection

Figure 5.3 shows the signal for the sensing-beam deflections in the vertical position for the acrylic-based R11 resin sample at a sliding frequency of about 3 Hz with a load of 16.37 mN and a track length of 66 μm. The vertical deflections show a stable closely sinusoidal variation with time with a period, indicated by the red line, of about 330 ms, consistent with the given sliding frequency (3 Hz) of the notch-flexure scanning mechanisms. However, this sinusoid carries a slightly larger,

mainly periodic signal of approximately 20 ms period, indicating the superimposition of a noise signed very similar to that shown in Figure 5.3. The basic signal arises because the sample surface is not sliding exactly orthogonal to the vertical axis of the sense beam. The about 40 mV peak-to-peak change represents about 2.5° misalignment over a 66 µm track, indicating the tilt of flat sample that would cause about 2 µm tilt-related height change. However, this value which would be difficult to eliminate during setting up on such a small-range measurement.

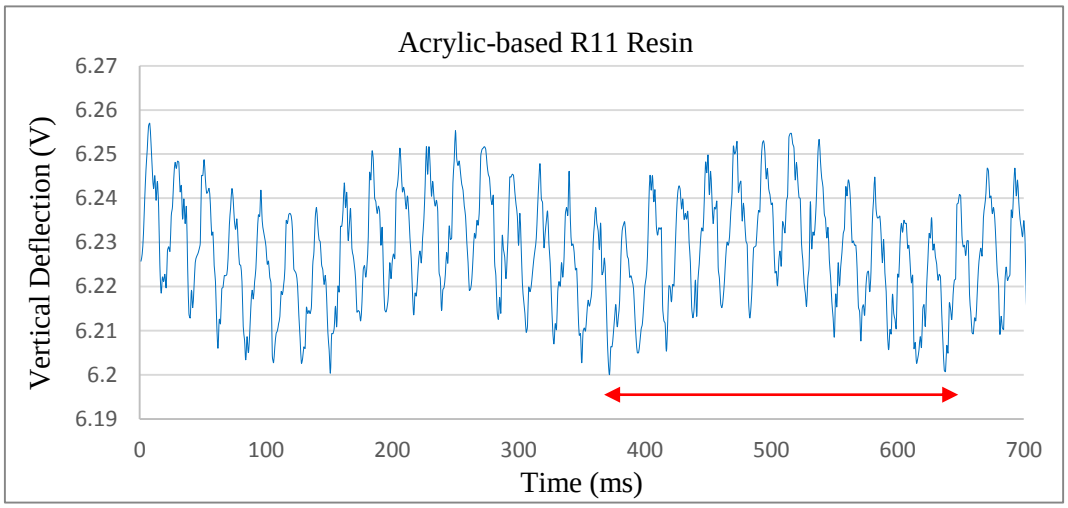

Figure 5.3 Signal variation of the deflection of the sensing beam in the vertical position for acrylic-based R11 resin at a sliding speed of 198 µm/s with the load of 16.37 mN and the track length of 66 µm

Figure 5.4 shows a slightly different pattern with the vertical deflection for a PTFE specimen at a sliding speed of 198 µm/s with a load of 26.79 mN. There is a much clearer 330 ms period nearly sinusoidal curve (red line), matching the sliding frequency of the notch-hinge mechanism. However, this curve has superimposed

small but not so obvious cycles at approximately 50 Hz but of considerably smaller amplitude than seen in Figure 5.3. The main 3 Hz signal has the similar 40 mV peak-to-peak change and the scan length is about 66 μm, the slope is about 2.5°, which indicating the tilt of flat sample that would cause the height change.

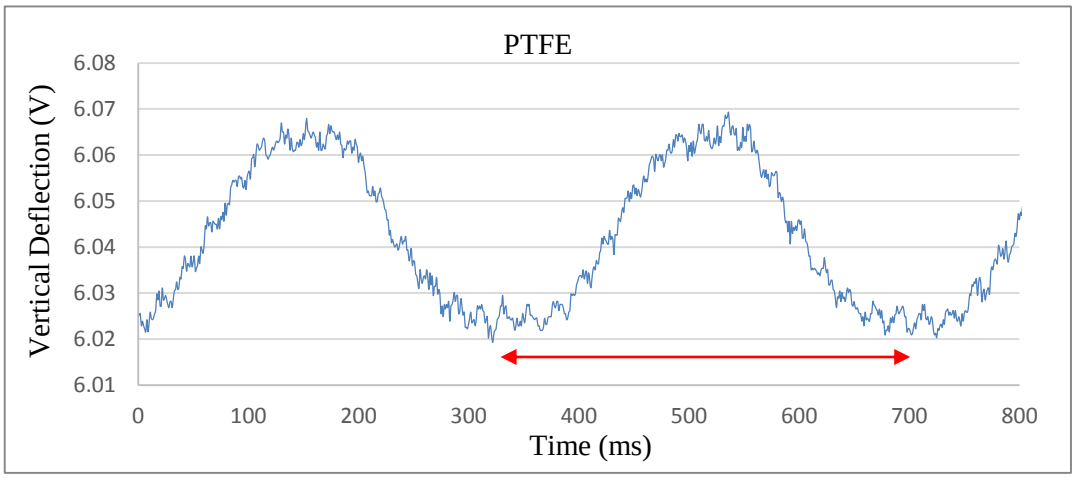

Figure 5.4 Signal variations of the deflection of the sensing beam in the vertical position for PTFE at a sliding speed of 198 μm/s with the load of 26.79 mN

The significant apparent suppression of the baseline noise level (Figure 4.4) has been observed on various occasions but not consistently and not on all measurements of PTFE specimens. This behaviour is not fully understood. The 50 Hz frequency strongly suggests that the primary effect is electrical, but sometimes a mechanical load can modify it. If probe contact was simply introducing damping to an induced mechanical vibration, a more consistent response would be expected. Perhaps then the loads in the force loops of the instrument are subtly altering potential (resistive) earth path. Whatever the cause, this suppression implies that

better instrument performance is achievable in principal, but for the present work the safe limit must be taken always as the full noise signal exemplified by Figure 5.3.

5.3.2 Signals Variation Analysis in the Lateral Deflection

Figure 5.5 shows some cycles of the signal from the lateral sensing-beam deflections for contact with an acrylic-based R11 resin specimen at a sliding frequency of 3 Hz with an applied load of 11.03 mN. The lateral deflection shows a consistent and stable signal with time. It is almost a rectangular wave with good symmetry at the top and bottom of the curves of each cycle, indicating behaviour similar to the ideal friction force signals in a reciprocating scan mode described in Chapter 4. A signal similar to that shown in Figure 4.7 is superimposed on this basic friction force response, just as seen in the vertical axis signals.

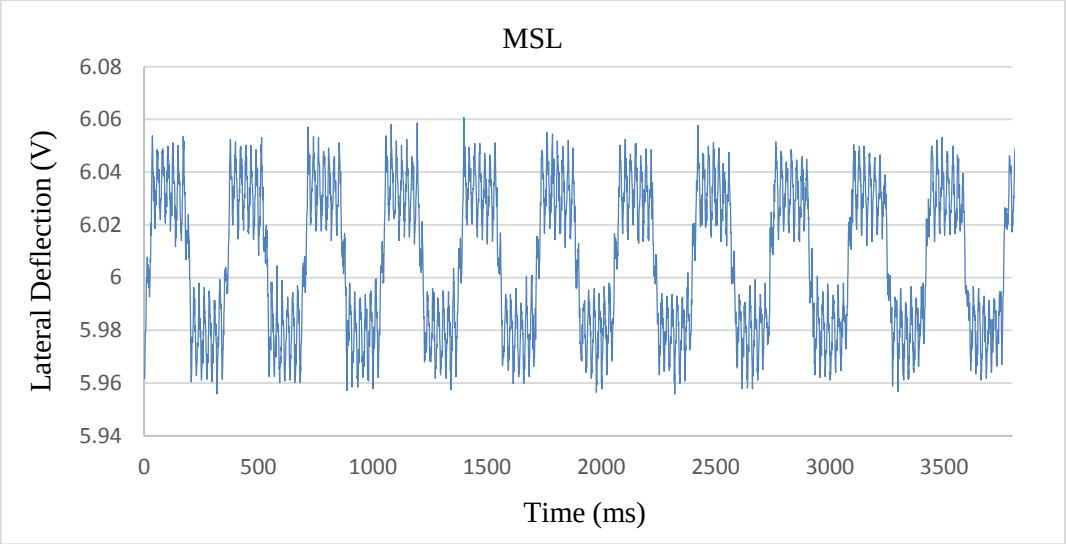

Figure 5.5 Signal variations of the deflection of the sensing beam in the lateral position for acrylic-based R11 resin at a sliding frequency of 3 Hz with the applied load of 11.03 mN

Figure 5.6 shows examples of the lateral signals of the sensing-beam for a PTFE sample at various sliding speeds and applied loads and a 66 μm track length. The friction force signals are consistent and stable with time, some having suppressed noise levels, but show different variations in the shapes of the curves. Both top and bottom sections of the ideally rectangular signal curves show different types of asymmetry in Figures 5.6. This phenomenon is difficult to describe accurately and can have complex, interacting causes. Some observations are:

1) If the sample scan is slightly tilted from the lateral axis of the sense-beam, the beam will be deflected up and down with the scan, changing the actual applied load and so the friction force. This would result in (ideally) the same slopes at the top and bottom sections, which is not seen in any of these examples.

2) Asymmetry implies a second phenomenon added to or instead of a static slope effect. Non-flat sample surfaces will result in different scanning angles at various measuring positions, but this is effect is likely to be symmetrical. Changes in the material properties or surface topography could lead to many patterns, but there is no independent evidence for suspecting significant effects here.

3) For Figure 5.6(a), the top and bottom curves show an equal ramp on the reverse. This could arise from overshoot and decay at the fast changes of the signals for reciprocating scan mode, but would not be expected to continue throughout such a slow scan. If this were a major cause, a similar, larger effect might be expected, but is not seen, in the higher frequency scan of Figure 5.6(c).

4) For Figure 5.6(b) and (c), the top or bottom curve shows smaller changes when

the opposite one is ramped. This phenomenon could possibly be caused by two effects including, for example, a consistent downwards ramp in both top and bottom curves, and growing equal ramped curves. Figure 5.6 shows some evidence for a progression of the pattern with increasing force.

5) If the static friction exceeds the dynamic friction, then there will be an increased magnitude in the lateral signal at the start of each half-cycle. The sliding speed immediately after each reversal will be very low, so it is quite plausible that it takes a little time before the measurement relaxes to the steady-sliding value. On short scans this effect could lead to a pattern where both the top and bottom sections of the ideal signal appear to start at a high value and then decay towards the axis. Such behaviours could be a major contributor to the signal pattern seen in Figure 5.6(a).

6) Internal misalignments and motion errors within the instrument could generate force-sensitive asymmetries. However, results such as that in Figure 5.6 strongly suggest that there is no large fully systematic effect. There might still be some contribution from instrument error that relate to specific set-ups, although the close similarity of all the set-ups used here seems unlikely to yield the amount of variability observed.

In conclusion, the phenomenon of various ramped but asymmetry curves for the lateral signals of the sensing-beam shown in Figure 5.6 is very complicated but not easy to give an explicit explanation. This might be caused by multiple factors, such as the interaction of the above-mentioned observations of (2), (4) and (5).

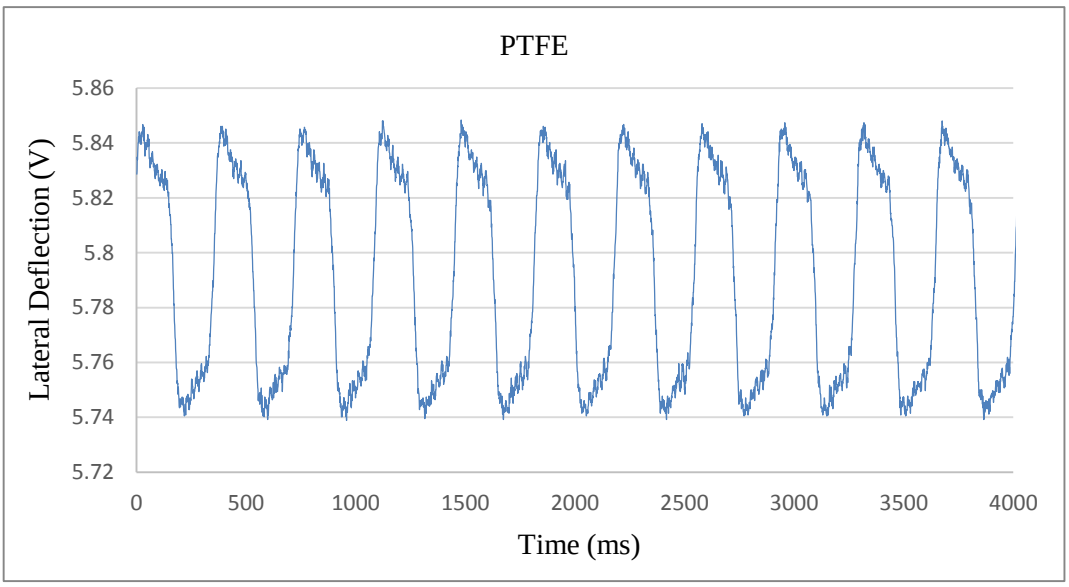

(a) Track Length = 66 µm, Frequency = 3 Hz, Normal Load = 26.79 mN

Figure 5.6 (part) Signal variations of the beam deflection in the lateral position for PTFE sample at various sliding speed with different loads and track lengths (continues)

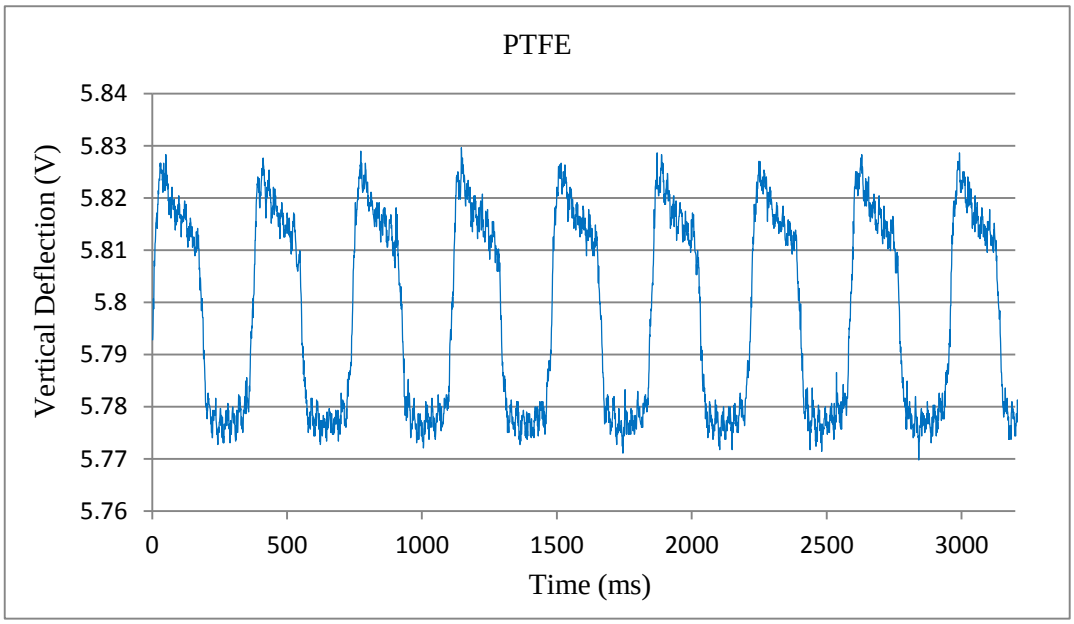

(b) Track Length = 66 µm, Frequency = 3 Hz, Normal Load = 0 mN

Figure 5.6 (part) Signal variations of the beam deflection in the lateral position for PTFE samples at various sliding speed with different loads and track lengths (continues)

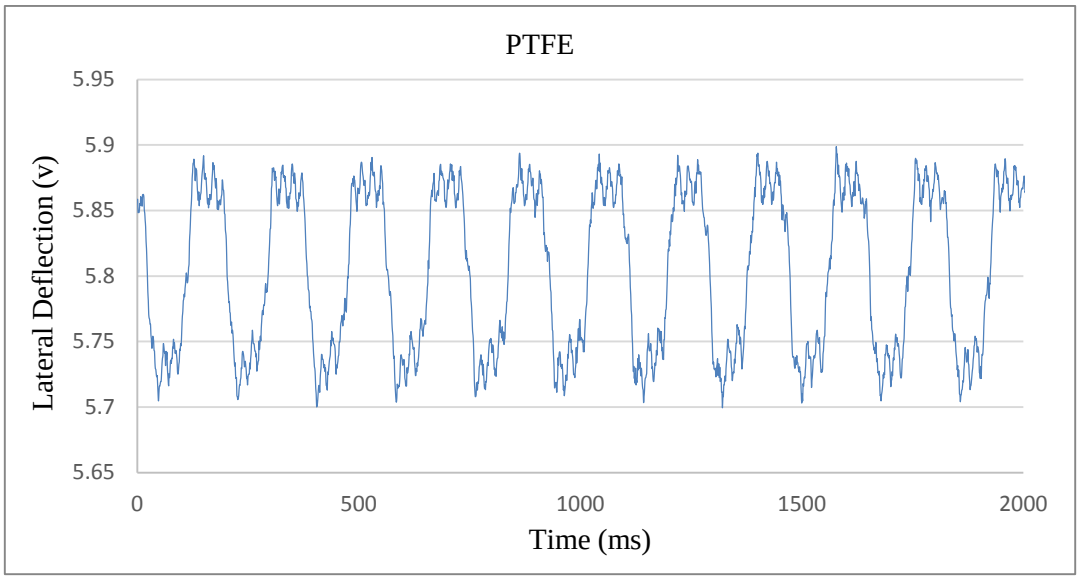

(c) Track Length = 66 µm, Frequency = 6 Hz, Normal Load = 51.95 mN

Figure 5.6 (continued) Signal variations of the beam deflection in the lateral position for PTFE samples at various sliding speed with different loads and track lengths

5.3.3 Calculation of Applied Normal Load and Friction Force

5.3.3.1 Analysis of Signals Selection for Applied Normal Load

The vertical deflections of the sensing beam Δz is calculated using Matlab software by taking the mean value of the sinusoidal signal curves collected from Labview as described in the section 4.3.2. Generally, the first 2-5 cycles at the start are ignored because they may be influenced by surface contamination or some transients such as overshoot and decay. Then, in order to check for any instrument inconsistencies or data trends from friction heating, unexpectedly rapid wear and so on, sub-section, of the signal were evaluated independently.

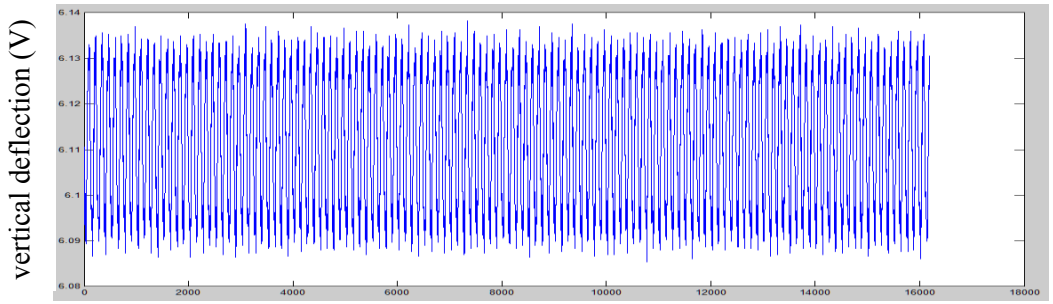

(a) Whole trace

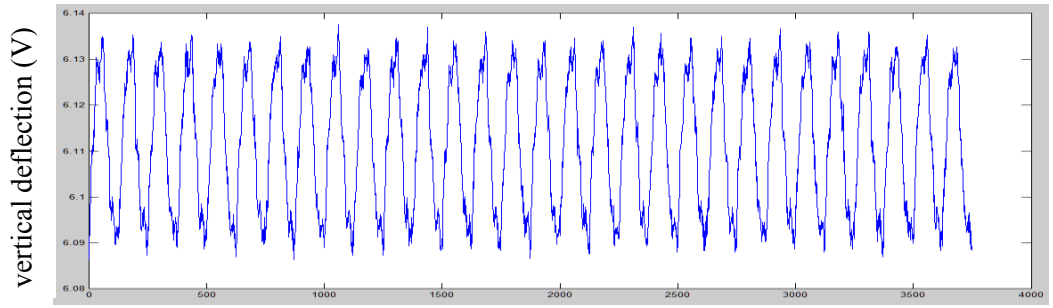

(b) Mid-30 cycles

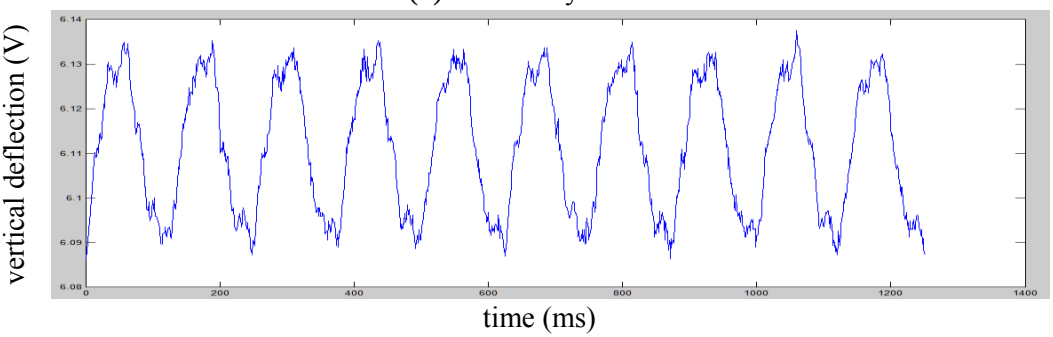

(c) First-10 cycles

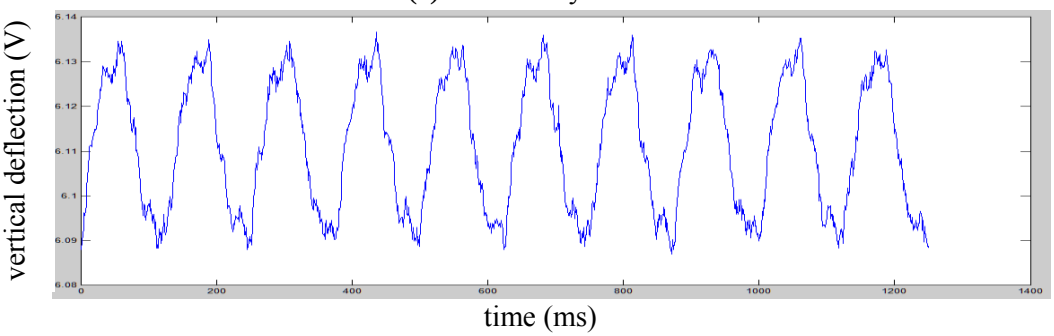

(d) Last-10 cycles

Figure 5.7 Vertical deflection chosen for an MSL specimen with the whole trace, mid-30, first-10 and last-10 cycles at a sliding frequency of 9 Hz with the load of 50 mN and the length of 130 μm

Four conditions were considered for measurements taken at loads and speeds high in the working range: the whole signal (sequence) ensuring that evaluation was over a whole number of trace; 30 successive cycles taken randomly from the middle region of the signal (mid-30); 10 successive cycles taken randomly from the front and rear of the trace (first-10 and last-10). Figure 5.7 shows a typical example for the whole-signal, mid-30, first-10 and last-10 cycles from an R11 MSL specimen at a sliding frequency of 9 Hz, load of 50 mN and length of 130 μm. All the cases analysed are very consistent and stable with time. The cycle shape includes slight ramps at the top and bottom of each cycle arising from residual tilt of the test specimen, visible in Figure 5.7 (c) and (d).

Table 5.2 shows a comparison of the calculated average voltage of the vertical deflection signal for polymers at the largest loads, longest length and highest sliding frequency for the four different analyses taken over the whole trace, mid-30, first-10 and last-10 cycles. For the acrylic-based R11 resin, these four mean values show remarkable consistency, while the slightly greater variation for the PTFE sample is still of no practical significance. With no more than 0.0002 V (equivalent to 0.023 mN) variation across all these assessment methods, the measurements are clearly highly insensitive to the choice between them. Thus, the whole signal, as saved in text file for each test condition, is used for the analyses here. This is convenient, requiring minimal data manipulation, and provides the greatest degree of averaging as protection against any occurrence of larger noise spikes.

Table 5.2 The comparison of the calculated average of the vertical deflection for polymers with the largest loads, longest length and highest sliding frequency for the whole trace, mid-30, first-10 and last-10 cycles

Materials	Test Conditions	Cycles Selected	Mean Value of Δz (volt)
MSL R11 resin	Track length -130 µm Sliding frequency – 9 Hz Normal load – 50 mN	Full	6.1116
		Mid-30	6.1116
		First-10	6.1115
		Last-10	6.1115
PTFE	Track length -130 µm Sliding frequency – 9 Hz Normal load – 50 mN	Full	6.0926
		Mid-30	6.0928
		First-10	6.0924
		Last-10	6.0927

5.3.3.2 Analysis of Signals Selection for Friction Force

Friction force is calculated using Matlab software from the height difference between the top and bottom regions of the curves of the lateral deflections of the sensing beam Δx collected from Labview as described in section 4.3.3.2. The first 2-5 cycles at the start of the trace are ignored to avoid uncertainty from effects such as contaminated specimen surface or signal transients. Then, in order to check for any instrument inconsistencies or data trends from friction heating, unexpectedly rapid wear and so on, sub-section, of the signal were evaluated independently. Three conditions were considered for measurements taken at loads and speeds high in the working range: whole signal (sequence) ensuring that evaluation was over full points, full points but not overshoot parts, parts of full points but not overshoot parts at the top and bottom of each cycle for the 10 successive cycles selected from the front and the rear of the whole trace.

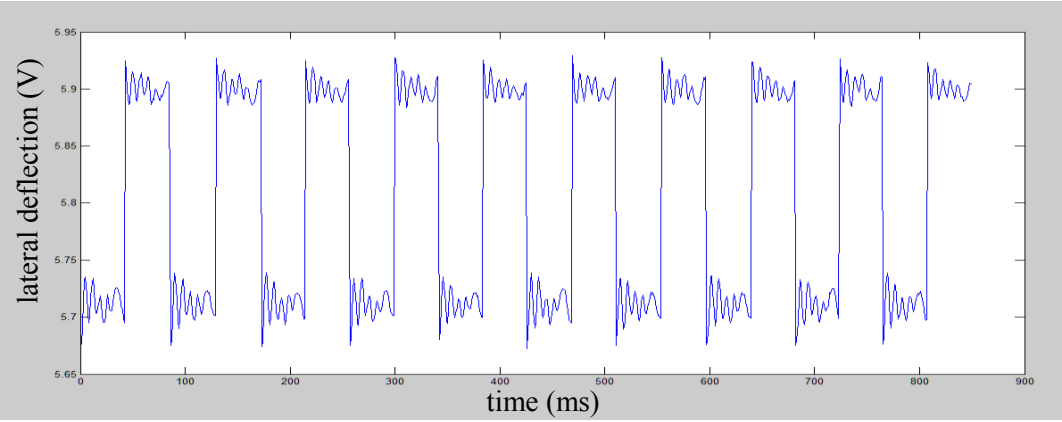

(a) Full points at the top and bottom of each cycle for the 10 successive cycles

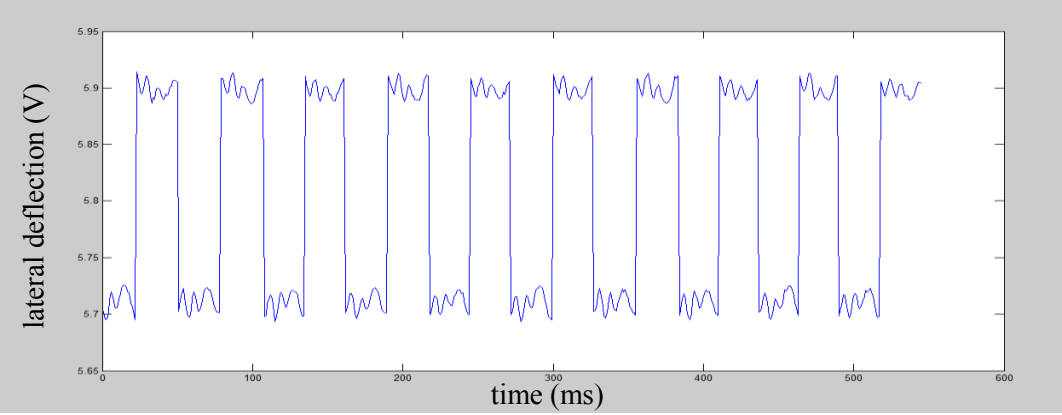

(b) Full points without overshoot parts in (a)

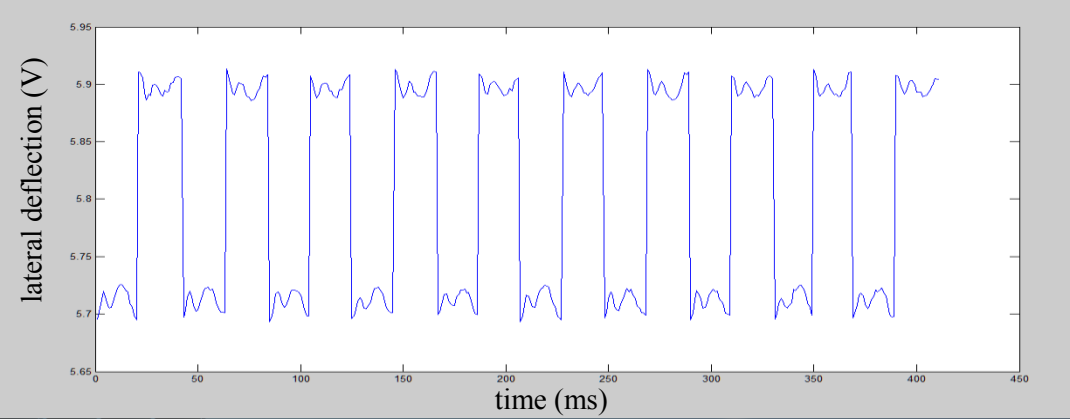

(c) Parts of full points collected in (b)

Figure 5.8 Signals of lateral deflection chosen for an MSL specimen with the full points, full points without overshoot and parts of full points without overshoot at the top and bottom of each cycle for the 10 successive cycles selected from the front of the whole trace

Figure 5.8 shows a typical example for an MSL R11 resin specimen at a sliding frequency of 9 Hz, load of 50 mN and length of 130 μm with the conditions including the full points, full points without overshoot and parts of full points without overshoot at the top and bottom of each cycle for the 10 successive cycles selected from the front of the whole trace. All the cases analysed are very consistent and stable with time. The cycle shape includes overshoot at the top and bottom of each cycle arising from oscillation of the collected signal, visible in Figure 5.8(a). Figure 5.8(b) shows a similar situation but the overshoot parts excluded, meanwhile, parts of the full points were selected at the top and bottom of each cycle shown in Figure 5.8(c) in order to analysis the consistent of the calculation precision.

However, Figure 5.9 shows a different situation for PTFE specimen at loads and speeds high in the working range. There is no obvious overshoot at the top and bottom of each cycle for the 10 successive cycles selected from the front of the whole signal shown in Figure 5.9 (a), and thus two conditions, including parts and full points selected at the top and bottom of each cycle, were considered for measurements to ensure the evaluation for the whole signal (sequence).

Based on the graphs, all the cases analysed are very consistent and stable with time. The cycle shape includes slight ramps at the top and bottom of each cycle arising from residual tilt of the test specimen, visible in Figure 5.9(a) and (b). Figure 5.9(b) shows a similar situation but fewer points selected at the top and bottom of each cycle in order to analysis the consistent of the calculation precision.

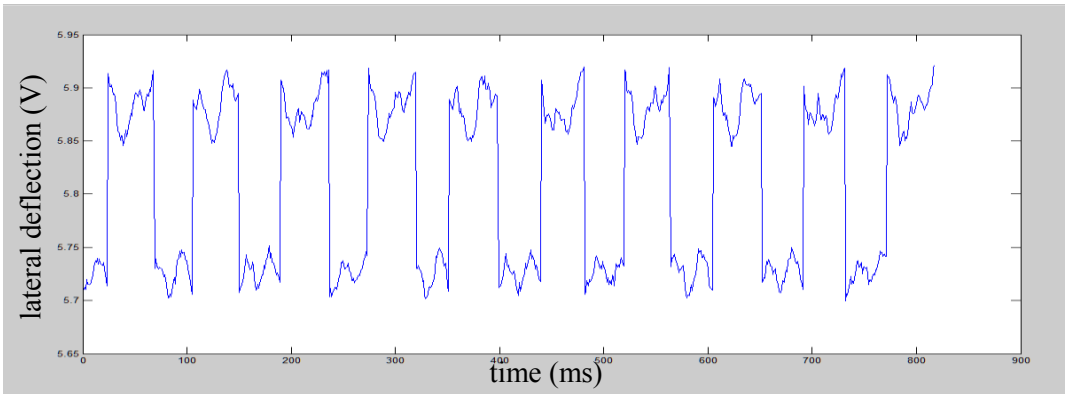

(c) Full points at the top and bottom of each cycle for the 10 successive cycles

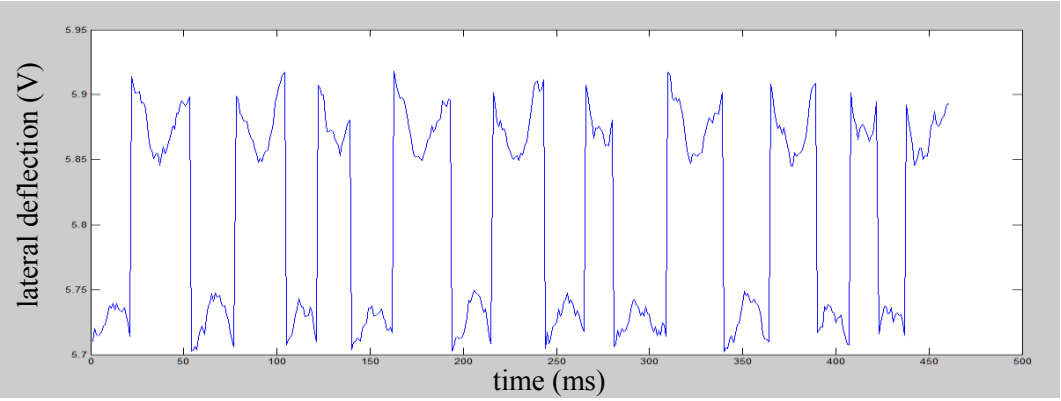

(d) Parts of full points collected in (a)

Figure 5.9 Signals of lateral deflection chosen for a PTFE specimen with the full points and parts of the full points at the top and bottom of each cycle for the 10 successive cycles selected from the front of the whole trace at a sliding frequency of 9 Hz with the load of 50 mN and the length of 130 μm

Table 5.3 shows a comparison of the calculated average voltage of the lateral deflection for polymers at the largest loads, longest length and highest sliding frequency for the different analyses taken over the full points and parts of full points considered with or without overshoot at the top and bottom of each cycle for the 10 successive cycles selected from the front and rear of the whole signal.

Table 5.3 Comparison of the calculated average of the lateral deflection for test specimens with the largest loads, longest length and highest sliding frequency for the full points and parts of full points at the top and bottom of each cycle in the 10 successive cycles selected from the front and rear of the whole trace

Material	Test Conditions	Data Selected at the Top and Bottom of Each Cycle	Mean (bottom) (volt)	Mean (top) (volt)	Δx (volt)
MSL R11 resin	Track length - 130 µm Frequency – 9 Hz Normal load – 50 mN (First-10 cycles)	Full points	5.7105	5.9006	0.1901
		Full points without overshoot	5.7102	5.8990	0.1888
		Parts of full points without overshoot	5.7109	5.8980	0.1871
	Track length - 130 µm Frequency – 9 Hz Normal load - 50mN (Last-10 cycles)	Full points	5.7102	5.9011	0.1910
		Full points without overshoot	5.7104	5.8991	0.1887
		Parts of full points without overshoot	5.7109	5.8978	0.1870
PTFE	Track length - 130 µm Frequency – 9 Hz Normal load – 50 mN (First-10 cycles)	Full points	5.7266	5.8827	0.1561
		Parts of full points	5.7258	5.8766	0.1508
	Track length - 130 µm Frequency – 9 Hz Normal load - 50mN (Last-10 cycles)	Full points	5.7260	5.8828	0.1568
		Parts of full points	5.7257	5.8743	0.1485

For the acrylic-based R11 resin, there is very significant change in these three mean values but the second one (full points without overshoot) shows remarkable consistency. However, variability itself that is significant for the PTFE specimen if the fewer points at the top and bottom of each cycle are selected.

With about 0.008 V (equivalent to 0.09 mN) variation across all these assessment methods, the measurements are clearly a little more sensitive to the

choice between them. Thus, the results are so sensitive to the choice of methods and so the full points without overshoot parts at the top and bottom of each cycle in any 10 successive traces of the whole signal will be used as likely to give best precision in providing the greatest degree of averaging as protection against any occurrence of larger noise spikes.

5.4 Main Experimental Results and Discussion

5.4.1 Variation of Friction with Normal Force at the Same Scan Speed

Figure 5.10 and Figure 5.11 show the variations of friction force and friction coefficient with normal load for an MSL polymeric specimen (acrylic-based R11 resin) at the same scan frequency of 9 Hz and over three different track lengths of 66 µm, 90 µm and 130 µm. Assuming the scan remains sinusoidal, the maximum and average sliding speeds for these conditions are about 650 µm/s, 900 µm/s and 1.3 mm/s and 450 µm/s, 630 µm/s and 1 mm/s respectively. Based on these graphs, linearity is excellent over the working range ($R^2 > 0.99$) for friction forces, which mostly remain in the range between 2 mN and 12 mN, at each different track length. However, there is a slightly decline in the friction force with the increase of the track length at the same normal load, shown in Figure 5.10. Although the differences between the individual points at any one set load might have limited significance relative to the measurement uncertainties, the consistent separation of the graphs suggests that there is a real physical effect here. Similarly, the CoF also has a downward tendency from around 0.2 to about 0.15 when the track length is

increasing from 66 µm to 130 µm. The most likely cause appears to be a slight (inverse) relationship between CoF and sliding speed within this test regime. However, there is almost no variation of CoF with normal load at a single test condition shown in Figure 5.11, and the small fluctuation in CoF might be caused by instrument effects or calculation accuracy.

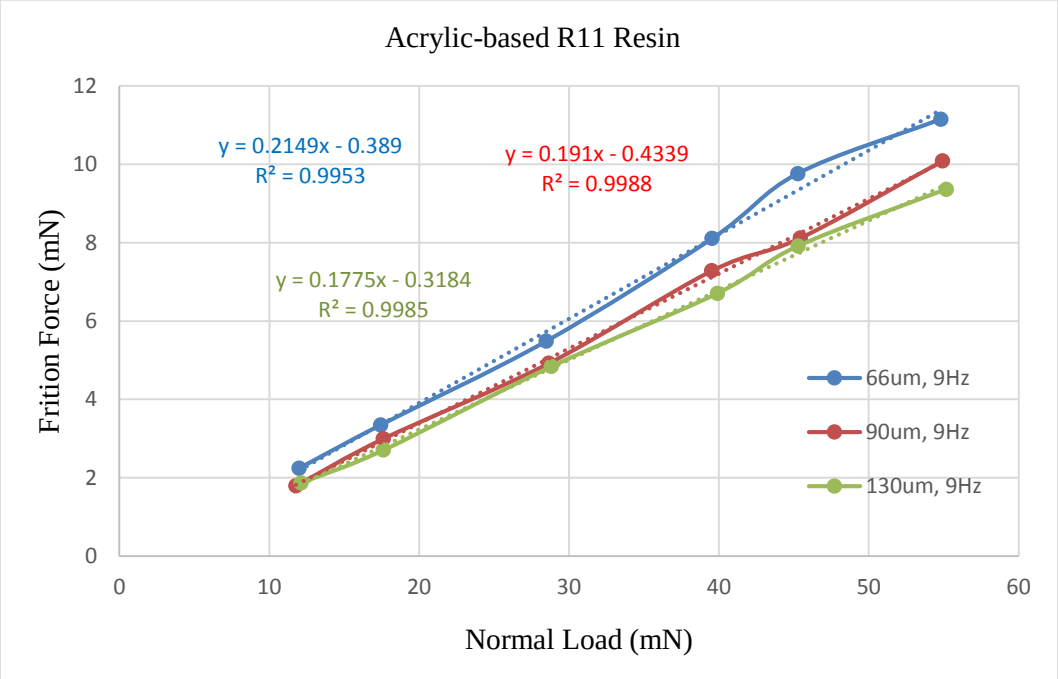

Figure 5.10 Variations of friction force with normal load for an MSL R11 resin sample at the same scan speed of 9 Hz and three different track lengths of 66 µm, 90 µm and 130 µm

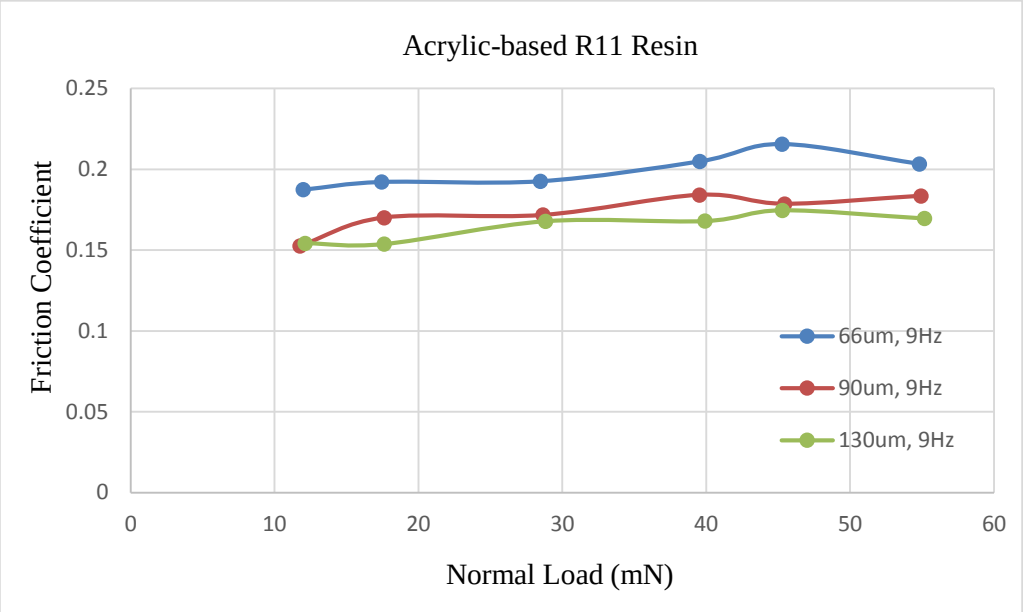

Figure 5.11 Variations of CoF with normal load for an MSL R11 resin specimen at the same scan speed of 9 Hz and three different track lengths of 66 µm, 90 µm and 130 µm

Figure 5.12 and Figure 5.13 show the variations of friction force and friction coefficient with normal load for a PTFE sample under the same test conditions as for the previous MSL polymeric specimen. Based on these graphs, linearity is somewhat poorer, but still good, over the working range ($R^2 > 0.99$) for friction forces compared to those of the MSL polymeric specimen shown in Figure 5.12. However, there is almost no change in the value for different scan lengths, in the range between 1 mN and 8 mN, which meaning the friction force is independent of track length (sliding speed) but has just the linear relationship with normal load predicted by Amonton's law in this test regime (Dowson, 1998). Note that other published work, including by Alsoufi using the original version of the current test-rig (Hutchings, 1992; Smith, 1993; Myshkin, 2005; Gerbig, 2006; Alsoufi,

2011), has suggested that the CoF for PTFE would rise perceptibly as the normal load reduces across this test range. Similarly, in Figure 5.13, the CoF has some obvious fluctuations but has no clear trend with track length, remaining in a stable range at around 0.12 when the normal load is applied from 10 mN to 60 mN. The CoF appear to be independent of the track length and sliding speed under these test conditions. Also, the lower CoF of PTFE specimen, close to 0.1, matches well with its known properties as an ideal oil-free lubrication material.

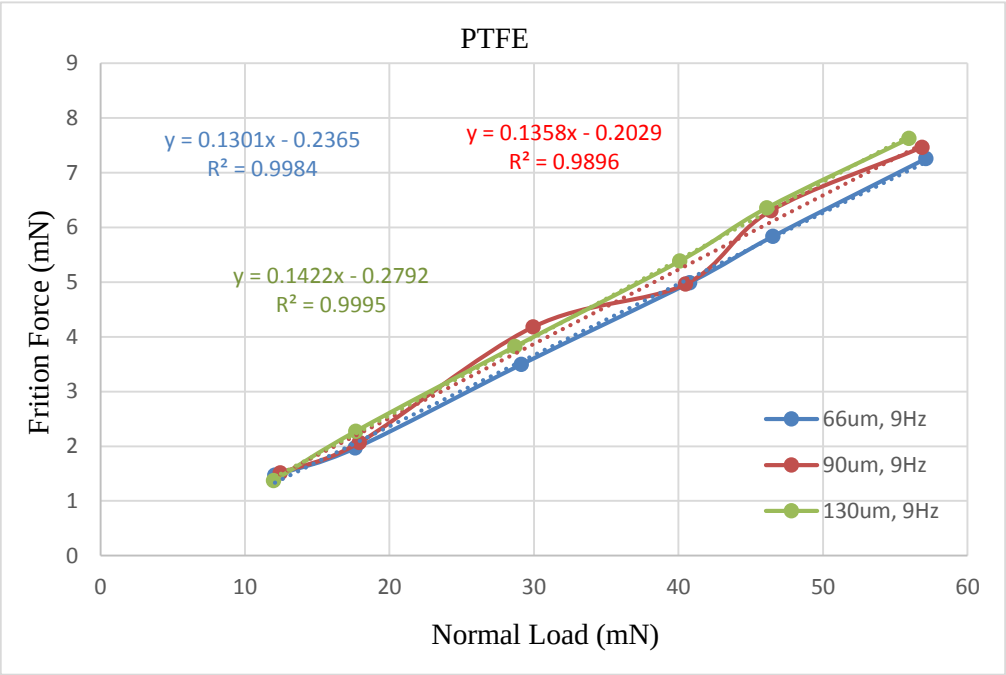

Figure 5.12 Variations of friction force with normal load for a PTFE specimen at the same scan speed of 9 Hz and three different track lengths of 66 µm, 90 µm and 130 µm

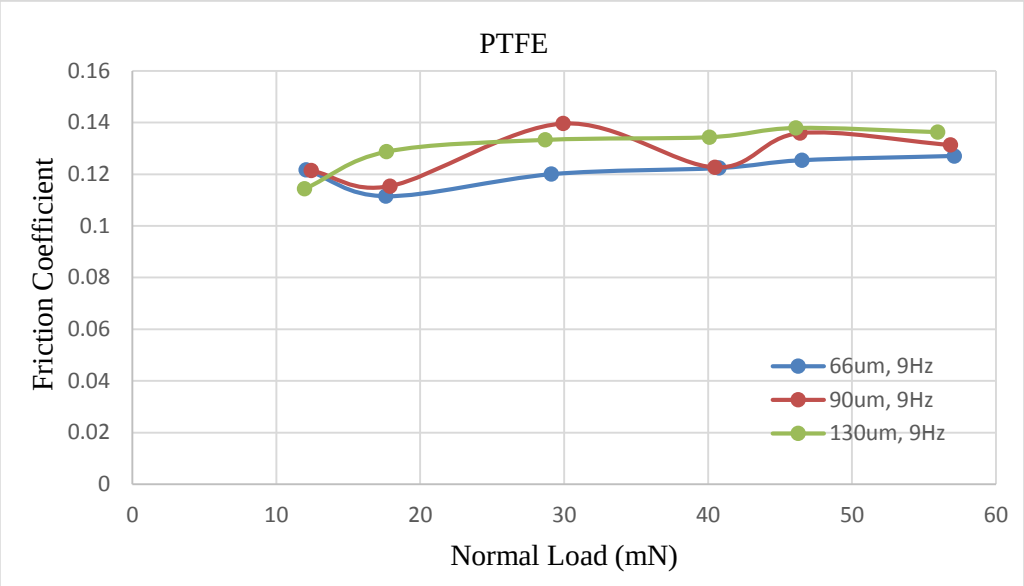

Figure 5.13 Variations of CoF with normal load for a PTFE specimen at the same scan speed of 9 Hz and three different track lengths of 66 µm, 90 µm and 130 µm

5.4.2 Variation of Friction with Normal Force at the Same Track Length

Figure 5.14 and Figure 5.15 show the variations of friction force and friction coefficient with normal load for an MSL polymeric specimen at the same scan length of 66 µm and three different scan frequencies of 3 Hz, 6 Hz and 9 Hz. Assuming the scan remains sinusoidal, the maximum and average sliding speeds for these conditions are about 150 µm/s, 300 µm/s and 440 µm/s and 100 µm/s, 200 µm/s and 300 µm/s respectively. Based on these graphs, linearity is excellent over the working range ($R^2 > 0.99$) for friction forces, in the ranges between 2 mN and 16 mN, when the normal load applied is from 10 mN to 60 mN. There is a declining tendency in the friction force with the increase of the sliding frequency at the same scan length, shown in Figure 5.14. Similarly, the CoF reduces from around 0.3 to

about 0.2 when the scan frequency is increased to 9 Hz. This drop could possibly be related to a higher contact repetition rate leading to some surface thermal variation but there is also increasing sliding speed. There is only slight fluctuation in CoF with normal load in each single frequency test condition, as shown in Figure 5.15. Therefore, it is reasonable to conclude that the friction force and CoF for MSL material are not independent of the sliding frequency at the same track length. Comparing these results with Figure 5.10 and Figure 5.11, it is seen that the CoF of the MSL polymeric specimen falls in a similar way with the increase of the track length and sliding frequency at normal loads applied in the range 10 mN to 60 mN. This strongly suggests that the common cause is an inverse relationship between CoF and sliding speed across the present test regime.

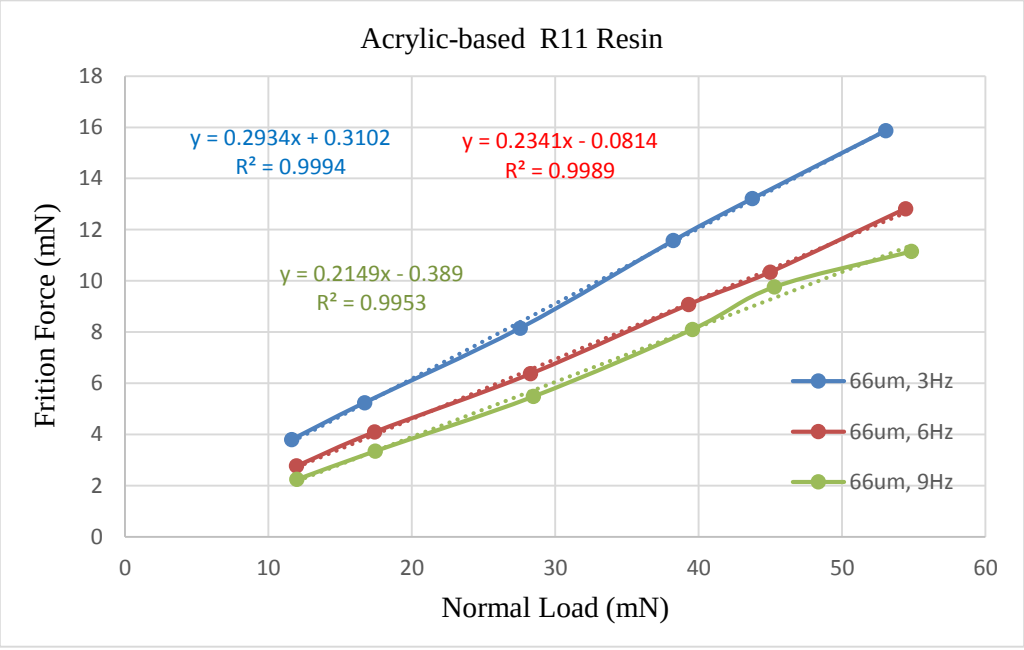

Figure 5.14 Variations of friction force with normal load for an MSL polymeric sample at the same scan length of 66 µm and three different scan speeds of 3 Hz, 6 Hz and 9 Hz

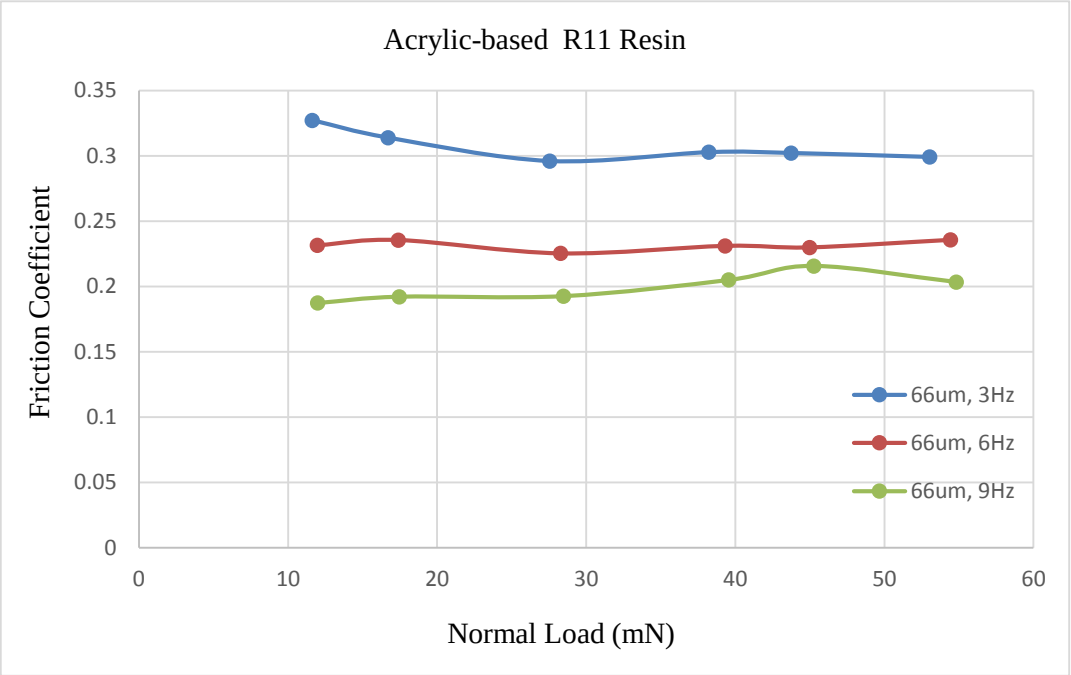

Figure 5.15 the variations of CoF with normal load for an MSL polymeric specimen at the same scan length of 66 µm and three different scan speeds of 3 Hz, 6 Hz and 9 Hz

Figures 5.16 and 5.17 show the variations of friction force and friction coefficient with normal load for a PTFE sample under the same test conditions as for the previous MSL specimen. Based on these graphs, linearity is as good over the working range ($R^2 > 0.99$) for friction forces against load as that of the MSL polymeric specimen shown in Figure 5.16. The friction force values remain in the 1 mN - 8 mN range but have an obvious upward tendency with the sliding frequency and normal load at the same scan length. Similarly, the CoF changes from around 0.09 to about 0.12 as the scan speed is increased to 9 Hz. However, there is little fluctuation in CoF with normal load at each single test condition, as shown in Figure 5.17.

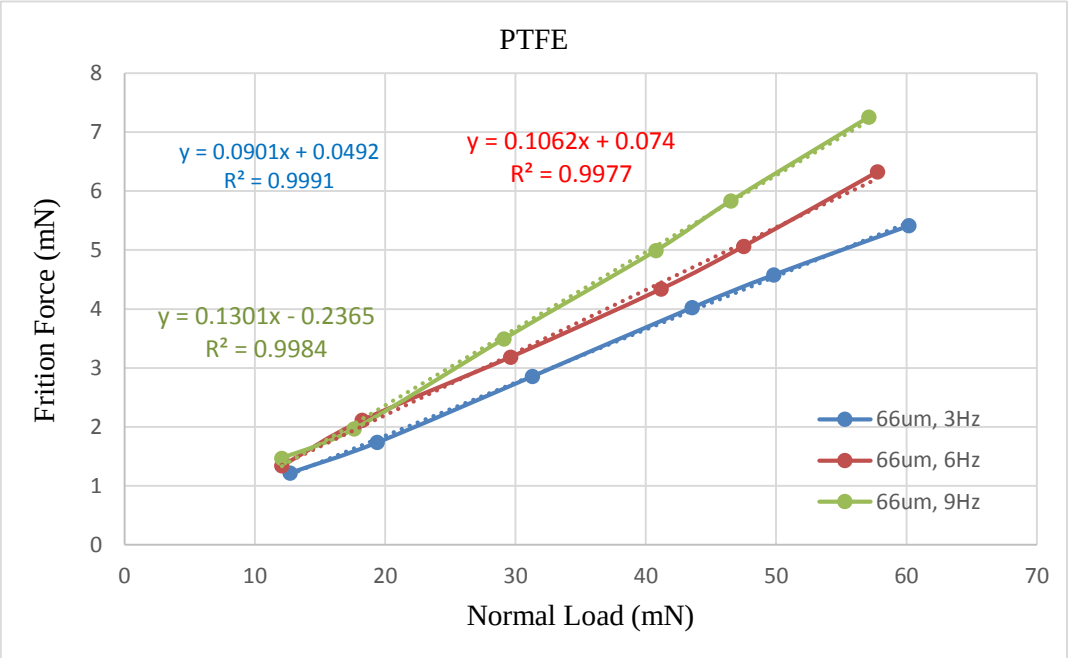

Figure 5.16 Variations of friction force with normal load for a PTFE specimen at the same scan length of 66 µm and three different scan speeds of 3 Hz, 6 Hz and 9 Hz

Comparing Figure 5.17 with Figure 5.15, the relationship between CoF and scanning frequency is of opposite sense for PTFE and acrylic resin in the present test regime. Given the lack of evidence in Section 5.3.1 for a sliding-speed dependence for the CoF of PTFE, this opens up the possibility that contact repetition rate in short reciprocating sliding contact adversely affects its performance, possibly by reducing the time for the surface conditions to relax following a perturbation. Also, the CoF of the PTFE material, drops to below 0.1 at a lowest scan speed and shortest scan length, as might be expected from its known properties and lubrication effect again.

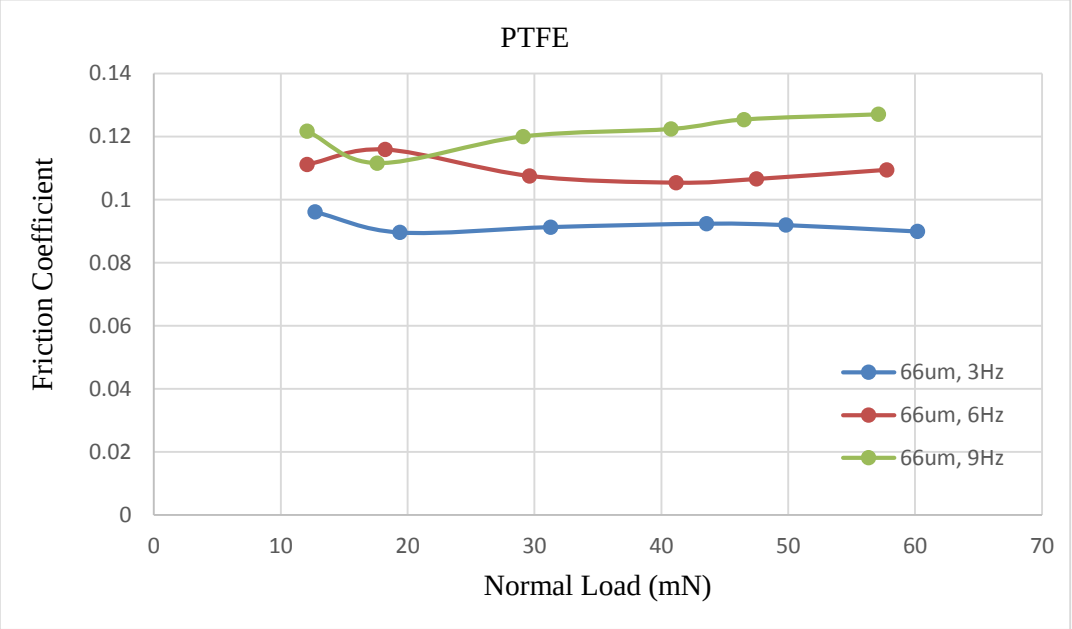

Figure 5.17 Variations of CoF with normal load for a PTFE specimen at the same scan length of 66 µm and three different scan speeds of 3 Hz, 6 Hz and 9 Hz

6 Correlations between Nano-indentation Measurement and Micro-friction

Overview
Nanoindentation tests tend to be easier to execute than micro-tribological ones, so this chapter explores whether existing contact theories might allow inferences of practical usefulness about friction to be obtained from indentation data. First, MEMS materials and MSL polymeric materials, including silicon wafer with silicon dioxide coating, PTFE, and acrylic-based R11 resin, were chosen to measure their mechanical properties using nanoindentation tester with a Berkovich indenter tip. Mathematical modelling was carried out to examine the friction force, coefficient of friction (CoF) and Berkovich nanoindentation against applied normal loads to obtain comparisons between the contact model theories and experimental investigations. Theoretical predictions of friction measurements for a ball-on-flat configuration at the microscale are compared to the trends of experimental friction force and CoF with similar normal loads.

6.1 Introduction

Studies so far suggest that the micro-tribological behaviour of the polymer materials varies enough that designers must take care to get relevant data. It will always be expensive to undertake regular routine tribology measurements of the type needed. It would therefore be very useful to have an easier measurement that might act as an approximate surrogate for routine quality control purpose. Nano-indentation hardness has some plausibility for this role, especially as it might sometimes be a functionally “non-destructive” method. So, this chapter attempts to discover whether a useful correlation exists between Berkovich tip nano-hardness and the micro-friction of polymeric samples.

Micro-friction testing is always likely to be a skilled activity and so a special challenge in production environments. Previous chapters show that the friction

properties of materials potentially used in MEMS (including polymers) vary enough that production monitoring of the materials will sometimes be advised. In contrast, nano-indentation, while by no means trivial, is rather easier to use in a routine way. Additionally, it can probably be applied on smaller specimen areas and might in some cases might be considered non-destructive. Indenter and tribometer instruments clearly share some common features, as do underpinning contact theories. These observations lead to the question of whether existing contact theory might provide a means to infer micro-friction behaviour of a MEMS material from nano-indentation measurements of it. If a correlation sufficiently precise to have practical use exists and can be calculated, then nano-indentation measurements alone might suffice for quality control purposes. This suggestion is attractive and so it is explored further in this chapter, which presents some nano-indentation experiments, discusses modelling of indentation, contact and friction and so attempts to predict friction properties for comparison with the real data presented in earlier chapters.

6.2 Nano-indentation testing

6.2.1 Sample Materials

The materials chosen for the nano-indentation study were three of those included in the micro-friction experiments, in order to allow direct comparisons. The flat specimens, nominally 10 mm square, were of a silicon wafer with a silicon dioxide film, Polytetrafluoroethylene (PTFE) and a MSL polymeric material, as seen in Figure 6.1. The silicon wafer, with thickness of 525 μm, is a typical commercial

product (type: N<100>P) with silicon dioxide coating deposited on it to a thickness of approximately 320 nm. Because optical microscopes were to be used to assess surface topographic quality, the PTFE sample was coated with a gold layer of 30 nm thickness due to its low reflectivity. The MSL specimens used a custom functional acrylic-based R11 resin formulation from Envisiontec and were fabricated by an Envisiontec Perfactory SXGA+ stereo-lithography machine.

While the experimental data collected here was obtained specifically to test correlation with friction, it also adds usefully to the general knowledge-base because micromechanical data on these materials, especially the R11 acrylic resin, is relative scarce and quite variable.

Before each measurement, all samples and tips were cleaned with isopropanol on a cotton bud and then blown dry with clean air, so that there would be no significant influence on the results from natural contaminant films. After the cleaning procedures, all the tests were carried out using a nanoindentation tester with Berkovich indenter tip in a controlled environment at nominally 22 ± 1˚C and 40 ± 5% relative humidity.

(a) Silicon wafer with SiO_2 coating (b) PTFE (c) Acrylic-based R11 resin

Figure 6.1 Pictures of the flat specimens

6.2.2 Nano-indentation tester with Berkovich Indenter tip

A Model NHT^2 nanoindentation tester developed by CSM Instruments and supplied by Anton Paar Company was used to measure the mechanical characteristics of the test specimens. The NHT^2, shown in Figure 6.2, is a modern, sophisticated nanoindentation tester designed to measure the mechanical characteristics of various surfaces including elastic modulus, hardness, fracture toughness and creep at the nano-scale. It has a unique top surface referencing technique, which allows an indentation measurement to be made in typically less than 3 minutes, without waiting for thermal stabilization. This system can be used to characterize organic, inorganic, soft or hard materials, many types of films and coatings. Also, bulk material surface mechanical characterization can be performed on hard or soft materials, including metals, semiconductors, glasses, ceramics, and composites. The normal load range is between 0.1 mN and 500 mN with a resolution of 0.04 μN. The maximum indentation depth is 200 μm with a resolution of 0.04 nm. Its load frame stiffness is greater than 107 N/m.

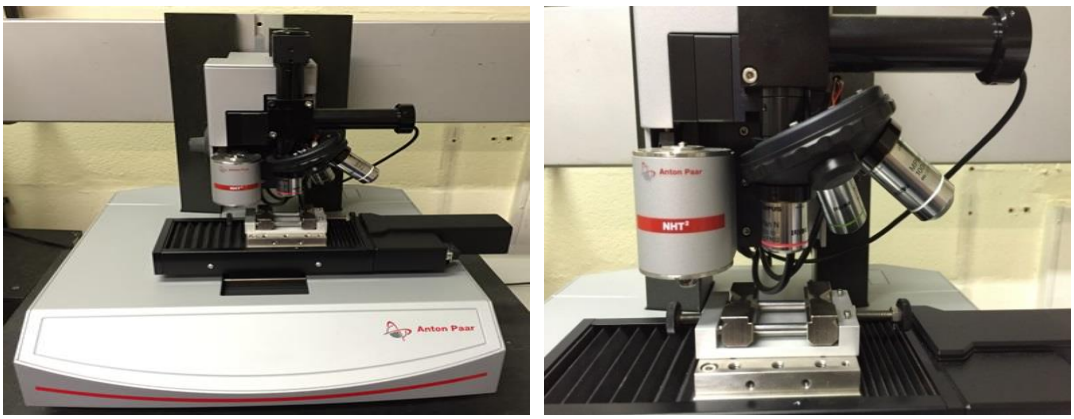

Figure 6.2 Pictures of Nano-indentation Tester NHT^2

Before the indentation tests, each sample was moved to observe the surface topography by using the microscope on the indenter successively with three objectives at the magnifications of 5x, 50x and 100x and thereby a smooth flat area was selected for the particular test. Then, the instrument settings including loading and unloading parameters, approach distance, approach speed, dwell time and contact stiffness were chosen for different tests of sample surfaces. The investigations used a set of maximum loads as the independent variable: typical values for other settings are given in Table 6.1. Finally, the specimen was moved by the CSM Instrument software for nanoindentation measurement under the NHT^2, and the obtained data was saved in configuration and data files for analysis.

Table 6.1 The instrument settings

Parameters	Hard Materials	Soft Materials
Loading & unloading rate	50 mN/min	20 mN/min
Approach distance	2000 nm	1000 nm
Approach speed	2000 – 3000 nm/min	2000 – 3000 nm/min
Dwell time	5 s	10 – 20 s
Contact stiffness	250 μN/μm	250 μN/μm

6.2.3 Mechanical Properties Measurement

As MEMS technology underwent rapid growth and the ranges of applied materials increase, the importance of mechanical engineering databases of MEMS materials built at the appropriate scaling of mechanical design was recognised by Muller in 1990 (Muller, 1990). Work followed to fully exploit the development of MEMS technology and fabricate new MEMS devices with various functional and structural

materials for potential users (Muller, 1997). In the past decade, much research work has been devoted to characterisation of MEMS materials for better understanding of fundamental mechanical properties such as elastic modulus, shearing strength and Poisson's ratio when subjected to forces and deflections typical of MEMS components, often in the context of essential information for the function of mechanical structures of micro-mechanical sensors. However, the newer MSL polymeric materials (acrylic-based R11 resin) and biomedical materials, have not yet been well characterized and there is not sufficient knowledge about their mechanical properties at small scales (particularly under 1 mm).

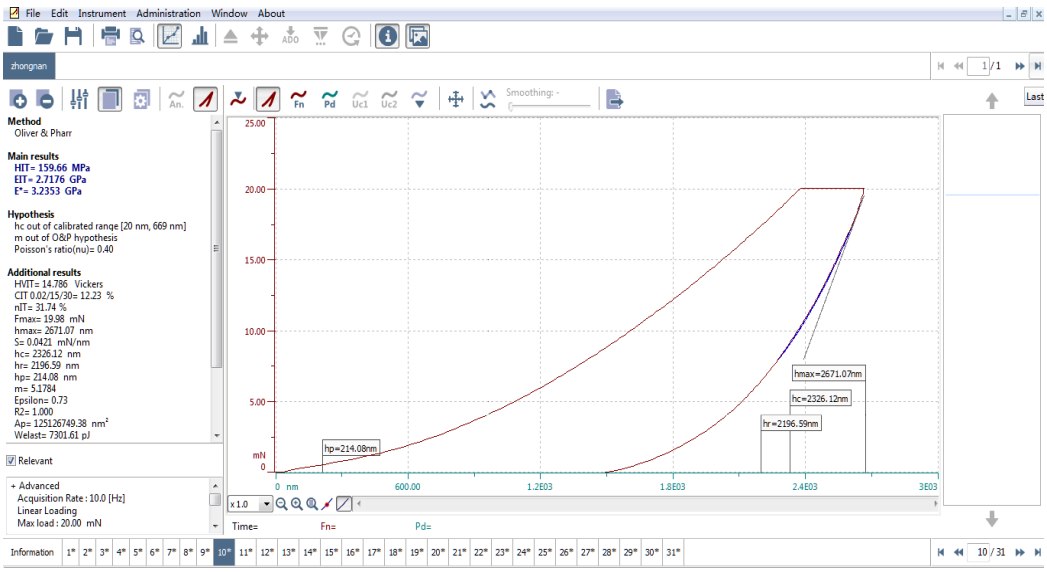

Figure 6.3 Loading & unloading curves of an R11 MSL sample with the load of 20 mN

For hard materials or softer coatings, their effective elastic modulus, hardness and the depth of indentation can easily be determined from loading and unloading curves measured by using a nanoindentation tester. In this section, the mechanical

properties of three types of specimens were examined with the applied loads ranging from 1 mN to 60 mN. Figure 6.3 shows a typical example of the loading and unloading curves for an MSL polymeric specimen measured with the load of 20 mN.

For each test specimen, selected loads between 1 mN and 60 mN were applied at least five times during the measurement. The Poisson's ratios of all these materials were set in the instrument software according to frequently used values quoted in other literature (Anonymous, 1988; Livermore, 2004; Rae, 2005). The mean value of experimental data including the elastic modulus, hardness, indentation depth and contact area were calculated to obtain reliable data and are shown from Table 6.2 to Table 6.4.

Table 6.2 Mean value of nano-indentation test data of a silicon wafer with SiO_2 coating

Load W (mN)	Elastic modulus E (GPa)	Hardness H (MPa)	Depth of indentation h_{max} (nm)	Contact area A (nm^2)	Poisson ratio υ
1.00	95.33	10530	80.47	95058	0.17
3.01	113.61	12052	137.20	249751	0.17
5.01	124.68	12071	176.67	415122	0.17
8.00	133.64	13430	216.95	595742	0.17
15.06	135.07	13324	295.44	1129829	0.17
18.05	137.10	13360	323.05	1351016	0.28
25.05	141.25	13416	381.07	1867026	0.28
35.04	142.40	13415	453.91	2611778	0.28
45.04	144.28	13857	513.06	3249808	0.28
60.02	144.49	14070	593.31	4265487	0.28

Table 6.3 Mean value of nano-indentation test data of a PTFE specimen

Load W (mN)	Elastic modulus E (GPa)	Hardness H (MPa)	Depth of indentation h_{max} (nm)	Contact area A (nm^2)	Poisson ratio υ
5.11	1.1139	50.58	2324.61	101444702	0.46
10.08	1.1434	49.16	3261.84	205184180	0.46
19.56	1.1496	64.48	4070.60	305026007	0.46
30.10	1.2105	71.37	4814.84	423406833	0.46
39.87	1.2911	80.02	5185.58	480676970	0.46
50.04	1.3624	92.567	5537.34	540528430	0.46
59.93	1.4485	105.50	5732.53	568189110	0.46

Table 6.4 Mean value of nano-indentation test data of an MSL polymeric specimen

Load W (mN)	Elastic modulus E (GPa)	Hardness H (MPa)	Depth of indentation h_{max} (nm)	Contact area A (nm^2)	Poisson ratio υ
5.01	2.7459	177.37	1337.87	28682816	0.36
10.02	2.9138	173.59	1845.58	57552846	0.36
19.99	2.7736	162.05	2671.94	124207110	0.36
25.00	2.3666	165.21	3024.50	151988354	0.36
39.96	2.8222	160.76	3737.69	248450884	0.36
49.97	2.8161	166.90	4118.85	299502301	0.36
60.37	2.8758	170.17	4475.29	354692018	0.36

Figure 6.4, Figure 6.5 and Figure 6.6 show the relationship between indentation depth and elastic modulus of the test specimens, respectively. The variations of indentation depth and elastic modulus and the ranges of the hardness in Tables 6.2 to 6.4 show similar tendencies to those in results from other literature (Anonymous, 1988; Bhushan, 1999d; Cabibbo, 2013; Rae, 2005; Xu, 2011; Achanta, 2009). The change of the measured elastic modulus for the silicon wafer with silicon dioxide coating shows an upward tendency with the loads and then stabilises at around 140 GPa for indentation depths of more than about 250 nm.

The consistent rise in elastic modulus during the early steps in load and indentation depth arise from the increasing influence on the stress field of the stiffer substrate material. Once the tip of the indenter penetrates through most of the oxide layer, the modulus settles to a value typical of silicon. Projecting the curve backwards to intercept the axis predicts a modulus of around 70 GPa, very typical of silicon dioxide and glass, as the load and depth tend to zero (red line). The PTFE specimen has a slight rise with loads in its elastic modulus. This trend is consistent and large enough to suggest that the very surface layer have a slightly different structure to the bulk materials, perhaps being of rather lower density. This is plausible given, for example, that it is well-known that sliding motion at a PTFE surface can induce a rather fibrous type of morphology. In contrast, the MSL resin sample appears to have constant properties: elastic modulus shows no trend against load and indentation depth, holding at about 2.8 GPa throughout the range of testing.

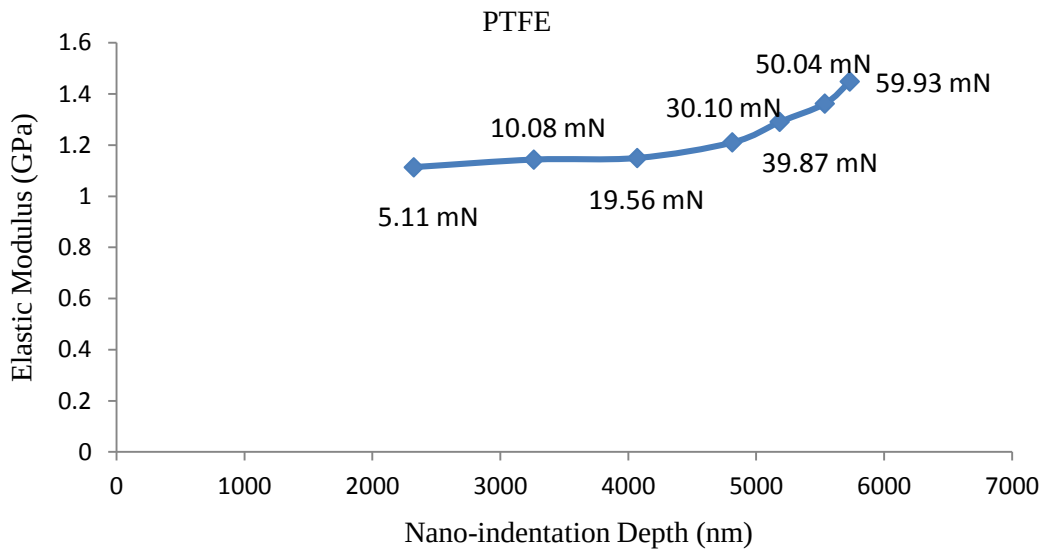

Figure 6.4 Relationship between the indentation depth and elastic modulus for PTFE sample

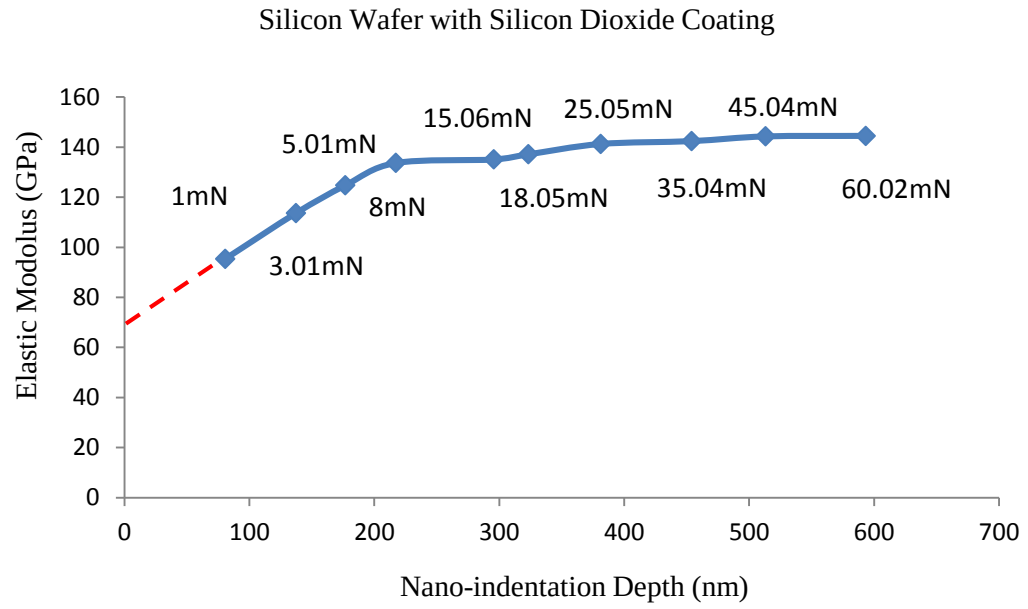

Figure 6.5 Relationship between the indentation depth and elastic modulus for a silicon wafer with silicon dioxide coating specimen

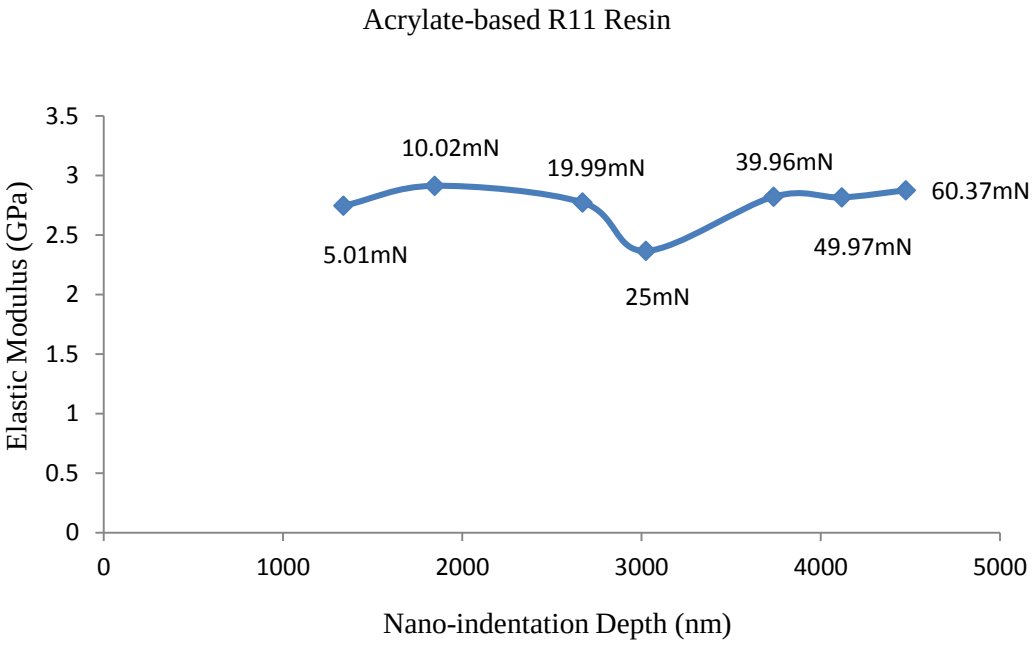

Figure 6.6 Relationship between the indentation depth and elastic modulus for an R11 resin

6.3 Models for Nano-indentation and Friction

6.3.1 Basic Ideas in Friction Modelling

According to the well-known Amonton-Coulomb friction law, the macroscopic friction force is linearly proportional to the applied load W, with

$$F_f = \mu W \tag{6-1}$$

where μ is the macroscopic coefficient of friction and F_f is independent of the macroscopic contact area A_{macro} and also of sliding speed other than a possible static/dynamic variation. This empirical relationship works well at larger areas and normal forces, but it is not universal. It has long been recognised that, for many materials, even in macroscopic tests, the coefficient of friction tends to increase somewhat when normal loads become very small.

In recent decades, many experiments and simulations have focused on sufficiently small sizes of contacts and corresponding small forces to investigate the friction mechanism between surfaces where Amonton's law does not apply simply. The nature of micro-scale contact lies at the heart of the study of the micro-tribology. When sample surfaces in contact are analysed, asperities can be considered as sections of elastic spheres and the contact between two sample surfaces can be seen as multi-asperity contact of a series of spheres with various heights and radii (Adams, 2003). Several factors, such as the loading range, tip radius, and materials properties will affect the real, local contact area and contact pressure. Under macroscopic conditions, there are likely to be sufficient asperity contacts to provide good statistical modelling. This situation will not, however, be

true if the nominal area or the normal force is so small that only the most extreme asperities are pushed into contact.

Based on the adhesion theory of friction proposed by Bowden and Tabor (1964), friction force F_f is given by

$$F_f = F_{shear} + F_{plough} \tag{6-2}$$

Where F_{shear} is the lateral force required to overcome the shear strength of the interface layer assumed to be "welding" the surface together wherever there is real contact; and F_{plough} is the force required to push material aside so as to maintain a constant depth of indentation of one part into the other (the ploughing effect). Both these terms relate to a failure stress in the softer material at the interface and to a projected area of contact (Ando, 2003).

Commonly, the projected area associated with shear stresses at a contact will be considerably larger than the projected area associated with the direct stresses from the ploughing effect. For a soft metal surface or extremely well lubricated surfaces, shearing force F_{shear} may become so small that the ploughing force F_{plough} is of comparable magnitude (Bisson, 1968). We assume that F_{plough} is generally small enough compared with F_{shear} to be neglected for unlubricated surfaces. When the ploughing force is negligible, F_f becomes just F_{shear}.

6.3.2 Analysis of Indentation by a Modified Berkovich Tip

Nowadays, indentation techniques are frequently used to evaluate the mechanical properties of materials including the Young's modulus (elastic modulus) and

hardness by measuring load-depth data from the Oliver and Pharr method (Oliver and Pharr, 1992). The Berkovich indentation test is the most widely used procedure in nanoindentation tests and this thesis a modified diamond Berkovich tip was used to investigate the plastic contact for three different specimens including a silicon wafer with SiO_2 coating, PTFE, and acrylic MSL polymeric material.

The indentation deformation at the maximum load and after unloading is shown in Figure 6.7(a). The curves of loading and unloading with a cycle of indentation, which are identified as a and b in Figure 6.7(b), are defined as the load F is applied and removed. At the peak load F_{max}, the maximum indentation depth h equals the sum of contact depth of the indenter with the sample h_c, and the elastic surface displacement at the perimeter of contact, h_s,

$$h = h_c + h_s \tag{6-3}$$

$$h_s = \frac{\varepsilon \cdot F_{max}}{S} \tag{6-4}$$

where ε is a geometric constant dependent on the indenter shape (Takakuwa, 2013). For the Berkovich tip,

$$\varepsilon = 2(\pi - 2)/\pi = 0.7268 \tag{6-5}$$

h_c is calculated according to the following equation,

$$h_c = h_{max} - \varepsilon \cdot (h_{max} - h_r) \tag{6-6}$$

where h_r is the tangent indentation depth and calculated from

$$h_r = h_{max} - \frac{F_{max}}{S} \tag{6-7}$$

The test force F and indenter displacement obey power-law relations, given as

$$F = F_{max}\left(\frac{h - h_p}{h_{max} - h_p}\right)^m \tag{6-8}$$

where the symbols are defined on Figure 6.7(b). The short dashed line *c* is tangent to the unloading curve *b* at maximum test force F_{max} and defines the contact stiffness *S*, which is given by

$$S = \frac{m \cdot F_{max}}{(h_{max} - h_p)} \tag{6-9}$$

where h_p (the permanent indentation depth) and h_{max} are experimentally derived parameters (see Figure 6.7) and *m* is a constant factor dependent on the geometry of the indenter shape. For the Berkovich tip, *m* is taken as 2.0 (Antunes, 2006).

In this technique, the Young's modulus of the specimen E_{IT} is related to plane strain modulus E^* and sample Poisson's ratio v_s,

$$E_{IT} = E^* \cdot (1 - v_s^2) \tag{6-10}$$

E^* is calculated from

$$E^* = \left(\frac{1}{E_r} - \frac{1 - v_i^2}{E_i}\right)^{-1} \tag{6-11}$$

with the given elastic modulus E_i (1141 GPa) and Poisson's ratio v_i (0.07) of the diamond indenter and the reduced modulus E_r is calculated as

$$E_r = \frac{\sqrt{\pi} \cdot S}{2 \cdot \beta \cdot \sqrt{A_p(h_c)}} \tag{6-12}$$

where β is the geometric factor which is dependent of the shape of the indenter tip and for the Berkovich tip, $\beta = 1.034$ (Joslin, 1990). A_p is the projected contact area of the indent at the peak load.

The hardness is a measure of the resistance to permanent deformation or damage, which is commonly defined as a stress determined from the peak load F_{max} and the area of indent A_p.

$$H_{IT} = \frac{F_{max}}{A_p} \tag{6-13}$$

F_{max} should be large enough to produce a good qualify indentation on the sample for a valid hardness test.

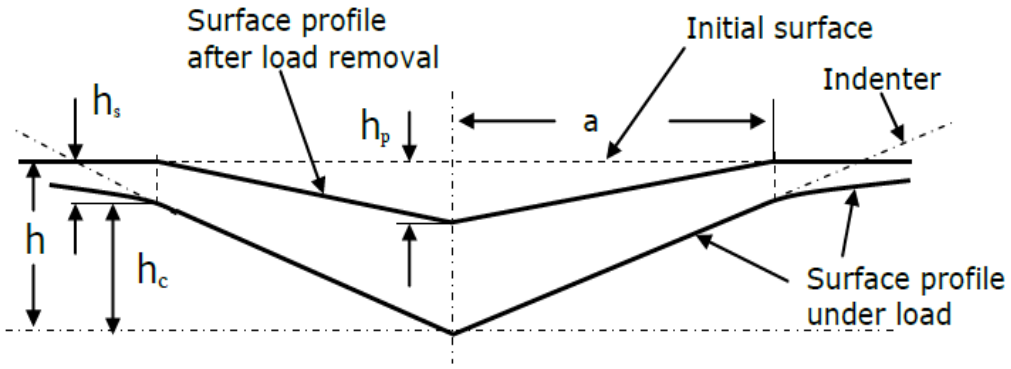

(a) Schematic representation of indenter – sample contact

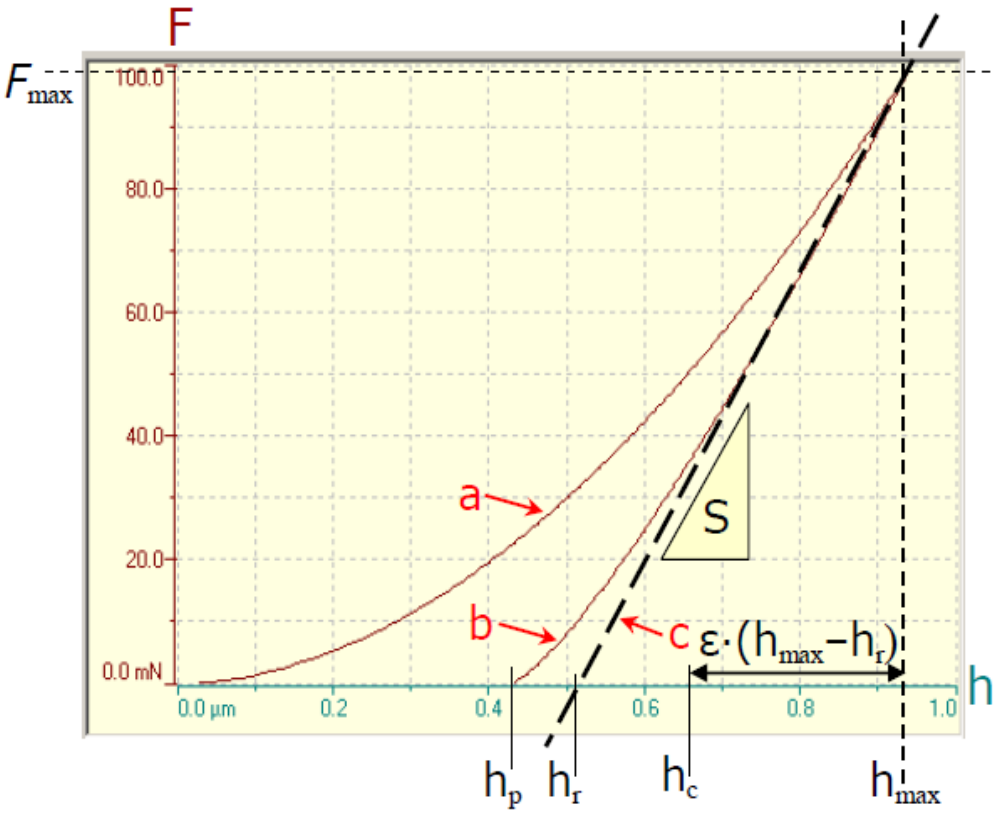

(b) Typical indentation curve

Figure 6.7 Schematic of Berkovich indentation test (Oliver and Pharr, 1992; Bao, 2004)

For the projected contact area A_p, if the indentation depth $h_c < 6\mu m$, the determination of the exact area function for the given indenter is required, given as (Sakharova, 2009)

$$A_p = \ 24.675h_c^2 + 0.562h_c + 0.003216 \tag{6-14}$$

However, for an indentation depth $h_c > 6\ \mu m$, a first approximation to the projected area may be used for a Berkovich indenter,

$$A_p = 24.494\ \ h_c^2 \tag{6-15}$$

When the pressure is high enough to produce plastic flow, the contacting regions deform plastically until the true area of contact is just large enough to support the load (Oliver and Pharr, 1992). Based on equation (6-2), the friction force of a diamond tip sliding on a flat is calculated as (Mo, 2009)

$$F_f = F_{shear} = \tau \cdot A_p \tag{6-16}$$

where τ is the shear strength of the material at the interface surface.

Combining equations (6-16), (6-13) and (6-1), the friction force and friction coefficient are given as, for this specific and rather specialised configuration,

$$F_f = \tau \cdot A_p = \tau \cdot \frac{F_{max}}{H_{IT}} \tag{6-17}$$

$$\mu = \frac{F_f}{W} = \frac{\tau \cdot A_p}{W} = \frac{\tau \cdot F_{max}}{H_{IT} \cdot W} = \frac{\tau}{H_{IT}} \tag{6-18}$$

where F_{max} is considered to be equal to the normal load W.

6.3.3 Hertzian Contact Theory and Friction for a Ball-on-flat Configuration

According to Hertzian contact theory (Mo, 2009), when an elastic sphere with the radius R and an elastic flat are in contact, the nominal contact area, as shown in Figure 6.8, will be a circle of radius a at an approach depth δ, which can then be calculated as

$$a = \sqrt{R\delta} = (\frac{3}{4}\frac{WR}{E_e})^{1/3} \tag{6-19}$$

where W is the applied load and E_e is the effective elastic modulus given by

$$\frac{1}{E_e} = \frac{1-v_{ball}^2}{E_{ball}} + \frac{1-v_{flat}^2}{E_{flat}} \tag{6-20}$$

with E_{ball} and v_{ball}, E_{flat} and v_{flat} being the elastic modulus and Poisson's ratios for the two bodies (Zhou, 2011; Johnson, 1997).

The approach, δ, between points distant from the contact in the two bodies depends on the maximum contact pressure, and so the load. In practice, we assume that the indentation depth shown as h in Figure 6.8 is the same as δ, with

$$\delta = \frac{a^2}{R} = (\frac{9W^2}{16E_e^2R})^{1/3} \tag{6-21}$$

The related contact stiffness is

$$\lambda_s = \frac{dW}{d\delta} = (6E_e^2WR)^{\frac{1}{3}} \tag{6-22}$$

The Hertz contact pressure distribution in the contact area is a function of distance from the centre of the circle given by

$$P(r) = P_0(1 - \left(\frac{r}{a}\right)^2)^{\frac{1}{2}} \tag{6-23}$$

Therefore, at $r = 0$, the maximum contact pressure P_0 can be derived as

$$P_0 = \frac{3W}{2\pi a^2} = (\frac{6WE_e^2}{\pi^3R^2})^{\frac{1}{3}} = (\frac{2E_e}{\pi}) \cdot (\frac{\delta}{R})^{\frac{1}{2}} \tag{6-24}$$

Note that in all representative situations $\delta \ll a$, so in Figure 6.8 $A_c \approx a\delta$ is much smaller than $A_r = \pi a^2$, so justifying that ploughing effects can be neglected here. When two bodies are sliding over each other, for each individual single-asperity elastic contact, the real contact area is not linear with the applied load. Therefore, Amonton's law is not precisely applicable for expressing the friction force. The real sliding friction force F can be expressed as (Qing, 2007; Bhushan, 1999; Wen, 1990)

$$F_f = F_{shear} = \tau \cdot A_r = \tau \cdot \pi a^2 = \tau \cdot \pi \cdot (\frac{3WR}{4E_e})^{\frac{2}{3}} \tag{6-25}$$

where τ is the shearing strength of the softer material. According to Bowden's adhesion theory of friction, the coefficient of friction μ is related to the contact pressure by (Qing, 2007; Bhushan, 1999; Wen, 1990)

$$\mu = \frac{F_f}{W} = \frac{\tau A}{W} = \frac{\tau \pi a^2}{W} = \frac{3\tau}{2P_0} \tag{6-26}$$

Combining equation (6-24) with equation (6-26) gives the friction coefficient as

$$\mu = \frac{3\pi\tau}{2}(\frac{R^2}{6WE_e^2})^{1/3} = \frac{3}{4} \cdot \frac{\tau\pi}{E_e} \cdot (\frac{\delta}{R})^{1/3} \tag{6-27}$$

However, while the whole equation (6-27) can be used to describe the tendency between friction coefficient and load, it does not necessarily determine the exact relationship between them. This is because τ and E_e are important parameters for the calculations of CoF but it is difficult to obtain exact values for them under representative experimental conditions. Furthermore, even at small scales, the real contact is unlikely to be modelled precisely as one (or even a set of identical) spherical asperity on a flat.

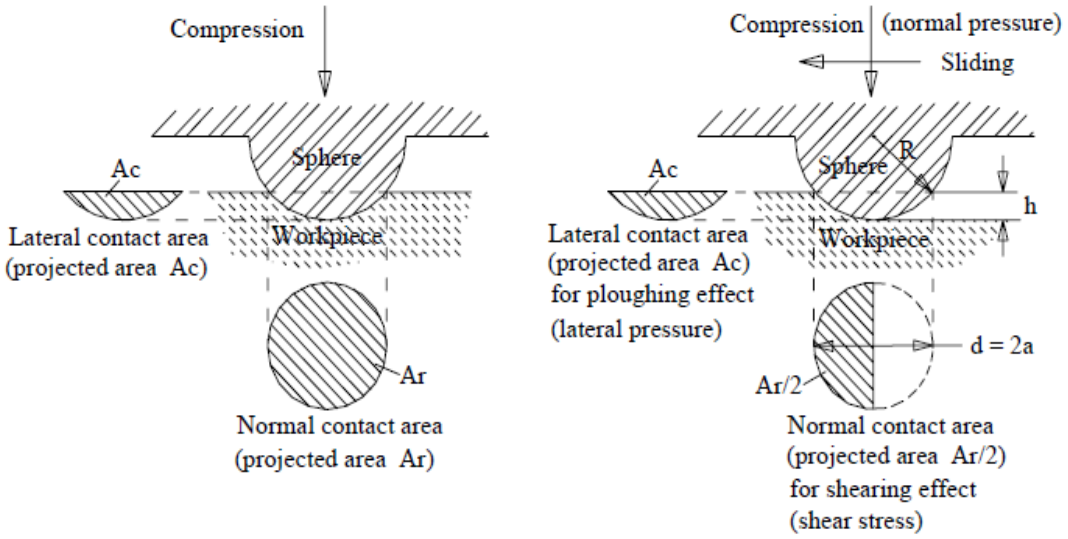

Figure 6.8 Schematic of Hertzian elastic contact model (Leu, 2011)

6.4 Prediction of Friction from Nano-indentation Data

To make a direct comparison between the theoretical analysis for a ball-on-flat configuration just discussed and experimental measurements with the friction test-rig, there is need first to establish correlations between Berkovich nano-indentation measurements and Hertzian contact model parameters because of the different tips used in two measurement methods. Table 6.5 gives the mechanical properties of materials, taken from published results (Qing, 2007; Tambe, 2004; Ando, 2003; Rae, 2005), such as elastic modulus, shear strength, and Poisson's ratio, that are used here to calculate the effective elastic modulus for test specimens in the ball-on-flat configuration. However, the shear strength of the acrylic resin is not directly available in the literature and thus a value has been estimated from the published tensile strength (Xu, 2011; Leigh, 2011).

Table 6.5 Summary of elastic modulus, shear strength and Poisson's ratio comparative to published results (Qing, 2007; Tambe, 2004; Ando, 2003; Rae, 2005; Leigh, 2011; Xu, 2011)

Specimen	Elastic modulus E (GPa)	Tensile strength σ (MPa)	Shear strength τ (MPa)	Poisson ratio υ
AISI 440C stainless steel ball	210			0.27 ~ 0.30
SiO_2 coating	70	100	50	0.17
Silicon wafer	130		64.1	0.22 ~ 0.28
PTFE			5	0.46 ~ 0.50
Acrylic R11 resin	3.1314	50 ~ 70	25 ~ 35	0.36

Several challenges, which require empirically-derived assumptions, arise when attempting to use nano-indentation results to infer friction in a ball-on-flat configuration. Relevant properties vary with, say, indentation depth for both a Berkovich and a spherical tip, but they do so in different ways. It is, then, not at all obvious what depth of Berkovich indent best reports the elastic modulus suited to a Hertz model having a specified depth, and so on. There are five parameters, plus the applied load, in these models but they are not independent: given any two, the rest are determined from the theory given in Section 6.3. One plausible approach is to assume, arbitrarily, that two parameters will take the same values in both the Berkovich and Hertz models and then to calculate estimates of the other from the indentation data. Since is unclear which pairs might reasonably be taken as equal, this study explores three options of commonality between the more feasible pairs: the same elastic modulus paired with each of the same contact area, the same load and the same indentation depth.

By these assumptions various equations in Section 6.3 can be used to transform the directly measured nano-indentation data into sets of parameters that can be used in the Hertzian model to predict friction force and coefficient. So, for example, assuming the same elastic modulus and indentation depth allows a Hertzian calculation of remain parameters such as contact radius and contact pressure from which an equivalent load for the Hertzian case can be derived and leading to estimates of the friction properties. Tables 6.6 to 6.8 list the transformed parameters sets for the Hertz model for all three assumed common pairs of parameters and for each sample material, taking data from Tables 6.2 to 6.4. Especially, the data displayed in red and black show the input values from nano-indentation tests and the calculated results for the prediction of Hertzian model of friction respectively. Note that the tables report the effective (or reduced) modulus needed for the Hertzian calculation, not the elastic modulus.

The transformed data for the test specimens shows a wide range of loads that go well beyond the working ranges of the test-rig calibrated in Chapter 3, under the assumption of the same elastic modulus and depth of indentation. There are always smaller values for applied forces predicted with the assumption of the same contact area. The modelling results in the previous section are used with the transformed parameters to obtain the friction force and the coefficient of friction for varying applied normal loads for the silicon wafer with SiO_2 coating, PTFE and MSL polymeric test specimens. As the silicon wafer has a layer of silicon dioxide with the thickness of 300 nm, the depths of indentation need to be considered for elastic

modulus calculation. From Table 6.2, the average depth of indentation with the load of 15 mN was approximately 295 nm and it increased to 323 nm when a load of 18 mN was applied. Therefore, the elastic modulus of the silicon dioxide coating should be used for the calculation of friction force and friction coefficient when the load is applied between 1 mN and 15 mN.

Table 6.6 Modelling results of a PTFE specimen from nano-indentation tests to be applied for Hertzian model of friction (red entries show input values)

	Load W (mN)	Elastic modulus E^* (GPa)	Contact radius a (nm)	Depth of indentation δ (nm)	Contact area A (nm^2)	Contact pressure p (GPa)
Same elastic modulus and contact area	0.6992	1.4043	5782.50	64.58	101444702	0.0103
	2.0285	1.4412	8081.58	130.62	205184180	0.0148
	3.6968	1.4490	9853.56	194.19	305026007	0.0182
	6.3637	1.5252	11609.23	269.55	423406833	0.0225
	7.5672	1.6261	11405.51	306.01	480676970	0.0236
	10.3225	1.7152	13116.98	344.11	540528430	0.0286
	11.8228	1.8228	13448.41	361.72	568189110	0.0312
Same elastic modulus and applied load	5.11	1.4043	11091.68	246.05	386496487	0.0198
	10.08	1.4412	13790.79	380.37	597487988	0.0253
	19.56	1.4490	17170.27	589.63	926200769	0.0317
	30.10	1.5252	19487.54	759.52	1193067258	0.0378
	39.87	1.6261	20949.65	877.78	1378810023	0.0434
	50.04	1.7152	22199.57	985.64	1548246165	0.0485
	59.93	1.8228	23101.78	1067.38	1676647538	0.0536
Same elastic modulus and depth of indentation	148.39	1.4043	34092.59	2324.61	3651496423	0.0610
	253.13	1.4412	40384.65	3261.84	5123698133	0.0741
	354.80	1.4490	45114.30	4070.60	6394098683	0.0832
	480.42	1.5252	49065.47	4814.84	7563151760	0.0953
	572.49	1.6261	50919.45	5185.58	8145510284	0.1054
	666.33	1.7152	52618.15	5537.34	8698052759	0.1149
	745.90	1.8228	53537.51	5732.53	9004658052	0.1243

Table 6.7 Modelling results of a Si/SiO_2 specimen from nano-indentation tests to be applied for Hertzian model of friction (red entries show input values)

	Load W (mN)	Elastic modulus E^* (GPa)	Contact radius a (nm)	Depth of indentation δ (nm)	Contact area A (nm^2)	Contact pressure p (GPa)
Same elastic modulus and contact area	0.0010	68.87	173.95	0.0605	95058	0.0153
	0.0046	77.63	281.95	0.1590	249751	0.0279
	0.0106	82.49	363.51	0.2643	415122	0.0382
	0.0190	86.21	435.47	0.3793	595742	0.0478
	0.0499	86.78	599.70	0.7193	1129829	0.0663
	0.0680	90.45	655.77	0.8601	1351016	0.0755
	0.1125	92.10	770.90	1.1886	1867026	0.0904
	0.1871	92.55	911.79	1.6627	2611778	0.1075
	0.2617	93.28	1017.08	2.0689	3249808	0.1208
	0.3939	93.36	1165.22	2.7155	4265487	0.1385
Same elastic modulus and applied load	1	68.87	1759.28	6.19	9723382	0.1543
	3.01	77.63	2440.75	11.91	18715237	0.2412
	5.01	82.49	2834.58	16.07	25242265	0.2977
	8.00	86.21	3264.78	21.32	33485666	0.3584
	15.06	86.78	4022.34	32.36	50828536	0.4444
	18.05	90.45	4214.98	35.53	55813843	0.4851
	25.05	92.10	4672.25	43.66	68580877	0.5479
	35.04	92.55	5216.83	54.43	85499634	0.6147
	45.04	93.28	5669.54	64.29	100982597	0.6690
	60.02	93.36	6223.80	77.47	121692033	0.7398
Same elastic modulus and depth of indentation	46.87	68.87	6343.11	80.47	126401980	0.5562
	117.62	77.63	8282.51	137.20	215513256	0.8187
	182.63	82.49	9398.67	176.67	277512587	0.9871
	259.73	86.21	10415.13	216.95	340784263	1.1432
	415.48	86.78	12154.01	295.44	464076067	1.3429
	495.15	90.45	12709.25	323.05	507445753	1.4637
	645.94	92.10	13803.44	381.07	598583356	1.6187
	843.83	92.55	15065.03	453.91	713000161	1.7752
	1022.03	93.28	16016.55	513.06	805912763	1.9023
	1272.06	93.36	17223.68	593.31	931969169	2.0474

Table 6.8 Modelling results of an acrylic-based R11 resin specimen from nano-indentation tests to be applied for Hertzian model of friction (red entries show input values)

	Load W (mN)	Elastic modulus E^* (GPa)	Contact radius a (nm)	Depth of indentation δ (nm)	Contact area A (nm^2)	Contact pressure p (GPa)
Same elastic modulus and contact area	0.23	3.1122	3021.59	18.26	28682816	0.0120
	0.69	3.2998	4280.14	36.64	57552846	0.0180
	2.08	3.1432	6287.79	79.07	124207110	0.0252
	3.95	3.0488	7863.32	123.66	194250723	0.0305
	6.00	3.1975	8892.93	158.17	248450884	0.0362
	7.92	3.1907	9763.93	190.67	299502301	0.0397
	10.42	3.2574	10625.52	225.80	354692018	0.0441
Same elastic modulus and applied load	5.09	3.1122	18110.85	656.01	1030451538	0.0074
	9.99	3.2998	23122.15	1069.27	1679600991	0.0089
	20.13	3.1432	28735.30	1651.43	2594067335	0.0116
	30.03	3.0488	32501.63	2112.71	3318640660	0.0136
	39.94	3.1975	36314.77	2637.52	4143014567	0.0145
	49.99	3.1907	39108.11	3058.89	4804890084	0.0156
	60.36	3.2574	41932.48	3516.67	5523965192	0.0164
Same elastic modulus and depth of indentation	143.59	3.1122	25863.78	1337.87	2101521282	0.1025
	246.67	3.2998	30377.46	1845.58	2899030285	0.1276
	409.29	3.1432	36550.92	2671.94	4197073537	0.1463
	549.13	3.0488	40724.81	3317.02	5210362832	0.1581
	688.87	3.1975	43230.14	3737.69	5871149723	0.1760
	795.20	3.1907	45380.89	4118.85	6469874451	0.1844
	919.45	3.2574	47303.75	4475.29	7029769093	0.1962

Figures 6.9 to 6.12 show the predicted friction force and the coefficient of friction against applied normal loads for the silicon wafer with silicon dioxide coating. The plots cover predictions from the Hertz model, equations (6-25) and (6-27), under all three trial assumptions and, for completeness, also show the direct Berkovich tip calculation from equations (6-17) and (6-18). Figure 6.9 shows an upwards tendency of friction force with normal loads across a broad scope for

Hertzian contact model; a clearer indication of friction force at smaller loads is given in Figure 6.10. The friction force shows an upwards tendency from 0.16 mN to 60 mN with normal loads applied from 0.18 mN to 1275 mN based on the different modelling assumptions, especially revealing a good consistency for two different assumptions including the same load and the same depth when the normal loads are applied between 45 mN to 60 mN. However, there is an almost no variation of friction force from the Berkovich tests over loads from 1 mN to 60 mN.

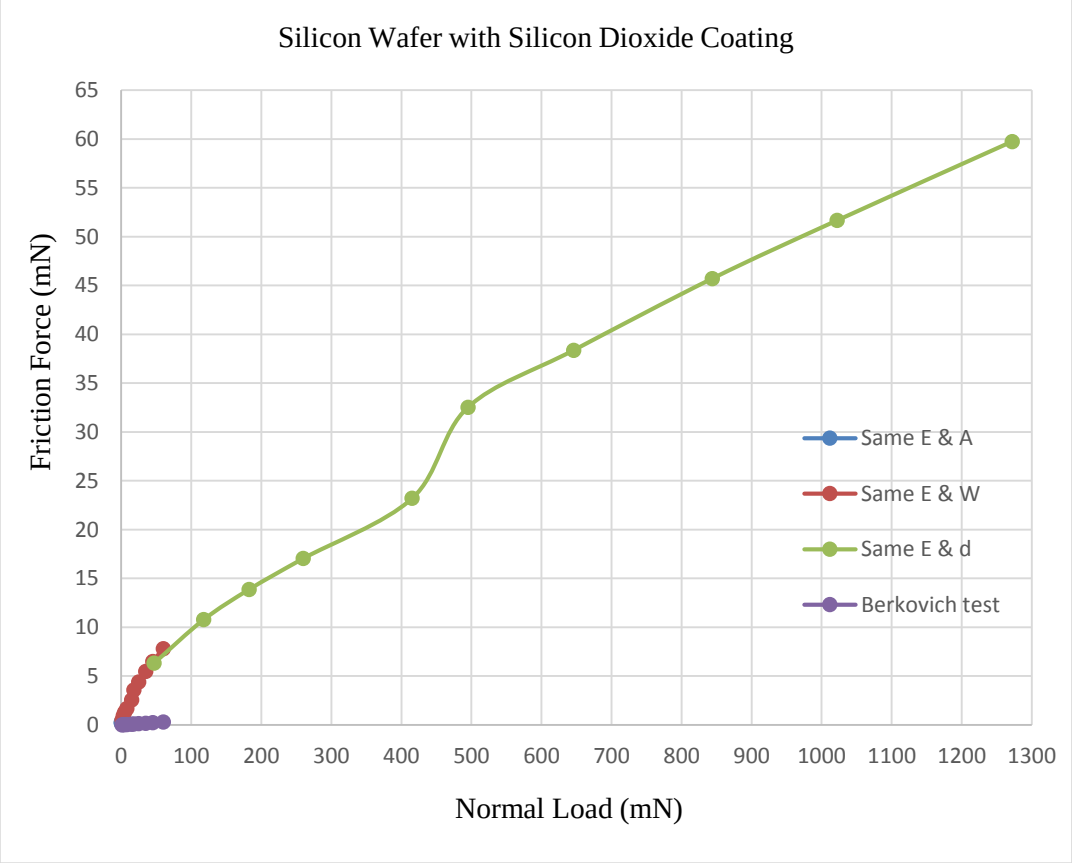

Figure 6.9 Predicted friction force against normal loads for the silicon wafer with silicon dioxide coating from both the Berkovich tests and the Hertzian contact model for the ball-on-flat configuration

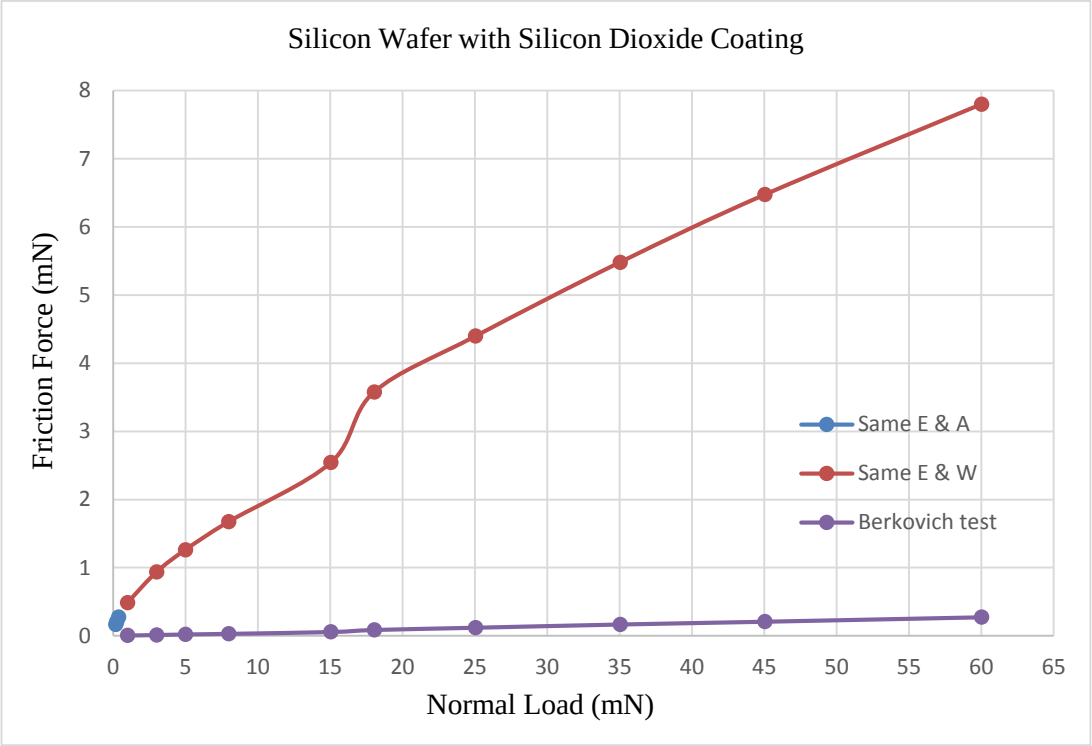

Figure 6.10 A clearer indication of friction force at smaller loads for just same E & A, same E & W and Berkovich test

There is a strong decreasing trend of friction coefficient with loads in the model of ball-on-flat configuration, as shown in Figure 6.11; a clearer indication of friction coefficient at smaller loads is given in Figure 6.12. At very low loads (below 1 mN), CoF reaches as high as 0.9 and then drops rapidly to nearly 0.1 when the loads are applied from 1 mN to 60 mN. Finally, it will gradually reduce to less than 0.1 with the increase of loads and remains stable at around 0.05 when the applied force is above 1 N. Especially, the CoF illustrates a similar variation tendency and good consistency for two different assumptions including the same load and the same depth when the normal loads are applied between 45 mN to 60 mN. However, in the

direct Berkovich tests with the loads applied from 1 mN to 60 mN the friction coefficient always stays at around 0.005. Note that the different empirical assumptions segregate into different load regimes. All three sections for the Hertz model of friction coefficient could plausible be parts of the same curve, despite the different expectations based on the literature (Hild, 2007; Stempfle and Takadoum, 2012), but values seem too low at high loads and too high at the lowest loads.

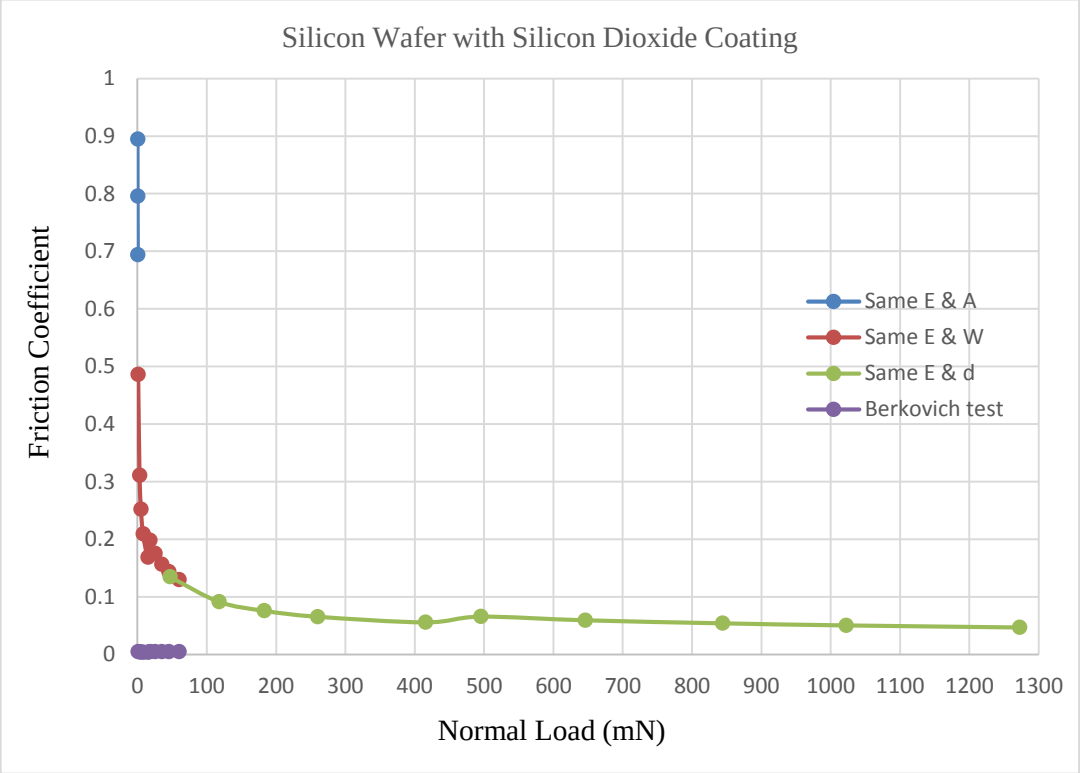

Figure 6.11 Predicted CoF against loads for the silicon wafer with SiO_2 coating from both the Berkovich tests and the Hertzian contact model for the ball-on-flat configuration

Comparing Figure 6.12 to the experimental results shown in Figure 4.17, Figure 4.19 and Figure 4.21, the trends are in agreement for the assumption of the

same load and ball-on-flat configuration of the test-rig with different sliding frequency and track length when the normal load is applied between 10 mN to 50 mN. The results for the CoF in both two situations show a good consistency, remaining stable between 0.15 and 0.2, close to Amonton's law prediction and match well with its known properties as an ideal silicon-based material.

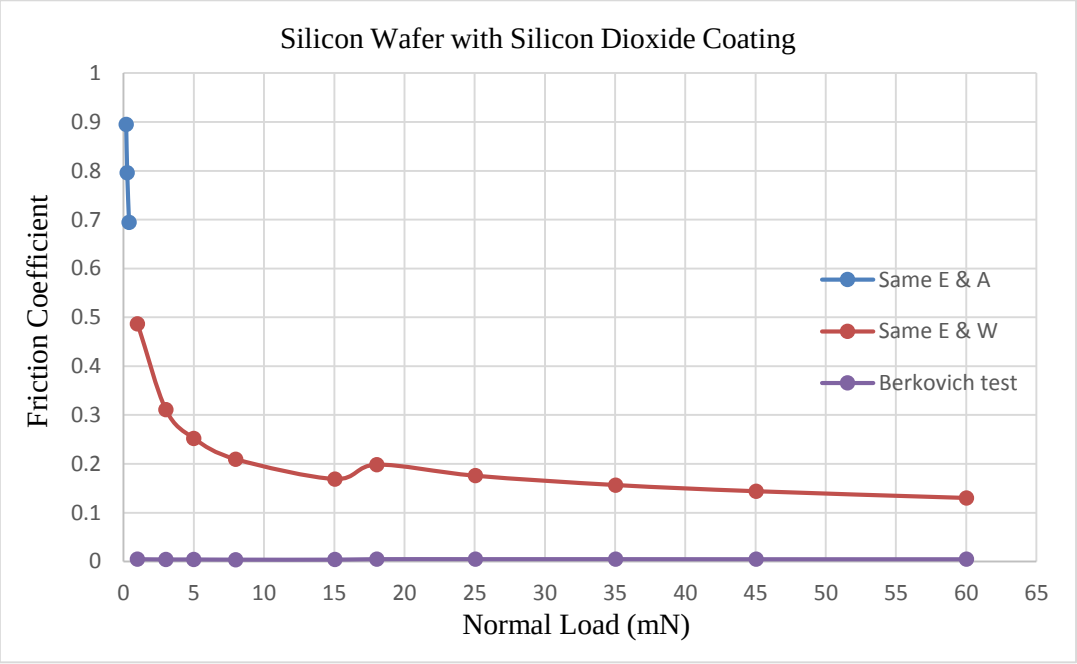

Figure 6.12 A clearer indication of CoF at smaller loads for just same E & A, same E & W and Berkovich test

Figure 6.13 and Figure 6.14 show the predicted friction force and the coefficient of friction against normal loads for PTFE from both the Berkovich tests and the Hertzian contact model for the ball-on-flat configuration. Figure 6.13 shows an upwards tendency of friction force from 0.5 mN to 45 mN with normal loads

applied from 0.6 mN to 750 mN based on the different modelling assumptions. Especially, friction force illustrates a similar variation tendency and good consistency for two different assumptions including the same load and the same contact area when the normal loads are applied between 5 mN to 12 mN. There is also a similar but smaller rising trend for the friction force from direct Berkovich tests when the load is applied from 5 mN to 60 mN.

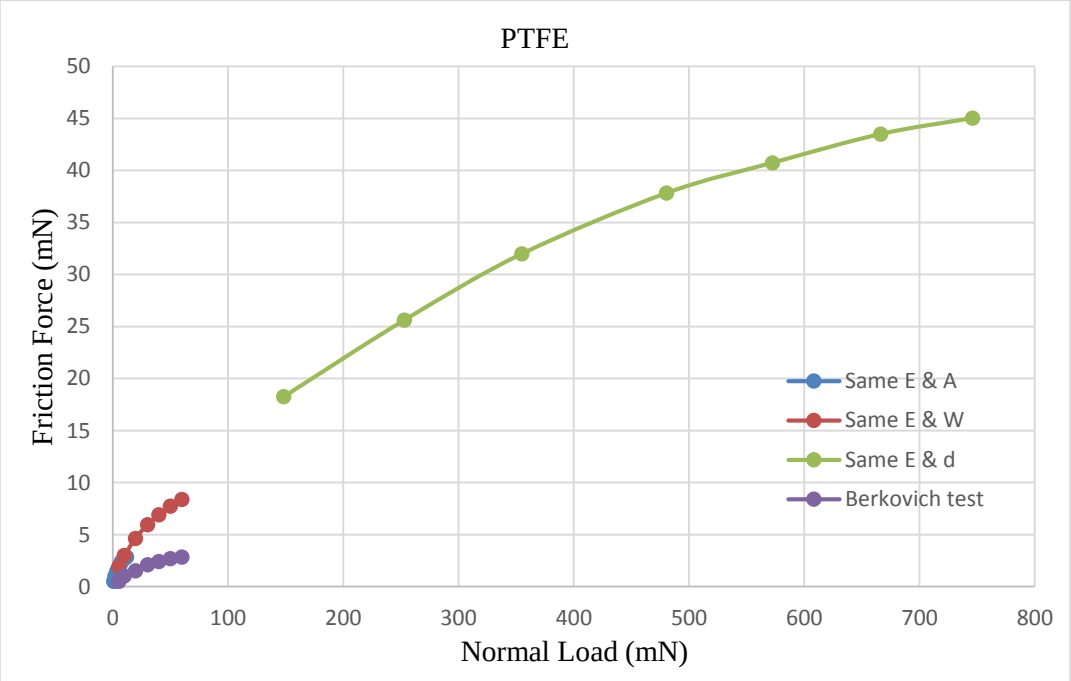

Figure 6.13 Predicted friction force against normal loads for PTFE from both the Berkovich tests and the Hertzian contact model for the ball-on-flat configuration

There is a similar, but relatively smaller, downtrend of friction coefficient with loads in the ball-on-flat configuration for PTFE than was predicted for the silicon wafer, as shown in Figure 6.14. At smaller loads (below 10 mN), CoF falls rapidly

from 0.7 to about 0.25 and then continues to drop when the assumption of the same elastic modulus and loads is applied. Finally, there is a slight decline of CoF and a trend to remain stable at around 0.06 with the forces applied from 150 mN to 750 mN using the same depth assumption. Especially, the CoF illustrates a similar variation tendency and good consistency for two different assumptions including the same load and the same contact area when the normal loads are applied between 5 mN to 12 mN. Friction coefficient in the Berkovich tests also has a declining tendency but with a smaller variation from 0.1 to around 0.05 when the loads are applied from 5 mN to 60 mN.

Comparing Figure 6.14 to the experimental results shown in Figure 5.13 and Figure 5.17, the trends are not in agreement for two situations when the normal load is applied in the same range. The result for CoF at the assumption of the same load shows a decrease tendency from about 0.4 to around 0.14, while it is always remaining in a stable range at around 0.12 for ball-on-flat configuration of the test-rig at the same scan speed of 9 Hz and three different track lengths of 66 μm, 90 μm and 130 μm, as well as the lower ones (below 0.1) in Figure 5.17. However, for the assumptions, Berkovich test and micro-friction test, the CoFs all tend to drop to below 0.1 with normal load or sliding speed, matching well with its known properties and lubrication effect.

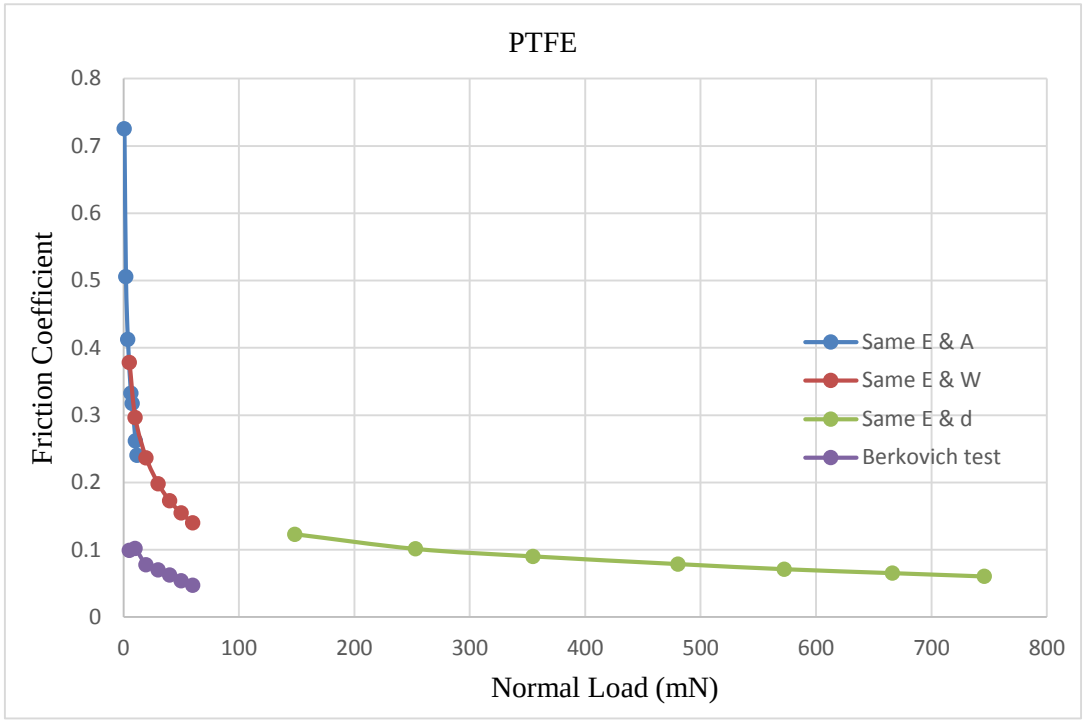

Figure 6.14 Predicted CoF against normal loads for PTFE from both the Berkovich tests and the Hertzian contact model for the ball-on-flat configuration

Figure 6.15 and Figure 6.16 show the predicted friction force and the CoF against load for the acrylic-based R11 resin in both Berkovich nano-indentation measurement and for the Hertz elastic contact model with ball-on-flat configuration. However, the predictions using the assumptions of the same elastic modulus and contact area or the same elastic modulus and applied loads are not within the plotted area. They return values of more than 1, even above 10 for the CoF, which is an order of magnitude error compared to expectations and not compatible with macro-scale tribology theory during sliding motion. Figure 6.15 shows incompatible upwards tendencies of friction force with normal loads for both the direct Berkovich test and the ball-on-flat configuration using the same depth assumption combined

with the range of the shear strength of the MSL polymeric material. Nevertheless, the linearity of friction force against normal load for the direct Berkovich test was still excellent over the working range ($R^2 > 0.99$) when the normal loads are applied between 5 mN to 60 mN, and a little poor but not bad ($R^2 > 0.9$) for the same depth assumption when the normal loads are applied between 100 mN to 950 mN.

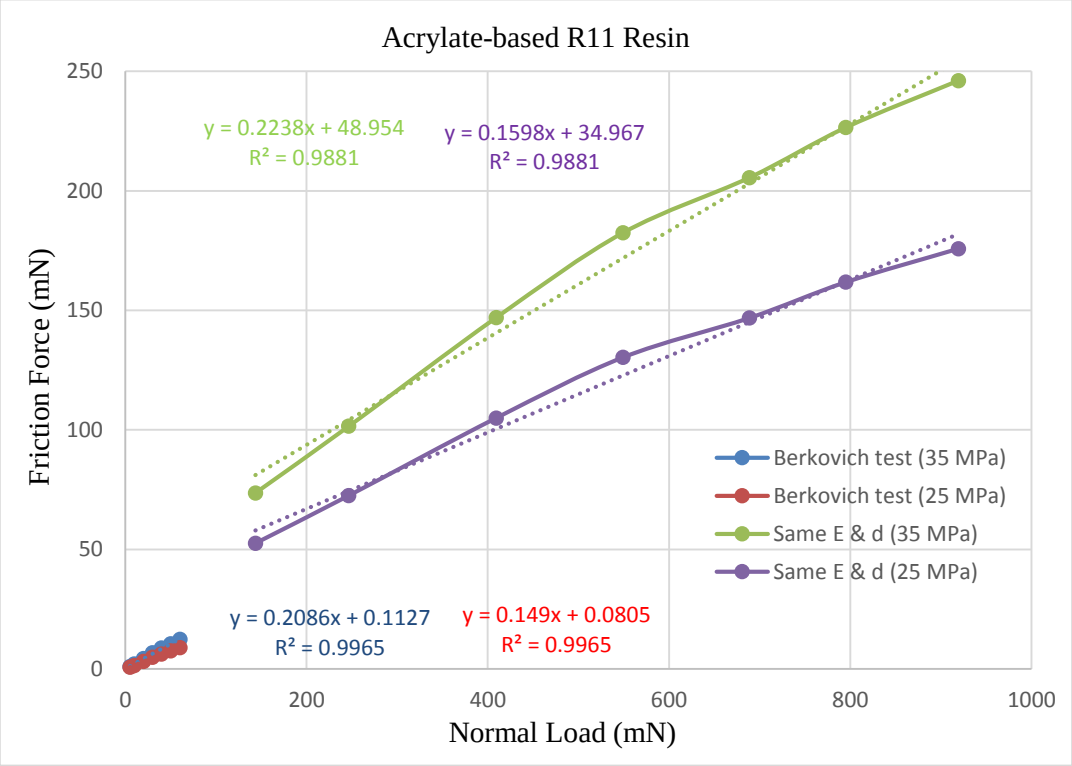

Figure 6.15 Predicted friction force against normal loads for the acrylic-based R11 resin in both Berkovich nano-indentation measurement and for the Hertz elastic contact model with ball-on-flat configuration

Figure 6.16 shows that the predicted CoF in the Berkovich tests has a slight but inconsistent fluctuation around 0.15 or 0.2 with loads of 5 mN – 60 mN. There is a

decreasing trend in CoF, from about 0.5 to around 0.25 or from about 0.35 to around 0.2, for the remaining assumption in the ball-on-flat configuration and that is for applied loads well beyond the working range of our test-rig.

Comparing Figure 6.16 to the experimental results shown in Figure 5.11 and Figure 5.15, the trends are again in agreement for Berkovich tests with different shear strength (35 MPa or 25 MPa) and ball-on-flat configuration of the test-rig at the same scan speed of 9 Hz and two different scan lengths of 66 µm and 130 µm when the normal load is applied between 10 mN to 50 mN. The results for the CoF in both two situations show a good consistency, remaining stable around 0.15 or 0.2, associated to Amonton's law prediction.

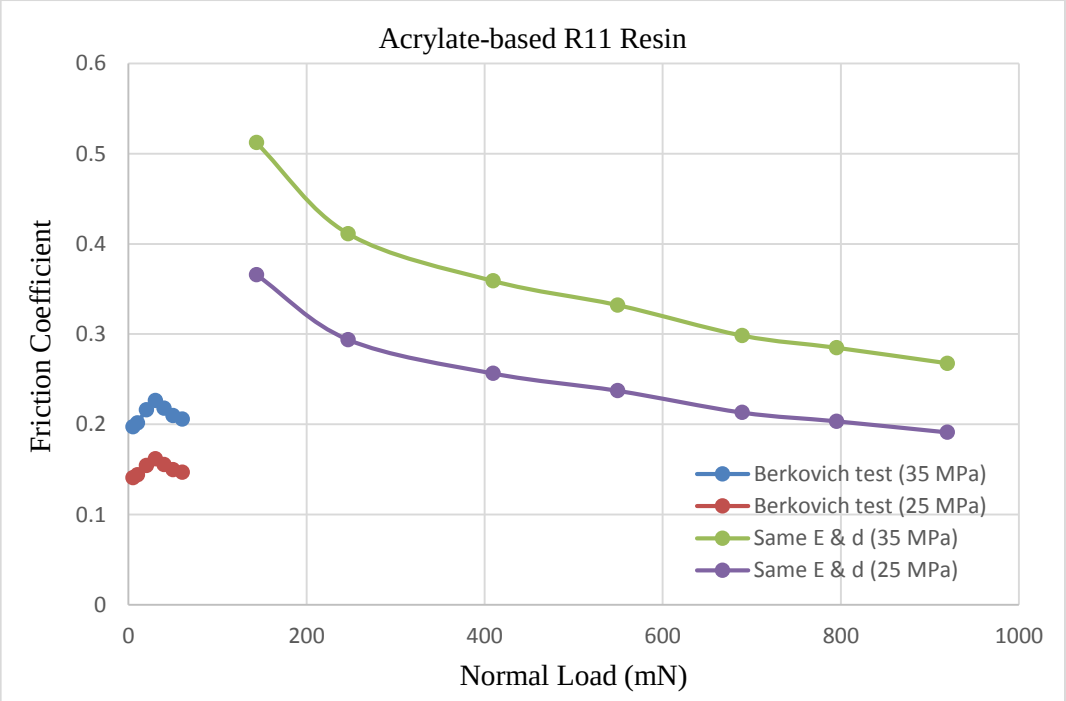

Figure 6.16 Predicted CoF against normal loads for the acrylic-based R11 resin in both Berkovich test and for the Hertz elastic contact model with ball-on-flat configuration

It is clear that none of the tested assumptions leads directly to a useful predictive model of the friction characteristics of the R11 MSL resin, which is a disappointing result because this is the material for which a strong correlation might have had the most significant benefits. While the other materials show better correlations between nano-indentation properties and friction, no specific modelling assumption appear to work consistently well. It is clear that the *E* values will need to be set empirically for specific cases, which represents a major practical concern about reliability. Hence, the provisional conclusion is that it will not be possible to replace micro-friction measurements by a reliable prediction from a nano-indentation test, even for routine production control.

7 Conclusions and Recommendations for Future Work

Overview

This chapter draws the conclusions about the work presented in this thesis and indicates directions of future research. The immediate challenge is that there is very little reliable information about the properties of this new generation of engineering materials due to insufficient understanding and characterization of their behaviour at the microscale under a wide range of experimental conditions. The capabilities of the instrument have been demonstrated by performing different types of engineering materials with ball-on-flat and comparing the consistency between ball-on-flat configurations and crossed-cylinders configurations in reciprocating scan mode. This study also provides new information of polymer materials used in MEMS applications and explores the potential usefulness of existing contact theories about friction by the nano-indentation tests compared to the micro-friction tests. Conclusions are hereby derived from three aspects including the custom-designed micro-tribometer, the micro-friction investigation of polymeric materials, and the correlations between nano-indentation measurement and micro-friction.

7.1 Conclusions

(1) Custom-designed Micro-tribometer

The next-generation micro-tribometer instrument, originally designed by Alsoufi (2011), was recommissioned at Warwick. Its main features have been described alongside its characteristics, including the novel micro-tribometer sensing head and notch-hinge mechanisms for driving the reciprocating scan mode. The test-rig was re-calibrated to regain the sensitivity of the sensors, the stiffness of the sensing beam in the vertical and lateral directions, the input-output relationship between the force actuator and applied normal load for the micro-tribometer measuring-head, and the parameter configurations of the reciprocating notch-hinge mechanisms. Calibration results were compared with the original ones for consistency checking. The modified control software (in LABview®) and repaired hardware provide the

parameters for efficient data processing and the control of critical friction-related test conditions including sliding velocity, scan length and applied forces in the vertical and lateral directions for micro-friction measurement at the micro-scale.

(2) Demonstration of the Test-rig

Prior to demonstration of the test-rig, the micro-tribological test method for the reciprocating micro-tribometer was introduced, and surface topography of test specimens, including silicon wafer with silicon dioxide film, steel and glass, were measured to test for any correlation between the sample surfaces and their friction properties. Then, tribometer signals from the sensing head were analysed in the vertical and lateral directions, when the beam is hanging freely or at a specified test condition including sliding frequency and normal load for silicon wafer with silicon dioxide film, steel and glass. Then, static and transient uncertainties at the small scale were considered to avoid the risk of misinterpreting certain types of results. After that, the calculation methods of reciprocating friction signals for normal load, friction force, and coefficient of friction were established for friction measurement according to our experiment calibrations and compared to the related literature. Finally, the calculations for normal load and friction force were analysed to highlight and explore the computational accuracy of friction measurement at the micro-scale.

The test-rig was demonstrated by illustrative experimental results on harder surface of silicon wafer with silicon dioxide film using ball-on-flat configurations at

three different scan lengths of 66 μm, 90 μm and 130 μm and three different scan frequencies of 3 Hz, 6 Hz and 9 Hz under dry sliding conditions where there were no applied lubricants. The experimental results showed that the friction force and CoF appear to be independent of track length and sliding speed, whereas friction force has just the linear relationship with normal load, matching well with Amonton's law in this test regime and with its known properties as an ideal silicon-based material.

Steel materials were used to analysis the availability and the consistency of developed test system for both ball-on-flat and crossed-cylinders configurations. The results showed that there was not a nearly consistent behaviour under the same test condition, but the considerable variation showed some common tendencies. Some possible reasons, such as the influence of different compositions of steel materials, and the modification of a hard oxide layer on the sample surface (without time to recover) during measurement, might be presented to explain the phenomenon. Nevertheless, there were still enough similarities in variations under the same test conditions between the two modes to show the availability and validity of the crossed-cylinders configuration. These relatively consistent tendencies illustrated a reasonable level of variations of the CoF with normal load for steel material, but the values were a little higher than expected ones in other literature.

Also, the crossed-cylinders configurations were used to provide very useful information for glass rod materials on the influence of the same parameters used in ball-flat configurations. The experimental results showed that the friction force and CoF for crossed glass rods were not independent of the sliding frequency at the same

track length. The CoF of the glass rod specimen fell with the increase of the track length and sliding frequency at normal loads applied in the range 10 mN to 60 mN, suggesting that the common cause was an inverse relationship between CoF and sliding speed across the present test regime, despite rather lower CoF of glass materials compared to those from the literature, led to some possible concerns about the use of this method with the current tribometer design. However, a different conclusion showed that the friction force and CoF for crossed glass rod were independent of the sliding frequency when the test conditions were at the same scan length of 130 μm and three different scan frequencies of 3 Hz, 6 Hz and 9 Hz, leading to a strong suspicion that this test was an outlier. Nevertheless, higher consistency in the pattern of behavior as parameter vary as the friction forces in both two scan lengths showed a good linear increase with applied normal loads. Thus, some possible reasons might be presented to explain the phenomenon, including the effects of sample cleaning, a fault in the set-up parameters or a wrong operational procedure during measurement, instrument limitations in the crossed-cylinder configuration.

(3) Micro-friction Investigation of Polymeric Materials

An initial set of experimental studies on nominally flat polymeric specimens of acrylic-based R11 resins, which derive from micro-stereo-lithography and PTFE that might be found in micro-mechanical system. The overall procedures, including surface topography measurement, tribometer signal analysis in both vertical and

lateral directions, and the calculations for normal load and friction force is broadly similar to, with test conditions in demonstrationg experiments at the micro-scale.

The experimental results are analysed to produce new data for the PTFE and MSL polymeric materials, which establishing the relationship between friction and nominal normal force with three different scan lengths of 66 μm, 90 μm and 130 μm and three different scan frequencies of 3 Hz, 6 Hz and 9 Hz under dry sliding conditions where there are no applied lubricants. For MSL polymeric materials, the friction forces show a excellent lineartiy over the working range ($R^2 > 0.99$) and experience a slightly decline with the increase of the track length at the same normal load or at the same scan length, but still remain in the range between 2 mN and 16 mN when the normal load applied is from 10 mN to 60 mN. The CoF falls in a similar way, from around 0.2 to about 0.15 with the increase of the track length and from around 0.3 to about 0.2 with the increase of sliding frequency when normal loads are applied from 10 mN to 60 mN. This drop could possibly be related to a higher contact repetition rate leading to some surface thermal variation but there is also increasing sliding speed. However, there is almost no variation of CoF with normal load at a single test condition, strongly suggesting an inverse relationship between CoF and sliding speed across the present test regime. Therefore, it is reasonable to conclude that the friction force and CoF for MSL material are not independent of the sliding frequency at the same track length.

For PTFE materials, the friction forces have somewhat poorer, but still good linearity, over the working range ($R^2 > 0.99$) and their values still remain in the 1

mN - 8 mN range for different scan frequencies and track lengths when the normal load applied is from 10 mN to 60 mN. The friction force is independent of track length at the same sliding speed but has just the linear relationship with normal load predicted by Amonton's law in this test regime, whereas it has an obvious upward tendency with the sliding frequency and normal load at the same scan length.

The CoF has some obvious fluctuations but has no clear trend with track length, remaining in a stable range at around 0.12 when the normal load is applied from 10 mN to 60 mN, illustrating that the CoF appear to be independent of the track length and sliding speed under these test conditions. However, the CoF changes from around 0.09 to about 0.12 as the scan speed is increased to 9 Hz and there is little fluctuation in CoF with normal load at each single test condition. In the present test regime, the relationship between CoF and scanning frequency is of opposite sense but lack of evidence for a sliding-speed dependence for the CoF of PTFE, this opens up the possibility that contact repetition rate in short reciprocating sliding contact adversely affects its performance, possibly by reducing the time for the surface conditions to relax following a perturbation. Nevertheless, the CoF of the PTFE material, drops to below 0.1 at a lowest scan speed and shortest scan length, matching well with its known properties as an ideal oil-free lubrication material. This study addresses one of the major motivations for this work by observing some behaviour patterns of the polymer materials, noting their variability and paving the way for future work.

(4) Correlations between Nano-indentation measurement and Micro-friction

Nano-indentation tests aimed to explores whether existing contact theories might allow inferences of practical usefulness about friction to be obtained from indentation data. MEMS materials and MSL polymeric materials, including silicon wafer with silicon dioxide coating, PTFE, and acrylic-based R11 resin, were chosen to measure their mechanical properties, such as the elastic modulus, hardness, indentation depth and contact area, using nanoindentation tester with a Berkovich indenter tip. Then, mathematical modelling was carried out to obtain the friction force, CoF and Berkovich nano-indentation against applied normal loads for comparisons between the contact model theories and experimental investigations.

The results for the CoF of silicon wafer with SiO_2 coating in both situations show a good consistency, remaining stable between 0.15 and 0.2 when the normal force is applied from 10 mN to 50 mN, close to Amonton's law prediction and match well with its known properties as an ideal silicon-based material.

However, the trends for PTFE specimens are not in agreement for two situations when the normal load is applied in the same range. The result for CoF at the assumption of the same load shows a decrease tendency from about 0.4 to around 0.14, while it is always around 0.12 for ball-on-flat configuration. However, the CoFs tend to drop to below 0.1 with normal load or sliding speed for the assumptions, Berkovich test and micro-friction test, matching well with its known properties and lubrication effect.

None of the tested assumptions leads to a useful predictive model of the friction

characteristics of the R11 MSL resin, possible due to its special surface properties. However, the trends are again in agreement for Berkovich tests with different shear strength (35 MPa or 25 MPa) and ball-on-flat configuration of the test-rig at the same scan speed of 9 Hz and two different scan lengths of 66 μm and 130 μm when the normal load is applied between 10 mN to 50 mN. The results for the CoF in both two situations show a good consistency, remaining stable around 0.15 or 0.2, associated to Amonton's law prediction.

It is clear that the E values will need to be set empirically for specific cases, which represents a major practical concern about reliability. Hence, the provisional conclusion is that it will not be possible to replace micro-friction measurements by a reliable prediction from a nano-indentation test, even for routine production control.

7.2 Recommendations for Future Work

(1) Extension of the Custom-designed Micro-tribometer

A pin-on-disc fixture with reasonable and constant sliding speeds over long, unidirectional traverses (essentially a small horizontal disc rotating with adequate precision under the ball) could be designed for use with the sensing-head designed by Alsoufi on the existing instrument. This configuration aims to give a high repetition rate of contact at the same points on the samples as an alternative to the 'spinning wire' scheme suggested and briefly discussed by Alsoufi, but after this further study regarded as possibly too difficult to control.

(2) Further Micro-tribological Studies

In the micro-friction study, only a few typical polymer materials were investigated in the ambient condition due to reasons discussed earlier. However, it would be worthwhile to study interesting materials especially with regards to the suitable coatings (spin-coating, dipping, spray-painting, *etc*.) and their thickness for high sliding speed and also to study the effect of humidity, temperature on micro-friction using the crossed-cylinders configurations of the test-rig.

Another investigation on how (uncompensated) sample tilt can affect estimates of friction coefficients could be carried out using the crossed-cylinders configuration. Nearly all practical micro-tribometers involve a spring in the generation of the normal force. Since friction coefficients are unlikely to be independent of normal loads of, say, <100 mN, an inclined sample can potentially provide misleading results by causing variations in the normal force along even fairly short traverses. The basic experiment runs sliding tests (back and forth) with sample tilts that will create notable, but practically plausible, changes to the normal force. Then, repeat the same test conditions with the normal force compensation mode enabled. The plan is to record decent amounts of data for some common materials (maybe, steel, silica and perspex rod) with the instrument in its passive mode and then analyse it by, e.g., taking mean values for normal and friction forces. Basic friction estimates can then be compared, as can graphs of how forces vary with position (or with time, which is similar). Choices of forces and tilts need to sensible and representative.

Overall, this work has identified the need for caution in applying the techniques investigated micro-tribometers at faster speeds than commercially available but also provides evidence of frictional behaviours that could be significant for next-generation polymer MEMS. There is clear benefit in undertaking further studies in this regime and extending it to a wider range of forces and speeds. Both new developments in the instrumentation and research into a wider range of polymer formulations are essential to this larger programme of future work.

References

Achanta, S., Drees, D., and Celis, J. P. (2005). Friction and nanowear of hard coatings in reciprocating sliding at milli-Newton loads, *Wear*, **259**: 719-729.

Achanta, S. *et al.* (2009). Friction mechanisms at the micro-scale, *Tribology International*, **42**: 1792–1799.

Adams, G. G. (2003). A scale-dependent model for multi-asperity contact and friction, *Journal of Tribology*, **125**: 700-708.

Adams, T. M. and Layton, R. A. (2010). Introductory MEMS, Fabrication and Applications, *Springer*, 9-11.

Alsoufi, M. S. (2011). A High Dynamic Response Micro-tribometer Measuring-head, Coventry: University of Warwick.

Ando, Y., *et al.* (1995). Friction characteristics and adhesion force under low normal load, *Journal of Tribology*, **117**(4): 569-574.

Ando, Y. (2003). Lowering friction coefficient under low loads by minimizing effects of adhesion force and viscous resistance, *Wear*, **254**: 965-973.

Angell, J. B., Terry, S. C. and Bath, P. W. (1983). Silicon, Micromechanical Devices, *Scientific American*, **248**(3): 36-47.

Anonymous (1998). Properties of silicon (EMIS Data Reviews Series No.4, London: INSPEC, institution of electrical engineers.

Antunes, J. M., *et, al.* (2006). Three-dimensional numerical simulation of Vickers indentation tests, *International Journal of Solids and Structures*, **43**: 784–806.

Bao, Y. W. (2004). Investigation of the relationship between elastic modulus and

hardness based on depth-sensing indentation measurements, *Acta Materialia*, **52**: 5397-5404.

Bertsch, A., Jiguets, S., Bernhard, P., Renaud, P. (2003). Micro-stereo-lithography: a review, *Mater Res Soc Symp Proc*, **758**: LL1.1.1–LL1.1.13.

Bhushan, B. (1995). Applications of micro/nano tribology to magnetic storage devices and MEMS, *Tribol. Int.*, **28**: 85-96.

Bhushan, B. (1999). Principles and Applications of Tribology, 1st ed. New York: Wiley-Interscience.

Bhushan, B (1999d). Chemical, mechanical and tribological characterization of ultra-thin and hard amorphous carbon coatings as thin as 3.5 nm: recent developments, *Diamond Relat. Mater.*, **8**: 1985-2015.

Bhushan, B. (2001). In Modern Tribology Handbook, CRC Press, Boca Raton, FL, **2**: 1515-1548.

Bhushan, B. (2005). Nanotribology and nanomechanics, *Wear*, **259**: 1507-1531.

Bisson, E. E. (1968). Friction, wear, and the influence of surfaces, *National aeronautics and space administration*, 1-2.

Blau, P. J. (2001). The significance and use of the friction coefficient, *Tribology international*, **34**(9): 585-591.

Bowden, F. P. and Tabor, D. (1964). The friction and lubrication of solids, Oxford, 52-53.

Bowden, F. P. and Tabor, D. (1964). The friction and lubrication of solids, Oxford, 124-169.

Burns D. J. (2004). On single-molecule DNA sequencing with atomic force microscopy using functionalized carbon nanotube probes, Cambridge: Massachusetts Institute of Technology.

Buyanovskii, A. (1994). Tribological test methods and apparatus, *Chemistry and Technology of Fuels and Oils*, **30**: 133-147.

Cabibbo, M., Ciccarelli, D., Spigarelli, S. (2013). Nanoindentation Hardness measurement in piling up SiO_2 coating, *Physics Procedia*, **40**: 100-112.

CETR-Bruker (2013). Universal Mechanical Tester and Tribometer, USA, Campbell: CETR-Bruker.

Chetwynd, D. G. and Alsoufi, M. S. (2010). A novel micro-friction measuring-head using force-feedback compensation, *SPIE*: Hangzhou, China, pp. 754417-9.

Cobb, J. A. (2008). A novel method for low load friction testing on living cells, *Biotechnology letters*, **30**(5): 801-806.

Corwin, D. and Boer, M. P. D. (2004). Effect of adhesion on dynamic and static friction in surface micromachining, *Applied Physics Letters*, **84**: 2451-2453.

Cruzadoa, A., *et al.* (2010). Fretting wear of thin steel wires. Part 1: Influence of contact pressure, *Wear*, **268**: 1409-1416.

Czichos, H. (1992). Design of friction and wear experiments, in Friction, Lubrication, and Wear Technology, *ASM Handbook* (ed. P.J. Blau), **18**.

Dowson D. (1998). History of tribology, 2nd ed., London: Professional Engineering Publishers.

Dvorak, S. D., Woodland, D. D. and Unertl, W. N. (1998). Nanotribometer: a new

instrument for nano-scale to micron-scale friction and wear measurements, *Tribology Letters*, **4**: 199-204.

Ehrfeld, W. and Munchmeyer D. (1991). Three-dimensional microfabrication using synchrotron radiation, *Nuclear instrument and methods in physics A*, **303**(3): 523-531.

Gardner, J. W., Varadan, V. K. and Awadelkarim, O. O. (2005). Microsensors MEMS and smart Devices, New York: JOHN WILEY & SONS, ISBN: 047186109X.

Gardos, M. N. (1999). Atmospheric effects of friction, friction noise and wear with silicon and diamond. Part I. Test methodology, *Tribology Letters*, **6**: 79-86.

Gee, M. G. *et al.* (2011). Micro-tribology experiments on engineering coatings, *Wear*, **271**: 2673-2680.

Gerbig, Y. B., Ahmed, S. I. U., Chetwynd, D. G. and Haefke, H. (2006). Topography-related effects on the lubrication of nanostructured hard surfaces, *Tribology International*, **39**: 945-952.

Guo, Z. S., Meng, Y. G., Wu, H., Su, C. J. and Wen, S. Z. (2007). Measurement of static and dynamic friction coefficients of sidewalls of bulk-microfabricated MEMS devices with an on-chip micro-tribotester, *Sensors and Actuators a-Physical*, **135**: 863-869.

Hasegawa, T. (2008). *Tribology Research Trends*, 1st ed. New York: Nova Science Publishers.

Hopton, B. (2009). Final report: Multi-test tribometer, University of Michigan:

MEMS Design and Manufacturing II.

Hutchings, I. M. (1992). Tribology, Friction and Wear of Engineering Materials, 1st ed. Oxford: Elsevier Limited.

Ikuta, K., Hirowatari, K. (1993). Real three dimensional microfabrication using stereo lithography and metal molding, *Proc IEEE MEMS*, 42-47.

Ikuta, K., Ogata, T., Tsubio, M., Kojima, S. (1996). Development of mass productive microstereolithography (Mass-IH process), *Proc IEEE MEMS*, 301–305.

Johnson, K. L. (1997). Adhesion and friction between a smooth elastic spherical asperity and a plane surface, *Proc. R. Soc. Lond. A*, **453**: 163-179.

Jones, S. E. *et al.* (2003). A one-dimensional analysis of rigid-body penetration with high-speed friction, *Proc. Instn Mech. Engrs Part C: J. Mechanical Engineering Science,* **217**: 411-422.

Joslin, D. L., Oliver, W. C. (1990). New method for analysing data from continuous depth-sensing microindentation tests, *Journal of Materials Research*, **5**(1): 123–126.

Kaneko, R. *et al.* (1996). Recent progress in microtribology, *Wear*, **200**: 296-304.

Katagi, T., Nakajima, N. (1993). Photoforming applied to fine machining, *Proc IEEE MEMS*, 173–178.

Kim, S. H., Asay, D. B., Dugger, M. T. (2007). Nanotribology and MEMS, *Nanotoday*, **2**: 22-29.

Kosinskiy M., *et al.* (2012). A compact reciprocating vacuum microtribometer, *Tribology International*, **56**: 81–88.

Kovaks, G. (1998). Micromachnined Tranducers Sourcebook, New York: WCB/Mc

Graw-Hill, ISBN: 0072907223.

Kragelsky, I. V. and Alisin, V. V. (1982). Friction, Wear, Lubrication: Tribology Handbook, Mir Publishers, Moscow, **1-3**.

Ku, I. S. Y. *et al.* (2010). A novel tribometer for the measurement of friction in MEMS, *Tribology International*, **43**: 1087–1090.

Le, H. R. *et al.* (2005). Friction and material transfer in micro-scale sliding contact between aluminium alloy and steel, *Tribology letters*, **18**(1): 99-104.

Leigh, S. J., *et al.* (2011). A miniature flow sensor fabricated by micro-stereolithography employing a magnetite/acrylic nanocomposite resin, *Sensors and Actuators A: Physical*, **168**: 66-71.

Leu, Daw-Kwei (2011), Evaluation of friction coefficient using indentation model of Brinell hardness test for sheeting metal forming, *Journal of mechanical science and technology*, **25**(6): 1509-1517.

Liu, H., *et al.* (2001). Microtribological properties of silicon and silicon coated with diamond like carbon, octadecyltrichlorosilane and stearic acid acdmium salt films: A comparative study, *Thin solid films*, **381**(1): 135-142.

Liu, H. W. and Bhushan, B. (2003). Adhesion and friction studies of microelectromechanical systems, nanoelectromechanical systems materials using a novel microtriboapparatus, *Journal of Vacuum Science & Technology*, **A21**: 1528.

Livermore, C. and Voldman, J. (2004). Material Properties Database.

Maboudian, R., Howe, R. T. (1997). Critical review: Adhesion in surface micromechanical structures, *J. Vac. Sci. Technol*, **B15**: 1-20.

Maboudian, R. (1998). Surface processes in MEMS technology, *Surface Science Reports*, **30**(6-8): 207-269.

Maboudian, R., Ashurst, W. R. and Carraro, C. (2000). Self-assembled monolayers as anti-stiction coatings for MEMS: characteristics and recent developments, *Sensors and Actuators A: Physical*, **82**(1-3), 219-223.

Maboudian, R. (2002). Tribological challenges in micromechanical systems, *Tribology Letters*, **12**(2): 95-100.

Man, K. F., Stark, B. H. and Ramesham, R. (1998). A Resource Handbook for MEMS Reliability, Rev. A. JPL Press, Jet Propulsion Laboratory, California Institute of Technology, Pasadena, CA.

Manish Roy (2011). Tribological investigation of nanocrystalline diamond films at low load under different tribosystems, *Diamond and related materials*, **20**(4): 573-583.

Marika Torbacke (2014). Tribological Test Methods, *Lubricants: Introduction to Properties and Performance*, **6**: 113-132.

Mikhail Kosinskiy, *et al.* (2012). A compact reciprocating vacuum microtribometer, *Tribology International*, **56**: 81–88.

Miller, B. P. *et al.* (2010). A Nano- to Macroscale Tribological Study of PFTS and TCP Lubricants for Si MEMS Applications, *Tribol Lett*, **38**: 69–78.

Mo, Yifei, *et, al.* (2009). Friction laws at the nanoscale, *Nature*, **457**: 1116-1119.

Mohr, J., Ehrfeld, W. and Munchmeyer, D. (1988). Journal of Vacuum Science & Technology B, 6, 2264.

Mollenhauer, O., *et al.* (2006). High-precision positioning and measurement systems for microtribotesting, *Lubrication Science*, **12**(3): 189-199.

Muller, R. S. (1990). *Microdynamics, Sensor and Actuator, A (Phys.)*, **A21-A23**: 1-8.

Muller, R. S. (1997). Microelectromechanical Systems, National Academy of Science, Washington, D. C.

Munchmeyer, D. and Langen, J. (1992). Manufacture of three-dimensional microdevices using synchrotron radiation, *Review of scientific instruments*, **63**, 713.

Myshkin, N. K., Petrokovets, M. I. and Kovalev, A. V. (2005). Tribology of polymers: Adhesion, friction, wear, and mass-transfer, *Tribology International*, **38**: 910-921.

Niels Tas (2000). Electrostatic Micro Walkers - Micro Electromechanics and Micro Tribology, Ph.D. Thesis, The Netherlands, Enschede: University of Twente.

Nosonovsky, M. and Bhushan, B. (2007). Multiscale friction mechanisms and hierarchical surfaces in nano- and bio-tribology, *Materials Science & Engineering R-Reports*, **58**: 162-193.

Oliver, W. C., Pharr, G. M. (1992). An improved technique for determining hardness and elastic-modulus using load and displacement sensing indentation experiments, *Journal of Materials Research*, **7**(6): 1564-1583.

Osamu Takakuwa (2013). Estimation of the yield stress of stainless steel from the Vickers hardness taking account of the residual stress, *Journal of surface engineered materials and advanced technology*, **3**: 262-268.

Philippe Stempfle and Jamal Takadoum (2012). Multi-asperity nanotribological behavior of single-crystal silicon: Crystallography-induced anisotropy in friction and wear, *Tribology International*, **48**: 35-43.

Provin, C., Monneret, S., Gall, H. L., Corbel, S. (2003). Three-dimensional ceramic microcomponents made using microstereolithography, *Advanced Materials*; **15**(12): 994–997.

Qing, T., Shao, T., Wen, S. (2007). Micro-friction and adhesion measurement for Si wafer and TiB_2 thin film, *Tsinghua Science and Technology*, **12**(3): 261-268.

Rae, P. J. and Brown, E. N. (2005). The properties of poly(tetrafluoroethylene) (PTFE) in tension, *Polymer*, 7615-7625.

Sakharova, N. A., *et al.* (2009). Comparison between Berkovich, Vickers and conical indentation tests: A three-dimensional numerical simulation study, *International Journal of Solids and Structures*, **46**: 1095–1104.

Singer, I. L. and Pollock, H. M. (1992). Fundamentals of Friction: Macroscopic and Microscopic Processes, Netherlands: Kluwer Academic, Dordrecht.

Singh, R. A. (2007). Replication of surfaces of natural leaves for enhanced micro-scale tribological property, *Materials Science and Engineering*, **C27**: 875-879.

Singh, R. A. (2009). Bio-inspired dual surface modification to improve tribological properties at small-scale, *Applied Surface Science*, **255**: 4821–4828.

Singh, R. A., Satyanarayana N. and Sinha, S. K. (2013). Nano/Micro-Tribological Properties of MEMS/NEMS Materials, *Nano-tribology and Materials in MEMS*,

Springer-Verlag Berlin Heidelberg.

Smith, S. T., Harb, S., Eastwickfield, V., Yao, Z. Q., Bartlett, P. N., Chetwynd, D. G. and Gardner, J. W. (1993). Tribological Properties of Electroactive Polymeric Thin-film Bearings, *Wear*, **169**: 43-57.

Takada, H., *et al.* (1997). Development of LIGA process using a superconducting compact synchrotron light source, *Electrical Engineering in Japan*, **120**(1): 40-48.

Tambe, N. S. and Bhushan, B. (2004). Scale dependence of micro/nano-friction and adhesion of MEMS/NEMS materials, coatings and lubricants, *Nanotechnology*, **15**: 1561-1570.

Tanner, D. M., *et al.* (1999). The effect of humidity on the reliability of a surface micromachined microengine, IEEE international reliability physics symposium, March 21–25, San Diego, 189-197.

TETRA GmbH (2008). BASALT–MUST Modular Universal Surface Tester, IImenau: TETRA GmbH.

Tichy, J. A. and Meyer, D. M. (2000). Review of solid mechanics in tribology, *International Journal of Solids and Structures*, **37**: 391-400.

Van Spengen M. W. (2003). MEMS reliability from a failure mechanisms perspective, *Microelectronics Reliability*, **43**: 1049–1060.

Van Spengen M. W. (2007). The leiden MEMS tribometer: real time dynamic friction loop measurements with an on-chip tribometer, *Tribology letters*, **28**: 149-156.

Wang, Y. and Yan, F. (2006). Tribological properties of transfer films of PTFE-based

composites, *wear*, **261**: 1359–1366.

Wasche, R., Hartelt, M. (2008). Wear testing with crossed cylinders - comparison of methods, in: W.J. Bartz (Ed.), Proceedings of the 16th International Colloquium on Tribology, Technische Akademie Esslingen, Ostfildern, January 15–17.

Wen, S. (1990). Principles of tribology, Beijing: Tsinghua University Press.

Wolfram Hild, *et al.* (2007). Microtribological properties of silicon and silicon coated with self-assembled monolayers: effect of applied load and sliding velocity, *Tribology Letters*, **25**(1): 1-7.

Xu, D., Chetwynd, D. G. and Covington, J. A. (2011). A method for tensile testing of delicate polymeric parts, *Proc. 11th euspen Int. Conf.*, Como, **1**: 175-178.

Yoon E. S. (2006). Tribological properties of bio-mimetic nano-patterned polymeric surfaces on silicon wafer, *Tribology letters*, **21**(1): 31-37.

Yoshihiro Hirata (2003). LIGA process–micromachining technique using synchrotron radiation lithography and some industrial applications, *Nuclear Instruments and Methods in Physics Research B*, **208**: 21-26.

Zhao, Y. P., Wang, L. S. and Yu, T. X. (2003). Mechanics of adhesion in MEMS - a review, *Journal of Adhesion Science and Technology*, **17**(4): 519-546.

Zhuang, Y. X. and Menon, A. (2005). On the stiction of MEMS materials, *Tribology Letters*, **19**(2): 111-117.

Zhou, B. (2011). A study of the frictional properties of senofilcon-A contact lenses, *Journal of the mechanical behavior of biomedical materials*, **4**: 1336-1342.

Appendix

A: Preliminary Test Results of Re-calibration of the Test-rig

(1) Sensing-beam stiffness in the lateral direction

	Deflection of the lateral sensor (V)							
Weight (g)	Test 1		Test 2		Test 3		Test 4	
1.0998	6.118	6.218	6.1111	6.1867	6.1092	6.195	6.1085	6.1925
2.0638	6.1181	6.272	6.1106	6.2648	6.1088	6.2562	6.1084	6.2605
5.1106	6.1143	6.48	6.1088	6.4746	6.1085	6.4813	6.1086	6.4754
10.2492	6.1163	6.8712	6.1103	6.833	6.1084	6.8634	6.1081	6.8713
20.2089	6.1125	7.5648	6.111	7.6236	6.107	7.5835	6.1083	7.5904

(2) Sensing-beam stiffness in the vertical direction

	Deflection of the vertical sensor (V)							
Weight (g)	Test 1		Test 2		Test 3		Test 4	
10.79123	5.9122	5.9968	5.9185	6.0009	5.9132	6.0024	5.915	6.0024
20.24998	5.9096	6.0707	5.916	6.0781	5.9147	6.078	5.918	6.0766
50.14516	5.9118	6.2923	5.917	6.3039	5.916	6.3101	5.9162	6.3049
100.565	5.9123	6.7124	5.9148	6.7051	5.9161	6.7049	5.9159	6.7037
198.2895	5.9135	7.4333	5.9138	7.4167	5.9172	7.4647	5.9152	7.475

(3) Sensitivity of the lateral sensor

	Lateral sensor (V)		
Displacement (μm)	Test 1	Test 2	Test 3
0	0.986	0.999	1
50	2.05	2.065	2.066
100	3.112	3.125	3.122
150	4.169	4.168	4.177
200	5.223	5.219	5.227
250	6.27	6.261	6.275
300	7.312	7.298	7.308
350	8.347	8.322	8.335
400	9.356	9.328	9.339
450	10.319	10.294	10.301
500	11.216	11.195	11.196

(4) Sensitivity of the vertical sensor

	Vertical sensor (V)		
Displacement (μm)	Test 1	Test 2	Test 3
0	0.992	1.003	1.001
50	2.251	2.273	2.266
100	3.524	3.549	3.54
150	4.792	4.811	4.802
200	6.027	6.04	6.031
250	7.198	7.201	7.194
300	8.306	8.253	8.244
350	9.194	9.142	9.136
400	9.888	9.842	9.84
450	10.394	10.353	10.351
500	10.731	10.692	10.692

(5) Relationship between force actuator and normal load

	Deflection of the vertical sensor (V)				
Force actuator (V)	Test 1	Test 2	Test 3	Test 4	Test 5
0	5.9087	5.9477	5.9474	5.9208	5.9538
0.25	5.9579	5.9957	5.9962	5.9699	6.0026
0.5	6.007	6.0444	6.0447	6.0191	6.0498
0.75	6.055	6.0914	6.0913	6.0667	6.0958
1	6.1014	6.1376	6.1374	6.1131	6.1367
1.25	6.1492	6.1839	6.183	6.1598	6.1842
1.5	6.1964	6.23	6.2292	6.2063	6.2294
1.75	6.2435	6.2762	6.2752	6.2534	6.2753
2	6.2905	6.3224	6.321	6.299	6.3276
2.25	6.3393	6.3689	6.3674	6.3454	6.3685
2.5	6.377	6.404	6.4017	6.3828	6.4039
2.75	6.3773	6.4029	6.4019	6.3834	6.407
3	6.3811	6.4033	6.4022	6.3838	6.4085

(6) Relationship between the gain of the power oscillator and the reciprocating displacement of the notch-hinge flexure

	Displacement of the notch-hinge mechanisms		
Gain (db)	Test 1 (4.5 Hz)	Test 2 (4.5 Hz)	Test 3 (7 Hz)
0	7.56693	6.90894	7.56694
1	7.56694	6.90894	8.22493
2	13.81788	16.77885	13.15989
3	32.24172	33.88671	33.22871
4	52.31054	50.99456	46.71759
5	63.82544	64.48344	65.79943
6	81.2623	80.6043	82.90728
7	85.53925	89.48723	89.81622
8	104.29209	107.58207	112.18802
9	124.36092	126.00591	129.95387
10	158.90562	160.8796	164.16958
11	226.67903	230.298	240.16792
12	294.12344	290.17548	303.00636
13	346.76299	348.07898	355.31691
14	410.58844	407.62746	416.18139

B: Original Programs of the Signals Analysis in Both Vertical and Lateral Deflections

(1) MatLab script file to calculate the vertical deflections, Δz, of the sensing-beam micro-tribometer

```
%%read the data
[x1]=textread('e:/chn0.txt','%f');
%%plot the original data
figure(1);
plot(x1);
a0=std(x1);
%%read the data above the mean and plot the data
y0=mean(x1);
b0=x1(469:760);
figure(2);
```

```
plot(b0);
y1=mean(b0);
a1=std(b0);
%%select the data you wanted
b1=x1(924:2031);
figure(3);
plot(b1);
a2=std(b1);
y2=mean(b1);
%%select the data you wanted
b2=x1(2803:4013);
figure(4);
plot(b2);
a3=std(b2);
y3=mean(b2);
```

(2) MatLab script file to calculate the lateral deflections, Δx, of the sensing-beam micro-tribometer

```
%read the data
[x1]=textread('e:/chn1.txt','%f');
%%plot the original data (first 10 cycles)
figure(1);
plot(x1);
%%select the data you wanted
b=x1(1:6200);
figure(2);
plot(b);
%%select the data sets
b1=b(83:88);
b2=b(143:146);
b3=b(196:200);
b4=b(254:259);
b5=b(304:307);
b6=b(364:367);
b7=b(412:416);
b8=b(479:481);
b9=b(524:528);
b10=b(586:590);
```

```
b11=b(637:639);
b12=b(695:699);
b13=b(745:749);
b14=b(803:806);
b15=b(858:861);
b16=b(916:919);
b17=b(968:971);
b18=b(1029:1032);
b19=b(1078:1082);
b20=b(1137:1140);
%%read the data above the mean and plot the data
y1=[b1;b2;b3;b4;b5;b6;b7;b8;b9;b10;b11;b12;b13;b14;b15;b16;b17;b18;b
19;b20];
figure(3);
plot(y1);
y2=[b1;b3;b5;b7;b9;b11;b13;b15;b17;b19];
y3=[b2;b4;b6;b8;b10;b12;b14;b16;b18;b20];
H=[max(y2),min(y2)];
L=[max(y3),min(y3)];
% %%read the data above the mean and plot the data
a1=std(y2);
% %%calculate the mean of the data
y11=mean(y2);
a2=std(y3);
% %%calculate the mean of the data
y22=mean(y3);
% %% calculate the distance between the two means
z1=mean(y11)-mean(y22);
```